Université de Liège
Faculté des Sciences
Département de physique

Bridging Concepts of Quantumness: Phase-space, Entanglement and Anticoherence in Spin Systems

Jérôme Denis

A thesis submitted in partial fulfillment of the requirements for the degree of Doctor of Philosophy in Sciences

supervised by Prof. John Martin

Academic year 2025-2026

Remerciements

Quelques semaines avant de finaliser ce manuscrit, une connaissance nouvellement diplômée m'a demandé si j'avais "apprécié mes années de doctorat" ? La question étant du genre de celles que je me pose rarement à moi-même, il m'aura fallu un certain temps d'introspection pour y répondre. Et bien que je sois enthousiasmé par mes résultats de recherche, qui m'auront amené plusieurs moments de grande béatitude, c'est finalement surtout les relations avec mes collègues, amis et camarades qui auront été à l'origine de tant de moments inoubliables ces six dernières années. J'aimerais donc en remercier ici un certain nombre d'entre eux. Profitez-en, ce sera la première et dernière fois.

Comme il se doit, je remercie tout d'abord mon superviseur, John Martin, pour sa disponibilité et son aide, surtout en début de thèse. Il aura toujours su encadrer mon travail de manière encourageante, avec une rigueur et une précision qui force le respect.

Many thanks to the jury members, Thierry Bastin, Nicolas Cerf, François Damanet, Giuseppe Vitagliano and Karol Życzkowski. I hope you will find as much pleasure in reading this manuscript as I found in carrying out the work behind it. I am also deeply grateful to my collaborators, Robert and Jack, it was a true pleasure working with you.

Merci aux collègues, qui auront rendu le B15a, le B15b, le B15c, ainsi que le B15b bis, aussi vivants que ce qu'un bloc de béton peut l'être. Particulièrement à François et Baptiste pour les premières soirées dans le Carré, dont les invités internationaux ont ensuite pu profiter aussi. A Colin, dont l'Irish est encodé dans l'hippocampe. A Céline et Pierre qui auront accompagné mes premières années à l'IPNAS. Et, last but not least, à Jonathan, a.k.a. le RRRrrat, et Eduardo, le plus mexicain des mexicains. On se revoit en Corée du... Sud.

A l'ordre des physiciens disparus et affiliés, Quentin, Nicolas, Bouglione, Olivier, Emilien, Adrienne, Adrien et Maxime (et Vincent ???). Merci pour les chapis de quand ils étaient mieux, les 421 à n'en plus finir, le beach-volley au granita et d'avoir toujours cru que je pouvais apprendre la belotte. A Virgi, pour le thé et les emails. T'inquiète, après les examens on se craque des boîtes sur la plage.

Aux camarades, et particulièrement Samuel et Olivier. J'aurai eu à surmonter les moments les plus stressants de ma vie avec vous, et j'en suis très content. Hasta la victoria siempre ![1]

A la famille, papa, maman, papy, granny, Nico, Arnaud, Anaëlle, Stéphanie et Valérie. Mention spéciale aussi à Nathalie.

Et enfin, merci Margot pour ton soutien toutes ces années et pour tout ce que tu m'app... Haha... non. Juste merci d'être cette personne étrange à mes côtés et dont la présence est si logique et naturelle et pourtant toujours si... surprenante ? Tu es celle qui me prouve qu'au final, ce qui compte, c'est le chemin et non la destination. J'espère que tu ne prendras pas les ampoules quand ce sera fini.

[1] Pas d'inquiétude, contrairement au Che, je ne quitte bien sûr pas le parti.

Contents

Abstract

In quantum physics, several concepts have been developed to capture the distinctive characteristics of quantum states that have no classical equivalent. Among the most important are non-locality, entanglement and non-classicality, the latter generally identified with the negativity of quasi-probability distributions in phase space. More recently, the idea of anticoherence, defined by the isotropy of spin states resulting from quantum superpositions, has emerged as another distinctive feature of quantum states.

Although these different forms of "quantumness" are becoming increasingly central to the understanding and development of quantum foundations and quantum technologies, and are becoming experimentally accessible, their fundamental nature and interconnections are still only partially understood. The aim of this thesis is two-fold. First, we study and characterise the quantum nature of spin states through entanglement, non-classicality and anticoherence, with a particular focus on the relationships between these concepts. Second, we propose and analyse experimental protocols for estimating the entanglement of multiqubit states and for generating maximally entangled anticoherent states, thereby paving the way for their use in future quantum applications.

Résumé

En physique quantique, plusieurs concepts ont été développés pour saisir les caractéristiques distinctives des états quantiques qui n'ont pas d'équivalent classique. Parmi les plus importants, on trouve la non-localité, l'intrication et la non-classicité, cette dernière étant généralement identifiée à la négativité des distributions de quasi-probabilité dans l'espace des phases. Plus récemment, l'idée d'anticohérence, définie par l'isotropie des états de spin résultant des superpositions quantiques, est apparue comme une autre caractéristique distinctive des états quantiques.

Bien que ces différentes formes de « quanticité » occupent une place de plus en plus centrale dans la compréhension et le développement des fondements quantiques et des technologies quantiques, et qu'elles deviennent accessibles expérimentalement, leur nature fondamentale et leurs interconnexions ne sont encore que partiellement comprises. L'objectif de cette thèse est double. Tout d'abord, nous étudions et caractérisons la nature quantique des états de spin à travers l'intrication, la non-classicité et l'anticohérence, en mettant particulièrement l'accent sur les relations entre ces concepts. Ensuite, nous proposons et analysons des protocoles expérimentaux pour estimer l'intrication des états multiqubits et pour générer des états anticohérents maximallement intriqués, ouvrant ainsi la voie à leur utilisation dans de futures applications quantiques.

Publications

This thesis builds upon the following works.

- J. Denis and J. Martin, *Extreme depolarization for any spin*, Phys. Rev. Res. 4, 013178 (2022).
- J. Denis, F. Damanet and J. Martin, *Estimation of the geometric measure of entanglement with Wehrl moments through artificial neural networks*, SciPost Phys. 15, 208 (2023).
- E. Serrano-Ensástiga, J. Denis and J. Martin, *Absolute-separability witnesses for symmetric multiqubit states*, Phys. Rev. A 109, 022430 (2024).
- J. Denis, J. Davis, R. B. Mann and J. Martin, *Polytopes of absolutely Wigner bounded spin states*, Quantum 8, 1550 (2024).
- J. Denis, C. Read and J. Martin, *Coherent Generation and Protection of Anticoherent Spin States*, arXiv:2505.06154 (2025).

Introduction

What is... entanglement?

Unknown author

This year 2025, declared the International Year of Quantum Science and Technology by the United Nations, marks a century since Werner Heisenberg's groundbreaking paper that transformed the "old quantum theory" into modern quantum mechanics. It also coincides with the 90th anniversary of the famous Einstein-Podolsky-Rosen (EPR) paper [1], widely regarded as the first to explicitly raise the question of non-locality in multipartite quantum systems. Yet, despite decades of study, the very nature of entanglement remains only partially understood. More intriguingly, a variety of other concepts, such as quantum discord, contextuality, magic, EPR steering and non-gaussianity, have since been introduced to capture the departure of quantum states from classicality. These notions have enriched our understanding of the quantum world, but they have also blurred the boundaries of what we truly mean by *quantumness*.

The persistence of such foundational questions on the nature of the quantum world, however, has not hindered the rapid development of quantum experiments and technologies. On the contrary, the rise of quantum information science has created new opportunities to illuminate quantum foundations themselves [2, 3], revealing a constant dialogue between theory and experiment, each nourishing and challenging the other. For entanglement, Bell inequalities and their experimental verifications constitute an emblematic illustration of this dialectical interplay. In this spirit, the present thesis, although theoretical in nature, pursues both new theoretical insights and original protocols aimed at making extreme form of quantumness experimentally accessible.

It is not new that quantum physics has shaped real-world technologies. The first quantum revolution, which led to the development of semiconductors, transistors, lasers, magnetic resonance imaging, and atomic clocks, was largely rooted in the exploitation of quantised energy levels of single quantum systems. In contrast, the emerging second quantum revolution relies on quantum resources such as coherence and superpositions of states in individual and multipartite quantum systems. The experimental platforms enabling this revolution include, among others, superconducting qubits and qudits, quantum dots, polarised photons, the (hyper)fine structure of atoms and energy levels of molecules, all examples of systems sharing the common feature of being finite-dimensional. Following this path, the present thesis explores single spin and multiqubit systems as paradigmatic finite-dimensional systems. We will focus on three distinct quantum features: entanglement, negativity of probability quasidistributions (that we will denote as non-classicality throughout this thesis) and anticoherence.

Entanglement

Entanglement in multipartite quantum systems is fundamentally characterised by the impossibility of describing the global state as a simple factorisation of its subsystems states. In other words, certain properties of the whole system do not reside in the individual subsystems taken separately, but emerge from their intercorrelations. For this reason, entanglement is often regarded as a genuinely non-local feature, exhibiting correlations stronger than any achievable within classical physics. The study of entanglement in multiqubit systems already has a long and rich history, with many profound results [4]. For instance, determining and quantifying entanglement is known to be an NP-hard problem [5], with a complete solution available only in the simplest cases [6, 7]. Consequently, the complete characterisation of the boundary of the set of entangled states, or, equivalently, of the set of separable states, remains unresolved.

In parallel, entangled states have become indispensable resources across virtually all areas of quantum physics, including quantum communication [8], quantum computing and quantum metrology [9]. This operational relevance is formally captured within the framework of quantum resource theories [10], where entanglement is established as a central resource. Within this context, a particular class of separable mixed states, known as Absolutely Separable (AS), is of special interest. AS states are considered free states in entanglement resource theory since they cannot be transformed into entangled states under any unitary evolution. From an experimental perspective, where unitary transformations constitute the natural set of accessible operations, absolute separability thus marks the boundary of mixedness beyond which entanglement can no longer be generated by unitary controls alone. The characterisation of the set of AS states, though still incomplete, has recently opened new lines of research and attracted renewed interest [11, 12, 13]. In this thesis, our exploration of quantumness in multiqubit states will naturally lead us to investigate the boundaries of the AS set.

Non-classicality

Remarkably, a few years before the formulation of the EPR paradox, Eugene Wigner introduced his celebrated quasiprobability distribution [14], originating from a map from operators on an infinite-dimensional Hilbert space to functions on phase space. This distribution, now known as the Wigner function, provides a natural generalisation of classical probability distributions to quantum systems. More than a mere visualisation tool, the Wigner function opened a new avenue for studying quantumness: it can take negative values, and Hudson's theorem shows that a pure state has an everywhere non-negative Wigner function if and only if it is Gaussian. Gaussian states and Gaussian operations are efficiently classically simulable [15], so Wigner negativity is naturally associated with non-classical behaviour and quantum advantage [16, 17, 18].

Following Wigner, two other phase-space functions became standard for infinite-dimensional systems. These are the Husimi Q function [19, 20] and the Glauber-Sudarshan P function [21, 22]. While introduced separately, it is now known that these three phase-space functions belong to a same family of phase-space representations parameterised by a continuous parameter $s \in [-1, 1]$. This family can be retrieved by the Stratonovitch-Weyl (SW) formalism, based on the symmetries of the quantum system, to define covariant maps from the linear operators space to functions space. For instance, the relevant symmetry of a d-mode bosonic system is expressed through the Heisenberg-Weyl group of

position and momentum translations. The SW covariance then implies that the phase-space manifold is $\mathbb{R}^{2d}$.

For finite-dimensional systems, both discrete and continuous phase-space constructions exist. On the discrete side, Wootters introduced a discrete Wigner function for qudits in 1987 [23]. In odd prime dimensions, a discrete version of Hudson's theorem holds: a pure state has a non-negative discrete Wigner function if and only if it is a stabiliser state. Stabiliser states are classically simulable under Clifford dynamics. This connects discrete Wigner negativity to magic and computational advantage [24]. Discrete phase-space methods have also powered applications in quantum state tomography.

By contrast, continuous phase-space representations for finite-dimensional systems have been comparatively less explored. They are nevertheless compelling as they can exhibit negativity. While strong evidence suggests that no pure spin state admits an everywhere-positive continuous Wigner function for finite-dimensional systems, to our knowledge a general proof remains open. This underlines the subtlety of continuous phase-space methods in finite dimension induced by the non-trivial manifold $\mathcal{S}^2$, i.e. the 2-sphere, over which these phase-space representations are defined. Interestingly, the SW formalism also applies to finite-dimensional systems and the counterpart of the s-parameterised family of phase-space representations, containing the Wigner, Husimi and Glauber-Sudarshan functions, can also be derived for finite-dimensional systems. A central goal of this thesis is to deepen our understanding of these three emblematic functions in finite-dimensional systems and to identify novel ways to exploit them.

Anticoherence

A third manifestation of quantumness investigated in this thesis is the recently introduced concept of anticoherence [25]. In spin systems, anticoherence is directly tied to the isotropy of spin expectation values. A paradigmatic example is the Schrödinger spin-cat state, a superposition of angular momentum states pointing in opposite directions and for which

$$\langle \mathbf{J} \rangle = 0,$$

where $\mathbf{J}$ is the spin operator, hence not favoring any particular direction. Anticoherence thus arises as a genuinely quantum feature enabled by superpositions of states. By constructing increasingly complex superpositions, one can further increase the isotropy of a spin state, in a way that can be formally quantified through anticoherence measures.

Anticoherent states have already found promising applications in quantum metrology [26–28], quantum computation [29], and the broader characterisation of quantumness [30]. Counterintuitively, the usefulness of anticoherent states in quantum metrology stems from the fact that they maximise the total variance of the spin operator $\mathbf{J}$, thereby maximising quantum uncertainty, exactly the opposite of coherent states. This stands in sharp contrast to spin-squeezed states, which are exploited in metrology precisely because they minimise uncertainty along a chosen degree of freedom. This capability of anticoherent states stems from their high degree of symmetry, often associated with Platonic solids, which makes them particularly advantageous when the direction of the applied transformation is unknown. Some anticoherent states have already been experimentally generated in multiphoton systems, where their utility for quantum rotosensing has been demonstrated [31]. However, their generation in atomic platforms has so far remained an open challenge.

Given the recent definition of anticoherence, it is reasonable to expect that new theoretical properties and practical applications will continue to emerge. Some of these advances are presented within this thesis.

Aim of this thesis

While conceptually distinct, one of the main goals of this work is to uncover and clarify the interconnections between these three features of quantumness (entanglement, nonclassicality and anticoherence) and to show how one can be used to characterise another. A second major goal is to find new ways to experimentally generate, measure and exploit these forms of quantumness.

The manuscript is organised as follows.

Chapter 1 introduces single spin and multiqubit systems (restricted to their symmetric Hilbert subspace) together with some of their emblematic states, along with the mathematical tools required to study them. We present both continuous and discrete phase-space representations derived from the Stratonovich-Weyl formalism and recall the properties of the Wigner, Husimi, and Glauber-Sudarshan functions. We also highlight a possible generalisation of these phase-space representations that will be exploited later. Finally, we briefly recall the notions of entanglement and separability and discuss the entanglement criteria and measures which will be used throughout the manuscript.

Chapter 2, based on [32, 33], investigates spin states whose SW phase-space representations remain everywhere-positive under any unitary transformations, namely the Absolutely Stratonovich-Weyl Positive (ASP) states. While the discussion mainly focuses on continuous phase-space, we also show how the results extend to the discrete case. We completely characterise the sets of ASP states for any spin quantum number j, which appear as polytopes in the simplex of mixed state eigenvalues. Exploiting the connection between positivity of the Glauber-Sudarshan function and separability, we identify new symmetric absolutely separable (SAS) multiqubit states. Furthermore, we develop explicit nonlinear generalisations of SW phase-space representations whose existence was previously known but never exploited, allowing us to further enlarge the set of known SAS states.

Chapter 3, based on [34], explores the use of the Husimi phase-space representation to quantify entanglement in multiqubit systems. We begin by establishing an analytical relation between the moments of the Husimi function and the geometric measure of entanglement (GME) of symmetric multiqubit states. Inspired by this relation, we employ modern machine learning tools to propose a new protocol that would allow to estimate the GME of symmetric multiqubit states from only partial information about the state, namely from the moments of the Husimi function. Finally, exploiting the concept of spherical designs, we show how these moments can be experimentally accessed from Stern-Gerlach projections.

Chapter 4, mainly based on [35], focuses on anticoherent states. We first recall the concept of anticoherence of pure states and illustrate its relation with delocalisation on phase-space representations. We then recall properties of anticoherent states for quantum metrology and show that they also are promising states for quantum error-correction. Next, we establish a precise relation between the degree of anticoherence of a state and its entanglement, which we then use to generalise anticoherence measures to mixed states. Finally, we propose a pulse-based protocol, relying solely on rotation and squeezing pulses, to generate anticoherent states in atomic platforms. Unlike a black-box approach, the

effectiveness of this protocol admits an intuitive explanation, and it is directly implementable with current experimental capabilities.

Chapter 5, mainly based on [36], studies the decoherence of multiqubit systems under a collective depolarisation master equation. Using the analytical solution of the mixed state dynamics, we show that anticoherent states are particularly fragile against collective depolarisation. We also demonstrate that entanglement is a necessary condition for the decoherence rate to scale quadratically with the number of qubits, a phenomenon known as superdecoherence. Finally, we show how these results may be exploited in dynamical dissipative quantum metrology, where the aim is to estimate dissipative rates. In this context, we identify the entangled states that are optimal for quantum thermometry and noisy magnetometry.

This manuscript concludes with a global summary, synthesising the results presented across the different chapters, followed by perspectives that I find particularly compelling.

The numerical simulations for this thesis were performed in the Julia programming language [37], with most figures generated using the Makie package [38]. Analytical derivations were performed with the assistance of Mathematica.

Chapter 1

Spin systems, phase space and entanglement

In this first chapter, we present the key concepts and known results that will serve as the foundation for the remainder of this thesis. Section 1.1 begins with an introduction to quantum spin systems (or, equivalently, multiqubit systems whose Hilbert space is restricted to the symmetric subspace), which constitute the central framework of our study. We describe the experimental platforms where such systems naturally arise and highlight several emblematic spin states that will play a central role in later chapters. In addition to the standard spin basis, we also introduce the multipolar tensor operator basis, which proves particularly useful for analysing spin systems. We end the section by introducing the Majorana representation which constitutes a convenient way to visualise symmetric multiqubit states.

Since one of the main objectives of this thesis is to explore the interplay between phase-space representations of spin states and their entanglement properties, Section 1.2 introduces a family of continuous phase-space representations derived from the Stratonovich-Weyl formalism. This family encompasses the well-known Husimi, Wigner, and Glauber-Sudarshan representations. To illustrate the broader scope of our following results, we also briefly discuss discrete phase-space representations.

Finally, in Section 1.3, we turn to the concept of entanglement, with a focus on symmetric multiqubit states. We discuss the criteria for characterising entanglement versus separability, and introduce the entanglement measures that will be used throughout this work to quantify quantum correlations.

1.1 Spin systems and where to find them

In this thesis, we investigate the most elementary quantum systems, that is individual quantum spin systems. They may originate from both the (rotational-)spatial structure of physical configurations and intrinsic particle properties such as spin. These systems are ubiquitous in nature, appearing in diverse contexts including atomic electronic structures, light polarisation, and Bose-Einstein condensates. The central objective of this section is to describe the unifying feature of these systems: their description in terms of quantum angular momentum operators $\{J_x, J_y, J_z\}$ which obey the canonical commutation relations

$$[J_\alpha, J_\beta] = i\epsilon_{\alpha\beta\gamma} J_\gamma \tag{1.1}$$

where $\epsilon_{\alpha\beta\gamma}$ is the Levi-Civita symbol. Rather than focusing on a specific physical realisation, the approach adopted in this work is intentionally abstract. The analysis is based solely on the mathematical structure common to all spin systems, thereby ensuring that the results are broadly applicable across various physical platforms.

The discussion begins with the qubit, the simplest and most familiar spin-1/2 system, characterised by its two-dimensional Hilbert space. From this foundation, we develop a general theoretical framework for arbitrary spin quantum numbers (qudits). We then turn to the most prominent examples of spin systems encountered in atomic physics experiments, illustrating their relevance and experimental realisations.

1.1.1 A qubit as the smallest spin

A qubit is a quantum system with two-dimensional Hilbert space $\mathcal{H} \simeq \mathbb{C}^2$. From the Stern-Gerlach experiment, it is deduced that some particles have a property, called spin, whose observables are associated with the vector of angular momentum operators $\mathbf{J} = (J_x, J_y, J_z)$. The smallest spin measured has quantum number $j = 1/2$ with two possible projections $m = \pm 1/2$, thus representing a two-level system, i.e. a qubit. For this case, the angular momentum operators are defined by 2×2 matrices given by

$$\mathbf{J} = \frac{\hbar}{2}\boldsymbol{\sigma} \tag{1.2}$$

where $\boldsymbol{\sigma} = (\sigma_x, \sigma_y, \sigma_z)$ is the vector of Pauli matrices

$$\sigma_x = \begin{pmatrix} 0 & 1 \\ 1 & 0 \end{pmatrix}, \qquad \sigma_y = \begin{pmatrix} 0 & -i \\ i & 0 \end{pmatrix}, \qquad \sigma_z = \begin{pmatrix} 1 & 0 \\ 0 & -1 \end{pmatrix}.$$

These matrices form a basis for the space of 2×2 Hermitian matrices over $\mathbb{R}$ and satisfy the commutation relations

$$[\sigma_\alpha, \sigma_\beta] = 2i\epsilon_{\alpha\beta\gamma}\sigma_\gamma.$$

The factor $\hbar$ in (1.2) ensures that $\mathbf{J}$ has the correct units of angular momentum . Throughout this thesis, we will adopt the natural units convention $\hbar = 1$. In this setting, the unitary operator representing a rotation of the spin of amplitude ϕ around an axis defined by a unit vector $\mathbf{n} \in \mathbb{R}^3$ is

$$U_{\mathbf{n}}(\phi) = e^{-i\phi\mathbf{n}\cdot\boldsymbol{\sigma}/2} = \mathbb{I}\cos\frac{\phi}{2} - i(\mathbf{n}\cdot\boldsymbol{\sigma})\sin\frac{\phi}{2}. \tag{1.3}$$

where $\mathbb{I}$ is the identity operator. To confirm that this operator represents a proper rotation, one must verify that for any state $|\psi\rangle \in \mathcal{H}$, the expectation value of the spin operator $\mathbf{J}$ (or equivalently $\boldsymbol{\sigma}$) transforms under $U_{\mathbf{n}}$ as

$$\langle\psi| U_{\mathbf{n}}^\dagger(\phi)\,\boldsymbol{\sigma} U_{\mathbf{n}}(\phi)\,|\psi\rangle = \langle\psi| R_{\mathbf{n}}(\phi)\,\boldsymbol{\sigma}\,|\psi\rangle$$

where $R_{\mathbf{n}}(\phi)$ represents the corresponding rotation matrix in three dimensions acting on the vector $\boldsymbol{\sigma}$. Since this must hold for all $|\psi\rangle$, we can express this equivalently as an operator identity

$$U_{\mathbf{n}}^\dagger(\phi)\,\boldsymbol{\sigma} U_{\mathbf{n}}(\phi) = R_{\mathbf{n}}(\phi)\,\boldsymbol{\sigma}.$$

Expanding the right-hand side using (1.3) and using the following Pauli matrix identities

$$[\mathbf{n}\cdot\boldsymbol{\sigma}, \boldsymbol{\sigma}] = -2i\mathbf{n}\times\boldsymbol{\sigma} \qquad (\mathbf{n}\cdot\boldsymbol{\sigma})\,\boldsymbol{\sigma}\,(\mathbf{n}\cdot\boldsymbol{\sigma}) = 2\mathbf{n}(\mathbf{n}\cdot\boldsymbol{\sigma}) - \boldsymbol{\sigma}$$

one obtains

$$U_{\mathbf{n}}^{\dagger}(\phi)\,\boldsymbol{\sigma}\,U_{\mathbf{n}}(\phi)=\boldsymbol{\sigma}\cos\phi+(1-\cos\phi)\,\mathbf{n}\,(\mathbf{n}\cdot\boldsymbol{\sigma})+\mathbf{n}\times\boldsymbol{\sigma}\sin\phi \tag{1.4}$$

which is indeed the expression of the rotation of a three-dimensional vector [39].

An interesting phenomenon arises when applying a 2π rotation to a qubit. In this case, the rotation operator becomes

$$U_{\mathbf{n}}(2\pi)=-\mathbb{I}$$

implying that the quantum state acquires a global phase factor of -1, and is not strictly restored to its original form. However, since physical observables are unaffected by global phases, the expectation values of angular momentum operators remain unchanged

$$\langle\psi|\,\boldsymbol{\sigma}\,|\psi\rangle=\langle\psi|\,U_{\mathbf{n}}^{\dagger}(2\pi)\,\boldsymbol{\sigma}\,U_{\mathbf{n}}(2\pi)\,|\psi\rangle\,.$$

This phase factor has been experimentally observed, for instance, by splitting a qubit ensemble into two subsets, applying a 2π rotation to only one of them, and detecting interference effects due to the relative phase shift [40, 41]. This implies that for each physical rotation $R_{\mathbf{n}}(\phi)\in\mathrm{SO}(3)$, there exists two distinct operators in SU(2), i.e. $U_{\mathbf{n}}(\phi)$ and $U_{\mathbf{n}}(\phi+2\pi)$. In fact, while SO(3) represents rotations in three-dimensional space, SU(2) is the group of spinor representations of such rotations. Each element of SO(3) corresponds to two elements of SU(2), making SU(2) a double cover of SO(3). As such, SU(2) is often considered the more fundamental symmetry group for describing spin systems. This phenomenon, while inherently quantum mechanical for point particles like electrons, can also be observed in certain classical systems with spatial extent. Such systems may require a full 4π rotation to return to their initial configuration [42]. Notable examples include the Dirac belt trick [43] and polarisation states of classical electromagnetic fields [44].

In the following subsection, we will formalise the concept of an abstract spin system based on the group structure of its rotation symmetry. As discussed above, this group is SU(2). We will focus on the definition of rotation operators for general spin-j systems, their generators, namely the spin angular momentum operators J_α, and demonstrate that these satisfy the canonical angular momentum commutation relations (1.1).

1.1.2 Systems with arbitrary spin quantum numbers

Let us consider a quantum system described by a Hilbert space $\mathcal{H}$ that is invariant under spatial rotations. This rotational invariance means that the set of probabilities of measurement outcomes remain unchanged when the entire system is subjected to a rotation. According to Wigner's theorem [45], any symmetry transformation that preserves transition probabilities is implemented on the Hilbert space by either a unitary or antiunitary operator. In the case of continuous symmetries such as rotations, the representation must be unitary [45, 46].

Thus, for any rotation $R_{\mathbf{n}}(\phi)$, there exists a unitary operator $U_{\mathbf{n}}(\phi)$ acting on $\mathcal{H}$, such that for all $|\psi_1\rangle\,,|\psi_2\rangle\in\mathcal{H}$ we have

$$|\langle\psi_1|\,\psi_2\rangle|^2=|\langle U_{\mathbf{n}}(\phi)\,\psi_1|\,U_{\mathbf{n}}(\phi)\,\psi_2\rangle|^2\,.$$

Experimentally, this expresses the fact that the physical predictions, such as measurement probabilities, are unaffected by applying a global rotation to the entire system. At first

glance, one might expect the operators $U_{\mathbf{n}}(\phi)$ to form a representation of the rotation group SO(3), which describes physical rotations in three-dimensional space. However, as we saw in the qubit case, the operators $U_{\mathbf{n}}(\phi)$ actually form a representation of the group SU(2) instead. This is due to the fact that quantum states are defined only up to a global phase, and physical predictions, such as transition probabilities, depend only on the modulus squared of the inner product

$$\left|\left\langle e^{i\alpha_1}\psi_1\right| e^{i\alpha_2}\psi_2\right\rangle\Big|^2 = \left|\langle\psi_1|\,\psi_2\rangle\right|^2 \quad \forall\alpha_1,\alpha_2\in\mathbb{R}.$$

Therefore, symmetry operations in quantum mechanics only need to preserve transition probabilities, not the inner product itself. Wigner's theorem then implies that symmetry operators are only defined up to a global phase, which means that the operators $U_{\mathbf{n}}(\phi)$ form a *projective* representation of SO(3). These projective representations correspond precisely to the ordinary representations of the group SU(2) [47]. Consequently, rotational symmetry in quantum mechanics is described using unitary representations of SU(2), rather than SO(3). For integer spin quantum numbers j, corresponding to odd-dimensional representations, the irreducible representations of SU(2) are isomorphic to that of SO(3). Therefore, rotations of quantum systems with spatial extension, such as orbital angular momentum states, are represented by SO(3), as expected.

To define spin systems explicitly, we now seek the form of the unitary operators $U_{\mathbf{n}}(\phi)$. The irreducible representations of SU(2) have dimension $2j+1$ where $j = 1/2, 1, 3/2, 2, \ldots$. According to Stone's theorem [47], any strongly continuous one-parameter unitary group $\{U(\phi)\}_{\phi\in\mathbb{R}}$, such as the subgroup of rotations around a fixed axis $\mathbf{n}$, is generated by a self-adjoint operator A, so that

$$U(\phi) = e^{i\phi A}.$$

Denoting by $J_{\mathbf{n}} = \mathbf{J}\cdot\mathbf{n}$ the operator associated with rotations around axis $\mathbf{n}$, we thus have

$$U_{\mathbf{n}}(\phi) = e^{i\phi J_{\mathbf{n}}} \quad \forall\phi\in\mathbb{R}.$$

Our next objective is to determine the algebraic structure of the generators $J_{\mathbf{n}}$ for different directions $\mathbf{n}$. These operators define the spin observables, and their commutation relations encode the angular momentum structure of the system. A known result from Lie theory tells us that a rotation $R_{\mathbf{m}}(\phi)$ of amplitude ϕ around an axis $\mathbf{m}$ given by

$$R_{\mathbf{m}}(\phi) = R_{\mathbf{n}_1}(\phi_1)\,R_{\mathbf{n}_2}(\phi_2)\,R^{-1}_{\mathbf{n}_1}(\phi_1)\,R^{-1}_{\mathbf{n}_2}(\phi_2)$$

verify to first order in angles [47]

$$\mathbf{m} = \frac{\mathbf{n}_1\times\mathbf{n}_2}{\|\mathbf{n}_1\times\mathbf{n}_2\|} \qquad \phi = \phi_1\phi_2\,\|\mathbf{n}_1\times\mathbf{n}_2\|\,. \tag{1.5}$$

Now consider the corresponding unitary evolution up to first order in ϕ

$$\begin{aligned} U_{\mathbf{m}}(\phi) &\simeq (1+i\phi_1\mathbf{n}_1\cdot\mathbf{J})\,(1+i\phi_2\mathbf{n}_2\cdot\mathbf{J})\,(1-i\phi_1\mathbf{n}_1\cdot\mathbf{J})\,(1-i\phi_2\mathbf{n}_2\cdot\mathbf{J}) \\ &\simeq 1-\phi_1\phi_2\,[\mathbf{n}_1\cdot\mathbf{J},\mathbf{n}_2\cdot\mathbf{J}] \end{aligned}$$

and the expansion of the rotation around axis $\mathbf{m}$ at first order

$$U_{\mathbf{m}}(\phi) \simeq 1 - i\phi_1\phi_2\,(\mathbf{n}_1\times\mathbf{n}_2)\cdot\mathbf{J}.$$

Equating both expressions, we obtain the commutation relation

$$[\mathbf{n}_1 \cdot \mathbf{J}, \mathbf{n}_2 \cdot \mathbf{J}] = (\mathbf{n}_1 \times \mathbf{n}_2) \cdot \mathbf{J}.$$

By choosing $\mathbf{n}_1, \mathbf{n}_2 \in \{\mathbf{e}_x, \mathbf{e}_y, \mathbf{e}_z\}$, this leads to the standard commutation relations for spin operators

$$[J_\alpha, J_\beta] = i\epsilon_{\alpha\beta\gamma} J_\gamma, \qquad \alpha, \beta, \gamma = x, y, z, \tag{1.6}$$

where $\epsilon_{\alpha\beta\gamma}$ is the Levi-Civita symbol. These relations define the Lie algebra $su(2)$, which underpins the structure of spin systems.

From the commutation relations of the $su(2)$ algebra, it is well known that the total angular momentum operator

$$J^2 = J_x^2 + J_y^2 + J_z^2$$

commutes with all components of the spin operator

$$\left[J^2, \mathbf{J}\right] = 0.$$

This means that J^2 and any component of $\mathbf{J}$, typically J_z, can be simultaneously diagonalised. As a result, the Hilbert space $\mathcal{H} = \mathbb{C}^{2j+1}$ of a spin-j system admits an orthonormal basis consisting of the simultaneous eigenstates of J^2 and J_z. This is the standard spin basis, denoted by

$$\{|j, m\rangle : m = -j, -j+1, \ldots, j\}.$$

These states satisfy the eigenvalue equations [48]

$$J^2 |j, m\rangle = j(j+1) |j, m\rangle \qquad J_z |j, m\rangle = m |j, m\rangle.$$

Transitions between neighboring states in the spin basis are mediated by the ladder operators

$$J_\pm = J_x \pm i J_y$$

which raise or lower the magnetic quantum number m by one

$$J_\pm |j, m\rangle = \sqrt{(j \mp m)(j \pm m + 1)} \, |j, m \pm 1\rangle.$$

1.1.3 Miscellaneous of spin systems

Spin systems play a central role in quantum physics and appear across a wide range of physical platforms. They provide a versatile framework for encoding and manipulating quantum information, and they serve as fundamental models for studying quantum entanglement and non-classical states.

Experimentally, spin systems can be realised in a variety of ways. For instance, using the orbital angular momentum of light [49], the polarisation of light in multiphoton systems [31], the electronic spin of magnetic atoms [50], the internal levels of trapped ions [51], superconducting circuits [52] or the rotational degree of freedom in molecules [53]. In the following, we focus on three representative types of spin systems that are widely used in experiments to generate non-classical spin states. These systems not only provide a high degree of quantum control but also constitute excellent experimental platforms for realising and exploring the phenomena discussed in the subsequent chapters.

1.1.3.1 Angular momentum in atoms

Atoms possess several angular momentum degrees of freedom. There is the orbital angular momentum $\mathbf{L}$, which arises from the motion of electrons around the nucleus. Each electron also possesses an intrinsic angular momentum under the form of a spin $\mathbf{S}$. In addition, the nucleus itself carries an angular momentum $\mathbf{I}$ due to its internal structure. Under their potential coupling, these different angular momentum degrees of freedom will give rise to the angular momenta [48]

$$\mathbf{J} = \mathbf{L} + \mathbf{S} \qquad \text{and} \qquad \mathbf{F} = \mathbf{J} + \mathbf{I},$$

associated with the fine and hyperfine structures, respectively. Depending on the atomic species, this structure give rise to multilevel spin systems that can be used for various quantum control protocols.

In the absence of external fields, the magnetic sublevels with magnetic quantum number m within a given fine or hyperfine manifold remain degenerate due to the rotational symmetry of the system. To lift this degeneracy and to gain precise control over the spin dynamics, it is necessary to apply an external magnetic field. This field breaks the rotational symmetry and defines a quantisation axis, which makes the magnetic sublevels energetically distinguishable (see Appendix 1.A). Such a field is crucial not only for enabling coherent manipulation of the spin but also for preventing decoherence. Otherwise, even a weak, uncontrolled magnetic field could induce unwanted transitions between degenerate sublevels, degrading quantum coherence.

To initialise the atom in a well-defined spin state, a process known as optical pumping is typically employed [54]. In this method, polarised laser light is tuned to a specific atomic transition, and through repeated cycles of absorption and spontaneous emission, the atom is driven into a target sublevel that is no longer coupled by the light. This dissipative process allows the atomic population to accumulate in a pure quantum state aligned with the quantisation axis. Once initialised, the atom can then be subjected to coherent quantum control protocols to generate the desired spin dynamics.

1.1.3.2 Orbital angular momentum of light

In the absence of charged sources, it is known that an electromagnetic field carries a linear momentum given by [55]

$$\mathbf{P} = \int_{\mathbb{R}^3} \mathbf{p}\,(\mathbf{r})\; d\mathbf{r} = \epsilon_0 \int_{\mathbb{R}^3} \mathbf{E} \times \mathbf{B}\, d\mathbf{r}$$

where $\mathbf{E}$ and $\mathbf{B}$ are the electrical and magnetic fields, respectively, $\mathbf{p}\,(\mathbf{r})$ is the momentum density vector field and the integral is taken over the entire space $\mathbb{R}^3$. Associated with this momentum is the total angular momentum of the electromagnetic field, given by

$$\mathbf{J}_T = \int_{\mathbb{R}^3} \mathbf{r} \times \mathbf{p}\, d\mathbf{r} = \epsilon_0 \int_{\mathbb{R}^3} \mathbf{E} \times (\nabla \times \mathbf{A})\; d\mathbf{r}$$

where we used $\mathbf{B} = \nabla \times \mathbf{A}$ with $\mathbf{A}$ the vector potential. This total angular momentum can be decomposed as

$$\mathbf{J}_T = \underbrace{\epsilon_0 \int_{\mathbb{R}^3} \sum_{\alpha=x,y,z} E_\alpha\, (\mathbf{r} \times \nabla)\, A_\alpha\, d\mathbf{r}}_{\equiv \mathbf{J}} + \underbrace{\epsilon_0 \int_{\mathbb{R}^3} \mathbf{E} \times \mathbf{A}\, d\mathbf{r}}_{\equiv \mathbf{S}},$$

where **J** corresponds to the orbital angular momentum (OAM), and **S** to the spin angular momentum (SAM) of the field.

The SAM is associated with the polarisation of light. For example, circularly polarized light carries spin angular momentum of $\pm\hbar$ per photon (left- or right-handed), while linearly polarized light carries zero SAM. In contrast, the OAM arises from the spatial distribution of the electromagnetic field and can take on an unbounded number of integer values of angular momentum, making it a useful resource for high-dimensional quantum information processing [56, 57] and optical multiplexing in telecommunication systems [58].

The OAM enables the definition of an effective spin system for individual photons. In this manner, a photon whose quantum state is entirely confined to the Hilbert space $\mathbb{C}^{2j+1}$ corresponding to a single OAM mode, defined by the eigenvalue of the total angular momentum operator $\mathbf{J}^2$, can be associated with a single spin-j system. In such a simulated spin system, the ladder operators $J_\pm$, which raise or lower the magnetic quantum number m, can be physically implemented using Q-plates [59]. These devices couple the photon's polarisation to its OAM, enabling controlled transitions between OAM states that simulate the action of spin-raising and lowering operators.

1.1.3.3 Two-mode systems

Another class of systems in which spin operators and their commutation relations naturally emerge is that of two-mode bosonic systems. A first example is provided by a two-beam interferometer, such as a Fabry-Pérot or Mach-Zender interferometer, where annihilation operators a_0 and a_1 are associated with the two arms of the interferometer [60]. Similarly, in Bose-Einstein condensates (BECs) where only the two lowest energy levels are significantly populated, the effective Hilbert space can be truncated and mapped to a spin system. Two physically distinct realisations of such two-mode dynamics are common [61]: a BEC confined in a double-well potential, where the two modes correspond to the lowest orbital in the left and right wells and a single-well BEC where atoms possess a two-level hyperfine structure for which the two modes are associated with the hyperfine ground and excited states. These systems are illustrated in Figure 1.1. A further example is an ensemble of indistinguishable photons, where the two modes may correspond to orthogonal polarisation states, such as left $|L\rangle$ and right $|R\rangle$ circular polarisations, or to OAM modes, such as $|l=0\rangle$ and $|l=1\rangle$.

To each mode $i=0,1$, we associate bosonic annihilation and creation operators a_i and $a_i^\dagger$, which satisfy the canonical commutation relations

$$\left[a_i, a_j^\dagger\right] = \delta_{ij}. \tag{1.7}$$

The number operators for each mode are defined as

$$N_0 = a_0^\dagger a_0 \qquad N_1 = a_1^\dagger a_1$$

and the total number operator is

$$N = N_0 \otimes \mathbb{I} + \mathbb{I} \otimes N_1.$$

In what follows, we assume particle number conservation, so the total number N is a conserved quantity. A basis state with $N-k$ particles in mode 0 and k particles in mode 1 can then be written in the Fock basis as

$$|N-k\rangle_0 \otimes |k\rangle_1 .$$

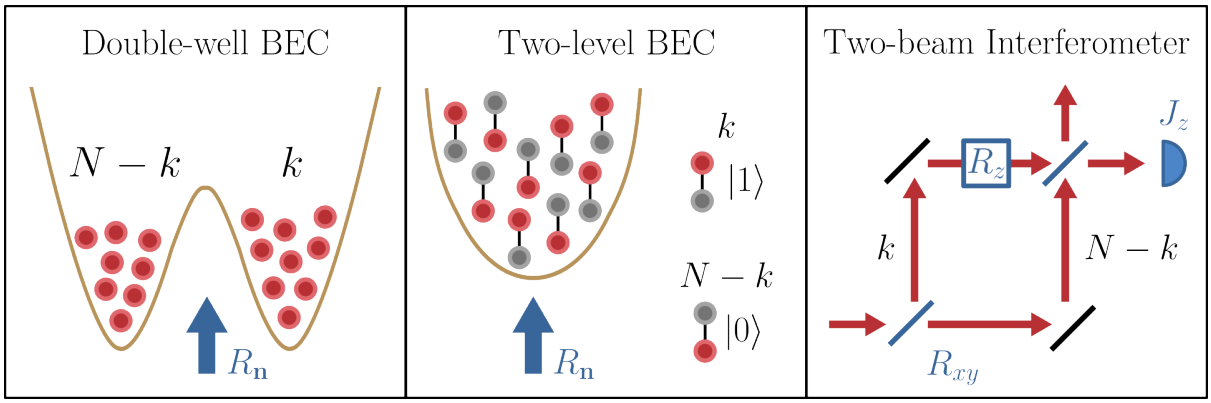

Figure 1.1: Representations of the different two-modes systems equivalent to a single spin $j = N/2$. In the case of a BEC, the rotations around any axis are obtained by applying a magnetic field. For two-beam interferometers, rotations around x and y are obtained by using beamsplitters, rotations around z are obtained by a phase shifter or an optical path length and photodetectors measure the operator J_z.

We can then define spin operators using the Schwinger-Jordan representation [62], which maps bosonic operators to angular momentum operators as

$$J_x = \frac{a_0^\dagger a_1 + a_1^\dagger a_0}{2} \qquad J_y = \frac{a_0^\dagger a_1 - a_1^\dagger a_0}{2i} \qquad J_z = \frac{a_0^\dagger a_0 - a_1^\dagger a_1}{2}.$$

These operators satisfy the usual spin commutation relations (1.6). The total spin operator squared is related to the total number of particles by

$$J^2 = \frac{N}{2}\left(\frac{N}{2}+1\right)\mathbb{I}$$

which remains conserved. It can be shown from the action of the bosonic operators that the two-mode Fock states $|N-k\rangle_0 \otimes |k\rangle_1$ are simultaneous eigenstates of J^2 and J_z

$$J^2 |N-k\rangle_0 \otimes |k\rangle_1 = \frac{N}{2}\left(\frac{N}{2}+1\right)|N-k\rangle_0 \otimes |k\rangle_1$$

$$J_z |N-k\rangle_0 \otimes |k\rangle_1 = \left(k - \frac{N}{2}\right)|N-k\rangle_0 \otimes |k\rangle_1 .$$

Finally, any spin eigenstate can be written compactly in terms of creation operators acting on the vacuum

$$|j,m\rangle = \frac{\left(a_1^\dagger\right)^{j-m}\left(a_0^\dagger\right)^{j+m}}{\sqrt{(j-m)!\,(j+m)!}}|0\rangle ,$$

where $|0\rangle$ is the vacuum of both modes. Thus, the states $|j = N/2, m = k - N/2\rangle$ span a spin-j representation of dimension $2j+1 = N+1$.

A directly related family of systems is the ensemble of symmetric multiqubit systems for which a basis of the Hilbert space is provided by the symmetric Dicke states, defined as

$$|D_N^{(k)}\rangle = \frac{1}{\sqrt{C_N^k}}\sum_\pi |\underbrace{0\ldots0}_{N-k}\underbrace{1\ldots1}_{k}\rangle,$$

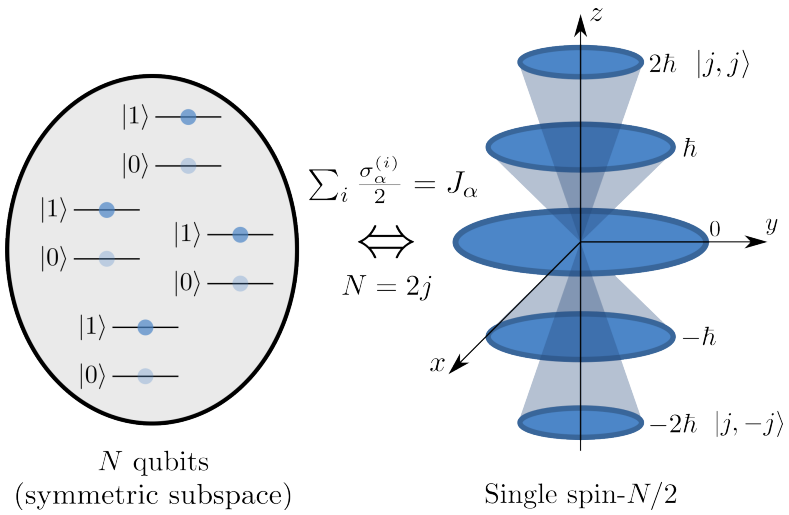

Figure 1.2: Representation of the isomorpism between a symmetric multiqubit system and a single spin.

where the sum runs over all distinct permutations π of the qubits. These states correspond exactly to the two-mode Fock states of the form

$$|D_N^{(k)}\rangle = |N-k\rangle_0 \otimes |k\rangle_1 .$$

This identification is more than just notational as the symmetric qubit states and two-mode bosonic states share the same algebraic structure. For instance, denoting $\sigma_\alpha^{(i)}$ the Pauli operators acting on the i-th qubit, the collective spin operators can be written as

$$J_\alpha = \sum_{i=1}^{N} \frac{\sigma_\alpha^{(i)}}{2}, \qquad \alpha = x, y, z$$

which satisfy the standard $su(2)$ commutation relations. From a mathematical perspective, the correspondence is underpinned by a structural isomorphism between the symmetric subspace $\mathcal{H}_S$ of the full Hilbert space $\mathcal{H} = \mathbb{C}^{2^N}$ of a multiqubit system and the Hilbert space of a two-mode system. For example, consider a BEC consisting of N two-level atoms. Since particles in a BEC are indistinguishable bosons, the global quantum state must be fully symmetric under particle exchange. This symmetrisation restricts the Hilbert space to the symmetric subspace $\mathcal{H}_S$, which is spanned by the Dicke states.

By extension, the Hilbert space of a single spin-$j = N/2$ system is also isomorphic to $\mathcal{H}_S$, as illustrated in Figure 1.2. Under this correspondence each Dicke state $|D_N^{(k)}\rangle$ maps to a spin state $|j = N/2, m = k - N/2\rangle$. From a mathematical standpoint, these two descriptions are equivalent, and any concept, operation, or measure defined for one system can be directly translated to the other. Throughout this thesis, we will freely move between the language of spin systems and that of multiqubit systems restricted to $\mathcal{H}_S$, using this isomorphism as a foundational bridge (see Table 1.1).

For instance, in a two-beam interferometer, rotations of the associated spin system around the x- and y-axes can be implemented using beam splitters, while rotations around the z-axis can be realised via phase shifters or differences in optical path length [60]. In this framework, interferometry becomes equivalent to performing a sequence of rotations on a spin system, where the photodetectors at the output effectively measure the expectation value of the spin operator J_z, as illustrated in Figure 1.1.

Single spin-j	Multiple qubits in symmetric subspace
spin quantum number $j = \frac{N}{2}$	number of qubits $N = 2j$
spin operators J_α	collective spin operators $\sum_{i=1}^{N} \frac{\sigma_\alpha^{(i)}}{2}$
standard spin basis $\{\|j,m\rangle\}$ with $m = -j,\ldots,j$	symmetric Dicke basis $\{\|D_N^{(k)}\rangle\}$ with $k = 0,\ldots,N$
magnetic quantum number $m = \frac{N}{2} - k$	number of excitations $k = j - m$
full space	symmetric subspace
(absolutely) classical	(absolutely) separable
spin coherent state $\|\mathbf{n}\rangle$	pure symmetric separable state $\|\phi\rangle^{\otimes N}$
pure anticoherent state of order t	pure maximally entangled symmetric state (state with maximally mixed t-qubit reductions in the symmetric sector)
rotation	symmetric local unitary transformation

Table 1.1: Dictionary of correspondence between spin-j states and symmetric states of N spin-1/2 or qubits.

1.1.4 Remarkable spin states

Among the infinite family of spin states, certain specific states play a central role in the study of spin systems. In this subsection, we introduce the properties of these states that will be essential for the developments that follow.

1.1.4.1 Coherent states

In a spin-j system, a coherent state $|\mathbf{n}\rangle$ is defined as a pure state whose mean value of the spin operator projection along a given direction $\mathbf{n} \in \mathbb{R}^3$, with $|\mathbf{n}| = 1$, is maximal, i.e. [63]

$$\mathbf{n}\cdot\mathbf{J}\,|\mathbf{n}\rangle = j\,|\mathbf{n}\rangle\,.$$

Equivalently, coherent states can be characterized by either of the following two properties

$$\sum_{\alpha=x,y,z} \langle J_\alpha\rangle^2 = j^2 \qquad\qquad \sum_{\alpha=x,y,z} (\Delta J_\alpha)^2 = j$$

where $(\Delta J_\alpha)^2$ denotes the variance of J_α. The second condition shows that spin coherent states minimise the total spin uncertainty, saturating the Heisenberg uncertainty bound. Because of this, they are often regarded as the "most classical" pure states of a spin system, much like coherent states of the harmonic oscillator in infinite-dimensional Hilbert spaces (e.g., light modes in quantum optics).

Spin coherent states are typically parameterised by spherical coordinates (θ,φ) and denoted $|\theta,\varphi\rangle \equiv |\Omega\rangle$, with the unit vector $\mathbf{n}$ given by $\mathbf{n} = (\cos\theta\cos\phi, \cos\theta\sin\phi, \sin\theta)$. One can construct a coherent state pointing in any direction by rotating the state $|j,j\rangle$, which points along the z-axis, and rotate it to the desired direction $\mathbf{n}$, as it is represented in Figure 1.3. This rotation is implemented by the rotation operator $U(\theta,\varphi) = e^{-i\varphi J_z} e^{-i\theta J_y}$, i.e.

$$|\theta,\varphi\rangle = U(\theta,\varphi)\,|j,j\rangle\,.$$

In the standard spin basis, the coherent state has the explicit expansion

$$|\theta,\varphi\rangle = \sum_{m=-j}^{j} \sqrt{C_{2j}^{j+m}} \left(\cos\frac{\theta}{2}\right)^{j+m} \left(\sin\frac{\theta}{2}\right)^{j-m} e^{-i(j-m)\varphi} |j,m\rangle\,. \tag{1.8}$$

In the context of multiqubit systems, the analogue of a spin-coherent state in the symmetric subspace of N qubits is a symmetric product state of the form

$$|\Omega\rangle = |\phi\rangle^{\otimes N} \tag{1.9}$$

where each qubit points in the same direction Ω on the Bloch sphere. These symmetric product states are the only pure symmetric spin states that are separable, making them particularly important for studying entanglement of symmetric multiqubit states.

Interestingly, the family of coherent states $\{|\mathbf{n}\rangle\}_{\mathbf{n}\in\mathcal{S}^2}$ is an infinite dimensional family of spin states which forms an overcomplete basis of the Hilbert space $\mathcal{H} = \mathbb{C}^{2j+1}$. That is, any spin state can be represented as a continuous superposition of coherent states and the number of elements is higher than in an orthogonal basis. Thus, they are not necessarily orthogonal among each other. In fact, their mutual overlap is given by [64]

$$|\langle\mathbf{n}_1|\,\mathbf{n}_2\rangle| = \left(\frac{1+\mathbf{n}_1\cdot\mathbf{n}_2}{2}\right)^{j}. \tag{1.10}$$

Nevertheless, they satisfy the identity

$$\frac{2j+1}{4\pi}\int |\Omega\rangle\langle\Omega|\,d\Omega = \mathbb{I}$$

where $d\Omega = \sin\theta d\theta d\varphi$ is the uniform measure on the sphere. It turns out that any pure or mixed spin state ρ can be decomposed as

$$\rho = \int P_\rho(\Omega)\,|\Omega\rangle\langle\Omega|\,d\Omega \tag{1.11}$$

where P_ρ is known as the Glauber-Sudarshan P function. This function is not unique as coherent states form an overcomplete basis. This decomposition plays a central role in the phase-space representation of spin systems and will be further explored in Section 1.2 and in Chapter 2.

1.1.4.2 Cat states

Another emblematic spin state used throughout this thesis is the spin cat state, named after Schrödinger's famous thought experiment. It is defined as a coherent superposition of two spin coherent states pointing in opposite directions on the Bloch sphere. For a given direction Ω, the spin cat state reads

$$|\psi_{\text{cat}}\rangle = \frac{1}{\sqrt{2}}\left(|\Omega\rangle + |-\Omega\rangle\right),$$

where $|-\Omega\rangle$ denotes the antipodal coherent state to $|\Omega\rangle$. Spin cat states are central in the study of quantumness and quantum metrology and are directly analogous to Schrödinger cat states in quantum optics.

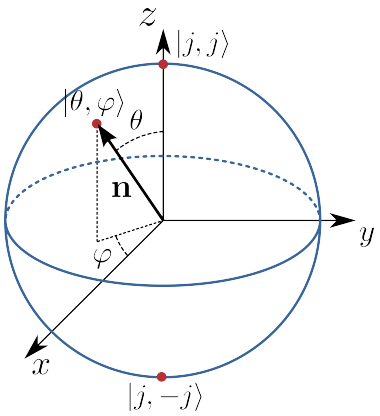

Figure 1.3: Representation of a coherent state $|\theta, \varphi\rangle$ on the $\mathcal{S}^2$ sphere as a rotated version of the state $|j, j\rangle$.

In the case of N qubits, spin cat states correspond to the well-known Greenberger-Horne-Zeilinger (GHZ) symmetric states [65]

$$|\mathrm{GHZ}\rangle = \frac{1}{\sqrt{2}}\left(|0\rangle^{\otimes N} + |1\rangle^{\otimes N}\right)$$

where $|0\rangle$ and $|1\rangle$ represent the ground and excited states of a single qubit, respectively. The GHZ state is highly sensitive to decoherence, making it a prototypical example of fragile quantum coherent superposition of states. Another analog to the spin cat state which appears in the context of a double-well Bose-Einstein condensate is the NOON state

$$|\mathrm{NOON}\rangle = \frac{1}{\sqrt{2}}\left(|N, 0\rangle + |0, N\rangle\right)$$

which describes all N particles being coherently delocalised between the two wells.

1.1.4.3 Anticoherent states

In the search for highly non-classical spin states, Zimba introduced in 2006 the concept of anticoherent spin states. These states were initially defined as the opposite of spin coherent states, in the sense that their spin expectation value is completely isotropic. That is, for an anticoherent state [25]

$$\langle \mathbf{J} \rangle = 0. \tag{1.12}$$

While coherent states minimise the total spin uncertainty, anticoherent states maximise it. For a spin-j system, the total variance of the spin operator of an anticoherent state is given by

$$\sum_{\alpha=x,y,z} \Delta J_\alpha^2 = \left\langle J_\alpha^2 \right\rangle - \underbrace{\left\langle J_\alpha \right\rangle^2}_{=0} = j\,(j+1)\,.$$

which is the maximal possible value for any pure spin-j state. One can go beyond the first-order condition (1.12), and impose isotropy on higher statistical moments of the spin components. This leads to the definition of anticoherent states of order t (t-AC states), which are defined such that

$$\frac{\partial}{\partial \mathbf{n}} \langle (\mathbf{J} \cdot \mathbf{n})^k \rangle = 0 \qquad \forall k = 1, 2, \ldots, t. \tag{1.13}$$

This means that the expectation value of $(\mathbf{J}\cdot\mathbf{n})^k$ is independent of the direction $\mathbf{n}$, for all $k = 1, 2, \ldots, t$. By definition, a t-AC state is also t'-AC for all $t' \leq t$. For example, a 2-AC state not only has vanishing mean spin but also isotropic spin variance, i.e.

$$\left\langle J_x^2 \right\rangle = \left\langle J_y^2 \right\rangle = \left\langle J_z^2 \right\rangle = \frac{j\,(j+1)}{3} \qquad \langle J_\alpha J_\beta + J_\beta J_\alpha \rangle = 0 \tag{1.14}$$

$\forall \alpha, \beta = x, y, z$ with $\alpha \neq \beta$. Hence, anticoherence quantifies the degree of isotropy in the spin components statistics of a spin state, and is related to quantumness as it is made possible only by quantum superposition. As shown in [66], AC states often exhibit in the Majorana representation (see Subsection 1.1.6) non-trivial point-group symmetries, making them interesting both geometrically and physically.

It is known that, for pure states, any order of anticoherence can be attained provided the spin number j is large enough [67]. However, determining which orders are attainable for a given finite j remains an open problem. The first known examples of 2-AC and 3-AC states appear at $j = 2$ and $j = 3$, respectively. To reach anticoherence of order 4 or 5, a spin number of at least $j = 6$ is required. Numerical studies have further indicated that the minimum spin number j needed to support a t-AC state scales approximately as $j \propto t^2$, suggesting that the maximum attainable order of anticoherence is proportional to the square root of the spin number j.

In this thesis, we refer to the known pure states that achieve the highest possible order of anticoherence for a given spin j as Highest-Order Anticoherent Pure (HOAP) states. For $j = 2$ and 3, the unique HOAP states (up to rotation) are 2-AC and 3-AC, respectively, and are given in the spin basis by

$$\left|\psi_{t=2}^{\mathrm{HOAP}}\right\rangle = \frac{1}{2}\left(|2,2\rangle + i\sqrt{2}\,|2,0\rangle + |2,-2\rangle\right)$$

and

$$\left|\psi_{t=3}^{\mathrm{HOAP}}\right\rangle = \frac{1}{\sqrt{2}}\left(|3,2\rangle + |3,-2\rangle\right).$$

Anticoherent states are extremal examples of non-classicality and will play a key role in our study of spin systems.

1.1.4.4 Maximally mixed state

When there is uncertainty about the actual quantum state $|\psi\rangle$ of a system, due either to imperfect state preparation or interaction with an environment, the system is no longer described by a pure state but by a mixed state, represented by a density matrix

$$\rho = \sum_i p_i \,|\psi_i\rangle\,\langle\psi_i|$$

where $p_i \geq 0$ and $\sum_i p_i = 1$. The degree of mixedness can be quantified by the purity of the state

$$R\,(\rho) = \mathrm{Tr}\left(\rho^2\right).$$

A pure state $|\psi\rangle$ satisfies $R\,(|\psi\rangle\,\langle\psi|) = 1$, while the least pure state, called the Maximally Mixed State (MMS), has minimal purity. The MMS and its purity are given by

$$\rho_0 = \frac{\mathbb{I}}{d}, \qquad R\,(\rho_0) = \frac{1}{d},$$

where d is the dimension of the Hilbert space. Since the MMS contains no coherence or entanglement, it is considered the most classical quantum state with the highest entropy. For this reason, it often serves as a reference point in the analysis of non-classicality, entanglement, and decoherence.

1.1.5 Multipolar operator basis

In order to study spin systems, it is often useful to represent their states in a basis that reveals their angular structure and symmetries more naturally than the standard spin basis $\{|j,m\rangle\}_{m=-j}^{j}$. The spin tensor multipolar basis (MPB) provides precisely such a framework.

For a spin-j system with Hilbert space $\mathcal{H}=\mathbb{C}^{2j+1}$, the MPB is composed of irreducible tensor operators $\{\mathbf{T}_L\}$ of rank $L=0,1,\ldots,2j$. Each tensor $\mathbf{T}_L$ contains $2L+1$ elements $\{T_{LM}\}$ where $M=-L,\ldots,L$. They can be defined by the condition that the rank of a given tensor $\mathbf{T}_L$ is preserved under rotation as we have [68]

$$[J_z,T_{LM}]=MT_{LM}\quad\text{and}\quad[J_\pm,T_{LM}]=\sqrt{(L\mp1)\,(L\pm M+1)}T_{LM\pm1},$$

for all $M=-L,\ldots,L$. The expansion of the multipolar tensor operators in the spin basis gives

$$\begin{aligned}T_{LM}&=\sum_{m,m'=-j}^{j}(-1)^{j-M}\sqrt{2L+1}\begin{pmatrix}j & L & j\\ -m & M & m'\end{pmatrix}|j,m\rangle\langle j,m'|\\&=\sqrt{\frac{2L+1}{2j+1}}\sum_{m,m'=-L}^{L}C^{jm'}_{jm,LM}\,|j,m'\rangle\langle j,m|\end{aligned}\tag{1.15}$$

where $\begin{pmatrix}j_1 & j_2 & j_3\\ j_4 & j_5 & j_6\end{pmatrix}$ is the $6j$-symbol and $C^{L_3M_3}_{L_1M_1,L_2M_2}$ are Clebsch-Gordan coefficients [69]. Interestingly, the MPB forms an orthonormal basis of the set $\mathcal{B}\left(\mathbb{C}^{2j+1}\right)$ of bounded linear operators acting on the spin Hilbert space $\mathbb{C}^{2j+1}$. These operators are in general non-Hermitian, and satisfy the orthonormality relations [69, 70]

$$\mathrm{Tr}\left(T_{LM}T^{\dagger}_{L'M'}\right)=\delta_{LL'}\delta_{MM'}\qquad T_{LM}=(-1)^M\,T^{\dagger}_{L-M}.\tag{1.16}$$

As a result, any spin state ρ can be expanded in the MPB as

$$\rho=\sum_{L=0}^{2j}\sum_{M=-L}^{L}\rho_{LM}T_{LM},$$

where the expansion coefficients $\rho_{LM}=\mathrm{Tr}\left(\rho T^{\dagger}_{LM}\right)$ are called the state multipoles and, due to the Hermiticity of ρ and to (1.16), these coefficients satisfy $\rho_{LM}=(-1)^M\,\rho^{*}_{L-M}$.

Physically, the multipolar expansion of a spin state is analogous to the multipolar expansion in classical electrodynamics, where a charge distribution is described in terms of monopole, dipole, quadrupole, and higher-order moments. Similarly, the MPB breaks down a quantum spin state into components of increasing angular complexity. The lowest-rank term, corresponding to $L=0$, is proportional to the identity operator and captures

the isotropic part of the state, playing a role similar to the classical monopole. The rank-1 components are associated with the expectation value of the spin operator $\langle \mathbf{J} \rangle$, thus characterising the net orientation of the spin and serving as the quantum analogue of the dipole moment. Rank-2 terms describe the anisotropy on the variances of the spin operator $\mathbf{J}$. Higher-rank components, with $L > 2$, encode subtler quantum features of pure quantum states such as high-order correlations. These higher-rank components are small for spin coherent states but become significant for non-classical states like spin cat states or anticoherent states.

Moreover, the connection between the MPB and spherical harmonics becomes explicit for spin coherent states. For a coherent state $\rho_{\theta\varphi} = |\theta, \varphi\rangle \langle \theta, \varphi|$, we have [70]

$$\mathrm{Tr}\left(\rho_{\theta\varphi} T_{LM}^{\dagger}\right) = \frac{\sqrt{4\pi}\,(2j)!}{\sqrt{(2j-L)!\,(2j+L+1)!}} Y_{LM}^{*}(\theta, \varphi)\,, \tag{1.17}$$

where the Y_{LM}'s are spherical harmonics. As we shall see in Section 1.2, since coherent states form an overcomplete basis of $\mathcal{B}(\mathbb{C}^{2j+1})$, this expression gives a direct geometric picture of the angular structure of a spin state in terms of spherical harmonics.

In Appendix 1.B, we show that, given a system of N qubits in a mixed symmetric state ρ, the state ρ_t of the subsystem composed only of t qubits, i.e. the t-qubit reduced state[1], can be expressed in the MPB as

$$\rho_t = \sum_{L=0}^{t} \sum_{M=-L}^{L} \tfrac{t!}{N!} \sqrt{\tfrac{(N-L)!(N+L+1)!}{(t-L)!(t+L+1)!}}\, \rho_{LM} T_{LM}^{(t)}. \tag{1.18}$$

It follows that the purity of a t-qubit reduced state is given by

$$R\left(\rho_t^2\right) = \sum_{L=0}^{t} \sum_{M=-L}^{L} \tfrac{(t!)^2}{(N!)^2} \tfrac{(N-L)!(N+L+1)!}{(t-L)!(t+L+1)!} \left|\rho_{LM}\right|^2. \tag{1.19}$$

1.1.6 Majorana representation

The Majorana representation provides a geometric way to visualise symmetric quantum states of N qubits. In this framework, a symmetric state $|\psi\rangle$ is represented by a set of N points on the Bloch sphere, analogously to how single-qubit states are represented [71]. This construction relies on the fact that any symmetric N-qubit state can be written as [72, 73]

$$|\psi\rangle = \mathcal{N}\left(\sum_{k=1}^{N_p} \left|\Omega_{\pi_k(1)}\right\rangle \otimes \left|\Omega_{\pi_k(2)}\right\rangle \otimes \cdots \otimes \left|\Omega_{\pi_k(N)}\right\rangle\right) \tag{1.20}$$

where each $|\Omega_i\rangle = \mu_i|0\rangle + \nu_i|1\rangle$ is a single-qubit state and $\mathcal{N}$ is a normalisation factor. Here, the sum is taken over all $N_p = (N+1)!$ permutations $\pi_k \in \mathcal{S}_{N+1}$ of the symmetric group on $N+1$ elements. Each component $|\Omega_i\rangle$ corresponds to a point on the Bloch sphere defined by spherical coordinates $\Omega_i = (\theta_i, \varphi_i)$. Hence, the state $|\psi\rangle$ can be represented by a configuration of N such points, often referred to as the Majorana constellation.

To construct the Majorana representation explicitly, we analyse the expression

$$\langle D_N^{(N)} | R^{-1}(\Omega) |\psi\rangle \tag{1.21}$$

[1] As the state ρ is symmetric under permutation of its subsystems, the different ways to partition the system of N qubits all give the same reduced state of t qubits. Hence, we can talk about the unique t-qubit reduced state ρ_t.

where $R(\Omega) = R_z(\varphi) R_y(\theta)$ is a collective rotation operator acting on all qubits. Since the state is symmetric, this global rotation is equivalent to applying the same single-qubit rotation $r(\Omega)$ to each qubit

$$R(\Omega) = \bigotimes_{i=1}^{N} r(\Omega).$$

The key idea is that for each qubit state $|\Omega_i\rangle$, there exists a rotation $r^{-1}(\Omega_i)$ such that $r^{-1}(\Omega_i)|\Omega_i\rangle = |0\rangle$. If the state $|\psi\rangle$ is expressed in the form of (1.20), then applying the inverse rotation $R^{-1}(\Omega_i)$ will align one of the Majorana points with the north pole of the Bloch sphere. In this case, since $\left|D_N^{(N)}\right\rangle = |1,1,\ldots,1\rangle$, the overlap with $|\psi\rangle$ will vanish, i.e.

$$\left\langle D_N^{(N)} \left| R^{-1}(\Omega_i) \right| \psi \right\rangle = 0.$$

To identify the Majorana points Ω_i, we thus search for the N directions at which this overlap vanishes. Expanding $|\psi\rangle$ in the Dicke basis

$$|\psi\rangle = \sum_{k=0}^{N} d_k \left|D_N^{(k)}\right\rangle$$

we have

$$\begin{aligned}
\left\langle D_N^{(N)} \left| R^{-1}(\Omega) \right| \psi \right\rangle &= \sum_{k=0}^{N} d_k \left\langle D_N^{(N)} \left| R^{-1}(\Omega) \right| D_N^{(k)} \right\rangle \\
&= \sum_{k=0}^{N} d_k \left\langle D_N^{(N)} \left| R_y(-\theta_i) R_z(-\varphi_i) \right| D_N^{(k)} \right\rangle \\
&= \sum_{k=0}^{N} d_k \left\langle D_N^{(N)} \left| R_y(-\theta_i) \right| D_N^{(k)} \right\rangle e^{i\varphi(N/2-k)}
\end{aligned}$$

The rotation matrix elements can be expressed using the Wigner D-matrix as

$$\left\langle D_N^{(N)} \left| R_y(-\theta_i) \right| D_N^{(k)} \right\rangle = D^{N/2}_{-N/2,N/2-k}(\theta,\varphi)\, e^{i\varphi(N/2-k)}$$

with the explicit form

$$D^{N/2}_{-N/2,N/2-k} = (-1)^k \sqrt{C_N^k} \sin^{N-k}\left(\frac{\theta}{2}\right) \cos^{k}\left(\frac{\theta}{2}\right).$$

Introducing the variable $z = \cot\left(\frac{\theta}{2}\right) e^{i\varphi}$, the overlap becomes proportional to the following Majorana polynomial of degree N

$$\sum_{k=0}^{N} (-1)^k d_k \sqrt{C_N^k} z^k.$$

The complex roots z_i of this polynomial define the N Majorana points on the Bloch sphere through the mapping

$$z_i = \cot\left(\frac{\theta_i}{2}\right) e^{i\varphi_i}. \tag{1.22}$$

These roots fully determine the symmetric quantum state $|\psi\rangle$, completing the Majorana representation. From a geometrical perspective, the relation (1.22) corresponds to the stereographic projection of the point (θ_i, φ_i) on the Bloch sphere, projected from the North pole onto the complex plane $\mathbb{C}$, as illustrated in Figure 1.4.

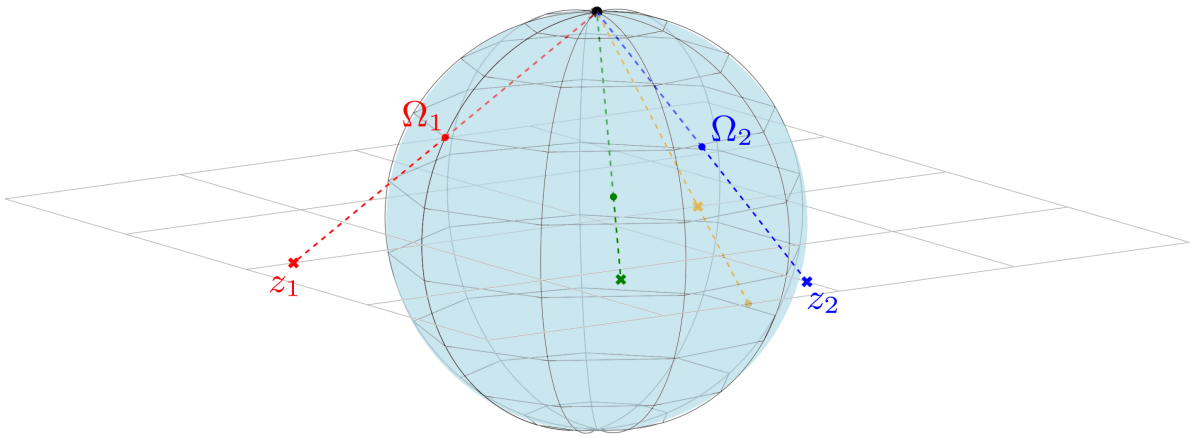

Figure 1.4: Illustration of the stereographic projection used in the Majorana representation. Colored points on the sphere represent the Majorana points $\Omega_i = (\theta_i, \varphi_i)$, which are projected onto the complex plane $\mathbb{C}$ via stereographic projection (1.22) from the North pole (shown in black). The corresponding colored crosses on the plane indicate the intersection points between the projection lines and the complex plane.

1.2 Non-classicality of spin systems

In classical and statistical physics, the phase-space formalism has provided deep insights into the behavior of classical systems and offers a natural framework to visualise their dynamics. In this section, we present the extension of the phase-space concept to quantum systems, with a particular focus on spin systems. We begin by outlining the desirable properties of a quantum phase-space representation and then specialise our discussion to the Stratonovich-Weyl correspondence, which provides a unifying framework for constructing a family of phase-space representations, including the Husimi, Wigner, and Glauber-Sudarshan functions. The relevance of phase-space methods in this thesis lies in their role as a foundation for defining and analysing the non-classicality of spin systems. One of the central goals of this work is to investigate this non-classicality and explore its connection to quantum entanglement.

1.2.1 From classical to quantum phase-space

To introduce the concept of phase-space for quantum spin systems, we begin by considering a particle in a 1-dimensional space, the simplest example of a physical system with a well-defined phase-space. Despite its simplicity, this case will help us illustrate some general and important features of quantum phase-space formulations. In classical statistical physics, a particle in one-dimensional space is not described by a single position x and momentum p, but rather by a probability distribution over phase-space. This distribution is a positive-valued function $f_c : (x, p) \to \mathbb{R}^+$ such that the probability of finding the system within a region $[x_1, x_2] \times [p_1, p_2]$ in phase space is given by

$$\mathcal{P}(x_1, x_2, p_1, p_2) = \int_{x_1}^{x_2} \int_{p_1}^{p_2} f_c(x, p)\, dpdx.$$

If we are interested only in the position or momentum, we can define the marginal

distributions over x and p by integrating out the momentum or the position, respectively

$$f(x) = \int_{-\infty}^{\infty} f_c(x,p)dp, \qquad f(p) = \int_{-\infty}^{\infty} f_c(x,p)dx$$

so that the probability of finding the particle in the position interval $[x_1, x_2]$ or momentum interval $[p_1, p_2]$ is

$$\mathcal{P}(x_1, x_2) = \int_{x_1}^{x_2} f_X(x)\, dx, \qquad \mathcal{P}(p_1, p_2) = \int_{p_1}^{p_2} f_P(p)\, dp. \tag{1.23}$$

More generally, the expectation value of any classical observable $O(x,p)$ is given by [74]

$$\langle O \rangle = \int_{-\infty}^{\infty}\int_{-\infty}^{\infty} O(x,p)\, f_c(x,p)\, dpdx.$$

In quantum mechanics, we can also define marginal probability distributions over position and momentum via the density operator ρ. Specifically, the probability densities for measuring position x or momentum p are given by

$$f_X(x) = \langle x|\rho|x\rangle, \qquad f_P(p) = \langle p|\rho|p\rangle$$

where $|x\rangle$ and $|p\rangle$ are eigenstate of the position and momentum operators, respectively. However, these functions are not phase-space distributions in the true sense, as they depend on only one of the phase-space variables, either x or p, but not both.

In analogy with classical statistical mechanics, we now seek to construct a function $f_O : \mathbf{x} \to \mathbb{R}$ that represents any operator $O \in \mathcal{B}(\mathcal{H})$, especially the density matrix ρ, over a phase-space. This function should allow us to compute expectation values of observables for a system in state ρ, without requiring direct access to the density matrix. We consider here a general phase-space manifold $\mathcal{M}$, whose geometry depends on the underlying quantum system and whose point coordinates are denoted $\mathbf{x}$. Several natural conditions can be imposed on a phase-space function [75, 76]:

1. **Informational-completeness**: There exists a one-to-one correspondence $O \leftrightarrow f_O$, such that any operator $O \in \mathcal{B}(\mathcal{H})$ can be uniquely reconstructed from its phase-space representation. The mapping need not be linear in O, but it must be invertible. In many standard formulations, the mapping is linear and defined via a family of self-adjoint operators $\{\Delta(\mathbf{x})\}_{\mathbf{x}\in\mathcal{M}}$ such that

   $$f_O(\mathbf{x}) = \mathrm{Tr}\left(O\Delta(\mathbf{x})\right), \qquad \forall \mathbf{x} \in \mathcal{M}.$$

   However, linearity is not essential for a valid phase-space representation. In this work, we allow for representations that may depend nonlinearly on the operator O, and in particular on the density matrix ρ.

2. **Expectation value computation**: The phase-space function must allow for the computation of expectation values. This is ensured if

   $$\mathrm{Tr}\left(O_1 O_2\right) = \int_{\mathcal{M}} f_{O_1}(\mathbf{x})\, f_{O_2}(\mathbf{x})\, d\mu(\mathbf{x}),$$

where $d\mu(\mathbf{x})$ denotes the integration measure associated with the manifold, such that for a state $\rho \equiv O_1$ and an observable $O \equiv O_2$,

$$\langle O \rangle = \mathrm{Tr}(\rho O) = \int_{\mathcal{M}} f_\rho(\mathbf{x}) f_O(\mathbf{x}) d\mu(\mathbf{x}).$$

Setting $O = \mathbb{I}$ ensures proper normalisation of the state

$$\mathrm{Tr}(\rho) = \int_{\mathcal{M}} f_\rho(\mathbf{x}) d\mu(\mathbf{x}) = 1.$$

3. **Covariance under symmetry transformations**: The phase-space function should transform covariantly under the symmetries of the physical system. For a particle in a one-dimensional space, this includes spatial and momentum translations. For instance, a spatial translation $x \to x + a$ of any operator $O(x)$, expressed in the position basis, implies the corresponding shift in the phase-space function

$$O(x) \to O(x + a) \iff f_O(x, p) \to f_O(x + a, p).$$

4. **Positivity**: The phase-space function associated to a state ρ is real and positive-valued, i.e. $f_\rho(\mathbf{x}) \geq 0$.

Historically, the existence of a phase-space probability distribution satisfying all of these properties was met with skepticism. This is famously illustrated by a 1945 letter from Dirac [77]:

> *I think it is obvious that there cannot be any distribution function which would give correctly the mean value of any function depending on position and momentum* P.A.M. Dirac.

However, Wigner had already introduced such a function in 1932 [14], now known as the Wigner function. It satisfies properties 1, 2 , and 3, but notably fails 4 as it can take negative values for certain quantum states. Wigner later proved that no phase-space function satisfying both informational completeness and expectation value consistency can be everywhere positive for pure states. This result implies a fundamental trade-off. One can construct phase-space functions that yield the correct expectation values, but they necessarily take negative values in some regions of phase space. Or, it is possible to define positive-valued phase-space functions, but these fail to reproduce the correct expectation values. Since neither type of function behaves like a genuine classical probability distribution, they are referred to as quasiprobability distributions. The appearance of negative values in such quasidistributions is widely recognised as a signature of the non-classical nature of quantum states[2]. From these results, it becomes clear that no single phase-space function can simultaneously satisfy all desirable properties. Each representation entails trade-offs, and different phase-space functions offer distinct advantages and disadvantages, depending on the specific application.

There are several advantages to studying a quantum system through its phase-space representation. The most immediate is visualisation as phase-space representations are

[2]To avoid ambiguity with other manifestations of quantumness, such as entanglement, we will, in this thesis, use the term non-classicality specifically to refer to the negativity of phase-space quasiprobability distributions.

real-valued and therefore more easily visualised and interpreted than complex-valued wavefunctions or density matrices [78]. Additionally, phase-space representations are of practical experimental relevance, as they allow for the reconstruction of the density matrix via quantum tomography [79, 80, 81] and the detection of entanglement in quantum states [82]. Due to their formal resemblance to classical phase space, phase-space formulations have also attracted interest in the study of the quantum-to-classical transition, whether through mathematical limiting procedures or the effects of decoherence [83]. Moreover, when a quantum state is sufficiently close to the MMS, its phase-space representation can become everywhere positive, allowing it to be interpreted as a genuine probability distribution. In such cases, the time evolution of the phase-space representation of the state may be classically simulable, typically through a Fokker-Planck equation and stochastic simulations [84, 85, 86]. Finally, discrete phase-space functions, which will be discussed later, have proven especially useful in quantum information theory, particularly in the study of contextuality and Wigner function negativity [87, 88].

As a final note on general phase-space functions, we emphasise that phase-space formulations constitute a complete and equivalent description of quantum mechanics, on the same theoretical footing as Hilbert space or path-integral approaches [89, 90, 77]. Uniquely, they offer a real-valued formulation of quantum theory, representing quantum systems entirely in terms of functions on classical-like phase-spaces.

1.2.2 Stratonovitch-Weyl phase-space representations of quantum spin systems

Since an angular momentum system is invariant under rotations, it is natural to define its phase-space manifold $\mathcal{M} = \mathcal{S}^2$ as the surface of a sphere. Physically, this choice is motivated by the fact that, in classical mechanics, an angular momentum system is described by the probability that the angular momentum vector points in a given direction $\Omega = (\theta, \varphi)$. To establish a meaningful connection between classical and quantum spin systems, it is therefore essential that their phase-space representations share the same underlying manifold.

In this context, we focus on a family of phase-space representations $\left\{\mathcal{W}_\rho^{(s)} : s \in [-1, 1]\right\}$, constructed through the Stratonovich-Weyl (SW) correspondence and parameterised by a continuous parameter $s \in [-1, 1]$. This family includes the three most commonly used quasiprobability functions, namely the Wigner function ($s = 0$), the Husimi Q function ($s = -1$), and the Glauber-Sudarshan P function ($s = 1$). The latter is often simply referred to as the P function, a convention we adopt throughout this thesis.

Within the SW formalism, one begins by selecting a reference self-adjoint operator $\Delta_0^{(s)} \equiv \Delta^{(s)}(0, 0)$ associated with the "North pole" of the sphere ($\theta = 0, \varphi = 0$) [91]. From this reference operator, one constructs an operator-valued kernel function defined over the sphere

$$\Delta^{(s)} : (\theta, \varphi) \to \Delta^{(s)}(\theta, \varphi) = R(\theta, \varphi)\, \Delta_0^{(s)} R^\dagger(\theta, \varphi) \tag{1.24}$$

where the rotation operator is given by $R(\theta, \varphi) = e^{i\varphi J_z} e^{i\theta J_y}$. The SW phase-space representation of an operator O is then defined as

$$\mathcal{W}_O^{(s)}(\theta, \varphi) = \mathrm{Tr}\left(O \Delta^{(s)}(\theta, \varphi)\right). \tag{1.25}$$

Due to the hermiticity of the kernel $\Delta(\theta, \varphi)$, this function is real-valued for any Hermitian operator O, and in particular for any density matrix $\rho \equiv O$. Furthermore, the SW

function transforms covariantly under rotations, a property inherited from the definition of the kernel.

To ensure conditions 1 and 2, the kernel must satisfy a generalised traciality condition [79, 92]

$$O = \int_{\mathcal{S}^2} \mathcal{W}_O^{(s)}(\Omega)\, \Delta^{(-s)}(\Omega)\, d\Omega \tag{1.26}$$

where the kernel $\Delta^{(-s)}(\Omega)$ (associated with the dual parameter $-s$) acts as a resolution of the operator space, and the function $\mathcal{W}_O^{(s)}(\Omega)$ serves as a set of expansion coefficients for the operator O. This relation implies a closure condition, which holds provided the kernel is normalised

$$\mathrm{Tr}\left[\Delta^{(s)}(\Omega)\right] = 1, \quad \forall s \in [-1, 1].$$

However, note that this generalised traciality condition does not directly yield the expectation value of an operator from a single SW function (except for $s = 0$). Indeed, we have

$$\langle O \rangle = \mathrm{Tr}(\rho O) = \int_{\mathcal{S}^2} \mathcal{W}_\rho^{(s)}(\Omega)\, \mathcal{W}_O^{(-s)}(\Omega)\, d\Omega, \tag{1.27}$$

such that both dual SW phase-space representations with parameters s and $-s$ are necessary.

All the conditions required of the SW kernel are satisfied if we choose as reference operator the spin parity operator [79, 91]

$$\Delta_0^{(s)} = \sum_{L=0}^{2j} \sqrt{\frac{2L+1}{2j+1}} \left(C_{jj,L0}^{jj}\right)^{-s} T_{L0}. \tag{1.28}$$

The corresponding rotated kernel is then given by

$$\Delta^{(s)}(\theta,\varphi) = R(\theta,\varphi)\, \Delta_0^{(s)} R^\dagger(\theta,\varphi) = \sqrt{\frac{4\pi}{2j+1}} \sum_{L=0}^{2j} \sum_{M=-L}^{L} \left(C_{jj,L0}^{jj}\right)^{-s} Y_{LM}^*(\theta,\varphi)\, T_{LM}. \tag{1.29}$$

With this choice, the s-parameterised SW phase-space representation of a spin-j state ρ takes the form

$$\mathcal{W}_\rho^{(s)}(\theta,\varphi) = \sqrt{\frac{4\pi}{2j+1}} \sum_{L=0}^{2j} \sum_{M=-L}^{L} \left(C_{jj,L0}^{jj}\right)^{-s} Y_{LM}(\theta,\varphi)\, \rho_{LM} \tag{1.30}$$

where the $\rho_{LM} = \mathrm{Tr}\left(\rho T_{LM}^\dagger\right)$ are the state multipoles.

The linearity of the relation (1.25) between the spin state ρ and the SW phase-space representation $\mathcal{W}_\rho^{(s)}$ imposes that the sum over L in (1.30) is restricted to $L \leq 2j$. This upper limit corresponds to the dimension of the spin-j Hilbert space and reflects the fact that a density matrix contains exactly $(2j+1)^2$ independent degrees of freedom. In Chapter 2, we will show how this restriction can be relaxed by assuming a nonlinear correspondence between ρ and $\mathcal{W}_\rho^{(s)}$. This allows us to extend the expansion (1.30) and construct more general phase-space functions.

To formalise this idea, we define the generalised SW phase-space representation as

$$\widetilde{\mathcal{W}}_\rho^{(s)}(\theta,\varphi) = \mathcal{W}_\rho^{(s)}(\theta,\varphi) + \sum_{L=2j+1}^{\infty} \sum_{M=-L}^{L} x_{LM}^{(s)} Y_{LM}(\theta,\varphi)$$

where the coefficients $x_{LM}^{(s)}$ are complex-valued and may depend nonlinearly on the state ρ. These coefficients must be chosen such that $\widetilde{\mathcal{W}}_\rho^{(s)}$ is real and covariant and that the informational completeness is preserved, i.e.

$$\rho = \int_{\mathcal{S}^2} \widetilde{\mathcal{W}}_\rho^{(s)}(\Omega)\, \Delta^{(-s)}(\Omega)\, d\Omega.$$

1.2.2.1 Wigner function

The Wigner function is the SW phase-space representation corresponding to $s = 0$, and is given by

$$\mathcal{W}_\rho^{(0)}(\theta, \varphi) = \sqrt{\frac{4\pi}{2j+1}} \sum_{L=0}^{2j} \sum_{M=-L}^{L} Y_{LM}(\theta, \varphi)\, \rho_{LM}.$$

This shows that the Wigner function directly associates each spherical harmonic Y_{LM} with the corresponding multipole ρ_{LM} of the state. A particular feature of the Wigner function, due to the choice $s = 0$, is that it is the only element of the SW phase-space representations family that allows the computation of expectation values without requiring the dual kernel. From (1.27), one has

$$\langle O \rangle = \int_{\mathcal{S}^2} \mathcal{W}_\rho^{(0)}(\Omega)\, \mathcal{W}_O^{(0)}(\Omega)\, d\Omega.$$

A direct consequence of this property is that for two orthogonal pure states $|\psi_1\rangle$ and $|\psi_2\rangle$, we have

$$|\langle \psi_1 | \psi_2 \rangle|^2 = \int_{\mathcal{S}^2} \mathcal{W}_{|\psi_1\rangle}^{(0)}(\Omega)\, \mathcal{W}_{|\psi_2\rangle}^{(0)}(\Omega)\, d\Omega = 0.$$

This implies that the Wigner function of any pure state must take negative values. This includes even spin coherent states, despite their semiclassical interpretation. In fact, this negativity can be traced to the vanishing of the overlap between antipodal coherent states (see (1.10)). Since all coherent states are related to each other by rotations, and the Wigner function is covariant under SU(2), the existence of negative values for one coherent state implies negativity for all. This behavior contrasts with the Wigner function in infinite-dimensional systems (as in quantum optics), where Hudson's theorem [93] states that a pure state has a non-negative Wigner function if and only if it is Gaussian. Thus, in that setting, coherent states have positive Wigner functions.

As negativity in phase-space representations is widely regarded as a signature of non-classicality, it can be used to quantify the degree of quantumness of a state. One such measure is the Wigner negativity volume [16] defined as

$$\delta(\rho) = \frac{1}{2}\left(\int_{\mathcal{S}^2} |W_\rho(\Omega)|\, d\Omega - 1\right) \geq 0 \tag{1.31}$$

which is invariant under SU(2) transformations and vanishes only when the Wigner function is positive everywhere. For spin systems, this quantity may vanish only when the state ρ is sufficiently mixed. In Appendix 1.C, we show that the negativity of states with an everywhere positive P function is upper bounded by the Wigner negativity of spin coherent states.

1.2.2.2 Husimi Q and Glauber-Sudarshan *P* functions

The Husimi and P functions correspond to the SW phase-space representations associated with parameters $s = -1$ and $s = 1$, respectively. We have already encountered the P function in the context of coherent states, where we showed that

$$\rho = \int_{\mathcal{S}^2} P_\rho(\Omega) |\Omega\rangle \langle\Omega| \, d\Omega.$$

Comparing this with the generalised traciality condition (1.26), it follows that the kernel associated with the Husimi function is simply the projector onto coherent states

$$\Delta^{(-1)}(\theta, \varphi) = |\theta, \varphi\rangle \langle\theta, \varphi| .$$

Consequently, the Husimi function of a spin state ρ is given by

$$\mathcal{W}_\rho^{(-1)}(\theta, \varphi) \equiv Q_\rho(\theta, \varphi) = \langle\theta, \varphi| \rho |\theta, \varphi\rangle .$$

This function is everywhere positive and can be interpreted as the probability density of obtaining the outcome $|\theta, \varphi\rangle$ in a projective measurement of the state ρ in the coherent state basis. It therefore indicates the extent to which ρ is aligned with the direction (θ, φ).

From the SW framework, the P function is defined as

$$P_\rho(\theta, \varphi) = \sqrt{\frac{4\pi}{2j+1}} \sum_{L=0}^{2j} \sum_{M=-L}^{L} \left(C^{jj}_{jj,L0}\right)^{-1} Y_{LM}(\theta, \varphi) \, \rho_{LM}.$$

Due to the growth of the inverse Clebsch-Gordan coefficient $\left(C^{jj}_{jj,L0}\right)^{-1}$ with increasing L, the P function amplifies higher-order L multipoles, making it highly sensitive to the detailed structure of the quantum state. This sensitivity makes the P function especially useful when analysing non-classical features of spin states, as it emphasises contributions from high angular harmonics that are often associated with quantum correlations and entanglement. In Appendix 1.D, we derive the analytical expression of the eigenvalues of the kernel $\Delta^{(1)}$ associated with the P function, which will prove useful in Chapter 2.

In Figure 1.5, we compare the Husimi, Wigner, and P functions for three representative symmetric states of four qubits, namely the coherent state $|\theta = 0, \varphi = 0\rangle$, the balanced Dicke state $|D_4^{(2)}\rangle$ and the GHZ state. For better readability, projections of the half-spheres facing the xy-, yz- and zx-planes are also shown. We observe that the Husimi function is strictly positive, while the Wigner function of the coherent state displays small regions of negativity. The coherent state is sharply peaked at the North pole of the Bloch sphere, reflecting its classicality and well-defined mean spin direction. In contrast, both the Dicke and GHZ states exhibit more delocalised distributions across the sphere. In particular, the state $|D_4^{(2)}\rangle$ is spread uniformly along the equatorial line and has a zero mean spin vector, $\langle \mathbf{J} \rangle = 0$, consistent with it being 1-AC. Such delocalisation on the phase-space representation of pure states is often interpreted as a hallmark of non-classicality, a concept that will be explored quantitatively in Chapter 3.

Finally, it is useful to note that the Husimi and Wigner functions can be seen as Gaussian smoothings of the Wigner and P functions, respectively [91]. This smoothing operation blurs out sharp features and suppresses extreme values. As a result, the positivity of the Husimi function can be understood as arising from the averaging of the

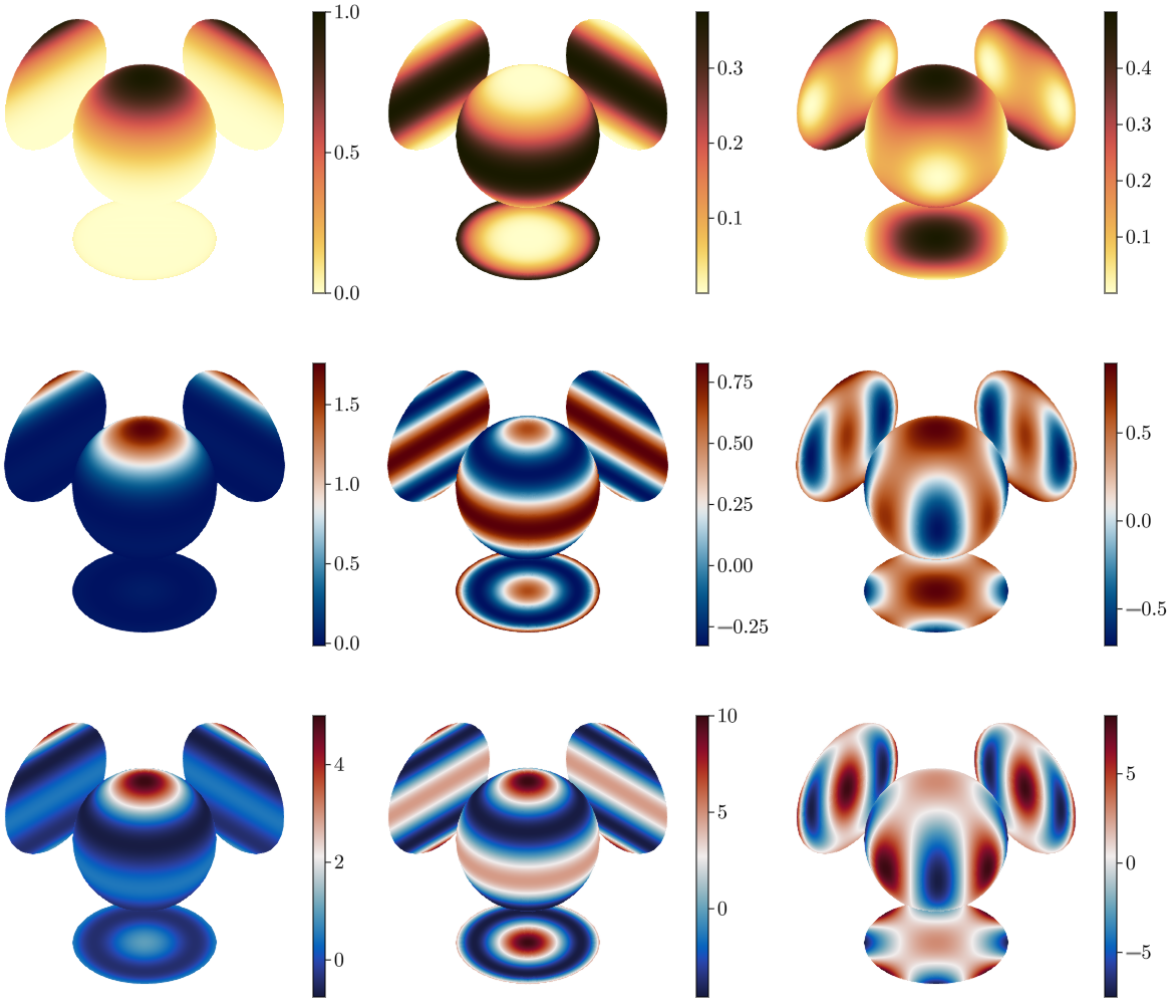

Figure 1.5: Phase-space representations and projections of the half-sphere facing the xy-, yz- and zx-planes of (from left to right) the coherent state $|\theta = 0, \varphi = 0\rangle$, the balanced Dicke state $|D_4^{(2)}\rangle$ and the GHZ state for $N = 4$. From top to bottom, we have the Husimi, Wigner and P functions.

Wigner function's negative and positive regions. This behavior is illustrated in Figure 1.5, where the fine angular structures present in the P function, particularly the ripples at the equator and at the South pole in the P representation of the coherent state, are entirely suppressed in the Wigner and Husimi functions.

1.2.3 Discrete phase-space functions

As previously discussed, the SW kernel $\Delta^{(s)}(\Omega)$ form a basis of the linear operator space $\mathcal{B}(\mathcal{H})$ via the generalised traciality condition (1.26). However, for a spin-j system, the space $\mathcal{L}(\mathbb{C}^{2j+1})$ of linear operators is $(2j+1)^2$-dimensional, so the continuous family $\left\{\Delta^{(s)}(\Omega) : \Omega \in [0, 2\pi]\right\}$ constitutes an overcomplete operator basis. This motivates the construction of a discrete set of spin operators that can also support phase-space representations, similar in spirit to the SW formalism but defined on a finite grid.

Analogous to the rotation operators $R_{\mathbf{n}}(\Omega)$ used to generate the SW kernel from a reference operator $\Delta^{(s)}(0)$, the discrete phase-space operators are generated using a

unitary representation of the discrete Heisenberg-Weyl group [94, 95]

$$\{\mathcal{T}_{pq} : p, q = 0, 1, \ldots, N\}.$$

To define these operators for a system of N qubits restricted to the symmetric subspace, we introduce generalised Pauli operators via their action on Dicke states

$$Z\left|D_N^{(k)}\right\rangle = \omega^k \left|D_N^{(k)}\right\rangle \qquad X\left|D_N^{(k)}\right\rangle = \left|D_N^{(k+1 \mod N+1)}\right\rangle$$

where $\omega = e^{2\pi i/d}$, where $d = N + 1$, is a primitive $(N + 1)$-th root of unity. Using these, we define the displacement operators

$$\mathcal{D}_{pq} = \omega^{\frac{(N+2)pq}{2}} Z^p X^q, \quad \text{with} \quad p, q = 0, 1, \ldots, N.$$

The set $\{\mathcal{D}_{pq}\}$ forms a unitary operator basis for $\mathcal{L}\left(\mathbb{C}^{N+1}\right)$.

Based on this construction, one defines a family of discrete phase-space representations $\mathbb{W}_\rho^{(s)}$ parameterised by $s \in [-1, 1]$ [96]

$$\mathbb{W}_\rho^{(s)}(p, q) = \mathrm{Tr}\left(\rho \Delta_{pq}^{(s)}\right) \tag{1.32}$$

where the kernel $\Delta_{pq}^{(s)}$, in order to be well-defined, must satisfy the following properties analogous to those in the continuous SW formalism:

1. **Hermiticity** : $\left(\Delta_{pq}^{(s)}\right)^\dagger = \Delta_{pq}^{(s)}$
2. **Normalisation** : $\mathrm{Tr}\left(\Delta_{pq}^{(s)}\right) = 1$
3. **Covariance** : $\Delta_{p-p' \mod N+1, q-q' \mod N+1}^{(s)} = \mathcal{D}_{p'q'} \Delta_{pq}^{(s)} \mathcal{D}_{p'q'}^\dagger$
4. **Traciality** : $\mathrm{Tr}\left(\Delta_{pq}^{(s)} \Delta_{p'q'}^{(-s)}\right) = N \delta_{pp'} \delta_{qq'}$.

Here, the discrete Heisenberg-Weyl displacement operators $\mathcal{D}_{pq}$ take the place of rotation operators in the covariance condition, establishing symmetry under phase-space translations. Each valid set of phase-point operators $\{\Delta_{pq} : p, q = 0, 1, \ldots, N\}$, satisfying the properties above, yields a one-to-one correspondence between density operators ρ and representations $\mathbb{W}_\rho^{(s)}$ on a discrete $(N + 1) \times (N + 1)$ grid. This grid is made topologically compact by periodicity in both p and q (as implied by the covariance condition), resulting in a discrete torus phase-space manifold.

A prominent example of such a function, for $s = 0$ and even N, is the Wootters discrete Wigner function, which is a natural generalisation of the continuous Wigner function to finite-dimensional systems [23].

1.3 Entanglement of symmetric multiqubit states

Entanglement is a foundational concept in quantum physics, first introduced in 1935 through the seminal works of Einstein, Podolsky, and Rosen [1], and Schrödinger [97]. For decades, it remained a subject of theoretical debate, particularly regarding its implications for locality and realism. The development of Bell inequalities in 1964 [98], and their subsequent experimental violation more than forty years ago [99, 100], provided decisive

evidence against local hidden variable theories and confirmed the non-classical nature of quantum correlations.

Today, despite ongoing discussions about the interpretation of quantum mechanics, entanglement is widely recognised as a key resource driving the emerging field of quantum technologies. It forms the backbone of the so-called second quantum revolution [101], enabling advances in quantum cryptography [102], quantum communications [8], quantum sensing [103] and quantum computing [104]. A major goal of this thesis is to contribute to the characterisation of entanglement, to investigate its relation with other properties of quantum systems, and explore its potential for future applications.

1.3.1 Separable states

Separability of pure states. Consider a quantum system composed of N subsystems, each of which can be a spin-j (with arbitrary j) or even an infinite-dimensional system, such as a mode of the electromagnetic field. A pure state of this composite system is said to be separable, i.e. not entangled, if it can be written as a tensor product [73]

$$|\psi\rangle = |\psi_1\rangle \otimes |\psi_2\rangle \otimes \cdots \otimes |\psi_N\rangle \tag{1.33}$$

where each $|\psi_i\rangle$ is the state of a single subsystem.

From this definition, it is clear that the state of each subsystem is well-defined. For instance, the state of the first subsystem is $|\psi_1\rangle$ and although measurement outcomes on $|\psi_1\rangle$ are inherently probabilistic, this state represents the most complete information one can obtain about that subsystem (provided no hidden variables exist). Therefore, in a separable state, the information about each subsystem is maximal. However, the state (1.33) is not the most general form of a pure state in a composite system. Due to the superposition principle, a consequence of the Hilbert space structure of quantum states, a general pure state may be expressed as

$$|\psi\rangle = \sum_{i=1}^{n} c_i \left|\psi_1^{(i)}\right\rangle \otimes \left|\psi_2^{(i)}\right\rangle \otimes \cdots \otimes \left|\psi_N^{(i)}\right\rangle, \qquad c_i \in \mathbb{C}, \sum_{i=1}^{n} |c_i|^2 = 1 \tag{1.34}$$

which reduces to (1.33) if $n = 1$. For $n \geq 2$, the state of each individual subsystem is no longer well-defined as it is not possible to assign a single pure state to any subsystem. This property unambiguously signifies the non-local nature of the state (1.34), as the global state $|\psi\rangle$ is fully known even though the states of its subsystems are not. This is in sharp contrast to classical systems, where the global state can always be retrieved from the states of its parts. Due to this global property, the state (1.34) is said to be entangled in the sense that its subsystems cannot be treated independently and are inherently inseparable. To describe individual subsystems in such an entangled state, one must use the partial trace operation. For example, the reduced state of the first subsystem is given by

$$\rho_1 = \mathrm{Tr}_{\neg 1}\left(|\psi\rangle\langle\psi|\right)$$

and the state of the two first subsystems is $\rho_{12} = \mathrm{Tr}_{\neg 12}\left(|\psi\rangle\langle\psi|\right)$. Based on definition (1.33), we now extend separability to mixed states.

Separability of mixed states. A N-partite mixed state ρ is separable if it can be expressed as a convex sum of pure separable states, namely [105]

$$\rho = \sum_i p_i |\Omega_i\rangle\langle\Omega_i|$$

where each $|\Omega_i\rangle$ is itself a separable pure state and the weights satisfy $p_i \geq 0$ and $\sum_i p_i = 1$.

In practice, certifying the full separability of a multipartite quantum state is a challenging task. Therefore, it is often more feasible to examine whether the state is separable with respect to a specific bipartition of the system. Consider an N-partite system divided into two subsystems A and B, such that the total Hilbert space factorizes as $\mathcal{H} = \mathcal{H}_A \otimes \mathcal{H}_B$. A pure state $|\psi\rangle \in \mathcal{H}$ is said to be separable with respect to the bipartition $A|B$ if it can be written as

$$|\psi\rangle = |\psi_A\rangle \otimes |\psi_B\rangle ,$$

where $|\psi_A\rangle \in \mathcal{H}_A$ and $|\psi_B\rangle \in \mathcal{H}_B$. However, even if a state is separable w.r.t. all possible bipartitions, this does not imply that the state is separable. In the special case of symmetric multiqubit systems, where the multiqubit states are constrained to the symmetric subspace, all bipartitions into t and $N-t$ qubits are equivalent under qubit permutations. Thus, it suffices to consider bipartitions of the form $t|N-t$ without specifying which particular qubits belong to each subset.

Another important line of research in the characterisation of entanglement concerns whether a given quantum state ρ can become entangled under some global unitary transformation. Indeed, in a region surrounding the MMS, there exist mixed states that remain separable under any global unitary. These are known as Absolutely Separable (AS) states. This question is particularly relevant in practice, since global unitaries are the types of operations typically accessible in laboratory settings. From the perspective of entanglement resource theory, where entanglement is treated as a resource, AS states are considered free states. Nevertheless, a complete characterisation of the set of AS states remains an open problem in quantum information theory.

Absolute Separability. A state ρ is said to be AS if $U\rho U^\dagger$ is separable for all $U \in \mathcal{U}(\mathcal{H})$, where $\mathcal{U}(\mathcal{H})$ is the set of unitary operator defined on the Hilbert space $\mathcal{H}$ [106].

The set of states $\left\{U\rho U^\dagger, U \in \mathcal{U}(\mathcal{H})\right\}$, known as the unitary orbit of ρ, consists of all states unitarily connected to ρ, and all such states share the same eigenvalue spectrum. Conversely, any two states with the same spectrum belong to the same unitary orbit. That is, the unitary orbit of ρ is uniquely determined by its eigenvalues, and vice versa. Hence, the absolute separability problem is sometimes rephrased as the separability by spectrum problem [107] since conditions for absolute separability are frequently expressed in terms of the eigenvalues shared in a same unitary orbit.

Obviously, a pure state $\rho = |\psi\rangle\langle\psi|$ can always be entangled via an appropriate global unitary transformation. Hence, the characterisation of AS states focuses on mixed states that remain separable under all unitaries. A foundational result in this area is the exact characterisation of the maximal ball of absolutely separable states centered on the MMS for bipartite systems [108]. Moreover, for qubit-qudit systems of dimension $2 \times d$, it is known that a state ρ is absolutely separable if and only if [107]

$$\lambda_1 - \lambda_{2d-1} - \sqrt{\lambda_{2d-2}\lambda_{2d}} \leq 0$$

where the eigenvalues $\lambda_1 \geq \lambda_2 \geq \cdots \geq \lambda_{2d}$ of ρ are sorted in decreasing order. However, the exact characterisation of the sets of AS states in general multipartite systems is still an open problem. In Chapter 2, we will be interested in extending the characterisation of the set of AS states of multiqubit systems in the symmetric subspace.

1.3.2 Entanglement criteria and entanglement measures

Several criteria have been proposed in the literature to determine whether a given quantum state is entangled or not [109, 110]. However, none of these criteria is entirely satisfactory. They are typically either only necessary or only sufficient, or they are impractical, that is, difficult to compute or verify experimentally. As a result, the problem of identifying a practical necessary and sufficient criterion for certifying separability, known as the separability problem, remains open.

Conversely, when a state is known to be entangled, various entanglement measures have been introduced to quantify the degree of entanglement it exhibits. In what follows, we focus on the entanglement criteria and measures that will be used in the subsequent chapters.

1.3.2.1 Entanglement criteria

One of the most widely used bipartite entanglement criteria, due to its simplicity and ease of computation, is based on the positivity of the partial transpose (PPT).

Proposition. *If a state ρ is separable w.r.t. bipartition $t|N-t$, then its partial transpose ρ^{T_t} is positive semi-definite [6, 7].*

Consequently, if a state is not PPT, meaning that its partial transpose has negative eigenvalues, under a given bipartition, then it is entangled w.r.t. that bipartition. In the special cases of pure states, and of mixed states in 2×2 or 2×3 dimensional systems, the PPT criterion is both necessary and sufficient for entanglement.

In the particular case of symmetric states, several others entanglement criteria (realignement criterion, spin-squeezing criterion,...) have been shown to be equivalent to the PPT criterion [111, 112]. Furthermore, symmetric N-qubit states are either genuinely entangled, i.e. entangled across any bipartition, or fully separable [113]. This implies that if a symmetric N-qubit state has zero negativity with respect to a given bipartition $t|N-t$, but non-zero with respect to some other bipartition, the state is genuinely entangled and, in particular, still entangled across the $t|N-t$ bipartition, despite the vanishing negativity.

A separability criterion based on the P function of symmetric multiqubit states will prove useful in the following chapters.

Proposition. *A symmetric multiqubit state ρ is separable if and only if there exists an everywhere positive P function P_ρ, that is [114]*

$$P_\rho(\Omega) \geq 0, \quad \forall \Omega \in \mathcal{S}^2 \qquad \text{and} \qquad \rho = \int_{\mathcal{S}^2} P_\rho(\Omega) \, |\Omega\rangle \langle\Omega| \, d\Omega.$$

This characterisation is intuitive since any coherent state $|\Omega\rangle$ is separable (see (1.9)). Hence, any state ρ that can be expressed as a convex sum of such states is also separable. While this criterion provides a necessary and sufficient condition for separability in the symmetric subspace, its main drawback is that explicitly constructing the corresponding positive P function for a given separable state ρ can be challenging. This is illustrated in Figure 1.5, where even for the coherent state $|j, j\rangle$, the associated P function takes negative values for certain polar angles θ, highlighting that not all P functions are everywhere positive even for separable states.

1.3.2.2 Entanglement measures

To quantify the degree of entanglement of a quantum state, one introduces entanglement measures.

Given a quantum system described by a Hilbert space $\mathcal{H}$, an entanglement measure E is a mapping from density matrices into positive real numbers. There is not a completely unified definition of a good entanglement measure but it is generally admitted that entanglement measures must satisfy, at least, the two following conditions [115, 4].

- **Vanishing on separable states:** $E(\rho_{\text{sep}}) = 0$ if the state ρ_{sep} is separable.
- **Monotonicity under LOCC:** Entanglement cannot increase under Local Operations and Classical Communications (LOCC).

Many more conditions can be imposed on an entanglement measure, such as normalisation, asymptotic continuity, additivity,... (see [4, 115]). An additional condition which is satisfied by numerous entanglement measures, including those we will use in this manuscript, is convexity. That is, for a convex combination of states ρ_i with weights p_i, we have

$$E\left(\sum_i p_i \rho_i\right) \leq \sum_i p_i E(\rho_i).$$

Based on the PPT criterion, a widely used entanglement measure is the negativity of the partial transpose, often simply referred to as the negativity [116].

Entanglement negativity. For a given bipartition $t|N-t$ of an N-qubit system in a symmetric state ρ, the negativity $\mathcal{N}_t(\rho)$ is defined as the sum of the modulus of the negative eigenvalues of the partial transpose ρ^{T_t}, i.e.

$$\mathcal{N}_t(\rho) = \sum_{i=1}^{t+1} \frac{|\lambda_i| - \lambda_i}{2}, \tag{1.35}$$

where the λ_i's are the eigenvalues of ρ^{T_t}. An important result is that a pure state is separable w.r.t. a given bipartition if and only if its negativity w.r.t. this bipartition is zero [7].

In the case of a pure state $\rho = |\psi\rangle\langle\psi|$, the eigenvalues of ρ^{T_t} can be related to the eigenvalues λ_i of the reduced state ρ_t of $|\psi\rangle$, which are equivalent to the Schmidt coefficients $\sqrt{\lambda_i}$ of $|\psi\rangle$. In this case, the negativity can be expressed as [117]

$$\mathcal{N}_t(|\psi\rangle) = \sum_{i>j=1}^{t+1} \sqrt{\lambda_i \lambda_j}. \tag{1.36}$$

From this expression, one can see that the negativity is maximal when the reduced state ρ_t is the MMS, i.e., when all $\lambda_i = 1/(t+1)$. In that case, the negativity reaches its maximal value [36]

$$\mathcal{N}_t(|\psi\rangle) = \frac{t}{2}.$$

For GHZ states, the t-qubit reduced states read $\rho_t = \text{diag}(1/2, 0, ..., 0, 1/2)$ and the negativity is equal to $1/2$ for any bipartition. For Dicke states, the Schmidt decomposition [73]

$$|D_N^{(k)}\rangle = \sum_{\ell=0}^{k} \sqrt{\frac{\binom{t}{\ell}\binom{N-t}{k-\ell}}{\binom{N}{k}}} |D_t^{(\ell)}\rangle \otimes |D_{N-t}^{(k-\ell)}\rangle$$

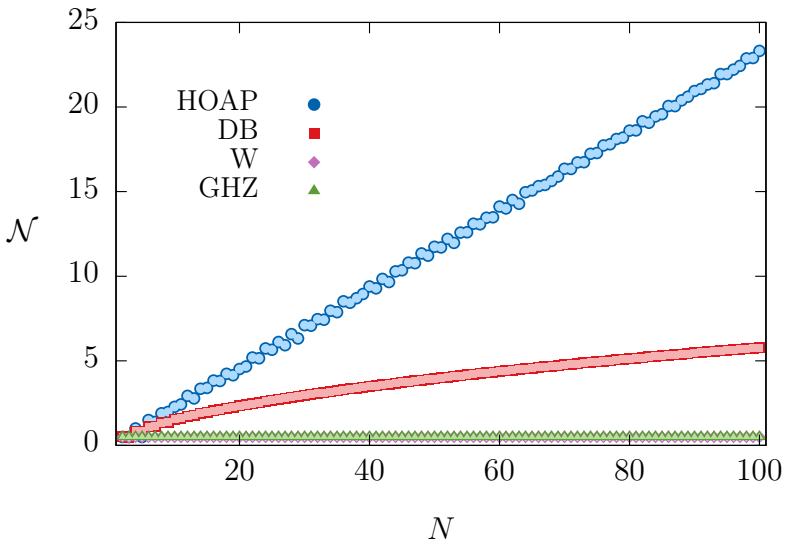

Figure 1.6: Entanglement negativity $\mathcal{N}$ with respect to the balanced bipartition $\lfloor N/2 \rfloor | \lceil N/2 \rceil$ of several families of pure states as a function of the number of qubits. We have $\mathcal{N} \approx 0.231\, N$ for HOAP states (blue circles), $\mathcal{N} \approx -0.469 + 0.625\sqrt{N}$ for balanced Dicke states $\left| D_N^{\lfloor N/2 \rfloor} \right\rangle$ (DB, red squares) and $\mathcal{N} = 1/2$ for W states (purple diamonds) and GHZ states (green triangles).

allows us to calculate the negativity across any bipartition $t|N-t$ through

$$\mathcal{N}\left(|D_N^{(k)}\rangle\right) = \binom{N}{k} \sum_{i=0}^{t} \sum_{j=0}^{i-1} \sqrt{\binom{t}{i}\binom{N-t}{k-i}\binom{t}{j}\binom{N-t}{k-j}}.$$

In particular, we get for W states

$$\mathcal{N}\left(|W\rangle\right) = \frac{\sqrt{(N-t)\,t}}{N}.$$

As already stated, the maximal negativity of pure states $\mathcal{N}_{\max} = t/2$ is reached when all eigenvalues λ_i are equal to $1/(t+1)$. For an equal bipartition $\lfloor N/2 \rfloor | \lceil N/2 \rceil$, the bound is equal to $N/4$ and thus scales linearly with the number of qubits. Figure 1.6 shows the negativity with respect to a balanced bipartition for several families of states as a function of the number of qubits. We observe that for the HOAP states found numerically in [118, 119], we observe a linear scaling of the negativity with N, but with a prefactor of 0.231 slightly smaller than the prefactor 1/4 of the upper bound.

Another entanglement measure is the geometric measure of entanglement (GME) which quantifies the minimal distance between a pure state $|\psi\rangle$ and the set of separable states $\mathcal{S}$. Intuitively, it is expected that a state which is far from $\mathcal{S}$ should be strongly entangled.

Geometric Measure of Entanglement Given an N-qubit pure state $|\Psi\rangle$, defined over the full Hilbert space $\mathbb{C}^{2^N}$, its GME is defined as [120]

$$E_G\left(|\Psi\rangle\right) = 1 - \max_{\{|\phi_i\rangle\}_{i=1}^N} \left| \langle \phi_1 \otimes \phi_2 \cdots \otimes \phi_N | \, \psi \rangle \right|^2, \tag{1.37}$$

where the maximisation is performed over the N single-qubit states $|\phi_i\rangle$. The GME satisfies $E_G\left(|\Psi\rangle\right) \leq 1$ and vanishes if and only if $|\Psi\rangle$ is separable. While the GME is a

genuine measure of multipartite entanglement, meaning that it vanishes only if the state is fully separable, it is generally difficult to compute. In Chapter 3, we explain a method based on machine learning to estimate the GME without full state tomography.

For symmetric multiqubit states, the maximisation appearing in (1.37) can be replaced by the simpler maximisation where all single-qubit states $|\phi_i\rangle$ are identical, i.e.

$$E_G\left(|\psi\rangle\right) = 1 - \max_{|\phi\rangle} |\langle \phi \otimes \phi \cdots \otimes \phi | \psi\rangle|^2$$

This is allowed by the fact that the closest separable state of a symmetric multiqubit state is also symmetric [121]. A (not tight) upper bound on the GME of N-qubit symmetric states is given by [122]

$$E_G\left(|\psi\rangle\right) \leqslant 1 - \frac{1}{N+1}. \tag{1.38}$$

Given an entanglement measure E defined on pure states, one can naturally extend it to mixed states via the convex-roof construction.

Convex-roof extension. Given an entanglement measure E defined on pure states, its convex-roof extension defined on mixed states is given by

$$E\left(\rho\right) = \min_{\{p_i, |\psi_i\rangle\}} \sum_i p_i E\left(|\psi_i\rangle\right)$$

where the minimum is taken over all possible pure state decompositions $\rho = \sum_i p_i |\psi_i\rangle \langle\psi_i|$.

In particular, the negativity of pure states can be extended through the convex roof extension of negativity [123]

$$\mathcal{N}_t^{CR}\left(\rho\right) = \min_{\{p_i, |\psi_i\rangle\}} \sum_i p_i \mathcal{N}_t\left(|\psi_i\rangle\right).$$

In contrast to the (ordinary) negativity of mixed states, it vanishes if and only if the state is separable w.r.t. the bipartition $t|N-t$. Similarly, the GME can be generalised to mixed states based on the convex roof construction

$$E_G\left(\rho\right) = \min_{\{p_i, |\psi_i\rangle\}} \sum_i p_i E_G\left(|\psi_i\rangle\right). \tag{1.39}$$

In [124], it was shown that this definition is equivalent to another definition based on the distance of ρ to the convex set $\mathcal{S}$ of separable mixed states

$$E_G(\rho) = 1 - \max_{\sigma_{\text{sep}} \in \mathcal{S}} F\left(\rho, \sigma_{\text{sep}}\right) \tag{1.40}$$

where

$$F\left(\rho, \sigma\right) = \text{Tr}\left(\sqrt{\sqrt{\rho}\sigma\sqrt{\rho}}\right)^2 \tag{1.41}$$

is the Uhlmann fidelity between any two mixed states ρ and σ.

1.A Rotational control of atomic spin systems

Spin systems appearing in atomic physics can originate either from multilevel structures defined by the (hyper)fine interaction in a single atom or from collective spins, such as an ensemble of atomic qubits in a gas or in a Bose-Einstein condensate (see e.g. [125]). In all such cases, the spin is associated with a magnetic moment given by $\mathbf{m} = -\gamma \mathbf{J}$ where γ is a proportionality constant (the gyromagnetic ratio) that depends on the specific physical implementation of the spin system. When an external magnetic field $\mathbf{B}$ is applied, the spin experiences a Zeeman interaction described by the Hamiltonian

$$H = -\mathbf{m} \cdot \mathbf{B}.$$

To define a quantisation axis, a static magnetic field is usually applied along the z-axis $\mathbf{B}_0 = B_0 \mathbf{e}_z$. This leads to a Hamiltonian of the form

$$H_0 = \gamma B_0 J_z = \omega_0 J_z \tag{1.42}$$

where $\omega_0 = \gamma B_0$ is the Larmor frequency. This field plays two key roles. First, the eigenstates $|j, m\rangle$ of the spin operators J_z and J^2 acquire different energies due to their magnetic quantum number m, since $\langle j, m| J_z |j, m\rangle = m$. This lifts any degeneracy between the $|j, m\rangle$ levels, helping to suppress unwanted transitions due to environmental noise and enabling specific control on the spin state.

Secondly, since the magnetic field $\mathbf{B}_0$ is constant, the spin state evolves according to

$$|\psi(t)\rangle = e^{-iH_0 t} |\psi(0)\rangle = e^{-i\gamma B_0 J_z t} |\psi(0)\rangle, \tag{1.43}$$

The evolution (1.43) is exactly of the form of a rotation around the z-axis (see Subsection 1.1.2). Hence, a magnetic field induces a rotation on an atomic spin state around the axis of the magnetic field.

However, this static Hamiltonian H_0 does not allow arbitrary control over the spin direction. To implement general spin rotations, e.g. around the x- or y-axis, it is necessary to apply a time-dependent magnetic field [126]. For instance, a rotation around the x-axis can be achieved by applying a magnetic field rotating in the xy-plane at frequency ω

$$\mathbf{B}_1 = B_1 (\cos(\omega t)\, \mathbf{e}_x + \sin(\omega t)\, \mathbf{e}_y).$$

This gives rise to a Hamiltonian in the lab frame

$$H = \omega_0 J_z + \omega_1 (\cos(\omega t)\, J_x + \sin(\omega t)\, J_y)$$

where $\omega_1 = \gamma B_1$ is the Rabi frequency. To understand the effect of this time-dependent drive, we move into the rotating frame w.r.t. the static magnetic field. In this frame, spin operators transform as

$$U_z^\dagger(\omega t) J_x U_z(\omega t) = \cos(\omega t) J_x - \sin(\omega t) J_y \qquad U_z^\dagger(\omega t) J_y U_z(\omega t) = \cos(\omega t) J_y + \sin(\omega t) J_x,$$

where $U_z(\omega t) = e^{-i\omega J_z t}$. Applying this transformation to the Hamiltonian, the effective Hamiltonian in the rotating frame becomes

$$\tilde{H} = (\omega_0 - \omega) J_z + \omega_1 J_x.$$

On resonance, that is, when the drive frequency matches the Larmor frequency $\omega = \omega_0$, the first term vanishes, and we are left with a time-independent Hamiltonian

$$\tilde{H} = \omega_1 J_x$$

which generates a pure rotation about the x-axis in the rotating frame. This is the foundation of coherent control in atomic spin systems, a static magnetic field defines the quantisation axis and lifts degeneracies, while an oscillating transverse field resonantly drives transitions and implements arbitrary rotations.

1.B Partial trace in the MPB

In this Appendix, we show that if ρ is an N-qubit symmetric state, with expansion in the MPB given by

$$\rho = \sum_{L=0}^{N} \sum_{M=-L}^{L} \rho_{LM} T_{LM}^{(N)}, \tag{1.44}$$

then its t-qubit reduction $\rho_t \equiv \mathrm{Tr}_{\neg t}(\rho)$ is given by

$$\rho_t = \sum_{L=0}^{t} \sum_{M=-L}^{L} \tfrac{t!}{N!} \sqrt{\tfrac{(N-L)!(N+L+1)!}{(t-L)!(t+L+1)!}} \rho_{LM} T_{LM}^{(t)} \tag{1.45}$$

where, for clarity, we have added a superscript to the multipolar operators indicating the number of qubits. Using the coherent spin states basis, the multipole operators read [127]

$$T_{LM}^{(N)} = \tfrac{N+1}{4\pi} \alpha_L^{(N)} \int_{\mathcal{S}^2} Y_{LM}(\Omega) |\Omega\rangle\langle\Omega| d\Omega, \tag{1.46}$$

with

$$\alpha_L^{(N)} = 2\sqrt{\pi}\, \frac{\sqrt{(N-L)!(N+L+1)!}}{(N+1)!}.$$

In the coherent state representation, the partial trace is readily performed because the partial trace of $|\Omega\rangle\langle\Omega|$ over any set of $N-t$ qubits is trivially $\left|\Omega^{(t)}\right\rangle\left\langle\Omega^{(t)}\right|$, where we use the superscript (t) to specify the number of qubits. Thus, the partial trace of (1.46) yields

$$\mathrm{Tr}_{\neg t}\left[T_{LM}^{(N)}\right] = \tfrac{N+1}{4\pi} \alpha_L^{(N)} \int_{\mathcal{S}^2} Y_{LM}(\Omega) \left|\Omega^{(t)}\right\rangle\left\langle\Omega^{(t)}\right| d\Omega$$

or, upon comparison with (1.46) where N has been replaced by t,

$$\mathrm{Tr}_{\neg t}\left[T_{LM}^{(N)}\right] = \begin{cases} \frac{N+1}{t+1} \frac{\alpha_L^{(t)}}{\alpha_L^{(N)}} T_{LM}^{(t)} & L \leqslant t, \\ 0 & L > t. \end{cases} \tag{1.47}$$

Equation (1.47) for $L > t$ holds true because the integral

$$\int_{\mathcal{S}^2} Y_{LM}(\Omega) \left|\Omega^{(t)}\right\rangle\left\langle\Omega^{(t)}\right| d\Omega$$

vanishes for $L > t$, as can be seen by substituting (1.17) for $(|\Omega\rangle\langle\Omega|)^{\otimes t}$ and using the orthogonality of spherical harmonics. In (1.47), the prefactor of $T_{LM}^{(t)}$ can also be written as

$$\tfrac{N+1}{t+1} \frac{\alpha_L^{(t)}}{\alpha_L^{(N)}} = \tfrac{t!}{N!} \sqrt{\tfrac{(N-L)!(N+L+1)!}{(t-L)!(t+L+1)!}}. \tag{1.48}$$

In the end, by linearity of the partial trace, using (1.44), (1.47) and (1.48), we get (1.45). A similar result was obtained in [128] by a different method.

1.C Bound on Wigner negativity volume

We show here that the Wigner negativity volume (1.31) of states with an everywhere positive P function, denoted hereafter by $\rho_{P\geqslant 0}$, is upper bounded by the Wigner negativity volume of spin coherent states. Indeed, such states can always be represented as a mixture of coherent states

$$\rho_{P\geqslant 0} = \sum_i p_i \left|\Omega_i\right\rangle \left\langle\Omega_i\right|$$

with $p_i \geqslant 0$ and $\sum_i p_i = 1$. Their Wigner negativity volume can then be upper bounded as follows

$$\begin{aligned}
\delta\left(\rho_{P\geqslant 0}\right) &= \frac{1}{2}\left(\int_{\mathcal{S}^2}\left|W_{\rho_{P\geqslant 0}}\left(\Omega'\right)\right| d\Omega' - 1\right) = \frac{1}{2}\int_{\mathcal{S}^2}\left|\sum_i p_i W_{|\Omega_i\rangle}\left(\Omega'\right)\right| d\Omega' - \frac{1}{2} \\
&\leqslant \underbrace{\sum_i p_i}_{=1}\underbrace{\left(\frac{1}{2}\int_{\mathcal{S}^2}\left|W_{|\Omega_i\rangle}\left(\Omega'\right)\right| d\Omega'\right)}_{=\delta(|\Omega\rangle)+\frac{1}{2}} - \frac{1}{2} = \delta\left(|\Omega\rangle\right)
\end{aligned}$$

where $\delta\left(|\Omega\rangle\right)$ is the Wigner negativity volume of a spin coherent state. Since it has been observed that such Wigner negativity volume decreases with j [129], the same is true for states with positive P function.

1.D Eigendecomposition of the P function kernel

Here we derive the eigendecomposition of the Stratonovitch-Weyl kernel for the P function. We start with the expression of the SW reference kernel (1.28), with $s = 1$

$$\begin{aligned}
\Delta_0^{(1)} &= \sum_{L=0}^{2j}\sqrt{\frac{2L+1}{2j+1}}\frac{T_{L0}}{C^{jj}_{jjL0}} \\
&= \sum_{m=-j}^{j}\left[\frac{(-1)^{j-m}}{\sqrt{2j+1}}\sum_{L=0}^{2j}\frac{\sqrt{2L+1}C^{L0}_{jmj-m}}{C^{jj}_{jjL0}}\right]\left|j,m\right\rangle\left\langle j,m\right| \\
&= \sum_{m=-j}^{j}\Delta_{j+m}\left|j,m\right\rangle\left\langle j,m\right|
\end{aligned}$$

where we used (1.15) for the multipole operators. The kernel operators $\Delta^{(1)}$ are covariant under rotations [130], i.e.

$$R(\Omega)\Delta_0^{(1)}R^\dagger(\Omega) = \Delta^{(1)}(\Omega).$$

Therefore, the eigenvectors of $\Delta^{(1)}\left(\Omega\right)$ are the standard spin eigenstates over the quantisation axis in the direction Ω, $\left|j,m;\Omega\right\rangle = R(\Omega)\left|j,m\right\rangle$. On the other hand, the eigenvalues Δ_{j+m} can be rewritten as

$$\Delta_{j+m} = \sum_{L=0}^{2j}\frac{(-1)^{j-m}}{(2j+1)!}C^{L0}_{jm,j-m}\times\sqrt{(2L+1)(2j-L)!(2j+L+1)!} \tag{1.49}$$

by using the identity [69]

$$C^{jj}_{jjL0} = (2j)!\sqrt{\frac{2j+1}{(2j-L)!(2j+L+1)!}}.$$

In order to evaluate the sum in (1.49), our strategy is to write a polynomial whose coefficients are proportional to the Δ_{j+m} eigenvalues deduced above. We start with a generating function of the Clebsch-Gordan coefficients in terms of the Legendre polynomials, given through the hypergeometric function ${}_2F_1(a_1,\, a_2;\, b_1;\, t)$ (see (5), p. 263 of [69] or [131], and (4), pp. 976 and 1005 of [132])

$$\begin{aligned}\sqrt{\frac{2L+1}{(2j-L)!(2j+L+1)!}}(t-1)^{2j}P_L\left(\frac{t+1}{t-1}\right) &= \sqrt{\frac{2L+1}{(2j-L)!(2j+L+1)!}} \\ &\quad\times(t-1)^{2j-L}{}_2F_1(-L,\,-L;\,1;\,t) \\ &= \frac{1}{(2j)!}\sum_{m=-j}^{j}\binom{2j}{j+m}C^{L0}_{jm,\,j-m}t^{j+m}.\end{aligned} \tag{1.50}$$

We now multiply (1.50) by the necessary factors and sum over L to bring out the eigenvalues Δ_{j+m}

$$\begin{aligned}(t-1)^{2j}\sum_{L=0}^{2j}\left(\frac{2L+1}{2j+1}\right)P_L\left(\frac{t+1}{t-1}\right) &= \sum_{m=-j}^{j}\binom{2j}{j+m}(-1)^{-j+m}\Delta_{j+m}t^{j+m} \\ &= \sum_{k=0}^{2j}\binom{2j}{k}(-1)^{-2j+k}\Delta_k t^k.\end{aligned} \tag{1.51}$$

Now, we can rewrite the left hand-side of (1.51) as

$$\sum_{L=0}^{2j}\left(\frac{2L+1}{2j+1}\right)P_L\left(\frac{t+1}{t-1}\right) = \frac{t-1}{2}\left[P_{2j+1}\left(\frac{t+1}{t-1}\right) - P_{2j}\left(\frac{t+1}{t-1}\right)\right],$$

where we used the Christoffel's identity (see (1), p. 986 of [132]) with $x = \frac{t+1}{t-1}$, $y = 1$ and $n = 2j$, that is

$$\sum_{k=0}^{n}\left(\frac{2k+1}{n+1}\right)P_k(x)P_k(y) = \frac{P_{n+1}(x)P_n(y) - P_n(x)P_{n+1}(y)}{x-y}.$$

Lastly, we use the power expansion of the Legendre polynomials [132]

$$(t-1)^L P_L\left(\frac{t+1}{t-1}\right) = \sum_{a=0}^{L}\binom{L}{a}^2 t^a \tag{1.52}$$

to get

$$\begin{aligned}(t-1)^{2j}\sum_{L=0}^{2j}\left(\frac{2L+1}{2j+1}\right)P_L\left(\frac{t+1}{t-1}\right) &= \frac{1}{2}\left[\sum_{k=0}^{2j+1}\binom{2j+1}{k}^2 t^k - (t-1)\sum_{k=0}^{2j}\binom{2j}{k}^2 t^k\right] \\ &= 1 + \sum_{k=1}^{2j}\left[\binom{2j+1}{k}^2 + \binom{2j}{k}^2 - \binom{2j}{k-1}^2\right]\frac{t^k}{2} \\ &= \sum_{k=0}^{2j}\binom{2j}{k}\binom{2j+1}{k}t^k.\end{aligned} \tag{1.53}$$

By comparing (1.51) and (1.53), we deduce that

$$\Delta_k = (-1)^{2j-k}\binom{2j+1}{k}, \quad \forall k = 0, \ldots, 2j.$$

Chapter 2

Absolute positivity of phase-space functions

The study of quantum multipartite mixed states naturally raises the question of the maximal entanglement achievable under arbitrary unitary evolution. Since interactions with the environment can reduce state purity, the maximal attainable entanglement is expected to diminish, eventually reaching a point where no entanglement can be generated unitarily. This observation has led to the concept of absolute separability, a property characterising mixed states that remain separable under any unitary transformation. Equivalently, as a unitary evolution can be associated to a change of basis, these states are separable in every possible basis of the full Hilbert space.

For N qubits in symmetric states, or equivalently a spin-j system with $j = N/2$, recent work has focused on characterising the non-trivial set of symmetric absolutely separable (SAS) states [11, 12, 133]. Notably, SAS states have been identified as forming balls centered on the maximally mixed state. Inspired by this research on entanglement, we investigate another measure of non-classicality given by the presence of negativity in the phase-space representations of finite-dimensional systems.

In this chapter, we provide a complete characterisation of the degree of negativity in SW phase-space representations for mixed states with a fixed spectrum. We define a spin-j state as Absolutely Stratonovitch-Weyl Bounded (ASB) if its SW function $\mathcal{W}_\rho^{(s)}$ remains above a certain bound under all symmetry-preserving unitaries $U \in \mathrm{SU}(2j+1)$. For a system of $N = 2j$ qubits, these unitaries correspond to the most general evolution within the symmetric subspace, preserving the state's spectrum. Of particular interest are Absolutely Stratonovitch-Weyl Positive (ASP) states, those whose SW representations remain non-negative under any $\mathrm{SU}(2j+1)$ transformation. These states serve as phase-space analogs of multiqubit SAS states. We focus on two key SW representations, namely the Wigner and P functions, which are known to exhibit negativity. Specifically, we characterise the sets of Absolutely Wigner Positive (AWP) and Absolutely P Positive (APP) states. A list of abbreviations is given in Table 2.1.

Our first objective is to derive conditions ensuring that the minimal value of an SW representation within the unitary orbit $\left\{U\rho U^\dagger, U \in \mathrm{SU}(2j+1)\right\}$ of a state ρ is bounded by some value $\mathcal{W}_{\min}$. That is, for a fixed parameter s, we seek conditions under which

$$\min_{\substack{\Omega\in S^2 \\ U\in \mathrm{SU}(2j+1)}} \mathcal{W}^{(s)}_{U\rho U^\dagger}(\Omega) \geq \mathcal{W}_{\min},$$

where $\mathcal{W}_\rho^{(s)}$ is a SW function uniquely defined for each ρ as

$$\mathcal{W}_\rho^{(s)}(\Omega) = \sqrt{\frac{4\pi}{2j+1}} \sum_{L=0}^{2j} \left(C_{jjL0}^{jj}\right)^{-s} \sum_{M=-L}^{L} \rho_{LM} Y_{LM}(\Omega). \tag{2.1}$$

Since all states in a unitary orbit share the same eigenvalues $\boldsymbol{\lambda} = \{\lambda_i, i = 1, 2, \ldots, N+1\}$, we expect ASB conditions to be expressible purely in terms of $\boldsymbol{\lambda}$, allowing for a geometric representation in the eigenvalue simplex.

Beyond theoretical interest, characterising states with non-negative phase-space representations has practical implications. A positive phase-space function can be interpreted as a genuine probability distribution, enabling efficient classical simulations. Recent work has leveraged the Wigner function to classicaly simulate large spin-system dynamics efficiently under certain conditions, such as dephasing, using stochastic trajectories [85, 86]. Similarly, discrete Wigner functions (e.g., Wootters function [23]) have been linked to classical simulability: pure states in odd dimensions with everywhere-positive Wootters functions admit efficient classical representations [134, 135]. Notably, stabilizer states, central to the Gottesman-Knill theorem, are classically simulable precisely because their discrete Wigner functions are non-negative [136, 137]. Conversely, negativity in discrete Wigner functions has been tied to quantum contextuality and computational advantage [87, 138–142]. Resource theories further suggest that greater negativity correlates with stronger non-classicality [143, 144]. Thus, characterising absolutely positive states refines our understanding of the boundary between classical and quantum computation.

As explained in Chapter 1, the most general continuous phase-space representation of a spin state ρ takes the form

$$\widetilde{\mathcal{W}}_\rho^{(s)} = \mathcal{W}_\rho^{(s)}(\Omega) + \sum_{L=2j+1}^{+\infty} \sum_{M=-L}^{L} x_{LM} Y_{LM}(\Omega), \tag{2.2}$$

where the x_{LM} are complex numbers. The $\widetilde{\mathcal{W}}_\rho^{(s)}$ function of a state is not unique because the variables x_{LM} can be any complex number provided that (2.2) is real, covariant under rotations and preserve the informational completeness. Our second objective is to extend SW representations, particularly the P function, to refine the characterisation of SAS states. By optimising the x_{LM}, we enlarge the set of APP states, which, due to the role of the P function in decomposing states into separable coherent states, directly correspond to SAS states.

The present chapter is structured in two parts. In the first part, we explore the ASB conditions based on the SW function $\mathcal{W}_\rho^{(s)}$ (2.1). This will allow us to find a linear necessary and sufficient condition for states to be ASB for a given bound $\mathcal{W}_{\min}$ which geometrically takes the form of ASB polytopes. A characterisation of these ASB polytopes is given in Section 2.2 for the Wigner and P functions. In this same section, we also explore the comparison between the sets of AWP and APP states with the set of SAS states.

In the second part of the chapter, we explore conditions for states to be SAS with the help of the extended phase-space representation (2.2) and more particularly for the P function. This allows us to extend the sets of SAS states compared to known results and to define non-linear conditions for a state to be SAS. While we focus on the P function in this part of the chapter, all our results can be straightforwardly extended to other phase-space representations and to different bounds $\mathcal{W}_{\min}$.

Abbreviations	Conditions
Absolutely Stratonovitch-Weyl Bounded (ASB)	$\mathcal{W}^{(s)}_{U\rho U^\dagger}(\Omega) \geq \mathcal{W}_{\min}$, $\forall \Omega \in S^2$ and $U \in \mathrm{SU}(2j+1)$
Absolutely Stratonovitch-Weyl Positive (ASP)	$\mathcal{W}^{(s)}_{U\rho U^\dagger}(\Omega) \geq 0$, $\forall \Omega \in S^2$ and $U \in \mathrm{SU}(2j+1)$
Absolutely Wigner Positive (AWP)	$\widetilde{\mathcal{W}}^{(0)}_{U\rho U^\dagger}(\Omega) \geq 0$, $\forall \Omega \in S^2$ and $U \in \mathrm{SU}(2j+1)$
Absolutely P Positive (APP)	$\widetilde{\mathcal{W}}^{(1)}_{U\rho U^\dagger}(\Omega) \geq 0$, $\forall \Omega \in S^2$ and $U \in \mathrm{SU}(2j+1)$

Table 2.1: Index of abbreviations and the related condition on the phase-space representations of the state. Note that the ASB and ASP conditions and the AWP and APP conditions apply on the SW and generalised phase-space representations, respectively.

2.1 Polytopes of absolutely Stratonovitch bounded states

In this section, for given parameter s and bound $\mathcal{W}_{\min}$, we prove that the set of ASB states based on the SW function (2.1) form a polytope in the simplex of state spectra and we fully characterise this polytope. We also determine a necessary and sufficient condition for a state to be inside the ASB polytope based on a majorisation criterion and relate our results to discrete phase-space representations such as the Wootters function. These results offer a strong characterisation of the classicality of mixed spin states.

2.1.1 ASB states set

For a given parameter s, the SW phase-space representation of a state ρ is given by (see Chapter 1)

$$\mathcal{W}^{(s)}_{\rho}(\Omega) = \mathrm{Tr}\left(\rho \Delta^{(s)}(\Omega)\right)$$

where $\Delta^{(s)}$ is the associated kernel of $\mathcal{W}^{(s)}(\Omega)$. The following proposition gives a complete characterisation of the set of ASB states based on the SW functions and is valid for any spin quantum number j.

Theorem. *Let* $\boldsymbol{\Delta}^{(s)\uparrow} = \left(\Delta_0^{(s)\uparrow}, \Delta_1^{(s)\uparrow}, \ldots, \Delta_N^{(s)\uparrow}\right)$ *denote the vector of kernel eigenvalues sorted in increasing order, and let*

$$\mathcal{W}_{\min} \in \left[\Delta_0^{(s)\uparrow}, \tfrac{1}{2j+1}\right]. \tag{2.3}$$

Then a spin state ρ *has in its unitary orbit only states whose SW function satisfies* $\mathcal{W}^{(s)}_{\rho}(\Omega) \geq \mathcal{W}_{\min}$ *for all* $\Omega \in \mathcal{S}^2$ *if and only if its decreasingly ordered eigenvalues* $\boldsymbol{\lambda}^{\downarrow}$ *satisfy the following inequality*

$$\boxed{\sum_{i=0}^{2j} \lambda_i^{\downarrow} \Delta_i^{(s)\uparrow} \geq \mathcal{W}_{\min}.} \tag{2.4}$$

For $\mathcal{W}_{\min} = 0$, this proposition provides a complete characterisation of the set of ASP states. We note that a similar proposition was expressed for the Wigner function with $W_{\min} = 0$ in [145, 146].

Proof. Consider a general spin state ρ. We are first looking for a necessary condition for any element $U\rho U^\dagger$ of the unitary orbit of ρ to have a SW function $\mathcal{W}^{(s)}_{U\rho U^\dagger}(\Omega) \geq \mathcal{W}_{\min}$ at any point $\Omega \in S^2$. Since the unitary transformation applied to ρ may correspond, in a particular case, to an SU(2) rotation, the value of the SW function of ρ at any point Ω corresponds to the value of the SW function at $\Omega = 0$ of an element in its unitary orbit (the rotated version of ρ). But since we are considering the full unitary orbit, i.e. all possible U's, we can set the SW function argument to $\Omega = 0$. The state ρ can always be diagonalised by a unitary matrix M, i.e. $M\rho M^\dagger = \Lambda$ with $\Lambda = \mathrm{diag}\,(\lambda_0, ..., \lambda_{2j})$ a diagonal positive semi-definite matrix. The SW function at $\Omega = 0$ of $U\rho U^\dagger$ is then given by

$$\mathcal{W}^{(s)}_{U\rho U^\dagger}(0) = \mathrm{Tr}\left[U\rho U^\dagger \Delta^{(s)}(0)\right] = \mathrm{Tr}\left[UM^\dagger \Lambda M U^\dagger \Delta^{(s)}(0)\right].$$

By defining the unitary matrix $V = UM^\dagger$ and calculating the trace in the Dicke basis, we obtain (where we drop the SW function argument in the following)

$$\mathcal{W}^{(s)}_{U\rho U^\dagger}(0) = \mathrm{Tr}\left[V\Lambda V^\dagger \Delta^{(s)}(0)\right] = \sum_{p,q,k,l=0}^{2j} V_{pq}\lambda_q \delta_{qk} V^*_{lk} \Delta^{(s)}_l \delta_{lp} = \sum_{q,p=0}^{2j} \lambda_q \left|V_{qp}\right|^2 \Delta^{(s)}_p.$$

The positive numbers $|V_{qp}|^2$ in the previous equation define the entries of a unistochastic matrix of dimension $(2j+1) \times (2j+1)$ which we denote by B,

$$B_{qp} = \left|V_{qp}\right|^2.$$

We give in Appendix 2.A a short introduction to bistochastic and unistochastic matrices. In this way, the minimal value of the SW phase-space function in the unitary orbit of the evolved state is

$$\min_{U \in \mathrm{SU}(2j+1)} \mathcal{W}^{(s)}_{U\rho U^\dagger}(0) = \min_{B \in \mathcal{U}_{2j+1}} \boldsymbol{\lambda} B \boldsymbol{\Delta}^{(s)} \tag{2.5}$$

where $\mathcal{U}_{2j+1}$ is the set of unistochastic matrices of dimension $(2j+1) \times (2j+1)$. In principle, the minimisation on the unistochastic matrices $\mathcal{U}_{2j+1}$ presented in (2.5) seems intractable to perform for $2j = N > 3$ due to the lack of a complete characterisation of $\mathcal{U}_{2j+1}$. However, we can extend the minimisation domain to the bistochastic matrices $B \in \mathcal{B}_{2j+1} \supset \mathcal{U}_{2j+1}$ to obtain a lower bound

$$\min_{B' \in \mathcal{U}_{2j+1}} \boldsymbol{\lambda} B' \boldsymbol{\Delta}^{(s)} \geq \min_{B \in \mathcal{B}_{2j+1}} \boldsymbol{\lambda} B \boldsymbol{\Delta}^{(s)}$$

and prove that this bound is in fact always tight. This follows from two key facts: i) for any bistochastic matrix B, one can always find a unistochastic matrix B' such that $\boldsymbol{\lambda} B = \boldsymbol{\lambda} B'$ for any vector $\boldsymbol{\lambda}$[1], and ii) the bistochastic matrix appears in the minimisation (2.5) only in the form $\boldsymbol{\lambda} B$. By the Birkhoff-von Neumann theorem, we know that B can be expressed as a convex combination of permutation matrices P_k, i.e.

$$B = \sum_{k=1}^{N_p} c_k P_k,$$

[1] In fact, for any product of a vector and a bistochastic matrix $\boldsymbol{\lambda} B$, one can find an orthostochastic matrix A (i.e. that comes from an orthogonal matrix) such that $\boldsymbol{\lambda} B = \boldsymbol{\lambda} A$ (See Theorem B.6 of [147]).

where $N_p = (2j+1)!$ is the total number of permutations $\pi_k \in S_{2j+1}$ with S_{2j+1} the symmetric group over $2j+1$ symbols and

$$c_k \geq 0 \quad \forall\, k = 1, 2, \ldots, N_p \quad \text{and} \quad \sum_{k=1}^{N_p} c_k = 1.$$

Consequently, we have

$$\mathcal{W}^{(s)}_{U\rho U^\dagger} = \sum_{p,q=0}^{2j} \lambda_p B_{pq} \Delta^{(s)}_q = \sum_{k=1}^{N_p} c_k \sum_{p,q=0}^{2j} \lambda_p \left[P_k\right]_{pq} \Delta^{(s)}_q = \sum_{k=1}^{N_p} c_k \sum_{p=0}^{2j} \lambda_p \Delta^{(s)}_{\pi_k(p)}$$

For a state ρ whose eigenspectrum $\boldsymbol{\lambda}$ satisfies the N_p inequalities

$$\sum_{p=0}^{2j} \lambda_p \Delta^{(s)}_{\pi(p)} \geq \mathcal{W}_{\min} \qquad \forall\, \pi \in S_{2j+1} \tag{2.6}$$

we then have

$$\mathcal{W}^{(s)}_{U\rho U^\dagger} = \sum_{k=1}^{N_p} c_k \sum_{p=0}^{2j} \lambda_p \Delta^{(s)}_{\pi_k(p)} \geq \mathcal{W}_{\min}$$

for any unitary U and we conclude. Conversely, a state has in its unitary orbits only states whose SW function satisfies $\mathcal{W}^{(s)}(\Omega) \geq \mathcal{W}_{\min}\ \forall\, \Omega \in \mathcal{S}^2$ if

$$\mathcal{W}^{(s)}_{U\rho U^\dagger} = \sum_{k=1}^{N_p} c_k \sum_{p=0}^{2j} \lambda_p \Delta^{(s)}_{\pi_k(p)} \geq \mathcal{W}_{\min} \qquad \forall\, U \in SU(2j+1).$$

In particular, the unitary matrix U can correspond to any permutation matrix P, so that we have

$$\mathcal{W}^{(s)}_{P\rho P^\dagger} = \sum_{p=0}^{2j} \lambda_p \Delta^{(s)}_{\pi(p)} \geq \mathcal{W}_{\min} \qquad \forall\, \pi \tag{2.7}$$

and we conclude that the state satisfies (2.6). In fact, it is enough to consider the ordered eigenvalues $\boldsymbol{\lambda}^\downarrow$ so that a state is ASB iff it verifies the most stringent inequality amongst all possible permutations of (2.7)

$$\boldsymbol{\lambda}^\downarrow \cdot \boldsymbol{\Delta}^{(s)\uparrow} = \sum_{p=0}^{2j} \lambda^\downarrow_p \Delta^{(s)\uparrow}_p \geq \mathcal{W}_{\min} \tag{2.8}$$

with the ordered eigenvalues of the kernel $\boldsymbol{\Delta}^\uparrow$. □

2.1.2 ASB polytopes

Since the conditions for being ASB depend only on the eigenspectrum $\boldsymbol{\lambda}$ of a state, it is sufficient in the following to focus on diagonal states in the Dicke basis. The condition (2.4) for a given $\mathcal{W}_{\min}$ defines a polytope of ASB states in the simplex of mixed spin states. Indeed, we start by noting that the equalities

$$\sum_{i=0}^{2j} \lambda_i \Delta^{(s)}_{\pi(i)} = \mathcal{W}_{\min} \tag{2.9}$$

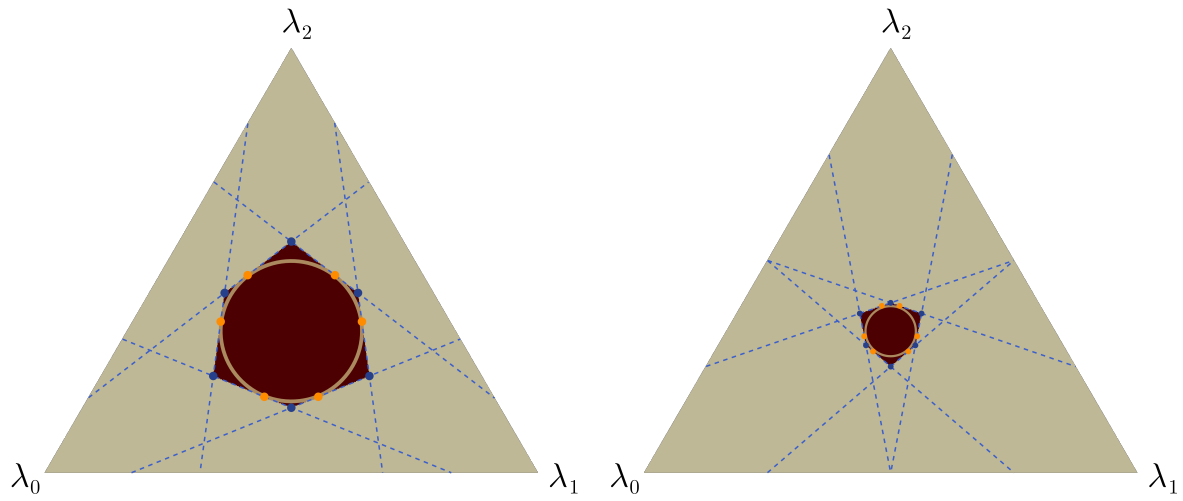

Figure 2.1: ASP polytope for $j = 1$ of the Wigner ($s = 0$) and P ($s = 1$) functions displayed in the barycentric coordinates system. The ASP polytope is the area shaded in dark red with the blue dashed lines marking the hyperplanes defined by (2.9). The circles are the surfaces of the ASP balls (see Subsection 2.1.4). The orange points represent all the permutations of the spectrum (2.19). The beige triangle corresponds to the full simplex of spin-1 states with spectrum $\boldsymbol{\lambda} = (\lambda_0, \lambda_1, \lambda_2)$.

define, for all possible permutations π, $(2j+1)!$ hyperplanes in $\mathbb{R}^{2j}$. Together they delimit a particular polytope that contains all ASB states. The ASP ($\mathcal{W}_{\min} = 0$) polytopes for $j = 1$ and $j = 3/2$ are respectively represented in Figures 2.1 and 2.2 in a barycentric coordinate system for the Wigner ($s = 0$) and P ($s = 1$) functions (see Appendix 2.B for a reminder about barycentric coordinates systems).

If we now restrict our attention to ordered eigenvalues $\boldsymbol{\lambda}^{\downarrow}$, we get a minimal polytope; see Figure 2.3 for the case of $j = 1$. The full polytope is reconstructed by taking all possible permutations of the barycentric coordinates of the vertices of the minimal polytope. These vertices can be found as follows. In general we need $2j+1$ independent conditions on the vector $\left(\lambda_0^{\downarrow}, \lambda_1^{\downarrow}, \ldots, \lambda_{2j}^{\downarrow}\right)$ to uniquely define (the unitary orbit of) a state ρ. One of them is given by the normalisation condition $\sum_{i=0}^{2j} \lambda_i^{\downarrow} = 1$. The others correspond to the fact that a vertex of the ASP polytope is the intersection of $2j$ hyperplanes each specified by an equation of the form (2.9). One of them is

$$\sum_{i=0}^{2j} \lambda_i^{\downarrow} \Delta_i^{(s)\uparrow} = \mathcal{W}_{\min}. \tag{2.10}$$

Let us focus on the remaining $2j-1$. For simplicity, consider a transposition $\pi = (p, q)$ with $p < q$. This is the permutation whose only non-trivial action is $\pi(p) = q$ and $\pi(q) = p$. The condition (2.9) for this transposition becomes

$$\lambda_p^{\downarrow} \Delta_q^{(s)\uparrow} + \lambda_q^{\downarrow} \Delta_p^{(s)\uparrow} + \sum_{\substack{i=0 \\ i \neq p,q}}^{2j} \lambda_i^{\downarrow} \Delta_i^{(s)\uparrow} = \mathcal{W}_{\min}$$

$$\Leftrightarrow \quad \lambda_p^{\downarrow} (\Delta_q^{(s)\uparrow} - \Delta_p^{(s)\uparrow}) + \lambda_q^{\downarrow} (\Delta_p^{(s)\uparrow} - \Delta_q^{(s)\uparrow}) = 0 \tag{2.11}$$

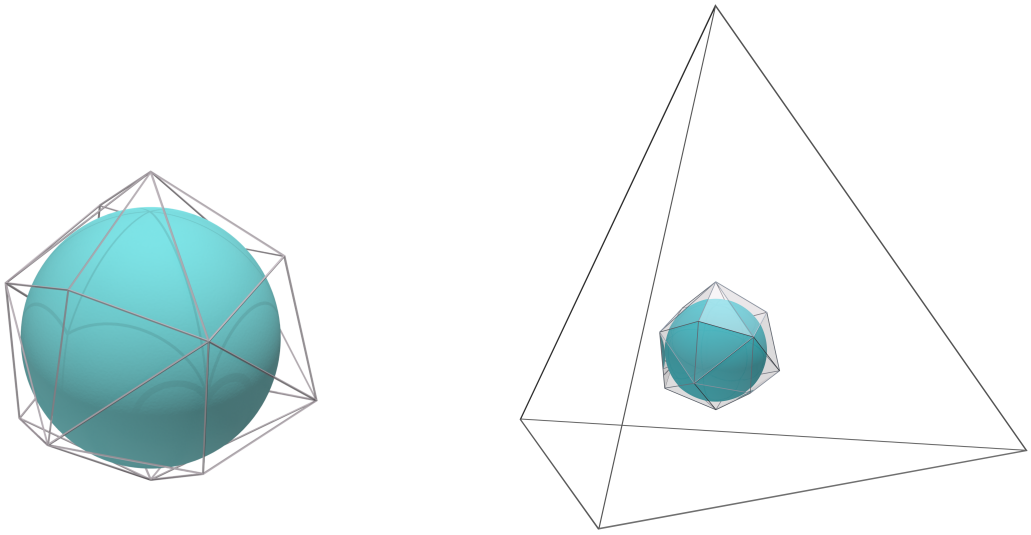

Figure 2.2: The AWP ($s = 0$) polytope for $j = 3/2$ in the barycentric coordinate system. The grey rods (shown in the enlarged polytope on the left) are the edges of the AWP polytope and the blue sphere is its largest inner ball, with radius $r_{\text{in}}^{\text{AWP}} = 1/(2\sqrt{15})$ (see Subsection 2.1.4).

where the second line comes from applying the constraint (2.10). It is clear that (2.11) is satisfied if and only if $\lambda_p^{\downarrow} = \lambda_q^{\downarrow}$. And because the eigenvalues are ordered, this also implies $\lambda_k^{\downarrow} = \lambda_p^{\downarrow}$ for all k between p and q. The only forbidden transposition is $(0, 2j)$ because it would give the MMS. Hence a given transposition (p, q) will correspond to a set of $q - p$ conditions $\lambda_l = \lambda_{l+1}$ for $l = p, \ldots, q-1$. Therefore, as any permutation is a composition of transpositions, the $2j - 1$ conditions that follow from (2.9) reduce to a set of $2j - 1$ nearest-neighbour eigenvalue equalities taken from the $2j$ elements set

$$\mathcal{E} = \left(\lambda_0^{\downarrow} = \lambda_1^{\downarrow}, \lambda_1^{\downarrow} = \lambda_2^{\downarrow}, ..., \lambda_{2j-1}^{\downarrow} = \lambda_{2j}^{\downarrow}\right). \tag{2.12}$$

Since we need $2j - 1$ conditions, we can draw $2j - 1$ equalities from $\mathcal{E}$ in order to obtain a vertex. This method gives $\binom{2j}{2j-1} = 2j$ different draws and so we get $2j$ vertices for the minimal polytope. Geometrically, (2.12) can also be seen as the set of non-trivial hyperplanes defining the minimal polytope, and the $\binom{2j}{2j-1} = 2j$ draws correspond to the different intersections of the hyperplane (2.10) with the 1-dimensional faces (i.e. edges) of the minimal polytope. The full set of hyperplanes defining the minimal polytope is (2.12) supplemented with $\lambda_{2j}^{\downarrow} = 0$ and the normalisation condition.

As explained previously, all other vertices of the full polytope are obtained by permuting the coordinates of the vertices of the minimal polytope. The entirety of the preceding discussion of the ASP polytope vertices naturally extends to the ASB polytope vertices for which we must replace 0 by $\mathcal{W}_{\min}$ in the right-hand side of the equality (2.9). However, for negative values of $\mathcal{W}_{\min}$, the polytope may extend beyond the simplex and some vertices will have negative-valued components, resulting in unphysical states.

A peculiar characteristic of the ASP polytope is that each point on its surface has a state in its orbit satisfying $\mathcal{W}_{\rho}^{(s)}(0) = \mathcal{W}_{\min}$. Indeed, for an eigenspectrum $\boldsymbol{\lambda}$ that satisfies (2.9) for a given permutation π, the diagonal state ρ in the Dicke basis with $\rho_{ii} = \lambda_{\pi^{-1}(i)}$

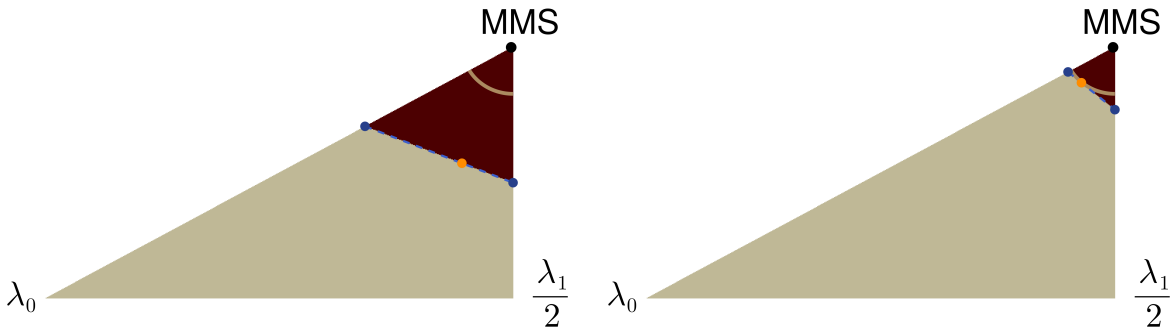

Figure 2.3: ASP minimal polytopes for $j = 1$ of the Wigner ($s = 0$, on the left) and P ($s = 1$, on the right) functions in the barycentric coordinate system. The structure is similar to Figure 2.1 but we only draw the part where the eigenvalues of the state are sorted in descending order. The dark point corresponds to the maximally mixed state.

satisfies

$$\mathcal{W}_\rho^{(s)}(0) = \sum_{i=0}^{2j} \lambda_i \Delta_i^{(s)} = \mathcal{W}_{\min}$$

and is in the unitary orbit of $\boldsymbol{\lambda}$. As negative values of the SW function are generally considered to indicate non-classicality, the value $\mathcal{W}_{\min} = 0$ plays a special role. Nevertheless, since (2.3) holds for any $\mathcal{W}_{\min} \in \left[\Delta_0^{(s)\uparrow}, \frac{1}{2j+1}\right]$ the corresponding sets of states also form polytopes, which become larger as $\mathcal{W}_{\min}$ becomes more negative, culminating in the entire simplex when $\mathcal{W}_{\min}$ is the smallest kernel eigenvalue $\Delta_0^{(s)\uparrow}$. There is thus a continuous transition between the one-point polytope, which represents the MMS, and the polytope containing the whole simplex. As discussed later, Figure 2.4 in Subsection 2.1.4 shows a special example of this family for spin-1. For the Husimi Q function, which is positive by construction, the polytope for $Q_{\min} = 0$ contains the entire simplex of state spectra. In this case it would become especially interesting to consider lower bounds $Q_{\min} > 0$ and study the properties of the associated polytopes.

2.1.3 Majorisation condition

The condition (2.4) for a state to be ASB can equivalently be expressed based on its majorisation by a mixture of the vertices of the minimal polytope. To show this, we first define the concept of the majorisation between two vectors.

Vector majorisation. For two vectors $\mathbf{u}$ and $\mathbf{v}$ of the same length n, we say that $\mathbf{u}$ majorises $\mathbf{v}$, denoted $\mathbf{u} \succ \mathbf{v}$, if and only if

$$\sum_{k=1}^{l} u_k^{\downarrow} \geq \sum_{k=1}^{l} v_k^{\downarrow}$$

for $l < n$, with $\sum_{k=1}^{n} u_k = \sum_{k=1}^{n} v_k$ and $\mathbf{u}^{\downarrow}$ denoting the vector $\mathbf{u}$ with components sorted in decreasing order.

Proposition. *A state ρ is ASB if and only if its eigenvalues $\boldsymbol{\lambda}$ are majorised by a convex combination of the ordered vertices $\{\boldsymbol{\lambda}_{\mathrm{v}_k}^{\downarrow}\}$ of the corresponding ASB polytope, i.e.*

$\exists\, \mathbf{c} \in \mathbb{R}_+^{2j}$ *such that*

$$\boldsymbol{\lambda} \prec \sum_{k=1}^{2j} c_k \boldsymbol{\lambda}_{\mathrm{v}_k}^{\downarrow} \tag{2.13}$$

with $\sum_{k=1}^{2j} c_k = 1$.

Proof. If $\boldsymbol{\lambda}$ is AWB then it can be expressed as a mixture of the vertices of the AWB polytope

$$\boldsymbol{\lambda} = \sum_k c_k \boldsymbol{\lambda}_{\mathrm{v}_k}$$

and the majorisation (2.13) follows. Conversely, it is known from the Schur-Horn theorem that $\mathbf{x} \succ \mathbf{y}$ if and only if $\mathbf{y}$ is in the convex hull of the vectors obtained by permuting the elements of $\mathbf{x}$ (i.e. the permutahedron generated by $\mathbf{x}$). Hence, if $\boldsymbol{\lambda}$ fulfils (2.13), it can be expressed as a convex combination of the vertices of the ASB polytope and is therefore inside it. □

2.1.4 Balls of Absolutely Stratonovitch Bounded states

In Subsection 2.1.1, we have fully characterised ASB polytopes for all finite dimensions based on the SW phase-space representations. Taking advantage of their geometry, we present here the sufficient condition for states to belong to the ASB set based on their purity alone. In the following, we denote by $r(\rho)$ the Hilbert-Schmidt distance between a state ρ and the MMS,

$$r(\rho) = \|\rho - \rho_0\|_{\mathrm{HS}} = \sqrt{\mathrm{Tr}\left[(\rho - \rho_0)^2\right]}. \tag{2.14}$$

Proposition. *The radius of the largest inner ball of the ASB polytope associated with a* $\mathcal{W}_{\min}$ *value such that the ball is contained within the state simplex is*

$$\boxed{r_{\mathrm{in}}^{(s)}\left(\mathcal{W}_{\min}\right) = \frac{1 - (2j+1)\mathcal{W}_{\min}}{(2j+1)\left((2j+1)|\boldsymbol{\Delta}^{(s)}|^2 - 1\right)}.} \tag{2.15}$$

It vanishes for the largest value of the SW bound $\mathcal{W}_{\min} = 1/(2j+1)$ *for which the ASB polytope reduces to the MMS.*

Proof. Let us first consider the radius $r_{\mathrm{in}}^{(s)}$ of the largest ball centered on the MMS contained in the polytope of ASB states and find a state ρ^* that lies both on the surface of this ball and on a face of the polytope. The Hilbert-Schmidt distance is equivalent to the Euclidean distance in the simplex between the spectra $\boldsymbol{\lambda}$ and $\boldsymbol{\lambda}_0$ of ρ and the MMS respectively, i.e.

$$r(\rho) = \sqrt{\left(\sum_{i=0}^{2j} \lambda_i^2\right) - \frac{1}{2j+1}} = \|\boldsymbol{\lambda} - \boldsymbol{\lambda}_0\|.$$

In order to find the radius $r_{\mathrm{in}}^{(s)}$ of the largest inner ball of the ASB polytope, we need to find the spectra on the hyperplanes of the ASB polytope with the minimum distance to the MMS. Mathematically, this translates in the following constrained minimisation problem

$$\min_{\boldsymbol{\lambda}} \|\boldsymbol{\lambda} - \boldsymbol{\lambda}_0\|^2 \quad \text{subject to} \quad \begin{cases} \sum_{i=0}^{2j} \lambda_i = 1 \\ \boldsymbol{\lambda} \cdot \boldsymbol{\Delta}^{(s)} = \mathcal{W}_{\min} \end{cases} \tag{2.16}$$

where $\boldsymbol{\Delta}^{(s)} = \left(\Delta_0^{(s)}, \Delta_1^{(s)}, ..., , \Delta_{2j}^{(s)}\right)$. For this purpose, we use the method of Lagrange multipliers with the Lagrangian

$$L = \|\boldsymbol{\lambda} - \boldsymbol{\lambda}_0\|^2 + \mu_1 \left(\boldsymbol{\lambda} \cdot \boldsymbol{\Delta}^{(s)} - \mathcal{W}_{\min}\right) + \mu_2 \left(1 - \sum_{i=0}^{2j} \lambda_i\right)$$

where μ_1, μ_2 are two Lagrange multipliers to be determined. The stationary point $\boldsymbol{\lambda}^*$ of the Lagrangian must satisfy the following condition

$$\frac{\partial L}{\partial \boldsymbol{\lambda}}\Big|_{\boldsymbol{\lambda}=\boldsymbol{\lambda}^*} = \mathbf{0} \quad \Leftrightarrow \quad 2\boldsymbol{\lambda}^* + \mu_1 \boldsymbol{\Delta}^{(s)} - \mu_2 \mathbf{1} = \mathbf{0} \tag{2.17}$$

with $\mathbf{1} = (1, 1, ..., 1)$ of length $2j + 1$. By summing over the components of (2.17) and using the normalisation of the kernel, we readily get

$$\mu_2 = \frac{\mu_1 + 2}{2j + 1}. \tag{2.18}$$

Next, by performing the scalar product of (2.17) with $\boldsymbol{\Delta}^{(s)}$ and using (2.18), we obtain the following Lagrange multipliers

$$\mu_1 = \frac{2\left(1 - (2j+1)\mathcal{W}_{\min}\right)}{(2j+1)|\boldsymbol{\Delta}^{(s)}|^2 - 1}, \quad \mu_2 = \frac{2\left(|\boldsymbol{\Delta}^{(s)}|^2 - \mathcal{W}_{\min}\right)}{(2j+1)|\boldsymbol{\Delta}^{(s)}|^2 - 1}.$$

Finally, upon substituting the above values for μ_1 and μ_2 into (2.17) and solving for the stationary point $\boldsymbol{\lambda}^*$, we obtain

$$\boldsymbol{\lambda}^* = \frac{\left(|\boldsymbol{\Delta}^{(s)}|^2 - \mathcal{W}_{\min}\right)\mathbf{1} - \left(1 - (2j+1)\mathcal{W}_{\min}\right)\boldsymbol{\Delta}^{(s)}}{(2j+1)|\boldsymbol{\Delta}^{(s)}|^2 - 1} \tag{2.19}$$

which leads us to

$$r_{\text{in}}^{(s)}\left(\mathcal{W}_{\min}\right) = r\left(\rho^*\right) = \frac{1 - (2j+1)\mathcal{W}_{\min}}{\sqrt{(2j+1)\left((2j+1)|\boldsymbol{\Delta}^{(s)}|^2 - 1\right)}} \tag{2.20}$$

with ρ^* any state with eigenspectrum (2.19). □

2.1.5 Relation with discrete phase-space functions

The results derived in Subsection 2.1.1 extend naturally to discrete phase-space representations (introduced in Chapter 1). Specifically, one can construct polytopes characterising absolutely bounded discrete phase-space functions in close analogy with the continuous case.

Proposition. *Let $\mathbb{W}_\rho^{(s)}$ be a discrete phase-space function of a spin-j state ρ whith eigenvalues $\boldsymbol{\lambda}^{\downarrow}$ ordered in decreasing order. Since the phase-point operators $\Delta_{pq}^{(s)}$ are Hermitian, they admit a diagonalisation. Let*

$$\Delta_{00}^{(s)} = M' D M'^{\dagger}$$

where D is diagonal with entries $\boldsymbol{\Delta}^{(s)\uparrow}$, the eigenvalues $\Delta_{00}^{(s)}$ ordered increasingly. Then, ρ is absolutely bounded by $\mathcal{W}_{\min}$ if and only if

$$\sum_{i=0}^{2j} \lambda_i^{\downarrow} \Delta_i^{(s)\uparrow} \geq \mathcal{W}_{\min}.$$

Proof. By the cyclic property of the trace, the discrete phase-space function satisfies

$$\begin{aligned} \mathbb{W}_{U\rho U^\dagger}^{(s)}(0,0) = \operatorname{Tr}\left[U\rho U^\dagger \Delta_{00}^{(s)}\right] &= \operatorname{Tr}\left[UM^\dagger \Lambda M U^\dagger M' D M'^\dagger\right] \\ &= \operatorname{Tr}\left[V \Lambda V^\dagger D\right] \end{aligned}$$

where $V = M'^\dagger U M^\dagger$ is unitary. Since all phase-point operators $\Delta_{p,q}^{(s)}$ are related by a unitary transformation, the minimal value of $\mathbb{W}_{U\rho U^\dagger}^{(s)}(p,q)$ over all $p,q = 0,1,\ldots,2j+1$ and all $U \in \mathrm{SU}(2j+1)$ coincides with that of $\mathbb{W}_{U\rho U^\dagger}^{(s)}(0,0)$. Hence,

$$\min_{\substack{p,q=0,1,\ldots,2j+1 \\ U \in \mathrm{SU}(2j+1)}} \mathbb{W}_{U\rho U^\dagger}^{(s)}(p,q) = \min_{U \in \mathrm{SU}(2j+1)} \operatorname{Tr}\left[V \Lambda V^\dagger D\right])$$

The result then follows directly from the analysis in Subsection 2.1.1. □

Although this thesis primarily focuses on continuous phase-space representations, the above proposition demonstrates that analogous constructions hold in the discrete setting as well. This opens a promising avenue for future work on polytopes of absolutely bounded discrete phase-space functions.

2.2 Wigner and P functions

We now have a general characterisation of the ASB polytopes and balls for any Stratonovitch-Weyl function and spin number j. In this section, we focus on the Wigner and P functions, which are phase-space representations that can develop negative values (in contrast to the Husimi function). In order to provide some intuition, a description of the AWB polytopes will be given for low spin number j. In addition, as non-classicality is expected for a negative valued phase-space function, a comparison of the ASP polytopes with the ensemble of SAS states is of particular interest. In particular, since a state with a positive P function is expressed as a mixture of separable states, all states contained within the APP polytope are also SAS.

To particularise the equations (2.19) and (2.15) to $s = 0$ and 1, we note that the eigenvalues of the P function ($s = 1$) kernel are (see Chapter 1)

$$\Delta_k^{(1)} = (-1)^{2j-k} C_{2j+1}^k \quad k = 0,1,\ldots,2j \tag{2.21}$$

and that the squared norms of the kernel eigenvalues vector of the Wigner ($s = 0$) and P functions are

$$|\boldsymbol{\Delta}^{(0)}|^2 = 2j+1 \qquad |\boldsymbol{\Delta}^{(1)}|^2 = C_{4j+2}^{2j+1} - 1.$$

Unfortunately, there is still no known closed-form expression for the eigenvalues of the Wigner function kernel.

2.2.1 Wigner function

The AWP polytopes for $j = 1$ and $3/2$ are represented on the left panel of Figure 2.1 and in Figure 2.2 respectively. The spectrum (2.19) representing states lying on both the borders of the AWB polytope and ball reduces to

$$\boldsymbol{\lambda}^* = \frac{[(2j+1) - \mathcal{W}_{\min}]\,\mathbf{1} - [1 - (2j+1)\mathcal{W}_{\min}]\,\boldsymbol{\Delta}^{(0)}}{4j(j+1)}. \tag{2.22}$$

Thus, by considering all permutations of the elements of $\boldsymbol{\lambda}^*$, we can find all states located where the AWB polytope is tangent to the AWB inner ball, as shown in Figures 2.1 and 2.3 in orange for $\mathcal{W}_{\min} = 0$ and $j = 1$. The inner ball containing only AWB states has radius

$$r_{\text{in}}^{(0)}(\mathcal{W}_{\min}) = \frac{1 - (2j+1)\mathcal{W}_{\min}}{2\sqrt{j(2j+1)(j+1)}}.$$

In the case that $\mathcal{W}_{\min} \neq 0$, the polytope and the inner ball sizes increase (decrease) as $\mathcal{W}_{\min}$ becomes more negative (positive). Let us first discuss this behaviour for positive values of $\mathcal{W}_{\min}$. The inner radius (2.15) vanishes for $\mathcal{W}_{\min} = 1/(2j+1)$, corresponding to the fact that only the MMS state has a Wigner function with this minimal (and constant) value. The radius then increases as $\mathcal{W}_{\min}$ decreases. At $\mathcal{W}_{\min} = 0$, it reduces to the radius of the largest ball of AWP states,

$$r_{\text{in}}^{(0)}(0) = \frac{1}{2\sqrt{j(2j+1)(j+1)}} \tag{2.23}$$

as appears in Figures 2.1 and 2.2. Expressed as a function of dimension $d = 2j + 1$ and re-scaled to generalised Bloch length, this result was also recently found in the context of SU(d)-covariant Wigner functions (i.e. as the phase space manifold changes dramatically with each Hilbert space dimension, rather than always being the sphere) [148]. Although our bound is tight for all j in the SU(2) setting (i.e. there always exist orbits infinitesimally farther away that contain Wigner-negative states), it is unknown if this bound remains tight for such $SU(d)$-covariant Wigner functions for $d > 2$.

At the critical value

$$\mathcal{W}_{\min} = \frac{\Delta_{j,j} - (2j+1)}{\Delta_{j,j}(2j+1) - 1} < 0, \tag{2.24}$$

the spectrum (2.19) acquires a first zero eigenvalue, $\lambda^*_{2j} = 0$. This corresponds to the situation where $\boldsymbol{\lambda}^*$ is simultaneously on the ball surface, on a face of the polytope, and on an edge of the simplex; see the orange dots in Figure 2.4. For more negative values of $\mathcal{W}_{\min}$, (2.19) no longer represents a physical state because λ^*_{2j} becomes negative. In this situation, in order to determine the radius of larger balls that contain only AWB states, additional constraints must be imposed in the optimisation procedure reflecting the fact that some elements of the spectrum of ρ are zero. Since the possible number of zero eigenvalues depends on j, we will not go further in this development. Note that the same behaviour appears for other SW functions where the AWB polytope size increases with $\mathcal{W}_{\min}$.

We now particularise the results of Section 2.1 to the case $\mathcal{W}_{\min} = 0$ in order to compare the AWP polytope with the set of SAS states for different spin number j.

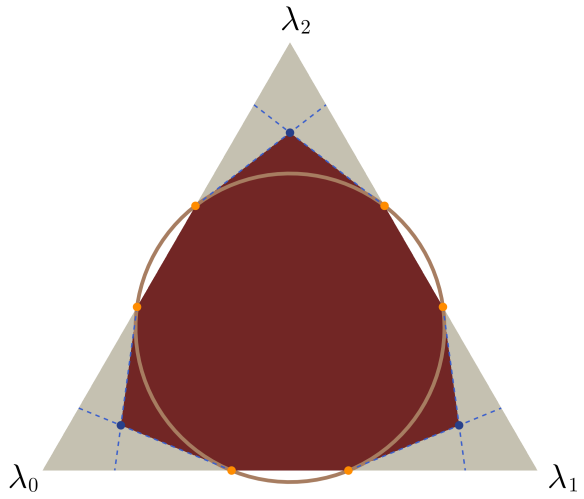

Figure 2.4: AWB polytope in the barycentric coordinates system for $j = 1$ and $W_{\min} = \frac{1}{3} + \frac{2}{3}\sqrt{2}\left(\sqrt{5} - 3\right) \approx -0.387$ as given by (2.24). The structure is similar to Figure (2.1) but the polytope occupies a larger portion of the state space. We omit the part of the polytope that is outside the simplex.

2.2.1.1 Spin $j = 1/2$

In the familiar case of a single qubit state ρ, the spectrum $(\lambda, 1-\lambda)$ is characterised by a single number λ. The kernel eigenvalues are

$$\Delta_0 = \frac{1}{2}(1 - \sqrt{3}), \quad \Delta_1 = \frac{1}{2}(1 + \sqrt{3}) = 1 - \Delta_0.$$

Letting $\lambda \geq \frac{1}{2}$ denote the larger of the two eigenvalues, the strong ordered condition (2.10) for $\mathcal{W}_{\min} = 0$ becomes

$$\lambda_0\Delta_0 + \lambda_1\Delta_1 = \lambda\Delta_0 + (1-\lambda)(1-\Delta_0) = \lambda(2\Delta_0 - 1) + 1 - \Delta_0 \geq 0.$$

Thus the AWP polytope is described, in the 1-dimensional projection to the λ-axis, as

$$\frac{1}{2} \leq \lambda \leq \frac{1-\Delta_0}{1-2\Delta_0} = \frac{1}{2} + \frac{1}{2\sqrt{3}}.$$

This may be equivalently expressed either in terms of purity R or Bloch length $|\mathbf{n}| = \sqrt{2\gamma - 1}$,

$$\frac{1}{2} \leq R \leq \frac{2}{3} \qquad \text{and} \qquad |\mathbf{n}| \leq \frac{1}{\sqrt{3}}.$$

Additionally, the distance to the maximally mixed state via (2.14) is $r \leq 1/\sqrt{6}$.

Regarding absolute separability, all qubit states are SAS. This is a consequence of the qubit pure states being equivalent to spin-1/2 coherent states. Thus AWP qubit states are a strict subset of SAS qubit states. Furthermore, due to the invariance of phase-space negativity under rigid rotation, for a single qubit there is no distinction between a state being positive and being absolutely positive. This means that any state with Bloch radius $|\mathbf{n}| \in [1/\sqrt{3}, 1]$ is SAS but has a negative Wigner function.

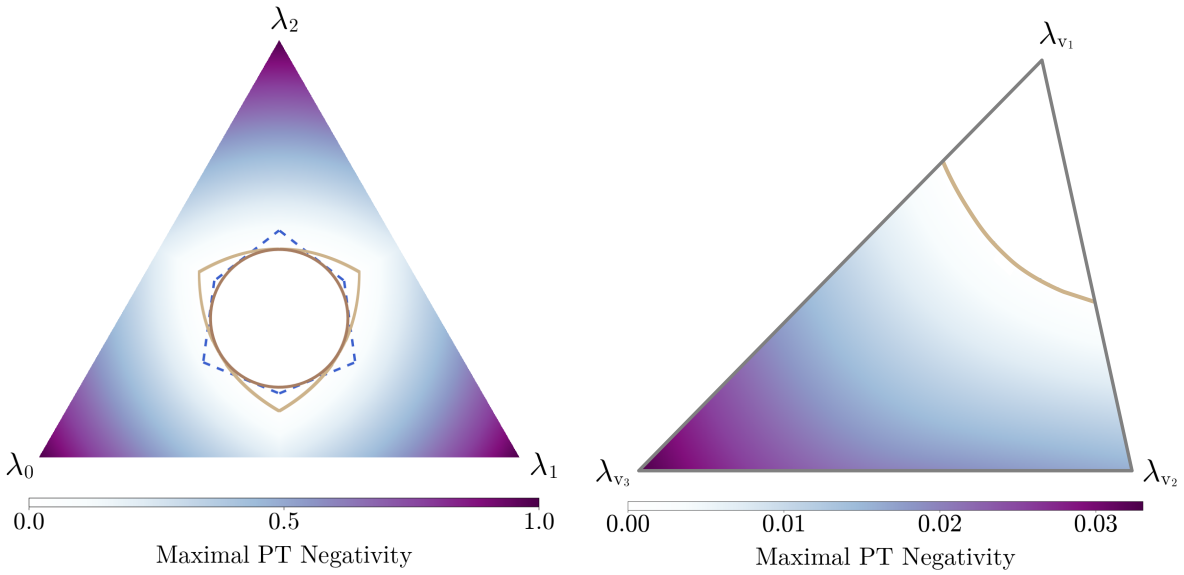

Figure 2.5: Left : Maximal PT negativity over each unitary orbit in the $j = 1$ simplex of state spectra. The dashed blue line and brown circle are respectively the AWP polytope and ball. Right : Maximal PT negativity over each unitary orbit on the surface of the minimal $j = 3/2$ AWP polytope (where $\mathcal{W}^{(0)}_{U\rho U^\dagger} = 0$ for all $U \in \mathrm{SU}(3)$). The notation of the vertices corresponds to the eigenspectra given in Table 2.3 in Appendix 2.C. The camel curves in both panels show the boundary on which the negativity along the unitary orbit becomes non-zero and is given by (2.26) for $j = 1$.

2.2.1.2 Spin $j = 1$

The sets of AWP and SAS states are both more complicated for qutrits than for $j = 1/2$, and neither is a strict subset of the other. For $j = 1$, it is known that the maximal value of the entanglement negativity, in the sense of the PPT criterion, in the unitary orbit of a two-qubit symmetric state ρ with spectrum $\lambda_0 \geq \lambda_1 \geq \lambda_2$ is [11]

$$\max\left[0, \sqrt{\lambda_0^2 + (\lambda_1 - \lambda_2)^2} - \lambda_1 - \lambda_2\right]. \tag{2.25}$$

It is also known that a state ρ is SAS if and only if its spectrum verifies

$$\sqrt{\lambda_1} + \sqrt{\lambda_2} \geq 1. \tag{2.26}$$

On the left panel of Figure 2.5, we plot the resulting maximal negativity in the $j = 1$ simplex with the AWP polytope. There are clearly regions of spectra that satisfy either, both, or neither of the AWP and SAS conditions. Thus already for spin-1 there exist states with a positive P function and a negative W function and vice-versa. For $j = 1$ specifically, it was also shown in [11] that the largest ball of SAS states has a radius $r^{(1)}_{\mathrm{in}}(0) = 1/(2\sqrt{6}) \approx 0.20412$, which is the same value as the radius $r^{(0)}_{\mathrm{in}}(0) = 1/(2\sqrt{6})$. Hence, for $j = 1$, the largest ball of AWP states coincides with the largest ball of SAS states as we can see in Figure 2.5.

2.2.1.3 Spin $j = 3/2$

For spin-3/2, a numerical optimisation (see [11] for more information) yielded the maximum negativity of the partial transpose in the unitary orbit of the states located on a face

of the polytope. The results are displayed on the right panel of Figure 2.5 where we depict the maximal entanglement negativity on the surface of the minimal AWP polytope. Similar to the spin-1 case, we observe both SAS and entangled states on this surface. A notable difference is that, for $j = 3/2$, the largest ball containing only SAS states has a radius $r_{\text{in}}^{(1)}(0) = 1/(2\sqrt{19})$ [11, 12] which is strictly smaller than $r_{\text{in}}^{(0)}(0) = 1/(2\sqrt{15})$. Therefore, the SAS states on the face of the polytope are necessarily outside this ball.

2.2.2 P function

The set $\mathcal{S}_1$ of APP states w.r.t. the P function (2.1) contained in the APP polytope for $j = 1$ is represented on the right panel of Figure 2.1. The kernel of the P function verifies $|\boldsymbol{\Delta}^{(1)}|^2 = C_{4j+2}^{2j+1} - 1$ which leads to the spectrum (2.19)

$$\boldsymbol{\lambda}^* = \frac{\left(C_{4j+2}^{2j+1} - 1 - \mathcal{W}_{\min}\right)\mathbf{1} - \left(1 - (2j+1)\mathcal{W}_{\min}\right)\boldsymbol{\Delta}^{(s)}}{2\left[(4j+1)C_{4j}^{2j} - (j+1)\right]}. \tag{2.27}$$

The inner ball containing only APB states has radius

$$r_{\text{in}}^{(1)}\left(\mathcal{W}_{\min}\right) = \frac{1 - (2j+1)\mathcal{W}_{\min}}{\sqrt{(4j+2)\left[(4j+1)\,C_{4j}^{2j} - (j+1)\right]}}$$

Hence, for $\mathcal{W}_{\min} = 0$, we can define the set $\mathcal{S}_0$ of APP states based on the P function (2.1) through the radius of the APP ball

$$r_{\text{in}}^{(1)}(0) = \frac{1}{\sqrt{(4j+2)\left[(4j+1)\,C_{4j}^{2j} - (j+1)\right]}}. \tag{2.28}$$

Remarkably, the radius (2.28) is exactly the same as that deduced in [149], albeit through a distinct approach.

2.2.2.1 Spin $j \leq 3/2$

For a qubit ($j = 1/2$), the kernel eigenvalues are given by

$$\Delta_0 = -C_2^0 = -1, \qquad \Delta_1 = C_2^1 = 2$$

and the ordered APP conditions are for the highest eigenvalue $\lambda \geq 1/2$

$$-\lambda + 2(1 - \lambda) \geq 0.$$

Thus, the APP polytope is defined by the following inequality

$$\frac{1}{2} \leq \lambda \leq \frac{2}{3}.$$

We see that not all qubit states are APP based on the P function defined through the SW phase-space function (2.1). However, as already explained for the AWP polytope for $j = 1/2$, all qubit states are SAS, meaning that for each qubit state ρ and each unitary $U \in \mathrm{SU}(2)$, there exists a P function such that $P_{U\rho U^\dagger} \geq 0$. This clearly shows that higher-order terms in the definition of the most general SW phase-space representations (2.2) are necessary to retrieve the full set of SAS qubit states.

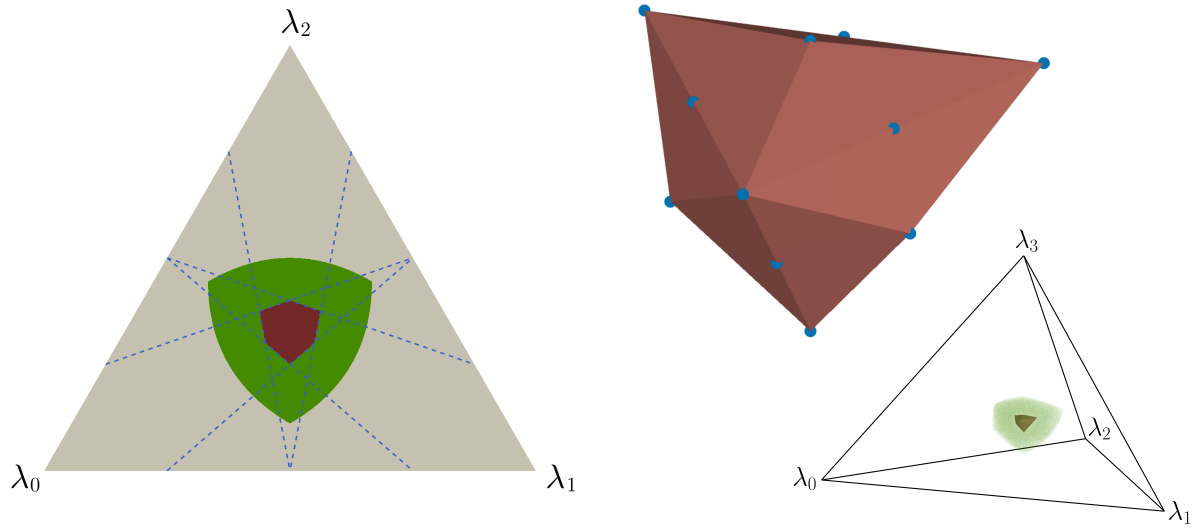

Figure 2.6: Left : Polytope of SAS states for $j = 1$ in the simplex of eigenvalues, displayed in barycentric coordinates. The blue dotted lines, corresponding to conditions (2.9), define the edges of the polytope. The green area delimited by the condition (2.26) represents the set of SAS states. Right : Polytope for $j = 3/2$ next to the full tetrahedron of states in barycentric coordinates. The vertices of the polytope are indicated by the blue dots. The twice degenerate eigenvalues Δ_i of the P function kernel (see second row of Table 2.2) produce degeneracy in the faces. As a result, some of the blue dots are in the middle of the edges of the polytope. The green points are SAS states obtained by numerical optimisation as described in [11].

In Figure 2.6, we depict the APP polytopes for $j = 1$ and $3/2$ and the full sets of SAS states which were obtained in [11, 12]. Once again, we can see that the set of APP states based on the P function does not cover the entire set of SAS states. In Section 2.3, we deal with the extension of the APP states set by using higher-order terms appearing in the generalised phase-space representations (2.2).

2.2.2.2 Spin $j > 3/2$

For $j > 3/2$, there is no known characterisation of the full set of SAS states. The best result known so far is that on the radius of a ball containing only APP states [149] which appears to be the inner ball of the APP polytope. Hence, the set of SAS states obtained through the APP polytope is the best characterisation of SAS states known so far for $j > 3/2$.

2.3 Beyond the polytopes

In this section, we extend the set of SAS states obtained through the characterisation of the set of APP states. Hence, we focus here only on the P function ($s = 0$). However, all the results can be straightforwardly applied to other phase-space representations. To set the notations, let us recall that the most general P function of a spin state ρ has the

form (2.2) [114]

$$P_\rho(\Omega) = P_\rho^{(0)}(\Omega) + \sum_{L=2j+1}^{+\infty} \sum_{M=-L}^{L} x_{LM} Y_{LM}(\Omega), \tag{2.29}$$

where $P_\rho^{(0)}$ is the P function given by the SW framework (2.1). The latter is uniquely defined for ρ as

$$P_\rho^{(0)}(\Omega) = \sqrt{\frac{4\pi}{2j+1}} \sum_{L=0}^{2j} \left(C_{jjL0}^{jj}\right)^{-1} Q_\rho^{(L)}(\Omega) \tag{2.30}$$

with the real functions (by the hermiticity of ρ) covariant under rotations

$$Q_\rho^{(L)}(\Omega) = \sum_{M=-L}^{L} \rho_{LM} Y_{LM}(\Omega). \tag{2.31}$$

where the ρ_{LM} are the state multipoles. Since any state ρ can be represented by a decomposition on the overcomplete basis of coherent states (pure product states)

$$\rho = \int_{\mathcal{S}^2} P_\rho(\Omega) |\Omega\rangle \langle\Omega|,$$

any separable state can be described by an everywhere positive P function. However, the P function P_0 is not always everywhere positive, even for separable states. Hence, the additional terms in (2.29) play a crucial role, as illustrated by examining a spin coherent state oriented along a specific direction Ω_0. A positive P realisation of $\rho = |\Omega_0\rangle \langle\Omega_0|$ is a Dirac delta function on the sphere, $P_\rho(\Omega) = \delta(\Omega - \Omega_0)$. However, it is clear that such a delta function cannot be obtained by truncating the infinite sum in (2.29). Indeed, if we did this, the resulting P function would always be negative somewhere on the sphere, as discussed in [149]. Hence, in order to extend the set of SAS states obtained through the characterisation of APP states, we consider the following minimisation

$$\min_{\substack{U \in \mathrm{SU}(2j+1) \\ \Omega \in S^2}} P_{U\rho U^\dagger}(\Omega) \geqslant 0 \tag{2.32}$$

where $P_{U\rho U^\dagger}$ potentially includes all the terms with $L > 2j+1$ in the general formulation of the P function (2.29).

2.3.1 Non-linear APP criteria

To simplify the complexity of the minimisation problem in (2.32) and facilitate the derivation of analytical results, we choose to focus exclusively on additional terms that arise from the product of Q_L functions, as defined in (2.31). Specifically, we consider only those extra terms, obtained by squaring the Q_L functions and then subtracting their lower angular momentum components so that only spherical harmonics with $L > 2j$ are involved. We thus add to P_0 terms proportional to

$$P_\rho^{(L)}(\Omega) \equiv \left(Q_\rho^{(L)}\right)^2 - \sum_{L'=0}^{2j} \sum_{M=-L'}^{L'} \left(\int \left(Q_\rho^{(L)}\right)^2 Y_{L'M}^* d\Omega \right) Y_{L'M}, \tag{2.33}$$

where only the integrals with L' even are non-zero. It is important to note that, by construction, the functions (2.33) are non-zero only for $L > 2j$ and are covariant under

rotations as inherited from each $Q_\rho^{(L)}$. Consequently, as explained in Subsection 2.1.1, we can work only with the P functions of a unitarily transformed state ρ evaluated at $\Omega = 0$

$$P_{U\rho U^\dagger}(0) = P^{(0)}_{U\rho U^\dagger}(0) + \sum_{L>j}^{2j} y_L P^{(L)}_{U\rho U^\dagger}(0), \tag{2.34}$$

where y_L are real numbers. Just like the x_{LM} variables in (2.29), each y_L can depend on the state ρ and U. However, for the sake of simplicity, we will only consider them as variables independent of the unitary and the state. The general idea for obtaining a larger SAS set is to reduce the minimisation problem on the full unitary orbit to a problem that requires minimisation on the unistochastic matrices only, as in the developments for obtaining the polytopes of SAS states.

A direct application of a formula giving the integral of a triple product of spherical harmonics (see e.g. (4), p. 148 of [69]) together with the equality $|\rho_{LM}| = |\rho_{L-M}|$ lead us to an algebraic expression for the functions $P_\rho^{(L)}(0)$ defined in (2.33),

$$P_\rho^{(L)}(0) = \frac{2L+1}{4\pi} \sum_{M=0}^{L} F(L,M) \left|\rho_{LM}\right|^2, \tag{2.35}$$

with $F(L,M)$ state-independent coefficients given by

$$F(L,M) = \begin{cases} 1 - \sum\limits_{\substack{L'=0 \\ L' \text{ even}}}^{2j} \left(C^{L'0}_{L0L0}\right)^2 & \text{if } M = 0 \\ 2(-1)^{M+1} \sum\limits_{\substack{L'=0 \\ L' \text{ even}}}^{2j} C^{L'0}_{L0L0} C^{L'0}_{LML-M} & \text{if } M \neq 0 \end{cases} \tag{2.36}$$

where the identity $C^{L'0}_{L0L0} = 0$ for L' odd restricts the sum to L' even. Some values of $F(L,M)$ are given in Table 2.4. Note that these coefficients are real and can be positive or negative. The factors $(2L+1)/4\pi$ in (2.35) can be absorbed into the variables y_L without loss of generality to rewrite (2.34) as follows

$$P_\rho(0) = P_\rho^{(0)}(0) + \sum_{L>j}^{2j} \sum_{M=0}^{L} y_L F(L,M) |\rho_{LM}|^2. \tag{2.37}$$

As the Hilbert-Schmidt distance $r(\rho)$ between any state ρ and the MMS ρ_0 can be written as

$$r^2(\rho) = \sum_{L=1}^{2j} \left(\rho_{L0}^2 + 2 \sum_{M=1}^{L} |\rho_{LM}|^2 \right)$$

we can isolate the component $|\rho_{2j\,1}|^2$ as

$$2|\rho_{2j\,1}|^2 = r^2 - \sum_{L=1}^{2j} \rho_{L0}^2 - 2 \sum_{L=1}^{2j} \sum_{M=1+\delta_{L,2j}}^{L} |\rho_{LM}|^2, \tag{2.38}$$

and then insert this expression into (2.37) to get

$$P_\rho(0) = P_\rho^{(0)}(0) + \Pi_\rho(0) + \tilde{\Pi}_\rho(0) \tag{2.39}$$

with

$$\Pi_\rho(0) = \left(\frac{y_{2j}F(2j,1)}{2}\right) r^2 + \sum_{L=1}^{2j}\left[y_L F(L,0)\Theta(L-j) - \frac{y_{2j}F(2j,1)}{2}\right]\rho_{L0}^2 \tag{2.40}$$

and

$$\tilde{\Pi}_\rho(0) = \sum_{L=1}^{2j}\sum_{M=1+\delta_{L,2j}}^{L}\left[y_L F(L,M)\Theta(L-j) - y_{2j}F(2j,1)\right]|\rho_{LM}|^2, \tag{2.41}$$

where $\Theta(x)$ is the Heaviside step-function defined here as

$$\Theta(x) = \begin{cases} 0 & x \leq 0 \\ 1 & x > 0 \end{cases}.$$

In what follows, we will omit the contribution of $\tilde{\Pi}_\rho(0)$ in (2.39), under the assumption that it is positive, i.e. $\tilde{\Pi}_\rho(0) \geq 0$. To ensure this assumption, we will need to put constraints on the possible values of the y_L's. This simplification allows us to reduce the requirement of positivity for P to the simpler condition of positivity for $P_\rho^{LB} \equiv P_\rho^{(0)} + \Pi_\rho$. The general form of the remaining function P^{LB} reads

$$P_\rho^{LB} = f(\rho) + \sum_{L=1}^{2j}\left(g_L\rho_{L0} + h_L\rho_{L0}^2\right), \tag{2.42}$$

where the function $f(\rho)$ and the coefficients g_L and h_L are deduced from (2.30) and (2.39) as being

$$\begin{aligned} f(\rho) &= \frac{1}{2j+1} + \left(\frac{y_{2j}F(2j,1)}{2}\right) r^2 \\ g_L &= \sqrt{\frac{2L+1}{2j+1}}\left(C_{jjL0}^{jj}\right)^{-1} \\ h_L &= y_L F(L,0)\Theta(L-j) - \frac{y_{2j}F(2j,1)}{2}. \end{aligned} \tag{2.43}$$

Note that g_L is a constant, h_L depends on the y_L variables, while the function $f(\rho)$ depends only on the $\mathrm{SU}(2j+1)$-invariant distance to the maximally mixed state r given by (2.14). Hence, f, g_L and h_L are constant along the unitary orbit of ρ.

In the end, the function P_ρ^{LB} only depends on the components $\rho_{L0} = \mathrm{Tr}\left(\rho T_{L0}^\dagger\right)$. By diagonalising the state $\rho = M^\dagger \Lambda M$, any state ρ' in the unitary orbit of ρ can be expressed as $\rho' = V\Lambda V^\dagger$ with $V = UM^\dagger$. Hence, a multipole ρ'_{L0} of ρ' reads

$$\rho'_{L0} = \mathrm{Tr}\left(V\Lambda V^\dagger T_{L0}^\dagger\right) = \sum_{m,m'=-j}^{j} V_{m'm}\lambda_m V_{m'm}^* t_{Lm'} = \boldsymbol{\lambda} B \mathbf{t}_L^T$$

with $\mathbf{t}_L = (t_{L,j}, , \ldots, t_{L,-j})$ the vector containing the eigenvalues of T_{L0}, $t_{L,m} = \langle j,m|\, T_{L0}\, |j,m\rangle$, and B the unistochastic matrix defined from V, with entries $B_{kl} = |V_{kl}|^2$. The expression of P_ρ^{LB} eventually reduces to

$$P_\rho^{LB} = f(\rho') + \sum_{L=1}^{2j}\left[g_L \boldsymbol{\lambda} B \mathbf{t}_L^T + h_L\left(\boldsymbol{\lambda} B \mathbf{t}_L^T\right)^2\right]. \tag{2.44}$$

Number of qubits $N = 2j$	$\mathcal{S}_1$	$\mathcal{S}_3$
2	$\boldsymbol{\lambda}\,(-3,1,3)^T \geqslant 0$	$r^2 \leqslant \frac{1}{78} \approx 0.01282$
3	$\boldsymbol{\lambda}\,(-6,-1,4,4)^T \geqslant 0$	$r^2 \leqslant \frac{1}{354} \approx 0.002825$
4	$\boldsymbol{\lambda}\,(-10,-5,1,5,10)^T \geqslant 0$	$r^2 \leqslant \frac{11}{25390} \approx 0.0004332$
5	$\boldsymbol{\lambda}\,(-15,-15,-1,6,6,20)^T \geqslant 0$	$r^2 \leqslant \frac{1595}{16058598} \approx 0.00009932$

Table 2.2: Condition for a state with eigenspectrum $\boldsymbol{\lambda} = (\lambda_0, \ldots, \lambda_N)$ sorted in descending order $\lambda_0 \geqslant \lambda_1 \geqslant \cdots \geqslant \lambda_N$ to be included in SAS sets $\mathcal{S}_1$ and $\mathcal{S}_3$.

As a result, we have moved from a minimisation problem over the full unitary orbit of a state to a simpler problem that necessitates a minimisation over the unistochastic matrices only,

$$\begin{aligned} \min_{\substack{U\in \mathrm{SU}(2j+1)\\ \Omega\in S^2}} P_{U\rho U^\dagger}(\Omega) &= \min_{U\in \mathrm{SU}(2j+1)} P_{U\rho U^\dagger}(0) \\ &\geqslant \min_{U\in \mathrm{SU}(2j+1)} P^{LB}_{U\rho U^\dagger} \\ &= \min_{\mathbf{b}\in \mathcal{U}_{2j+1}} P^{LB}_{U\rho U^\dagger} \end{aligned} \tag{2.45}$$

where in the second line we have used our assumption $\tilde{\Pi}_\rho \geq 0$ and in the last line we refer to a parametrization $\mathbf{b}$ of unistochastic matrices $B \in \mathcal{U}_{2j+1}$, as discussed in Appendix 2.A. In particular, the terms $\boldsymbol{\lambda} B \mathbf{t}_L^T$ in $P^{LB}_{U\rho U^\dagger}$ are linear expressions of the $\mathbf{b}$-variables of the bistochastic matrices. It follows that $P^{LB}_{U\rho U^\dagger}$ is quadratic over $\mathbf{b}$ (see also Appendix 2.D).

Using the same result from Subsection 2.1.1 to enlarge the minimisation over unistochastic matrices into a minimisation over bistochastic ones, we can now derive from (2.45) another set of SAS states, denoted as $\mathcal{S}_2(\{y_L\})$, or just $\mathcal{S}_2$ for short, taking the form of a quadratic optimisation problem on the $\mathbf{b}$-variables of the bistochastic matrix (see Appendices 2.A and 2.D, in particular (2.62)), with the y_L parameters constrained by the positivity condition $\tilde{\Pi}_\rho(0) \geq 0$ (2.41).

Proposition. ***SAS set $\mathcal{S}_2(\{y_L\})$****: A symmetric N-qubit state ρ is SAS if*

$$\min_{\mathbf{b}\in \mathcal{B}_{2j+1}} P^{LB}_{U\rho U^\dagger} \geqslant 0, \tag{2.46}$$

where $P^{LB}_{U\rho U^\dagger}$ is given by (2.44) and y_L are real parameters restricted by the inequalities

$$y_L F(L,M)\Theta(L-j) - y_{2j} F(2j,1) \geqslant 0, \tag{2.47}$$

for $L = 1, \ldots, 2j$ and $M = 1, \ldots, L$, where the coefficients $F(L,M)$ are defined in (2.36).

One can relax the minimisation problem to the whole real domain $\mathbf{b} \in \mathbb{R}^{4j^2}$ while retaining a useful SAS set provided that $h_L > 0$, otherwise the Hessian (2.63) of the quadratic function $P^{LB}_{U\rho U^\dagger}$ (2.44) has a negative eigenvalue and hence $P^{LB}_{U\rho U^\dagger}$ has a minimum equal to negative infinity.

The latter requirement implies that

$$y_L F(L,0)\Theta(L-j) > \frac{y_{2j}F(2j,1)}{2} \tag{2.48}$$

for all L. Under these assumptions, the global minimum of P_ρ^{LB} on $\mathbf{b} \in \mathbb{R}^{4j^2}$ has an algebraic solution given by (see Appendix 2.D for details)

$$\min_{\mathbf{b}\in\mathcal{U}_{2j+1}} P_\rho^{LB} \geqslant \min_{\mathbf{b}\in\mathbb{R}^{4j^2}} P_\rho^{LB} = f(\rho) - \frac{1}{4}\sum_{L=1}^{2j}\frac{g_L^2}{h_L}. \tag{2.49}$$

Any state for which the r.h.s. of (2.49) is positive is then SAS, which after a bit of algebra can be rewritten as an upper bound on r

$$r^2(\rho) \leqslant \left(\frac{-2}{y_{2j}F(2j,1)}\right)\left(\frac{1}{2j+1} - \frac{1}{4}\sum_{L=1}^{2j}\frac{g_L^2}{h_L}\right). \tag{2.50}$$

Note that we have used the inequality $y_{2j} \geqslant 0$, which is a direct consequence of $F(2j,1) < 0$ shown in Appendix 2.E (see (2.64)) and the inequality (2.47) for $L = 1$. In order to obtain the best SAS set, we need to maximise the r.h.s. of the last equation over the admissible parameters y_L. If we first maximise (2.50) with respect to y_L for $L \neq 2j$, we find that we need to maximise the h_L variables (2.43) and consequently maximise the y_L variables, which are upper bounded by the conditions (2.47). Our numerical observations (see (2.65)) show that the strictest upper bound is $y_L \leqslant y_{2j}F(2j,1)/F(L,1)$. We can then evaluate y_L at these apparently tight upper bounds. Finally, we maximise (2.50) with respect to y_{2j}, to obtain the extremal point

$$\begin{aligned} y_L &= \frac{F(2j,1)}{F(L,1)}y_{2j} \quad \text{for } j < L < 2j \\ y_{2j} &= \frac{(2j+1)}{F(2j,1)}\sum_{L=1}^{2j}\frac{g_L^2}{2\Theta(L-j)\frac{F(L,0)}{F(L,1)} - 1} \end{aligned} \tag{2.51}$$

In particular, $y_L \geqslant 0$ implies that $h_L > 0$ is fulfilled, as required above. Thus, we obtain a simpler SAS set $\mathcal{S}_3$, weaker than $\mathcal{S}_2$, but with an analytical expression.

Proposition. ***SAS set $\mathcal{S}_3$*** *: A symmetric N-qubit state ρ is SAS if its distance r to the MMS in the symmetric sector fulfills*

$$r^2(\rho) \leqslant \frac{1}{(2j+1)^2}\left(\sum_{L=1}^{2j}\frac{g_L^2}{1 - 2\Theta(L-j)\frac{F(L,0)}{F(L,1)}}\right)^{-1} \tag{2.52}$$

with $F(L,M)$ and g_L state-independent constants defined in (2.36) and (2.43). Note that (2.52) gives a better radius on the set of SAS states than previous results, such as the inner ball of the APP polytope [149].

2.3.2 Two- and three-qubit symmetric states

In this section, we exemplify our SAS sets in the specific cases of $N = 2$ and $N = 3$, in order to clarify all the technical aspects of our method.

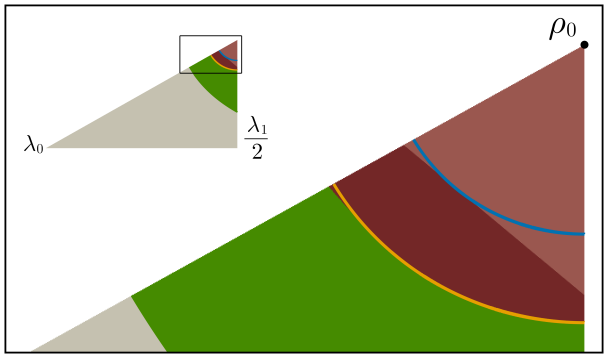

Figure 2.7: SAS states in the first Weyl chamber ($\lambda_0 \geq \lambda_1 \geq \lambda_2$) for $N = 2$ represented in barycentric coordinates. The curves correspond to the bounds of the sets $\mathcal{S}_0$ (blue) and $\mathcal{S}_3$ (orange). The green area encompasses all the remaining SAS states, as completely characterised by the condition (2.26). The set $\mathcal{S}_1$ is depicted in light red. Lastly, $\mathcal{S}_2$ with $y_2 = 455/12$ is formed by the light and dark red regions. We note that $\mathcal{S}_2$ is only very slightly bigger than $\mathcal{S}_3$.

2.3.2.1 2 qubits (spin $j = 1$)

In this case, the set $\mathcal{S}_1$ of states in the APP polytope is given by

$$\boldsymbol{\lambda}^{(\uparrow)}(-3, 1, 3)^T \geqslant 0.$$

We plot in Figure 2.7 the set $\mathcal{S}_1$ in one Weyl chamber. In contrast, the other two sets, $\mathcal{S}_2(\{y_L\})$ and $\mathcal{S}_3$, rely on the P function (2.34) with only one extra term

$$P_\rho(\Omega) = P_\rho^{(0)}(\Omega) + y_2 P_\rho^{(2)}(\Omega), \tag{2.53}$$

with

$$\frac{4\pi}{5} P_\rho^{(2)}(0) = \frac{6}{35}\left(3\rho_{20}^2 - 4|\rho_{21}|^2 + |\rho_{22}|^2\right). \tag{2.54}$$

By scaling y_2 with the factor $5/4\pi$, and performing the change of variable (2.38) in (2.53) and (2.54), reading explicitly

$$2|\rho_{21}|^2 = r^2 - \sum_{L=1}^{2} \rho_{L0}^2 - 2\sum_{L=1}^{2}\sum_{M=1+\delta_{L,2}}^{L} |\rho_{LM}|^2,$$

we get

$$P_\rho(0) = P_\rho^{(0)}(0) + \Pi_\rho(0) + \tilde{\Pi}_\rho(0),$$

with

$$\Pi_\rho(0) = \frac{6}{35} y_2 \Big(-2r^2 + 2\rho_{10}^2 + 5\rho_{20}^2 \Big) \qquad \tilde{\Pi}_\rho(0) = \frac{6}{35} y_2 \Big(4|\rho_{11}|^2 + 5|\rho_{22}|^2 \Big).$$

The inequality $P_\rho \geqslant P_\rho^{(0)} + \Pi_\rho \equiv P_{LB}$ defines the admissible region (2.47) of the y_2 variable, here $y_2 \geqslant 0$. The function P_{LB} has now the form (2.42) with factors (2.43) given by

$$f(\rho) = \frac{1}{3} - \frac{12}{35} y_2 r^2 \qquad (g_1, g_2) = \left(\sqrt{2}, 5\sqrt{\frac{2}{3}}\right) \qquad (h_1, h_2) = \frac{6}{35}(2y_2, 5y_2)$$

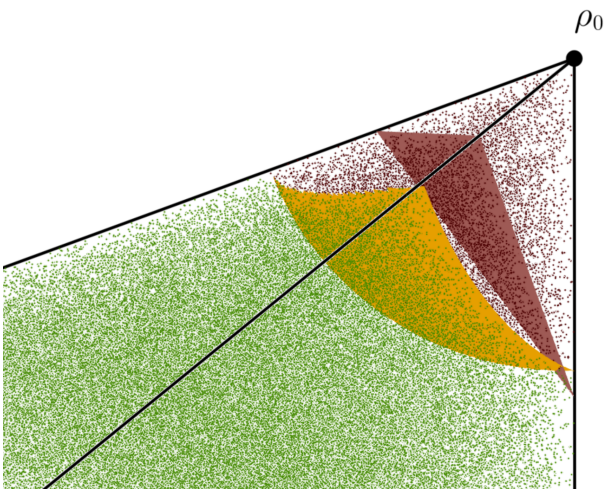

Figure 2.8: SAS states in the first Weyl chamber ($\lambda_0 \geq \lambda_1 \geq \lambda_2 \geq \lambda_3$) for $N = 3$. The dark red and orange surfaces are respectively the boundaries of $\mathcal{S}_1$ and $\mathcal{S}_3$, respectively. The dark red points are the states contained in $\mathcal{S}_2(\{y_L\})$ with y_L equal to (2.51). The green points are SAS states obtained numerically as described in [11].

which are the elements needed to calculate the set $\mathcal{S}_2(\{y_L\})$ defined by (2.46). Lastly, we use (2.52) to calculate our third set at $y_2 = 455/12$ (2.51)

$$\mathcal{S}_3 \text{ for 2 qubits}: \ \rho \in \mathcal{A}_{\text{sym}} \ \text{ if } \ r^2 \leqslant \frac{1}{78}.$$

The surface of the ball spanned by this radius r is depicted in orange in Figure 2.7.

2.3.2.2 3 qubits (spin $j = 3/2$)

The linear set $\mathcal{S}_1$, plotted in Figure 2.8 in dark red, is given by

$$\boldsymbol{\lambda}^{(\uparrow)}(-6,-1,4,4)^T \geqslant 0.$$

Now, for the extended phase-space representation, we start by defining the respective P function (2.34) which has two additional terms

$$P = P_0 + y_2 P_\rho^{(2)} + y_3 P_3^{(3)}, \tag{2.55}$$

where $P_\rho^{(2)}$ for 3 qubits is also given by (2.54) and

$$\frac{4\pi}{7} P_\rho^{(3)}(0) = \frac{2}{21}\left(7\rho_{30}^2 - 6|\rho_{31}|^2 - 3|\rho_{32}|^2 + 2|\rho_{33}|^2\right).$$

By using (2.38) to substitute $|\rho_{31}|^2$ in the P function, we get $P_\rho = P_\rho^{(0)} + \Pi_\rho + \tilde{\Pi}_\rho$ with

$$\Pi_\rho = \frac{2}{7}\left[x_3\left(\rho_{10}^2 - r^2\right) + \left(\frac{9y_2 + 5y_3}{5}\right)\rho_{20}^2 + \frac{10}{3} y_3 \rho_{30}^2\right],$$

$$\tilde{\Pi}_\rho = \frac{2}{7}\left[2y_3|\rho_{11}|^2 + \frac{2}{5}\left(5y_3 - 6y_2\right)|\rho_{21}|^2 + \left(\frac{3}{5}y_2 + 2y_3\right)|\rho_{22}|^2 + y_3|\rho_{32}|^2 + \frac{8}{3}y_3|\rho_{33}|^2\right].$$

Again, $P_\rho \geqslant P_\rho^{(0)} + \Pi_\rho \equiv P^{LB}$ when all the coefficients of the terms in $\tilde{\Pi}_\rho$ are positive, i.e.,

$$y_3 \geqslant 0\,, \quad 5y_3 - 6y_2 \geqslant 0\,, \quad \frac{3}{5}y_2 + 2y_3 \geqslant 0. \tag{2.56}$$

Let us remark that y_2 may take negative values.

Now, we can calculate the factors (2.43) which are necessary to calculate P_ρ^{LB} and the set $\mathcal{S}_2(\{y_L\})$. They are given by

$$f(\rho) = \frac{1}{4} - \frac{2}{7}y_3 r^2 \quad (g_1, g_2, g_3) = \left(\frac{\sqrt{5}}{2}, \frac{5}{2}, \frac{7\sqrt{5}}{2}\right) \quad (h_1, h_2, h_3) = \frac{2}{7}\left(y_3, \frac{9}{5}y_2 + y_3, \frac{10}{3}y_3\right)$$

Finally, for $\mathcal{S}_3$, we have the extra condition $h_L > 0$ (2.48) for the y_L values

$$9y_2 + 5y_3 > 0,$$

which is always satisfied for the extremal y_L values given in (2.51), which read

$$y_2 = \frac{2065}{16}\,, \quad y_3 = \frac{1239}{8}.$$

The set $\mathcal{S}_3$ eventually reads

$$\mathcal{S}_3 \text{ for 3 qubits}: \ \rho \in \mathcal{A}_{\text{sym}} \ \text{ if } \ r^2 \leqslant \frac{1}{354}.$$

Conclusion

Given the ever-rising importance of spin phase-space representations in fields like quantum information science [137, 134, 135, 138], quantum many-body dynamics [84–86], and quantum thermodynamics [150], we have studied in this chapter the properties of the SW phase-space representations of finite-dimensional quantum systems. Our work has advanced the characterisation of non-classicality in mixed spin-j states, establishing rigorous bounds on the unitary evolution of quantum states and their phase-space negativity.

Our first result gives a complete characterisation for any spin quantum number j of the set of absolutely Stratonovitch-Weyl bounded (ASB) states in the form of a polytope centred on the MMS in the simplex of state eigenvalues. We have compared our results on the set of absolutely Wigner positive states with the set of SAS states. The spin-1 and spin-3/2 cases, for which analytical results are known, were closely examined and important differences were highlighted, such as the existence of SAS states whose Wigner function is negative, and, conversely, the existence of entangled absolutely Wigner positive states. This novel fact represents a key distinction from the infinite-dimensional setting where a positive Glauber-Sudarshan function (equivalent to the P function) trivially implies a positive Wigner function [151, 152]. Moreover, the characterisation of the APP polytopes, i.e. the SAS set $\mathcal{S}_1$, allowed us to show that the SAS ball previously derived in [149] is in fact the largest ball enclosed in the APP polytope, directly connecting our work with previous results.

Building on top of the set $\mathcal{S}_1$ of SAS states contained in the APP polytope, we have derived two new families of even larger SAS sets $\mathcal{S}_2$ and $\mathcal{S}_3$, both being nonlinear w.r.t. the state eigenvalues. Among our sets, $\mathcal{S}_1$ and $\mathcal{S}_3$ are simple functionals on the spectrum

and the purity of the state. In contrast, $\mathcal{S}_2(\{y_L\})$, which is capable of detecting a larger subset of SAS states, necessitates solving a quadratic optimisation problem over the bistochastic matrices. Our observations on the cases $N = 2$ and $N = 3$ indicate that the disparity between the SAS subsets detected by $\mathcal{S}_3$ compared to $\mathcal{S}_2$ seems to be minimal, as illustrated in Figure 2.7. It is also important to note that none of our sets provides complete characterisation of all SAS states, i.e. the full SAS set.

This motivates several strategies for future work. To efficiently uncover more SAS states, instead of scrutinizing $\mathcal{S}_2$, a viable approach is to include additional terms in the P function, as outlined in (2.33). The minimum number of terms to be added for a complete characterisation of SAS set remains as an open question, even in the case of two qubits. Another direction for witnessing larger sets of SAS states is to use the convexity property of SAS[2]. In particular, we can immediately establish a larger SAS set defined by the convex hull of all SAS sets $\mathcal{S}_2(\{y_L\})$ depending on the y_L's.

Note that another possible alternative to the characterisation of the set of SAS states, for integer j, is through the characterisation of the set of Symmetric Absolutely PPT (SAPPT) states [154], i.e. states whose partial transpose remain positive under any unitary evolution. Indeed, for integer j, a still pending question is if the sets of SAS and SAPPT states are identical. If true, then the full characterisation of SAPPT states conducted in [12] would also give a full characterisation of the sets of SAS states. For half-integer j, it was recently shown that the set of SAPPT is strictly included in the SAS set [13] and more work is thus definitely needed to fully characterise the SAS set of half-integer j systems.

Other future researches could explore the ratio of the volume of the ASB polytopes to the volume of the full simplex; this would basically be a *global indicator of classicality* like those introduced and studied in [145, 148, 155] particularised to spin systems. Another perspective, as briefly mentioned in Section 2.1, is to apply the techniques presented here to other distinguished quasiprobability distributions. For example, future work could explore the relation between absolutely Husimi bounded (AHB) polytopes and the geometric measure of entanglement of mixed multiqubit symmetric states (see Chapter 3 for the link between the Husimi function and the geometric measure of entanglement). It would also be intriguing to connect the lower bound on the SW phase-space functions in the unitary orbit to the accuracy achievable in simulating the general unitary (or even dissipative) many-body quantum dynamics of spin systems efficiently using stochastic trajectories [84–86]. Indeed, it could be expected that states with a positive lower bound would be more accurately simulated by these trajectories where the SW phase-space functions are used as an actual probability distribution obeying a certain Fokker-Planck equation. Additionally, this bound could be linked to potential quantum advantages in applications such as parameter estimation, where the presence of negative values in quasiprobability distributions might enhance the precision of quantum sensing protocols.

Finally, in terms of experimental implementation, measuring the state spectrum is required to check if a state belongs to $\mathcal{S}_1$ and $\mathcal{S}_2$, while, for $\mathcal{S}_3$, it relies on evaluating the state's purity. Importantly, both the spectrum and purity of a quantum state can be estimated without the need for full quantum tomography [156].

[2]The proof of the convexity of the set of symmetric absolutely separable states is a special case of the convexity of the absolutely separable case [153].

2.A Unistochastic and bistochastic matrices

Let $B \in \mathcal{B}_d$ be a $d \times d$ *bistochastic* matrix [147]. Bistochastic matrices possess positive entries, and the sum of entries in each column or row equals 1. The set of bistochastic matrices, denoted as $\mathcal{B}_d$, forms a polytope in $\mathbb{R}^{(d-1)^2}$. One approach to parameterise this set involves introducing free variables in a $(d-1) \times (d-1)$ minor of a bistochastic matrix B, and then the remaining entries are determined by satisfying the bistochastic conditions. For instance, $\mathcal{B}_3$ can be parametrized by $\mathbf{b} = (b_1, b_2, b_3, b_4) \in [0,1]^4$ as

$$B(\mathbf{b}) = \begin{pmatrix} b_1 & b_2 & 1-b_1-b_2 \\ b_3 & b_4 & 1-b_3-b_4 \\ 1-b_1-b_3 & 1-b_2-b_4 & \sum_{i=1}^4 b_i - 1 \end{pmatrix}, \tag{2.57}$$

where the positivity condition of the entries of B defines the domain of the b_k variables [157, 158]

$$\begin{aligned} \mathcal{B}_3 \;=\; & \Big\{ B(\mathbf{b}) \Big| \mathbf{b} \in [0,1]^4, 1 \leq \sum_i b_i, b_1 + b_2 \leq 1, \\ & b_1 + b_3 \leq 1,\, b_2 + b_4 \leq 1,\, b_3 + b_4 \leq 1 \Big\}. \end{aligned} \tag{2.58}$$

For the sake of simplicity, we simply write $\mathbf{b} \in \mathcal{B}_3$ whenever $\mathbf{b}$ satisfies these conditions. Another useful parameterization of bistochastic matrices follows from the fact that they are the convex hull of permutation matrices σ_π [147]

$$B = \sum_{\pi \in S_d} c_\pi \sigma_\pi, \tag{2.59}$$

where $c_\pi \geq 0$, $\sum_\pi c_\pi = 1$.

A special subset of bistochastic matrices are the *unistochastic* matrices $B \in \mathcal{U}_d$ whose entries are specified by a unitary matrix $V \in \mathrm{SU}(d)$, $B_{ij} = |V_{ij}|^2$. While for $d = 2$, $\mathcal{U}_2 = \mathcal{B}_2$, a similar equality does not hold for $d \geq 3$ [157–159]. For example, the vectors $\mathbf{b}$ defining a unistochastic matrix $B \in \mathcal{U}_3$ must satisfy, in addition to the condition $\mathbf{b} \in \mathcal{B}_3$, an extra condition related to the positive area of a triangle (see [157, 158, 160] for more details), so that

$$\mathcal{U}_3 = \mathcal{B}_3 \cap \{ B(\mathbf{b}) | A(\mathbf{b}) \geq 0 \}, \tag{2.60}$$

with

$$A(\mathbf{b}) \equiv 4 b_1 b_2 b_3 b_4 - (b_1 + b_2 + b_3 + b_4 - 1 - b_1 b_4 - b_2 b_3)^2. \tag{2.61}$$

Note that there is no known characterisation of unistochastic matrices for $d > 3$ [159, 160].

2.B Barycentric coordinates

A mixed spin-j state necessarily has eigenvalues λ_i that are positive and add up to one, i.e.

$$\lambda_i \geq 0, \qquad \sum_{i=0}^{2j} \lambda_i = 1.$$

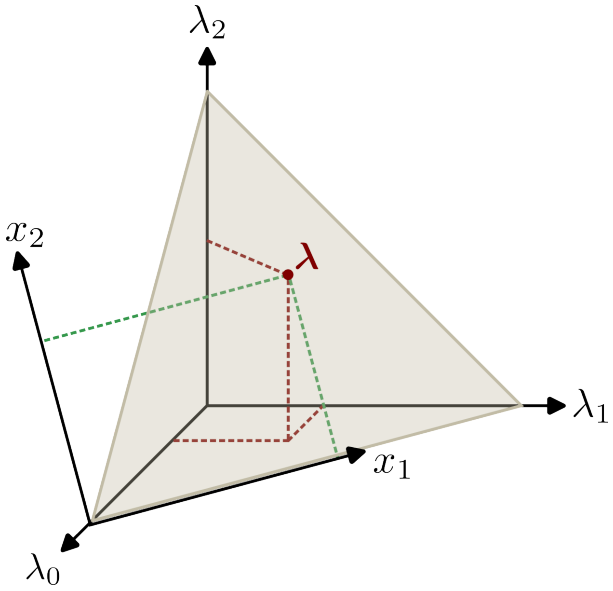

Figure 2.9: Barycentric and cartesian coordinate systems of spin state spectra for $j = 1$. The simplex in this case is an equilateral triangle, shown here in gray. The red dot corresponds to a given spectrum and its projections onto the barycentric and Cartesian coordinate system are indicated by the red and green dashed lines respectively.

This means that every state ρ has its eigenvalue spectrum in the probability simplex of dimension $2j$. For example, for $j = 1$, this simplex is a triangle shown in grey in Figure 2.9. In geometric terms, the spectrum $(\lambda_0, \lambda_1, \lambda_2)$ defines the barycentric coordinates of a point $\boldsymbol{\lambda}$ in the simplex, as it can be considered as the centre of mass of a system of $2j$ masses placed on the vertices of the triangle.

Let's explain how to go from the barycentric coordinate system to the Cartesian coordinate system spanning the simplex. If we denote by $\left\{\mathbf{r}^{(i)} : i = 0, \ldots, 2j\right\}$ the set of $2j + 1$ vertices of the simplex, the Cartesian coordinates of a point $\boldsymbol{\lambda}$ are given by

$$x_k = \sum_{i=0}^{2j} \lambda_i \, r_k^{(i)}$$

where $r_k^{(i)}$ is the k-th Cartesian coordinate of the i-th vertex of the simplex. For $j = 1$, the simplex is an equilateral triangle with vertices having Cartesian coordinates $\mathbf{r}_1 = (0, 0)$, $\mathbf{r}_2 = (1, 0)$ and $\mathbf{r}_3 = (1/2, \sqrt{3}/2)$. For $j = 3/2$, it is a regular tetrahedron with vertices having Cartesian coordinates $\mathbf{r}_1 = (0, 0, 0)$, $\mathbf{r}_2 = (1, 0, 0)$, $\mathbf{r}_3 = (1/2, \sqrt{3}/2, 0)$ and $\mathbf{r}_4 = (1/2, (2\sqrt{3})^{-1}, \sqrt{2/3})$.

2.C AWP and APP polytope vertices for $j \leq 2$

We give in Table 2.3 for $1/2 \leq j \leq 2$ the spin state spectra associated with the vertices of the minimal AWP and APP polytopes as they can be determined as explained in Subsection 2.1.2.

j	AWP vertices	APP vertices
1/2	$\boldsymbol{\lambda}_{\mathrm{v}_1} \approx (0.789, 0.211)$	$\boldsymbol{\lambda}_{\mathrm{v}_1} \approx (0.666, 0.333)$
1	$\boldsymbol{\lambda}_{\mathrm{v}_1} \approx (0.423, 0.423, 0.153)$ $\boldsymbol{\lambda}_{\mathrm{v}_2} \approx (0.544, 0.228, 0.228)$	$\boldsymbol{\lambda}_{\mathrm{v}_1} \approx (0.375, 0.375, 0.25)$ $\boldsymbol{\lambda}_{\mathrm{v}_2} \approx (0.4, 0.3, 0.3)$
3/2	$\boldsymbol{\lambda}_{\mathrm{v}_1} \approx (0.294, 0.294, 0.294, 0.119)$ $\boldsymbol{\lambda}_{\mathrm{v}_2} \approx (0.33, 0.33, 0.170, 0.170)$ $\boldsymbol{\lambda}_{\mathrm{v}_3} \approx (0.4, 0.2, 0.2, 0.2)$	$\boldsymbol{\lambda}_{\mathrm{v}_1} \approx (0.266, 0.266, 0.266, 0.2)$ $\boldsymbol{\lambda}_{\mathrm{v}_2} \approx (0.266, 0.266, 0.233, 0.233)$ $\boldsymbol{\lambda}_{\mathrm{v}_3} \approx (0.28, 0.24, 0.24, 0.24)$
2	$\boldsymbol{\lambda}_{\mathrm{v}_1} \approx (0.226, 0.226, 0.226, 0.226, 0.097)$ $\boldsymbol{\lambda}_{\mathrm{v}_2} \approx (0.24, 0.24, 0.24, 0.14, 0.14)$ $\boldsymbol{\lambda}_{\mathrm{v}_3} \approx (0.266, 0.266, 0.156, 0.156, 0.156)$ $\boldsymbol{\lambda}_{\mathrm{v}_4} \approx (0.313, 0.172, 0.172, 0.172, 0.172)$	$\boldsymbol{\lambda}_{\mathrm{v}_1} \approx (0.204, 0.204, 0.204, 0.204, 0.184)$ $\boldsymbol{\lambda}_{\mathrm{v}_2} \approx (0.206, 0.206, 0.206, 0.156, 0.156)$ $\boldsymbol{\lambda}_{\mathrm{v}_3} \approx (0.208, 0.208, 0.195, 0.195, 0.195)$ $\boldsymbol{\lambda}_{\mathrm{v}_4} \approx (0.216, 0.196, 0.196, 0.196, 0.196)$

Table 2.3: Barycentric coordinates (corresponding to the eigenspectrum of a mixed spin state) of the vertices of the minimal polytope of AWP states.

2.D Proof of (2.49)

We begin by noting that P_ρ^{LB}, as given in (2.42), depends only on the components ρ_{L0}, and on r which, however, is constant along the unitary orbit of ρ. These components can be expressed for a generic state within the unitary orbit, $\rho = U\Lambda U^\dagger$, with Λ being a diagonal matrix in the $|j,m\rangle$-basis whose diagonal entries are the eigenvalues of ρ, as follows

$$\rho_{L0} = \boldsymbol{\lambda} B \mathbf{t}_L^T = \mathbf{v}_L \mathbf{b}'^T,$$

where $\mathbf{t}_L$ is the vector of eigenvalues of T_{L0} with the entries $t_{L,m} = \langle j,m| T_{L0} |j,m\rangle$, $B_{ij} = |U_{ij}|^2$ is a unistochastic matrix (hence also bistochastic) parametrized by a generalization (2.57) in the b_k variables, and the new variables $b_k = b'_k + \frac{1}{N+1}$ are defined to remove an irrelevant constant term. The vectors $\mathbf{v}_L$ have the components

$$[\mathbf{v}_L]_k = \boldsymbol{\lambda} \frac{\partial B}{\partial b'_k} \mathbf{t}_L^T$$

for $k = 1, \ldots, N^2$, where the derivative of B has all elements zero with the exception of

$$\left[\frac{\partial B}{\partial b'_k}\right]_{i,j} = \left[\frac{\partial B}{\partial b'_k}\right]_{N+1,N+1} = 1, \qquad \left[\frac{\partial B}{\partial b'_k}\right]_{i,N+1} = \left[\frac{\partial B}{\partial b'_k}\right]_{N+1,j} = -1$$

where $i = \left\lfloor \frac{k-1}{N} + 1 \right\rfloor$ and $j \equiv k-1 \pmod N$. The function P_ρ^{LB} defined in (2.42), written as a quadratic function on the coefficients of $\mathbf{b}'$, then reads

$$P_\rho^{LB} = f + 2\,\mathbf{q}\mathbf{b}'^T + \mathbf{b}' H\, \mathbf{b}'^T\,, \tag{2.62}$$

with

$$\mathbf{q} = \frac{1}{2}\sum_{k=1}^{N} g_k \mathbf{v}_k \qquad H = \sum_{k=1}^{N} h_k \mathbf{v}_k^T \mathbf{v}_k. \tag{2.63}$$

$N=2j$	L	$F(L,M)$ for $M=0,\dots,L$
2	2	$\left(\frac{18}{35},-\frac{24}{35},\frac{6}{35}\right)$
3	2	$\left(\frac{18}{35},-\frac{24}{35},\frac{6}{35}\right)$
	3	$\left(\frac{2}{3},-\frac{4}{7},-\frac{2}{7},\frac{4}{21}\right)$
4	3	$\left(\frac{100}{231},-\frac{50}{77},\frac{20}{77},-\frac{10}{231}\right)$
	4	$\left(\frac{250}{429},-\frac{90}{143},-\frac{20}{143},\frac{10}{39},-\frac{10}{143}\right)$
5	3	$\left(\frac{100}{231},-\frac{50}{77},\frac{20}{77},-\frac{10}{231}\right)$
	4	$\left(\frac{250}{429},-\frac{90}{143},-\frac{20}{143},\frac{10}{39},-\frac{10}{143}\right)$
	5	$\left(\frac{2}{3},-\frac{80}{143},-\frac{40}{143},\frac{20}{429},\frac{30}{143},-\frac{12}{143}\right)$

Table 2.4: Numerical values of $F(L,M)$ defined in (2.36) for several number of qubits and $N \geqslant L > N/2$.

We assumed in Section 2.3 that the eigenvalues h_L of the matrix H are non-negative. On the other hand, the vectors $\mathbf{v}_1,\dots,\mathbf{v}_L$ can be completed to form an orthogonal basis $\mathcal{V}=\{\mathbf{v}_k\}_{k=1}^{N^2}$. We now define the dual basis $\tilde{\mathcal{V}}=\{\tilde{\mathbf{v}}_k\}_{k=1}^{N^2}$ of $\mathcal{V}$ as the set of vectors satisfying

$$\tilde{\mathbf{v}}_k\mathbf{v}_l^T=\delta_{kl}.$$

We use this basis to define a new affine transformation $\mathbf{b}'=\mathbf{b}''-\tilde{H}\mathbf{q}^T$ with

$$\tilde{H}=\sum_{k=1}^{N}h_k^{-1}\tilde{\mathbf{v}}_k^T\tilde{\mathbf{v}}_k.$$

Now, P_ρ^{LB} written in terms of the new variables reads

$$P_\rho^{LB}=f+\mathbf{b}''H\mathbf{b}''^T-\mathbf{q}\tilde{H}\mathbf{q}^T=f+\mathbf{b}''H\mathbf{b}''^T-\frac{1}{4}\sum_{k=1}^{N}\frac{g_k^2}{h_k},$$

where we have used that $H\tilde{H}\mathbf{q}^T=\mathbf{q}^T$. The global minimum of P_ρ^{LB} is achieved for $\mathbf{b}''=\mathbf{0}$ because H is a non-negative matrix, which proves the result (2.49).

2.E Properties of $F(L,M)$

Here we present some inequalities associated with the function $F(L,M)$ defined in (2.36).

Proposition. *For $L=2j$ and $M=1$, we have*

$$F(L=2j,M=1)<0. \tag{2.64}$$

Proof. Writing $N=2j$, we have

$$\begin{aligned}F(N,1) &= 2\sum_{L=0}^{N}C_{N0N0}^{L0}C_{N1N-1}^{L0}=2\sum_{L=0}^{N}\left(C_{N0N0}^{L0}\right)^2\left(\frac{L(L+1)}{2N(N+1)}-1\right)\\ &< 2\sum_{L=0}^{N}\left(C_{N0N0}^{L0}\right)^2\left(\frac{N(N+1)}{2N(N+1)}-1\right)<0\end{aligned}$$

where we used an identity between the C^{L0}_{N0N0} and C^{L0}_{N1N-1} given in (7), p. 253 of [69]. □

Proposition. *For all* $M = 0, \ldots, L$,

$$F(L,1) \leqslant F(L,M) \quad \textit{and}\ F(L,1) < 0. \tag{2.65}$$

This inequality is a conjecture supported by the explicit evaluation of $F(L,M)$ for several (L,M)-values, as shown in Table 2.4 for $j \leq 5/2$. These inequalities become relevant for specifying the allowed domain of the x_L parameters restricted by (2.47)-(2.48). If we assume that (2.65) is true, then the inequality that gives the best upper bound on x_L for $L > j$ comes from $M = 1$

$$x_L \leqslant \frac{F(2j,1)}{F(L,1)} x_{2j},$$

where we have used (2.64) and the fact that $x_{2j} \geqslant 0$.

Chapter 3

Entanglement from phase-space distributions

As discussed in Chapter 2, the non-classicality of phase-space representations of spin systems and the entanglement of symmetric multiqubit states are closely related, though not fully equivalent. Nevertheless, a fundamental result states that a quantum state ρ is separable if and only if it admits a positive Glauber-Sudarshan P function. This establishes that phase-space distributions can indeed provide rigorous statements about entanglement [161, 17, 162, 163, 164]. Together with phase-space negativity and magic [143, 165], entanglement lies at the very heart of quantum physics and constitutes a key resource for quantum technologies [101]. Yet, detecting and quantifying entanglement is notoriously challenging, making the development of new theoretical methods and experimental protocols essential. Established approaches include entanglement witnesses [112], in particular around specific symmetric multiqubit states [166, 167], as well as criteria based on collective measurements [167] or PPT mixtures [168], which allow the detection of certain classes of entanglement. The purpose of this chapter is to explore the use of modern machine learning tools to estimate the entanglement of symmetric multiqubit states from partial information extracted from their phase-space representations.

More specifically, the focus will be on the geometric measure of entanglement (GME) of symmetric multiqubit states. The GME of a multiqubit state, whether pure or mixed, is an entanglement measure that quantifies its distance to the nearest separable state [169]. Intuitively, one might expect a state close to the set of separable states to be less entangled than a state far from it. The GME is therefore a quantitative measure of the degree of entanglement of a state, making it a significant quantity in the field of multipartite entanglement. However, it should be noted that, in contrast to the entanglement negativity for example, the calculation of the GME requires the exact knowledge of the state. This makes the GME a challenging quantity to be accessed experimentally, as it would necessitate a complete tomography of the state.

In order to render the GME an experimentally accessible quantity, we will exploit the direct relation between the GME of symmetric multiqubit pure states and the Husimi function. This is achieved through the moments of the Husimi function, otherwise known as Wehrl moments, which contain partial information about the state. It is shown that the GME of any symmetric multiqubit pure state can be predicted based on the ratio of successive Wehrl moments, utilising artificial neural networks (ANNs). The method proves to nicely scale with the number of qubits and show resilience to measurement errors and noise. Finally, it is demonstrated that these moments are accessible through

experimental means by employing spherical designs, thus establishing this work as a potential tool in the experimental estimation of entanglement.

This chapter is organised as follows. In Section 3.1, we define the GME, the Wehrl moments and their relations to each other for pure symmetric multiqubit states. We also explain how the GME of pure and mixed symmetric multiqubit states can be efficiently estimated numerically. In Section 3.2, we succinctly explain how ANNs are defined and how they can be trained through deep learning techniques. In Section 3.3, we present how we generate the datasets of GME and Wehrl moments used throughout this work to train our ANNs. In Section 3.4, we introduce two different approaches to estimate the GME of the dataset: a first one based on the two highest known successive Wehrl moments and a second one based on a trained ANN. We then compare and analyse our results. In Section 3.5, we propose a protocol for experimentally determining Wehrl moments. It is based on the measurement of a set of multiqubit observables whose number scales only quadratically with the number of qubits. We then conclude and present perspectives of our work. Finally, this chapter ends with a series of technical appendices with additional information on the training of our ANNs, their efficacy for different symmetric multiqubit states than those considered in the main text and their robustness against noise impacting the Wehrl moments values.

3.1 Geometric measure of entanglement and Wehrl moments

3.1.1 Geometric measure of entanglement

We introduced, in Chapter 1, the GME of N qubit symmetric states as [120, 121]

$$E_G\left(|\psi\rangle\right) = 1 - \max_{|\phi\rangle} \left|\left\langle \phi^{\otimes N} \middle| \psi \right\rangle\right|^2, \tag{3.1}$$

where the maximisation is performed over the single-qubit separable state $|\phi\rangle$. This measure of entanglement quantifies the distance between the state $|\psi\rangle$ and the nearest separable state. The GME has an operational interpretation, as states with high GME are difficult to distinguish by local operations [170]. It has been used to prove that, in measurement-based quantum computation, more entanglement does not necessarily mean more computational power. In fact, certain highly entangled states can be less useful than states with less entanglement [135, 171]. The GME was also employed to study quantum phase transitions, demonstrating that it exhibits non-analytic behavior at critical points in quantum spin chains [172, 173]. This behavior highlights the effectiveness of the GME as a diagnostic tool for identifying quantum criticality in many-body systems.

Using the isomorphism between the set of N-qubit symmetric states and the set of spin $j = \frac{N}{2}$ states, we can identify any multiqubit symmetric separable state $|\Omega\rangle$ with its corresponding coherent spin state $|\theta, \varphi\rangle$. We are thus left with the problem of finding the maximum of the Husimi function Q of $|\psi\rangle$ on the sphere $\mathcal{S}^2$, that is

$$\max_{|\Omega\rangle} \left|\langle \Omega| \psi\rangle\right|^2 = \max_{\substack{\theta\in[0,\pi] \\ \varphi\in[0,2\pi[}} \left|\langle \theta, \varphi| \psi\rangle\right|^2 = \max_{\substack{\theta\in[0,\pi] \\ \varphi\in[0,2\pi[}} Q_{|\psi\rangle}\left(\theta, \varphi\right).$$

This is an important relation as it means that the GME of any symmetric multiqubit

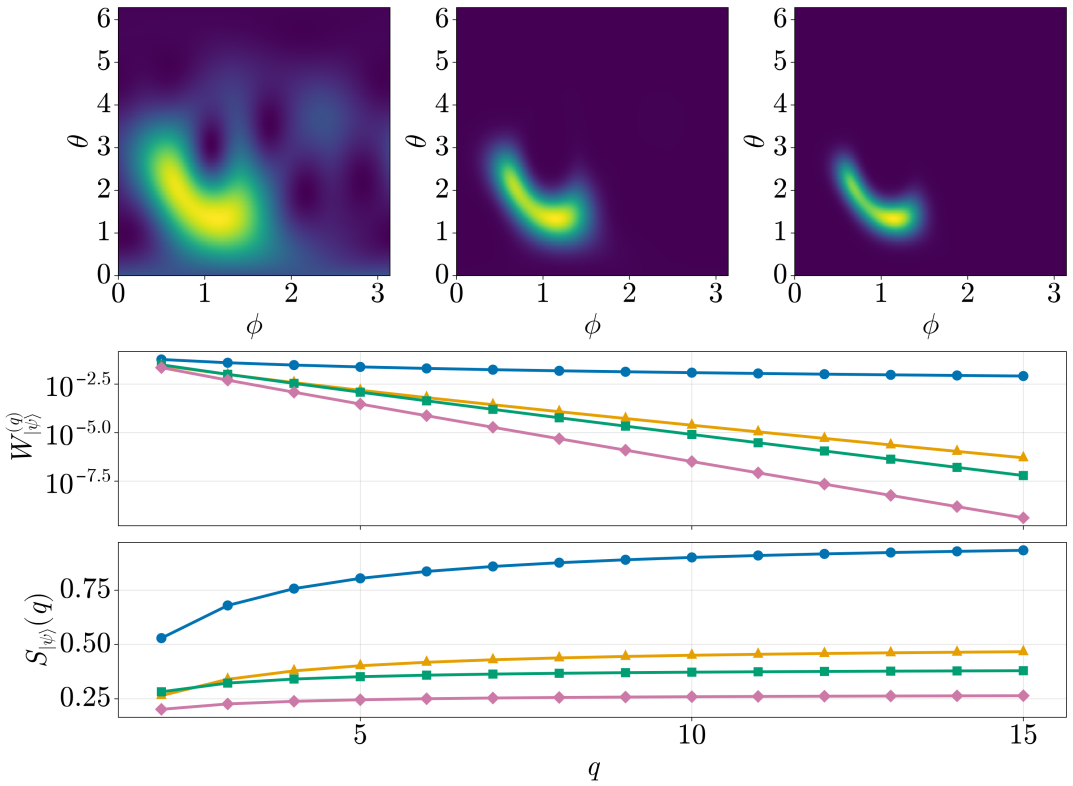

Figure 3.1: Top : Husimi function to the power $q = 1$, 4 and 8 (from left to right) of a random symmetric state of $N = 8$ qubits (the color scale is different in each panel). Middle and bottom : Wehrl moments $W^{(q)}_{|\psi\rangle}$ and their ratios $S_{|\psi\rangle}(q)$ for the states $\left|D^N_N\right\rangle$ (in blue), GHZ (in orange), W (in green) and $|D^{N/2}_N\rangle$ (in pink) for $N = 8$.

state can be related directly to the Husimi function of its corresponding spin state as

$$E_G\left(|\psi\rangle\right) = 1 - \max_{\substack{\theta\in[0,\pi]\\ \varphi\in[0,2\pi[}} Q_{|\psi\rangle}\left(\theta,\varphi\right). \tag{3.2}$$

Under experimental conditions, the quantum state of a system is never perfectly pure due to the interaction of the system with its environment, resulting for example in depolarisation. It is therefore important to address the case of mixed states as well. For a mixed state ρ, the GME can be generalised based on the convex roof construction (see Section 1.3)

$$E_G\left(\rho\right) = \min_{\{p_i,|\psi_i\rangle\}} \sum_i p_i E_G\left(|\psi_i\rangle\right) \tag{3.3}$$

where the minimum is taken over all pure state decompositions $\{p_i, |\psi_i\rangle\}$ of ρ, i.e. $\rho = \sum_i p_i |\psi_i\rangle\langle\psi_i|$. In [124], it was shown that this definition is equivalent to another definition based on the distance of ρ to the convex set $\mathcal{S}$ of separable mixed states

$$E_G(\rho) = 1 - \max_{\sigma_{\text{sep}}\in\mathcal{S}} F\left(\rho,\sigma_{\text{sep}}\right). \tag{3.4}$$

We will explain in Subsection 3.1.4 how the two definitions (3.3) and (3.4) can be used to numerically compute the GME of mixed states.

3.1.2 Wehrl moments

From an experimental perspective, the estimation of the GME necessitates full state tomography, a process that can prove to be fastidious as it requires numerous measurements. Hence, it would be interesting to be able to estimate the GME of any state from only partial information of it. To do so, we define the Wehrl moments $W^{(q)}_{|\psi\rangle}$ of integer order q

$$W^{(q)}_{|\psi\rangle} = \frac{1}{4\pi}\int_{S^2} \left(Q_{|\psi\rangle}(\Omega)\right)^q d\Omega \tag{3.5}$$

which are SU(2) invariant and directly related to the Rényi-Wehrl entropy $\mathcal{S}^{(q)}_{|\psi\rangle} = 1/(1-q)\log W^{(q)}_{|\psi\rangle}$ [174]. The Wehrl moments have already been used as a measure of localisation in phase space [174, 175], in detection of phase transitions in different materials [176, 177] and, specifically for $q = 2$, as a measure of complexity of quantum states [178]. Indeed, the idea is that the Husimi function of a delocalised state takes smaller values in phase space than a localised state. Therefore, the effect of raising the Husimi function up to a certain power $q > 1$ will have a greater impact on a delocalised state, since Q is normalised, and the value of its Wehrl moment will be smaller than that of a localised state. The top panel of Figure 3.1 shows the effect of raising the Husimi function of a random symmetric state of $N = 8$ qubits up to $q = 1$, 4 and 8.

A tight upper bound for Wehrl moments of order $q > 1$ that is valid for any state is given by [174, 179]

$$W^{(q)}_{|\psi\rangle} \leqslant \frac{1}{Nq+1},$$

where the equality holds only for coherent states which are the most localised states [180]. At the middle of Figure 3.1, we plot the Wehrl moments of several symmetric states of $N = 8$ qubits. It appears that the Wehrl moments of the coherent and most localised state $\left|D^N_N\right\rangle$ are greater than for the entangled states GHZ, W and $|D^{N/2}_N\rangle$.

An explicit expression for the Wehrl moments of symmetric multiqubit states in terms of Dicke coefficients d_k has been given by Gnutzmann and Życzkowski [174], and reads in our notations

$$W^{(q)}_{|\psi\rangle} = \sum_{m=0}^{qN} \frac{1}{qN+1}\binom{qN}{m}^{-1} \left| \sum_{i_1,\ldots,i_q} \prod_{k=1}^{q} \sqrt{\binom{N}{i_k}}\, d_{i_k} \right|^2,$$

where the inner sum goes from 0 to N for each i_k with the restriction $\sum_{k=1}^{q} i_k = m$. This relation is exact and allows us to calculate the Wehrl moments when we know the expansion of a symmetric state in the Dicke basis.

3.1.3 Bounds on the GME from Wehrl moments

The introduction of the Wehrl moments for the estimation of the GME is motivated by the fact that the maximum of the Husimi function can be bounded with the help of successive Wehrl moments. For any integers $q > p > 1$ and any state $|\psi\rangle$, it holds that

$$\max_{\substack{\theta\in[0,\pi]\\ \varphi\in[0,2\pi[}} Q_{|\psi\rangle}(\theta,\varphi) \geqslant \frac{W^{(q+1)}_{|\psi\rangle}}{W^{(q)}_{|\psi\rangle}} \geqslant \frac{W^{(p+1)}_{|\psi\rangle}}{W^{(p)}_{|\psi\rangle}}. \tag{3.6}$$

This is a consequence of the integral Hölder's inequality [181],

$$\|fg\|_1 \leqslant \|f\|_r \|g\|_m,$$

where $\|f\|_r = \left(\int_X |f|^r d\mu\right)^{\frac{1}{r}}$, $r, m \in [1, \infty]$ with $1/r + 1/m = 1$, and f and g are functions defined on X. By taking $f = Q_{|\psi\rangle}$, $g = Q^q_{|\psi\rangle}$, $X = S^2$, $d\mu = d\Omega/4\pi$, $r = \infty$ and $m = 1$, we readily get (3.6) by noting that $\|f\|_\infty = \max_X f$ where $\|\cdot\|_\infty$ denotes the spectral norm. Equation (3.6) provides us with a chain of better and better upper bounds for the GME as q and p increase. In fact, defining the sequence (for integer $q > 1$)

$$S_{|\psi\rangle}(q) = \frac{W^{(q)}_{|\psi\rangle}}{W^{(q-1)}_{|\psi\rangle}}, \tag{3.7}$$

we have that

$$E_G\left(|\psi\rangle\right) \leqslant 1 - S_{|\psi\rangle}(q) \quad \forall q > 1, \tag{3.8}$$

and

$$E_G\left(|\psi\rangle\right) = 1 - \max_{\substack{\theta\in[0,\pi] \\ \varphi\in[0,2\pi[}} Q_{|\psi\rangle}\left(\theta, \varphi\right) = 1 - \lim_{q\to\infty} S_{|\psi\rangle}(q). \tag{3.9}$$

Equation (3.9) shows that the GME can be extracted from the limit of the sequence $S_{|\psi\rangle}(q)$ of ratios of successive Wehrl moments. The bottom panel of Figure 3.1 shows the ratios of Wehrl moments of different symmetric states for $N = 8$ qubits. For symmetric Dicke states $\left|D_N^{(k)}\right\rangle$, the Wehrl moments are explicitly given by

$$W^{(q)}_{|D_N^{(k)}\rangle} = \frac{\left(C_N^k\right)^q}{(Nq+1)C_{Nq}^{kq}}.$$

This then leads to

$$1 - E_G\left(\left|D_N^{(k)}\right\rangle\right) = \lim_{q\to\infty} S_{|D_N^{(k)}\rangle}\left(q\right) = \begin{cases} C_N^k \left(\frac{k}{N}\right)^k \left(\frac{N-k}{N}\right)^{N-k} & 0 < k < N-1, \\ 1 & k = 0, N. \end{cases}$$

in agreement with known results for the GME of Dicke states [120].

While it is now clear from (3.8) that there is a direct link between the GME and the ratios of Wehrl moments, it would be interesting to study how precisely we can estimate the GME from the ratios of the lower Wehrl moments. To this end, we will turn our interest into ANNs which are able to learn the relation between different quantities. To train these ANNs we however need to generate different data sets containing the GME and the Wehrl moments of random states which represent the large diversity of entanglement that can arise in multiqubit symmetric states [182]. The first step is to compute the GME of pure and mixed symmetric multiqubit states.

3.1.4 Computation of the GME

In this subsection, we present different algorithms to compute the GME of pure and mixed states. For the reader interested in the results of the ANNs training, they can directly go to Section 3.2.

3.1.4.1 Pure states

There are two strategies to compute the GME of a pure state depending on whether the state is considered to be a multiqubit symmetric state or a spin state. In the latter case, the GME of a symmetric multiqubit state $|\psi\rangle$ can be computed by finding the maximum of the Husimi function of its associated spin state with the help of (3.2). As a coherent state in the standard angular momentum basis is given by

$$|\theta,\varphi\rangle = \sum_{m=-j}^{j} \sqrt{C_{2j}^{j+m}} \left(\cos\frac{\theta}{2}\right)^{j+m} \left(\sin\frac{\theta}{2}\right)^{j-m} e^{-i(j-m)\varphi}|j,m\rangle,$$

finding the maximum of the Husimi function can be achieved by optimising the two angles (θ,φ) which define a coherent state. This is a highly non-linear optimisation which can be handled by any non-linear solver such as Ipopt [183]. While this method can offer satisfactory results, it is not optimal and better results can be obtained, in terms of accuracy and computation speed, by considering the system as an ensemble of qubits in the symmetric subspace instead.

In this case, we can adapt to the symmetric subspace an algorithm first presented in [184]. Consider a multiqubit state $|\psi\rangle$ in the full Hilbert space of N qubits for which we want to find the closest separable state. We start from a random separable state $|\Phi_0\rangle = \left|\phi_1^{(0)} \otimes \phi_2^{(0)} \cdots \otimes \phi_N^{(0)}\right\rangle$ and, by tracing out the first qubit, compute the unnormalised single-qubit state

$$|\tilde{\psi}\rangle = \left\langle \phi_2^{(0)} \cdots \otimes \phi_N^{(0)} \middle| \psi \right\rangle.$$

To maximise the overlap between $|\psi\rangle$ and $|\Phi_0\rangle$, we then update the first qubit state $\left|\phi_1^{(0)}\right\rangle$ with

$$\left|\phi_1^{(0)}\right\rangle \to \left|\phi_1^{(1)}\right\rangle = \frac{|\tilde{\psi}\rangle}{\sqrt{\langle\tilde{\psi}|\tilde{\psi}\rangle}}.$$

As $\left|\phi_1^{(1)}\right\rangle$ is a pure single-qubit state, it is guaranteed that $\left|\phi_1^{(1)}\right\rangle$ is always separable. The procedure can then be repeated by tracing out only the second qubit and then the third qubit, and so on. After n iterations, we get a separable state $|\Phi_n\rangle = \left|\phi_1^{(n)} \otimes \phi_2^{(n)} \cdots \otimes \phi_N^{(n)}\right\rangle$ closer to the state $|\psi\rangle$ [184]. It is demonstrated that this algorithm allows to find a generalised Schmidt decomposition of the multipartite state $|\psi\rangle$ with arbitrary precision. However, this decomposition is not unique (except for bipartite system) and the final quantity $1 - \left|\left\langle \phi_1^{(n)} \otimes \phi_2^{(n)} \cdots \otimes \phi_N^{(n)} \middle| \psi \right\rangle\right|^2$ does not necessarily correspond to the GME. This is expected as the estimation of the GME is a non-linear optimisation problem. Hence, it may be necessary to run the algorithm several times with different initial state $|\Phi_0\rangle$ to find the GME of $|\psi\rangle$. Interestingly, for symmetric multiqubit states, this algorithm can be modified such that only symmetric states are used, greatly reducing the required numerical resources. Indeed, a symmetric state $|\psi\rangle$ can be split across a bipartition $t|N-t$ as [73]

$$|\psi\rangle = \sum_{q=0}^{t} \left|D_t^{(q)}\right\rangle \otimes \left|v_t^{(q)}\right\rangle \tag{3.10}$$

where

$$\left|v_t^{(q)}\right\rangle = \sum_{k=q}^{N-t+q} \sqrt{\frac{C_t^q C_{N-t}^{k-q}}{C_N^k}} d_k \left|D_{N-t}^{(k-q)}\right\rangle .$$

We can then start from an N-qubit separable symmetric state $\left|\Omega^{(0)}\right\rangle = \left|\phi^{(0)} \otimes \phi^{(0)} \cdots \otimes \phi^{(0)}\right\rangle$ and, using (3.10) for $t = 1$, compute the unnormalised single qubit state

$$\begin{aligned} |\tilde{\psi}\rangle &= \underbrace{\langle \phi^{(0)} \otimes \cdots \otimes \phi^{(0)}}_{N-1} |\psi\rangle \\ &= \sum_{q=0}^{1} \left\langle \phi^{(0)} \otimes \cdots \otimes \phi^{(0)} \right| \left|v_1^{(q)}\right\rangle \left|D_1^{(q)}\right\rangle \end{aligned} \tag{3.11}$$

Then, as we work in the symmetric subspace, we can update the entire separable state $|\Omega_0\rangle$ at once using

$$\left|\phi^{(0)}\right\rangle \to \left|\phi^{(1)}\right\rangle = \frac{|\tilde{\psi}\rangle}{\sqrt{\langle\tilde{\psi}|\tilde{\psi}\rangle}}$$

and we get $\left|\Omega^{(1)}\right\rangle = \left|\phi^{(1)} \otimes \phi^{(1)} \cdots \otimes \phi^{(1)}\right\rangle$. Starting over from (3.11) with this new state $\left|\Omega^{(1)}\right\rangle$, we can then compute an updated state $\left|\Omega^{(2)}\right\rangle$ and so forth. Again, for this algorithm to compute the GME of the symmetric state $|\psi\rangle$ with arbitrary precision, it must run multiple times with different initial state $|\Omega_0\rangle$. While this algorithm was designed to compute the GME of multiqubit pure states, it can also serve to compute the maximal value of the Husimi function of a pure spin state through (3.2).

3.1.4.2 Mixed states

The geometric measure of entanglement of mixed states can be numerically estimated based on its convex roof construction (3.3) or its definition based on the fidelity (3.4). In the first case, the algorithm for the estimation of the GME of pure states can be used with the results from [185]. In the second case, an algorithm for multiqubit states in the full Hilbert space is presented in [184].

We propose here another algorithm to compute the GME exclusively for a symmetric multiqubit/spin system. The advantage of these systems is that a closed-form of separable states is known. Note that an other method to circumvent the problem of separable states characterisation is to use the ensemble of PPT states, which gives a lower bound on the GME [186]. As the ensemble of separable states is convex, by the Caratheodory's theorem, any N-qubit symmetric separable state can always be expressed in the following form

$$\rho_{\text{sep}} = \sum_{i=1}^{(N+1)^2} p_i \left|\theta_i, \varphi_i\right\rangle \left\langle\theta_i, \varphi_i\right|$$

where $p_i \geq 0$, $\sum_{i=1}^{(N+1)^2} p_i = 1$ and the $|\theta_i, \varphi_i\rangle$ are coherent pure states. Hence, in order to find the GME of a multiqubit symmetric state ρ, we need to solve the following optimisation problem

$$\text{Find} \quad \max_{\{p_i\},\{\theta_i,\varphi_i\}} F\left(\rho, \rho_{\text{sep}}\right) \tag{3.12}$$

$$\begin{aligned} \text{subject to} \quad & p_i \geq 0 \\ & \sum_{i=1}^{(N+1)^2} p_i = 1 \\ & |\theta_i, \phi_i\rangle \in \mathcal{S}_{\mathrm{C}} \end{aligned}$$

where $\mathcal{S}_{\mathrm{C}}$ is the set of pure coherent states. Consequently, to find the GME of a state, we need to solve the optimisation problem (3.12) involving $3(N+1)^2$ parameters. Here, we propose to use the Nelder-Mead non-linear optimisation algorithm to obtain the optimal angles $\{\theta_i, \varphi_i\}$. For the weights $\{p_i\}$, a more efficient algorithm can be used. Indeed, it was showed that the fidelity $F(\rho, \sigma)$ between two arbitrary states ρ and σ is equal to the maximal value obtained from the following SDP problem [187, 188]

$$\text{Find} \quad \max_X \left[\frac{1}{2} \mathrm{Tr}\left(X\right) + \frac{1}{2} \mathrm{Tr}\left(X^\dagger\right) \right]$$

$$\text{subject to} \begin{pmatrix} \rho & X \\ X^\dagger & \sigma \end{pmatrix} \geq 0$$

where X is a matrix with complex entries.

Based on this preliminary explanation, the algorithm we propose is the following:

1. Randomly initialise the $(N+1)^2$ weights p_i and the $2\,(N+1)^2$ angles (θ_i, φ_i).

2. For these angles, optimise the weights with the following SDP problem

$$\text{Find} \quad \max_{\{p_i\}, X} \left[\frac{1}{2} \mathrm{Tr}\left(X\right) + \frac{1}{2} \mathrm{Tr}\left(X^\dagger\right) \right]$$

$$\begin{aligned} \text{subject to} & \begin{pmatrix} \rho & X \\ X^\dagger & \rho_{\text{sep}} \end{pmatrix} \geq 0 \\ \rho_{\text{sep}} = & \sum_{i=1}^{(N+1)^2} p_i \, |\theta_i, \varphi_i\rangle \langle \theta_i, \varphi_i| \end{aligned}$$

3. Using the previously found weights, optimise the fidelity $F\left(\rho, \rho_{\text{sep}}\right)$ with the Nelder-Mead algorithm using the angles $\{\theta_i, \varphi_i\}$ as the optimisation parameters.

4. Repeat steps 2 and 3 until the difference on the fidelities obtained from two consecutive optimisations is lower than a given value ϵ.

We note that, in addition to the value of the GME, this algorithm also gives the decomposition of the nearest separable mixed state into a weighted sum of coherent pure states. If ρ is separable, then the algorithm directly gives the decomposition of the mixed state into pure states.

To benchmark the algorithm, we computed the GME of the depolarized GHZ states for $N = 2, 3, 4, 5$ and 6. Starting from the GHZ state density matrix

$$\rho_{GHZ} = |\mathrm{GHZ}\rangle \langle \mathrm{GHZ}|$$

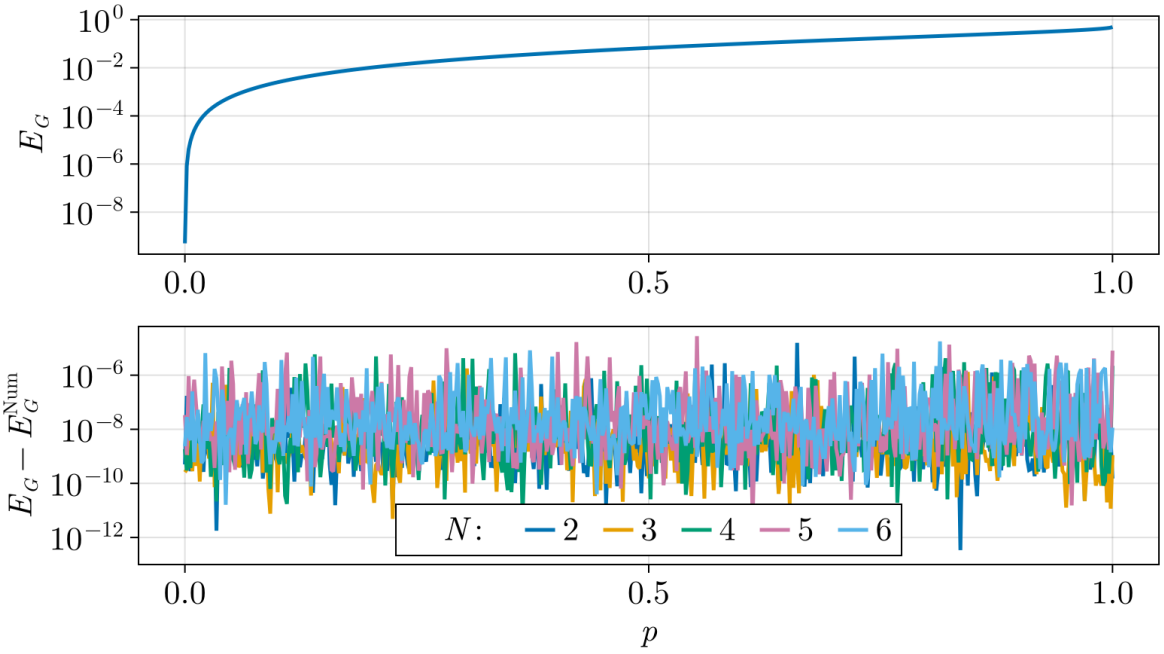

Figure 3.2: Top : GME of the depolarised GHZ state given by (3.13). Bottom : Difference between the GME obtained numerically E_G^{Num} and the analytical value (3.13) for $N = 2, 3, 4, 5$ and 6.

we then obtain the symmetric depolarised state by removing the diagonal elements in the Dicke basis

$$\rho_{ij}^{(p)} = \begin{cases} \rho_{ij} & i = j \\ p\rho_{ij} & i \neq j \end{cases}$$

with $p \in [0, 1]$. It is known that the GME of $\rho^{(p)}$ for any number of qubits N and all $p \in [0, 1]$ is given by [186]

$$E_G\left(\rho^{(p)}\right) = \frac{1 - \sqrt{1 - p^2}}{2}. \tag{3.13}$$

We show in Figure 3.2 the difference between the GME obtained numerically and the analytical GME given by (3.13).

3.2 Artificial Neural Networks

In recent years, with the rapid increase in computer processing power, the field of machine learning has expanded rapidly. One of its subfield is Artificial Neural Networks (ANNs) which has become one of the main area of artificial intelligence and have gained momentum in quantum physics [189, 190]. In the context of quantum state tomography, they have been used to reconstruct density matrices from measurement results [191, 192] and to find an optimal measurement basis [193]. In quantum optics, artificial neural networks have been trained to detect multimode Wigner negativity [194]. Deep reinforcement learning and recurrent neural networks have also been exploited for quantum information theory purposes, such as quantum state preparation [195] and quantum error-correction [196, 197].

In the context of entanglement theory, ANNs have been used to quantify the amount of entanglement in multipartite quantum systems [198, 199] and to classify the entanglement in pure states [200] and mixed states [201]. In [198], the authors trained complex-valued ANNs to predict the GME of symmetric states. To do so, they reformulated the GME computational problem as the search for the best rank-one tensor approximation of complex tensors, for which they used ANNs. Other authors have used deep learning methods to compute the concurrence and mutual information from an incomplete tomography of mixed qubit states [199]. In quantum many-body physics, convolutional neural networks were employed to compute e.g. the entanglement entropy from the variance on the number of particles in an electron chain [202].

Fundamentally, an ANN is a non-linear regression function that updates its parameters during a learning phase in order to mimic as closely as possible the real (unknown) function that connects the data points of interest. It therefore seems perfectly suited to our objective of estimating the GME of multiqubit symmetric states on the basis of their first Wehrl moments. In this subsection, we briefly explain how ANNs and deep learning work.

3.2.1 Structure of an artificial neural network

The smallest unit of an ANN is a neuron which is characterised by a vector of n weights $\boldsymbol{w} = (w_1, w_2, \ldots, w_n)$ and a bias b. The neuron receives n real values $\boldsymbol{x} = (x_1, x_2, \ldots, x_n)$ and outputs a single real value

$$z\left(\boldsymbol{w}, b\right) = \boldsymbol{x} \cdot \boldsymbol{w}^T + b = \sum_{i=0}^{n} w_i x_i + b$$

as represented in Figure 3.3. As it stands, the neuron can only represent a linear function between the inputs and the output. In order to add some non-linearities, one adds a non-linear function $f : z \to f(z)$, known as the activation function. The output of the neuron is then

$$y\left(\boldsymbol{w}, b\right) \quad = \quad f\left(\boldsymbol{x} \cdot \boldsymbol{w}^T + b\right). \tag{3.14}$$

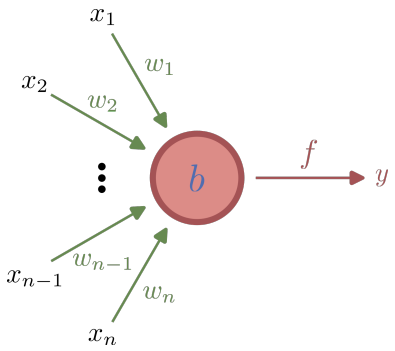

Figure 3.3: Representation of a single neuron.

The activation function is arbitrary and is often taken as a simple function which can be efficiently computed. Here, we will use the Rectified Linear Unit (ReLU) function defined by

$$\mathrm{ReLU}(x) \quad = \quad \begin{cases} x & x \geq 0 \\ 0 & x < 0 \end{cases}$$

and shown in Figure 3.4.

With this elementary brick, a neural network is built as a set of layers, indexed by l, containing a given number n_l of single neurons (see Figure 3.8 which depicts the ANN structure used for the estimation of the GME). From this construction, the i-th neuron of the l-th layer outputs a real value

$y_i^{(l)}$ based on its inputs, these inputs being themselves the outputs of the neurons in the previous layer. The output of a neuron in the first layer $y_i^{(0)}$ is simply the data which we feed to the neural network, in our case the Wehrl moment ratios $S^{(q)}_{|\psi\rangle}$. By feeding the nodes of one layer with the values of the previous layer, the data flows through the network and finally the last layer contains the value of the regression, in our case an estimate of the GME. Initially, the weights and biases are chosen at random but the training process, known as deep learning, updates them to increase the accuracy of the ANN's predictions.

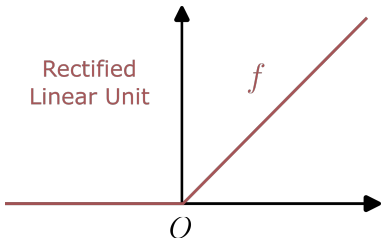

Figure 3.4: Graph of the ReLU function.

The predominance of neural networks comes in part from the fact that nearly all operations in ANNs can be put in the form of matrix multiplications. Hence, the processing power of GPUs (graphics processing units) can be leveraged to reduce the computation time of the learning stage. To see this, we point out that each neuron of the l-th layer of size n_l will receive n_{l-1} inputs from the previous layer. Hence, the parameters of a layer can be expressed in the form of a matrix of weights

$$W^{(l)} = \begin{pmatrix} w_{11} & w_{12} & \dots & w_{1n_l} \\ w_{21} & w_{22} & \dots & w_{2n_l} \\ \vdots & \vdots & \ddots & \vdots \\ w_{n_{l-1}1} & w_{n_{l-1}2} & \dots & w_{n_{l-1}n_l} \end{pmatrix}$$

where w_{ij} is the i-th weigth of the j-th neuron, and a vector of biases

$$\boldsymbol{b}^{(l)} = (b_1, b_2 \dots, b_{n_l})$$

where b_i is the bias of the i-th neuron. In this form, we can gather the output of the neurons of the layer in a vector

$$\boldsymbol{y}^{(l)} = f^{(l)} \cdot \left(\boldsymbol{z}^{(l)}\right) = f^{(l)} \cdot \left(\boldsymbol{y}^{(l-1)} W^{(l)} + \boldsymbol{b}^{(l)}\right)$$

where the notation $f \cdot (\mathbf{z})$ means that the function f is applied on each element of $\mathbf{z}$. Initially, the weights $W^{(l)}$ and the biases $\boldsymbol{b}^{(l)}$ are randomly generated. To get an ANN that makes useful predictions, we need to train it. This means updating the weights and biases so that the non-linear function representing the ANN closely resembles the one that actually relates the inputs of the ANN and the desired output. The way this is done is known as deep learning.

3.2.2 Deep Learning

There exists different ways to train a neural network. Here, as we are able to compute the Wehrl moments and the GME of any state, we will use supervised learning. In supervised learning, we train an ANN from a data set for which we know the correct output vector $\hat{\boldsymbol{y}}$ such that we can easily inform the neural network if it improves or not during the training process. Two other emblematic learning methods are unsupervised learning and reinforcement learning. Regardless the method used, we must define a loss function which

serves as a comparison between the expected values the neural network should output and the actual value that it outputs.

For our task of predicting the GME, we simply use the mean squared error cost function

$$\begin{aligned}\epsilon\left(\hat{\boldsymbol{y}}, \boldsymbol{y}^{(D)}\right) &= \frac{1}{n_D}\sum_{k=1}^{n_D}\left(\hat{y}_k - y_k^{(D)}\right)^2 \\ &\equiv \left(E_G(\psi) - E_G^{\text{pred}}(\psi)\right)^2\end{aligned}$$

where D is the number of layers in the network (also called the depth), n_D is the number of neurons of the last layer and E_G^{pred} is the GME of the state $|\psi\rangle$ as predicted by the ANN. Clearly, we want to update the parameters of the neural network to get the minimal possible value of ϵ. Based on this loss function, we can update the weights and biases of the ANN with the algorithm of gradient descent. To explain the algorithm, let us consider the derivative of the loss function w.r.t. a given weight $\partial\epsilon/\partial w_{ij}$ (a similar reasoning of course holds for the biases). In Figure 3.5, we see that by following the opposite of the derivative, we can update the weight in order to obtain a smaller value for the loss function. Using the chain rule, the derivative of ϵ w.r.t. a weight in the l-th layer is

$$\frac{\partial\epsilon}{\partial w_{ij}^{(l)}} = 2\sum_{k=1}^{n_D}\left(\hat{y}_k - y_k^{(D)}\right)\left.\frac{df^{(D)}}{dz}\right|_{z=z_k^{(D)}}\frac{\partial z_k^{(D)}}{\partial w_{ij}^{(l)}} \tag{3.15}$$

where the last factor needs to be expanded. For any $l' > l$, we have

$$\frac{\partial z_k^{(l')}}{\partial w_{ij}^{(l)}} = \sum_{m=1}^{n_{l'-1}} w_{km}^{(l')}\left.\frac{df^{(l'-1)}}{dz}\right|_{z=z_m^{(l'-1)}}\frac{\partial z_m^{(l'-1)}}{\partial w_{ij}^{(l)}}$$

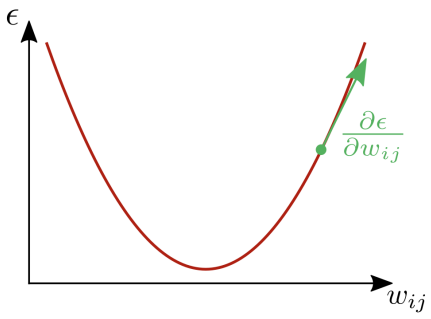

Figure 3.5: Derivative of the loss function with respect to a weight.

and we see that the derivative of $z_k^{(l)}$ depends on the one of $z_k^{(l-1)}$. Consequently, applying the chain rule successively allows us to go through the consecutive neural network layers to finally get the l-th layer containing the neuron with the weight $w_{ij}^{(l)}$. The derivative of the output of this neuron then reads

$$\frac{\partial z_m^{(l)}}{\partial w_{ij}^{(l)}} = y_j^{(l-1)}\delta_{im}.$$

Hence, we can get a formula for which, by passing the input data in the ANN to get all the $\boldsymbol{y}^{(l)}$ values, we can compute the derivative of ϵ w.r.t. any weight of the ANN. Once it is done, we update the weight by using gradient descent

$$w_{ij}^{(l)} = w_{ij}^{(l)} - \alpha\frac{\partial\epsilon}{\partial w_{ij}^{(l)}}$$

where $\alpha > 0$ is a quantity called the learning rate. This value must not be too high, otherwise the update will overshoot the minimum of ϵ. But it should not be too small for the algorithm to converge in a reasonable time. In fact, there exists a whole subdomain of ANNs which studies how the learning rate should be updated at each update of the parameters, but we will not dive into this. For completeness, we specify that we use in the following the ADAM algorithm for the update of the learning rate [203].

The ANN we use here is a Multilayer Perceptron (MLP) neural network for which a neuron is connected to all neurons of the next layer and an output is given by (3.14). However, there exists a lot of different network architectures. Examples are the Convolutional Neural Networks (CNNs), often used in image analysis, Recurrent Neural Networks (RNNs) for time series and the attention unit used in Large Language Models (LLMs).

3.3 Data sets and performance metrics

As our goal is to determine the best estimate of the GME of a state from its first few Wehrl moments, we need a set of representative pure and mixed symmetric multiqubit states on which to test our methods and calculate some metrics to compare their respective performances (see Section 3.4). This section aims to explain how we generated these representative multiqubit states and what our performance measures are.

3.3.1 Generation of the data sets

3.3.1.1 Pure states

First, we need a data set of pure symmetric multiqubit states from which we compute their first Wehrl moments and their GME. This way, we can input the ratio of the Wehrl moments in the ANN, retrieve the prediction $E_G^{\text{pred}}(\psi)$ and compare it to the true GME $E_G(\psi)$ as required in (3.15) to apply gradient descent. In fact, we need two data sets, one for the training of the neural network and a second to test it. The reason is that ANNs sometimes begin to specialise too much on the data set on which they are trained. At this point, they do not learn anymore but simply remember to associate a given value to another one with no real significance. This phenomenon is called overfitting. To prevent it we need a second data set on which we test the ANN during its training to prevent that it overfits on the training data set. So, if the ANN starts to overfit, the loss function will decrease over the training data set but will increase rapidly over the test data set.

Another point to take care of is to use a large enough variety of symmetric states to generate the data sets. If the set of states is too restrictive, the ANN will make excellent predictions on these but will be unable to generalise to other kind of symmetric states. Here, we generate three different subsets of states. Subset 1 is made of symmetric states with randomly and uniformly distributed Majorana points [71] on the Bloch sphere. Subset 2 is made of random states for which *degenerated* Majorana points are uniformly distributed on the Bloch sphere, with random degeneracy tuples drawn uniformly from all partitions of N. Finally, the subset 3 is made of superpositions of GHZ and Dicke states, i.e.

$$|\psi(\alpha, k)\rangle = \mathcal{N}\left[\alpha\ |\text{GHZ}\rangle + (1-\alpha)\ |D_N^{(k)}\rangle\right]$$

with random real number $\alpha \in [0, 1]$ and random integer k between 0 and N. For each number of qubits N, 20000 states are randomly drawn for each subset. All these states

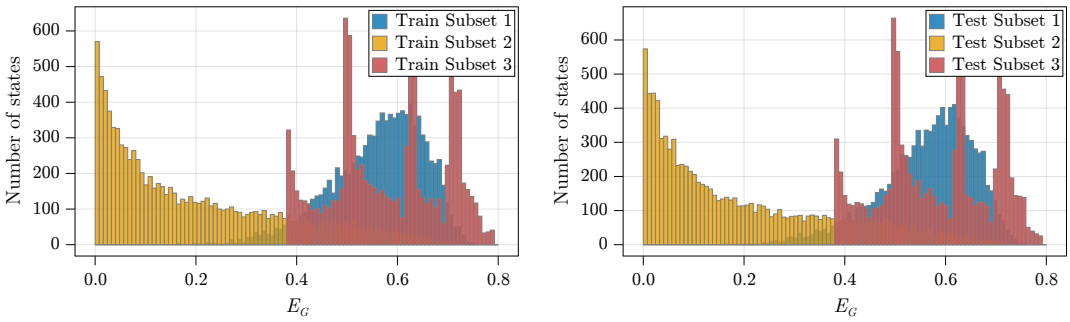

Figure 3.6: Frequency distributions of GME of the training set (left) and test set (right) for $N = 8$ qubits, where the three subsets of states are represented by different colors. The number of states in the data sets is large enough to generate a similar GME distribution for the training and test sets. For $N = 8$, the maximal GME is $E_G \approx 0.816$ [204], while (1.38) gives the upper bound $E_G(|\psi\rangle) \leqslant 8/9 \approx 0.889$.

are then divided into two equally sized sets: one for training the ANN and the other for testing it. The Wehrl moments up to $q_{\max} = 8$ and the GME E_G are computed for all states.

Figure 3.6 shows the GME probability distribution of training states (left) and test states (right) for $N = 8$. We find that these three subsets have very different entanglement distributions and are therefore a good set of training and test data. In particular, subset 2 (yellow histograms) is mostly made up of weakly entangled states, while subset 3 (red histograms) contains a significant proportion of very highly entangled states.

3.3.1.2 Mixed states

In the case of mixed states, we will train ANNs on two different subsets separately. We do so because the training outcomes will exhibit significant differences between the two sets.

The first set is obtained by drawing 1000 pure random states $|\psi\rangle$ and mixed random states ρ and mixing them as follows

$$\rho = (1 - k) |\psi\rangle \langle\psi| + k\rho. \tag{3.16}$$

with $k = 0.05$. As the relation between the GME and the Husimi function (3.2) does not hold for mixed states, it is not expected that the Wehrl moments are able to predict the GME for states of any degree of mixedness. Consequently, this set encompasses states that are only marginally mixed but that are nevertheless typically obtained in experiments targeting pure states.

For the second set, we generate 1000 depolarised mixed states for each number of qubits $N \in \{2, 3, 4\}$. The mixed states were obtained by drawing pure random states $|\psi\rangle$ according to the Haar measure and mixing them with the MMS $\rho_0 = \mathbb{I}/(N + 1)$ as follows

$$\rho = (1 - k) |\psi\rangle \langle\psi| + k\rho_0, \tag{3.17}$$

where $k \in [0, 0.5]$ is a parameter quantifying the degree of depolarisation. It follows that this set, in contrast to the first one, is composed of states presenting very different degree of mixedness. The reason behind this choice will become evident upon the presentation of the results of the ANNs training.

3.3.2 Performance metrics

In order to quantify the precision of the estimation of the GME given by the ANNs, we first define the relative difference between the predicted GME and the actual GME as

$$\delta_i = \frac{E_G\left(|\psi_i\rangle\right) - E_G^{\text{pred}}\left(|\psi_i\rangle\right)}{E_G\left(|\psi_i\rangle\right)},$$

where $E_G^{\text{pred}}\left(|\psi_i\rangle\right)$ stands for the predicted GME of state $|\psi_i\rangle$ of the test dataset. Then, we define the mean absolute relative difference, hereafter called *mean relative error* (MRE)

$$\Delta = \frac{1}{M}\sum_{i=1}^{M}|\delta_i|, \tag{3.18}$$

where we sum over all states of the test dataset. As the distribution of the absolute relative difference $|\delta_i|$ is not Gaussian, the standard deviation is not a good estimate for error bars. Instead, we calculate a low error bar and a high error bar so as to include 68.2% of the $|\delta_i|$ distribution in the error bar and have 15.9% of the distribution below (above) the low (high) error bar, as would be the case for an interval of one standard deviation centered around the mean for a Gaussian distribution.

3.4 Estimation of the geometric measure of entanglement

In this section, we finally estimate the GME of the states of the test datasets presented previously based on the knowledge of their Wehrl moments from $q = 1, \ldots, q_{\max}$, expecting a better estimate of the GME as $q_{\max}$ increases. To give a first crude comparison point for pure states, we first compute an estimate of the GME of the test data set based on the ratio of the two highest known Wehrl moments, see (3.9). Then, we apply our trained ANNs to estimate the GME of the test data set for pure and mixed states. We are particularly interested in the performance of the ANNs as a function of the highest considered order $q_{\max}$ and of the number of qubits N.

3.4.1 Pure states

3.4.1.1 Ratios of Wehrl moments

As the ratios of successive Wehrl moments (3.7) converge to the maximum of the Husimi function when $q \to \infty$, a first estimate of the GME of the test states based on these ratios is given by

$$E_G^{\text{pred}}(|\psi\rangle) = 1 - S_{|\psi\rangle}\left(q_{\max}\right). \tag{3.19}$$

The predictive power of (3.19) is illustrated in Figure 3.7 for different maximal orders $q_{\max}$ and number of qubits N. As expected from the inequality (3.8), we observe that the estimate (3.19) is always larger than the actual value of the GME (left panels), which results in a positive relative difference (middle panels). As $q_{\max}$ increases, the estimate becomes better and better, with a decrease in mean relative error (MRE) as a function of $q_{\max}$ (top right panel). However, even with $q_{\max} = 8$, the MRE remains above 10%. The MRE increases slightly with N before stabilising quickly, as shown in the bottom right panel.

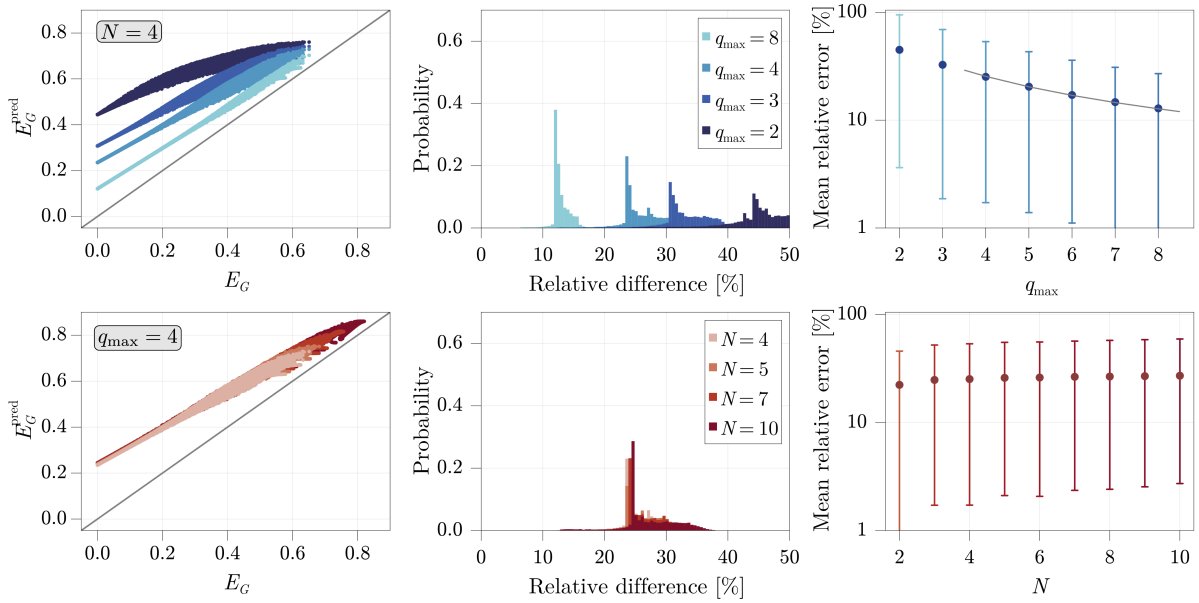

Figure 3.7: Predictions of E_G based directly on Wehrl moment ratios $S_{|\psi\rangle}(q_{\max}) = W_{|\psi\rangle}^{(q_{\max})}/W_{|\psi\rangle}^{(q_{\max}-1)}$ for $N = 4$ and different maximal orders $q_{\max}$ (top) and for $q_{\max} = 4$ and different number of qubits N (bottom). Left panels: Predicted value versus actual value of GME for all states of the test dataset. Middle panels: Probability to predict the GME with a certain relative difference. The bin size is 0.5%. Right panels: Mean relative error (**??**) as a function of $q_{\max}$ and N. The grey solid line in the top right panel shows a fit of equation $\Delta(q_{\max}) = A/q_{\max}$ with $A \approx 102$.

3.4.1.2 Artificial neural networks

We now want to train ANNs so that when we feed them with the finite sequence

$$\left\{S_{|\psi\rangle}(q) : q = 2, \ldots, q_{\max}\right\}$$

for some state $|\psi\rangle$, they output an estimate for $E_G(|\psi\rangle) = 1 - \lim_{q\to\infty} S_{|\psi\rangle}(q)$, as schematically represented in Figure 3.8. To be able to compare the trainings based on different $q_{\max}$ and N, we choose to always use the same network architecture

$$(q_{\max} - 1, 512, \text{ReLU}, 256, \text{ReLU}, 128, \text{ReLU}, 64, \text{ReLU}, 32, 1)$$

where ReLu is the nonlinear Rectified Linear Unit introduced in Section 3.2. The number of parameters in our neural network is of the order of 10^5 which is relatively small (the largest LLMs are composed of dozens of billions of parameters).

For the learning process, we take a batch size of 500 and, for each $q_{\max} \in 2, 3, \ldots, 8$ and $N = 2, 3, \ldots, 10$, we train the ANN in a supervised manner for 5000 epochs with the ADAM optimiser. Our loss function is the squared difference averaged over the batch. Remarkably, even after 5000 epochs, no overfitting is observed (see Figure 3.14 and the additional discussion in Appendix 3.A).

We show in Figure 3.9 the results of the different trainings applied to the test dataset. We find that ANNs give quite reliable predictions already for $q_{\max} = 3$ with a MRE at 1%, two order of magnitude less than with the Wehrl moments ratios. More surprisingly, even on the basis of the first non-trivial Wehrl moment $W_{|\psi\rangle}^{(2)}$, ANNs give a good estimate for weakly and strongly entangled states. When we take into account more Wehrl moments,

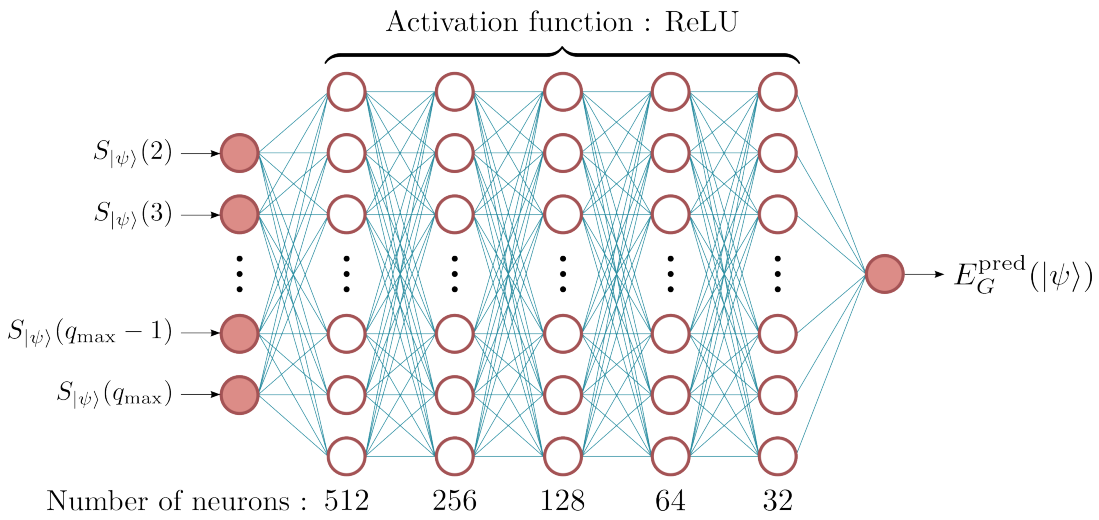

Figure 3.8: Representation of the ANN architecture used for the estimation of the GME.

the ANNs are able to predict the GME more accurately. For a fixed number $q_{\max} = 4$ of Wehrl moments (see Appendix 3.A for $q_{\max} = 8$), we find that the MRE increases as we increase the number of qubits but eventually saturates. We believe that for a higher number of qubits, there is a greater spectrum of states with the same first Wehrl moments but different GMEs. This would imply that the input to the ANN is not sufficient to distinguish between these different states and would explain the observed increase in error. We also observe that at $q_{\max} = 4$, the MRE saturates at about 1% for $N \gtrsim 5$. This result is quite remarkable as it shows that with ANNs the MRE seems to scale very favourably with N.

3.4.2 Mixed states

The results on the test data for mixed states are represented in Figure 3.10 for $k = 0.05$ by yellow diamonds for depolarised states (3.17) and red squares for random mixed states (3.16) and a reduced batchsize of 50 states. For comparison, we also show the lower MRE obtained for pure random states by blue dots. We see that for depolarised states, the MRE is around 0.1% or even below for $N = 2$ and 3 and below 1% for $N = 4$ for $q_{\max} \geqslant 4$. For the random mixed states (3.16), the error is systematically higher than that obtained for the depolarised states, but it remains at an acceptable level for $q_{\max} \geqslant 4$.

The data displayed in Figure 3.10 shows that Wehrl moments remain useful quantities for predicting entanglement of slightly mixed states in multiqubit systems. It is interesting to note that even for highly depolarised states of the form (3.17), ANNs are still able to predict with high accuracy the GME. This is shown in Figure 3.11, where we consider higher degrees of depolarisation k. Counter-intuitively, we find that the predictions on the GME improve as k increases (see middle and right panel). This is probably due to the specific class of mixed states we have considered and the fact that the range of GME values that the ANN has to account for decreases with k (see left panel). It does, however, show that for a typical decoherence model such as depolarisation, Wehrl moments still contain essential information for predicting the GME even for highly mixed states.

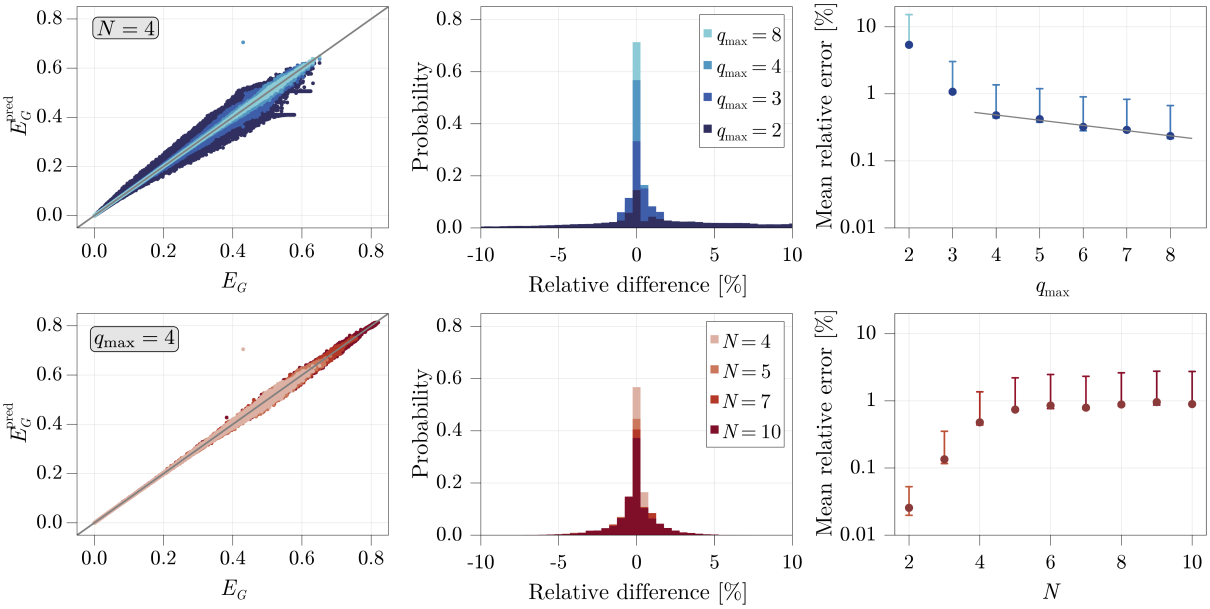

Figure 3.9: Same representation and parameters as in Figure 3.7, but with predictions based on trained ANNs. The grey solid line in the top right panel shows a decreasing exponential fit of equation $\Delta(q_{\max}) \approx 0.989 \exp(-0.179\, q_{\max})$.

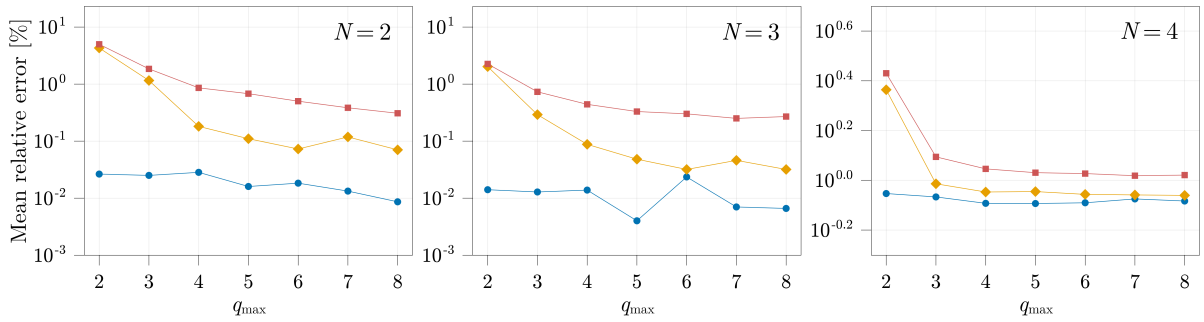

Figure 3.10: Results of the training of the ANNs on mixed states of the form (3.17) (yellow diamonds) and (3.16) (red squares) for $k = 0.05$. The blue dots represent the MRE for the predictions of the ANNs trained for pure states and applied to the pure states used in the equations (3.17) and (3.16) to generate the mixed states forming the test dataset.

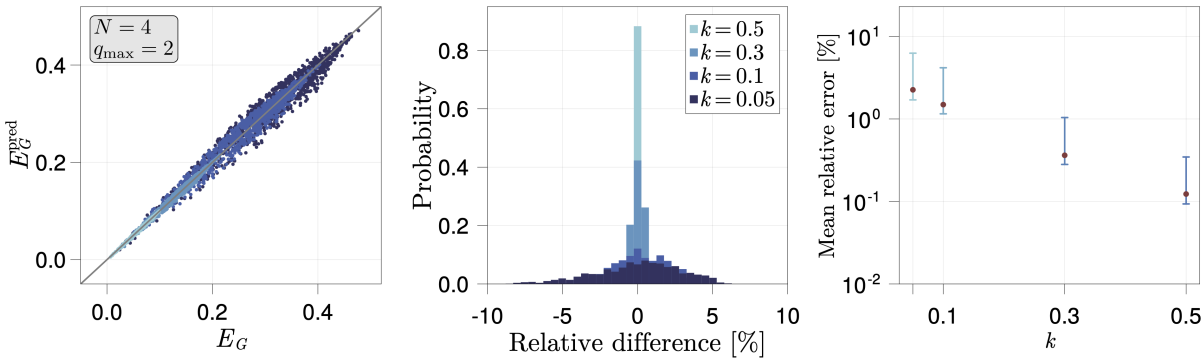

Figure 3.11: Results obtained by training ANNs on depolarised states of the form (3.17) for different degrees of depolarisation $k \in \{0.05, 0.1, 0.3, 0.5\}$. Here, $N = 4$ and $q_{\max} = 2$.

3.4.3 Discussion of the main results

The excellent performance of the ANNs to obtain estimates of the GME of pure states is clearly evident. We consistently find that the ANNs outperform a first estimation based only on Wehrl moment ratios. The differences in performance are quite large, with ANNs outperforming the Wehrl moment ratios by two orders of magnitude. For the method based on ANNs, the MRE decreases very rapidly from $q_{\max} = 2$ to $q_{\max} = 4$. Then, it seems that the MRE decreases exponentially at roughly the same rate. For $q_{\max} = 4$, the MRE obtained with ANNs seems to quickly saturate to about 1% for large number of qubits ($N \gtrsim 5$). We have also tested the ANN on a set of pure states that have been dynamically generated from spin squeezing. This set is characterised by a GME distribution that differs strongly from those used to train the ANN (see Appendix 3.A for more details). In this case, we find that the ANN also works very well with similar performance, demonstrating its great flexibility upon variations of input data. Furthermore, we show in Appendix 3.B that an ANN trained on noisy Wehrl moments is still able to predict the GME quite accurately.

For mixed states, the performance of ANNs with Wehrl moments remains satisfactory for general high purity states. This is evidenced by the fact that the GME is still obtained with a maximal error of 1% for $N = 4$. It is clear that, while the correlation between the GME and the Husimi function is less pronounced in the mixed state scenario when compared to the pure state, the Wehrl moments do offer valuable insights concerning the entanglement of mixed states. It would be interesting in latter work to find better correspondance between the Husimi function and the GME of multiqubit mixed states. Interestingly, the method is still robust for depolarised states, suggesting that the relation between the GME and the Husimi function remains substantial in such states.

3.5 Experimental determination of Wehrl moments

In this section, we propose a simple protocol based on spherical t-designs that allows the experimental determination of Wehrl moments of various orders from the same set of measurement outcomes of Stern-Gerlach experiments. A spherical t-design is a set of n_t points on the unit sphere, located at angles $\Omega_k = (\theta_k, \varphi_k)$ with $k \in \{1, \ldots, n_t\}$, such that [205, 206]

$$\frac{1}{4\pi} \int_{S^2} P(\Omega)\, d\Omega = \frac{1}{n_t} \sum_{k=1}^{n_t} P\left(\Omega_k\right) \tag{3.20}$$

for *all* trigonometric polynomials P of degree at most t. Taking $P(\Omega) = (Q_\rho(\Omega))^q$, and assuming for the moment that t is sufficiently large, we obtain by combining Eqs. (3.5) and (3.20)

$$W_\rho^{(q)} = \frac{1}{n_t} \sum_{k=1}^{n_t} \left(Q_\rho\left(\Omega_k\right)\right)^q$$

from which we can conclude that it is sufficient to measure the Husimi function in a finite number n_t of directions to determine the Wehrl moments. Some examples of t-designs on the sphere are shown in Figure 3.12. Given sufficient number of points n_t, it is known that a t-design for any t exists.

The Husimi function at Ω can be rewritten as

$$Q_\rho(\Omega) \equiv |\langle\Omega|\rho|\Omega\rangle|^2 = |\langle D_N^{(0)}|R(\Omega)^\dagger \rho R(\Omega)|D_N^{(0)}\rangle|^2 = |\langle D_N^{(0)}|\rho_\Omega|D_N^{(0)}\rangle|^2 = p_0^\Omega$$

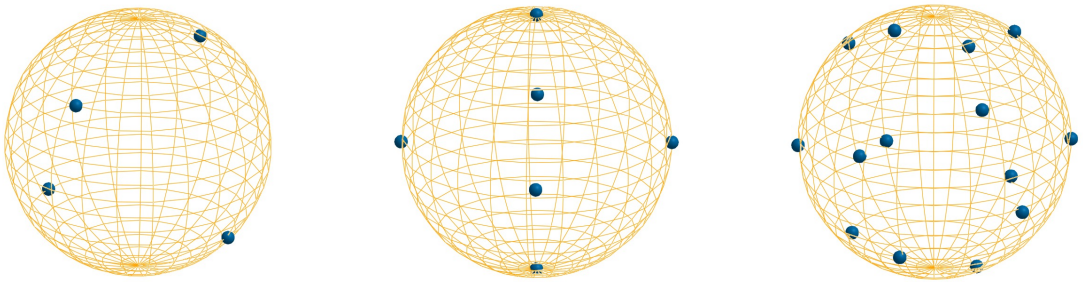

Figure 3.12: Examples of t-designs with $t = 2$, 3 and 4 (from left to right).

where $R(\Omega)$ is the rotation operator which maps the Dicke state $|D_N^{(0)}\rangle$ to the product state $|\Omega\rangle$, $\rho_\Omega = R(\Omega)^\dagger \rho R(\Omega)$ is the rotated state and p_0^Ω is the probability that the system in state ρ_Ω is found in state $|D_N^{(0)}\rangle$. The latter probability can be measured from a Stern-Gerlach experiment giving access to $\left\{p_k^\Omega = |\langle D_N^{(k)}|\rho_\Omega|D_N^{(k)}\rangle|^2 : k = 0, \ldots, N\right\}$ or, in the case of an atomic system, by driving a dipole transition to an auxiliary energy level and then observing the resonance fluorescence to obtain p_0^Ω [207].

The advantage of our protocol, which consists of measuring the Husimi function in a finite number of directions and extracting the Wehrl moments, is that it is totally independent of the state under consideration. Indeed, the Husimi function of any N-qubit symmetric state is a polynomial function of degree N. By choosing $t = Nq$, all Wehrl moments can be extracted exactly, up to order q, irrespective of the state ρ. As regards spherical designs, it has been shown numerically that $n_t \approx t^2/2$ [208], so to extract the Wehrl moments up to order q, we should measure the Husimi function in approximately $(Nq)^2/2$ points. Note that our protocol is not necessarily optimal and that there might be clever ways of using the full set of probabilities $\{p_k^\Omega\}$ obtained in Stern-Gerlach experiments (instead of only p_0^Ω) to find a better approximation of the Wehrl moments.

3.5.1 Results from approximate Wehrl moments

Since ANNs are, to a certain extent, intrinsically robust to noise, it is not necessary to have perfect determination of the Wehrl moments in order to obtain good estimates of the GME (see Appendix 3.B for more details). This suggests the possibility of using spherical designs of order t less than Nq to obtain approximate Wehrl moments up to order q via

$$W_\rho^{(q)} \approx \frac{1}{n_t} \sum_{k=1}^{n_t} \left(Q_\rho\left(\Omega_k\right)\right)^q . \tag{3.21}$$

Equation (3.21) approximates all Wehrl moments with $q > t/N$ from the same set of Husimi function values. Therefore, as long as this improves the prediction of the ANN, we can give it approximate Wehrl moments of increasing order.

We show in Figure 3.13 the results of the training of ANNs based on the spherical t-design with $t = 13$ and the same test set of pure states as presented in Sec.3.3. They

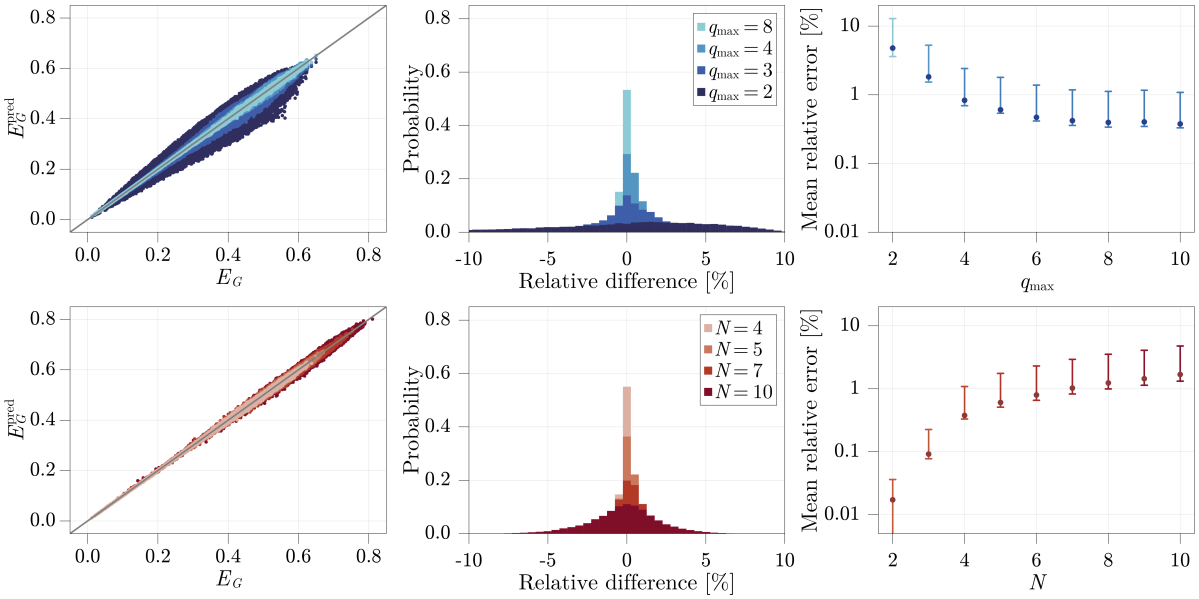

Figure 3.13: Same representation and parameters as in Figure 3.7, but with predictions based on Wehrl moments obtained from Eq. (3.21) with Ω_k the points defining a spherical t-design with $t = 13$ and $n_t = 94$. For the lower panels, we took $q_{\max} = 10$ instead of $q_{\max} = 4$.

show that the MRE can be brought down to a level of 1% with $t = 13$ even for a number of qubits up to 10. We chose this particular value of t because the spherical design contains antipodal points and the Husimi function at two antipodal points can be measured by a single Stern-Gerlach experiment. The number of directions in which the Stern-Gerlach experiment must be performed can therefore be halved in this case (from $n_t = 94$ to 47).

Conclusion

In this work, we have studied how ANNs can be used to give a reasonably accurate estimate of the geometric measure of entanglement (GME) of pure and mixed symmetric multiqubit states based on their first Wehrl moments (moments of their Husimi function). This shows that, while entanglement and phase-space functions are distinct concepts, they can nonetheless be related and even use their connection as an advantage. We also proposed an experimental protocol for measuring Wehrl moments and showed that it can be coupled with ANNs to obtain a good estimate of the GME. This provides opportunities for the experimental estimation of entanglement on the basis of a few Wehrl moments.

This work opens up several perspectives. First, while we have focused on the determination of GME, our approach could have been used to determine e.g. Wehrl entropy [209, 210], as both GME and such entropy are based on Wehrl moments, opening up characterisations of quantum chaos and phase transitions via ANNs. Secondly, it is known that determining the GME of a quantum state is a considerably more complex task for mixed states than for pure states. Nevertheless, as we have shown in Subsection 3.4.2, the GME of a depolarised state can still be predicted with high accuracy from its first Wehrl moments. Remarkably, we even found that GME predictions improve as the state purity decreases, probably because the entanglement also decreases in this case. It would be of great interest to know for which other types of mixed states ANNs also

give reliable estimates of the GME. In addition, our approach could be generalised to non-symmetric many-body quantum states where one is confronted with the exponential many-body wall, as it can be expected that ANNs will also perform well in this context [211]. More generally, an approach similar to the one used in this work could be followed to estimate the maximum or minimum of a quasi-probability distribution other than the Husimi function from its first moments, such as the Wigner and the P functions.

3.A Additional information on ANNs

Figure 3.14 shows an example of the evolution of the loss function on the test dataset throughout the training of the ANN for different numbers of qubits and $q_{\max} = 4$. We observe no overfitting, with the loss function decreasing even after a large number of epochs.

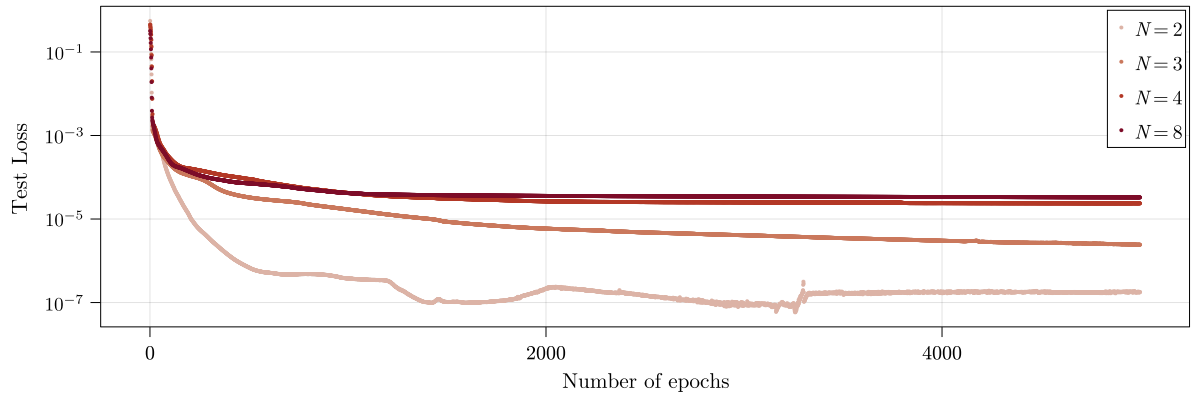

Figure 3.14: Loss function (averaged squared error) of the test dataset as a function of the number of training epochs for a maximal order $q_{\max} = 4$ and different numbers of qubits N.

Figure 3.15 shows the performance of the ANNs for a larger number of qubits and a larger maximal order than the results presented in the main text. For the top panels $N = 8$ and for the bottom panels $q_{\max} = 8$. The same general observations as in the main text apply in this case, in particular the fact that the mean relative error is below 1% already for $q_{\max} = 4$.

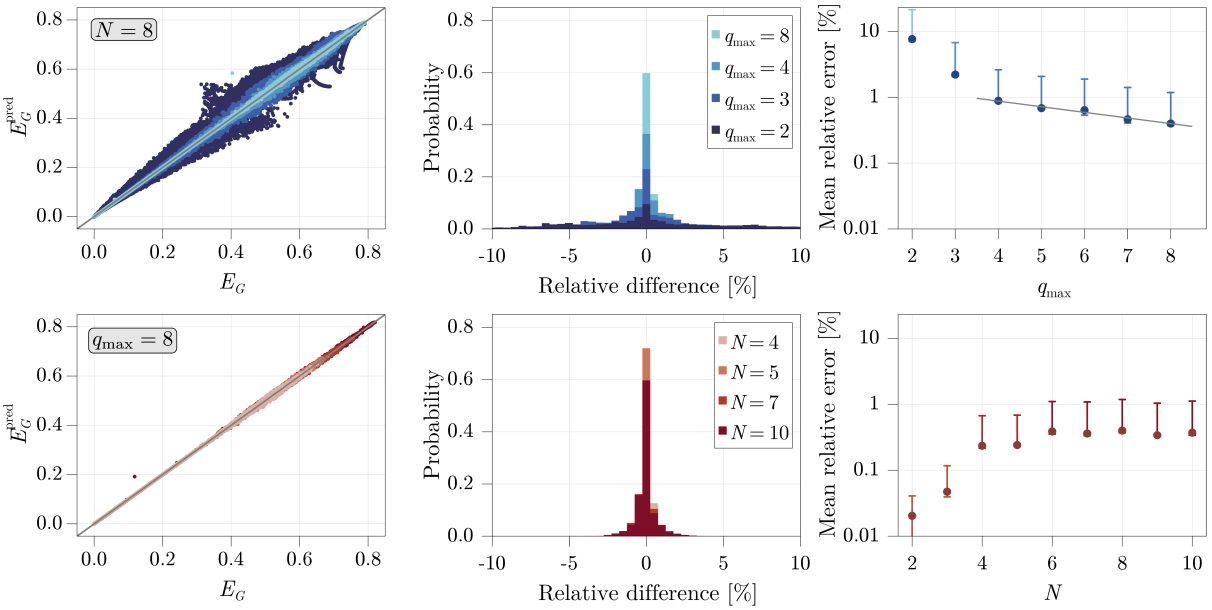

Figure 3.15: Same as Figure 3.9 for $N = 8$ (top) and $q_{\max} = 8$ (bottom). The grey solid line in the top right panel shows a decreasing exponential fit of equation $\Delta(q_{\max}) \approx 1.919 \exp(-0.197\, q_{\max})$.

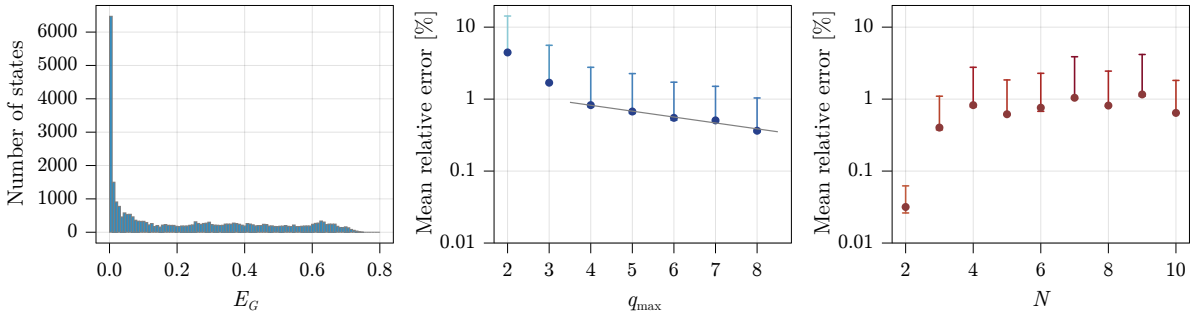

Figure 3.16: Left panel: Frequency distribution of GME of 30 000 squeezed states generated for $N = 8$ qubits. Middle and right panels: mean relative error on the estimate of the GME obtained from ANNs for $N = 4$ and $q_{\max} = 4$ respectively. The grey solid line shows a decreasing exponential fit of equation $\Delta(q_{\max}) \approx 1.745 \exp(-0.189\ q_{\max})$.

In order to further test the performance of ANNs, we generated another set of states resulting from the dynamical evolution corresponding to a spin squeezing. We calculated the time evolution of the initial coherent/product state $|D_N^{(0)}\rangle$ under the Hamiltonian

$$H \quad = \quad \chi_x J_x^2 + \chi_y J_y^2 + \chi_z J_z^2.$$

where χ_x, χ_y, χ_z are squeezing rates along the three spatial directions. At regular times, we sampled the state of the system and calculated its Wehrl moments and GME. After 500 time steps $\Delta t = 0.1$, we ended the evolution and started again from the same initial state. The χ_α rates were chosen randomly between 0 and 1 at the beginning of each evolution. In this way, we generated 30 000 states on which we tested the previously trained ANNs. The results are presented in Figure 3.16. We find that the ANNs still predict the GME very well even though they have never handled this type of states before. This shows that the training set was sufficiently large and representative to obtain ANNs capable of inferring beyond the states on which they have been trained.

3.B Noisy Wehrl Moments

In our previous developments, we used the exact value of the Wehrl moments for each multiqubit state. However, the Wehrl moments may not be known exactly, e.g. because of noises that are inevitably present in an experiment. This provides an incentive to test ANNs with noisy inputs. As a first approach, we applied Gaussian noise to our inputs $S_{|\psi\rangle}(q)$ (from the same training and test data sets as before). More precisely, for each q, we first calculated the average value of the ratio of Wehrl moments over the whole data set, $\overline{S_{|\psi\rangle}(q)}$. Based on this value, we defined a normal distribution with a mean value of zero and a standard deviation given by

$$\sigma = \eta\, \overline{S_{|\psi\rangle}(q)}$$

where η is a real number that quantifies the magnitude of the noise. Then we applied noise, sampled from the normal distribution, to each Wehrl moment ratio and fed these noisy Wehrl moments to ANNs trained in two different ways: ANNs trained as before on noiseless Wehrl moments and ANNs trained directly on noisy Wehrl moments. The results are shown in Figure 3.17 for $\eta = 0.01$. We find that the least satisfactory predictions are obtained from ANNs that have not been trained on noisy Wehrl moments

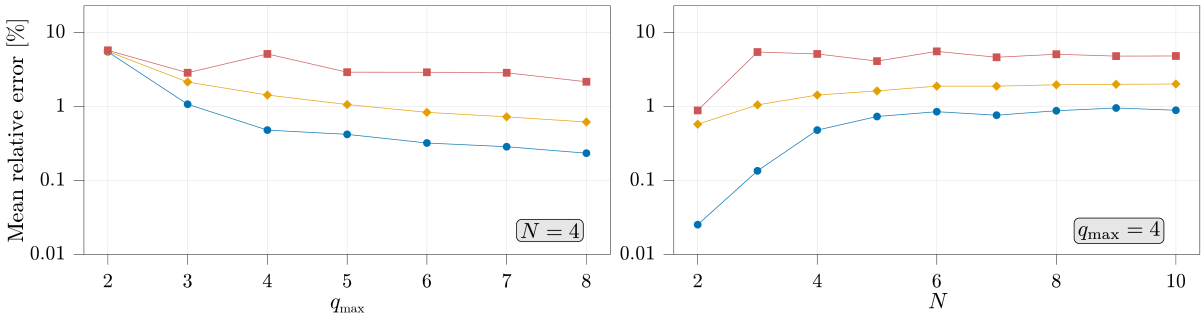

Figure 3.17: Mean relative error (MRE) on the GME obtained from ANNs fed with noisy input data. The red and yellow symbols give the MRE for ANNs trained respectively on noiseless and noisy Wehrl moments. For comparison, the blue dots give the MRE for ANNs trained and tested on noiseless Wehrl moments (see Figure 3.9).

(red squares). The explanation we see is that ANNs trained on noiseless Wehrl moments become excellent at predicting GME with such data but are unable to generalise on noisy data (a phenomenon similar to overfitting). However, ANNs trained on noisy Wehrl moments work much better and give a low mean relative error, around 1%, for $q_{\max} \geqslant 4$ (yellow diamonds). For a higher noise level, the MRE increases and is of the order of 2.6% for $\eta = 0.03$ with $q_{\max} = 4$ and $N = 4$.

Chapter 4

Anticoherent states, their entanglement and how to generate them

In the previous chapters, we explored quantumness in spin systems from a general perspective, without focusing on particular spin states. In this chapter, we turn our attention to anticoherent (AC) states, a family of spin states that exhibits a high degree of non-classicality and entanglement. These states were introduced relatively recently, especially when compared to other paradigmatic spin states such as GHZ states [65, 25]. Since then, their properties were explored further and AC states revealed to be promising candidates for several quantum metrological tasks. Notably, they are optimal for frame alignment [212] and rotation and magnetic field sensing when the direction of the rotation or the field is unknown [27, 28, 213, 214]. More recently, it was discovered that AC states could also be useful for toponomic quantum computing [29].

As introduced in Chapter 1, the anticoherence of a pure spin state is closely linked to the isotropy of its spin operator expectation value. This observation has led to the development of several measures of anticoherence, that quantify the degree of isotropy of a pure spin state [215]. These measures have proven fruitful in contexts such as quantum rotosensing [28] and in characterising the quantumness of orthonormal bases in Hilbert space [30]. The goal of this chapter is to review the known properties of AC states and introduce new results that advance our theoretical understanding of them and that could allow their generation in various experimental platforms.

In Section 4.1, we first relate the definition of AC states of order t (t-AC states) with their phase-space representations. This will highlight that AC states are highly delocalised in phase-space, a hallmark of non-classicality, as previously discussed in Chapter 3. We then present two additional equivalent definitions of t-AC states, each illuminating a different aspect of their structure. Notably, one of these definitions reveals that pure t-AC states maximise the entanglement negativity with respect to the bipartition $t|N-t$, thus identifying them as the most entangled multiqubit symmetric pure states. We then define the anticoherence measures that will be used throughout this thesis. Similarly to entanglement, no single universally accepted measure of the degree of anticoherence exists. This diversity is advantageous, as different measures can be used to derive complementary properties of AC states. We also introduce t-AC subspaces which are subspaces of the spin Hilbert space containing only t-AC states [213, 216], which will prove instrumental in deriving a new property of AC states.

In Section 4.2 we recall known results on how t-AC measures can be employed to demonstrate that AC states are optimal for rotation sensing around an unknown axis.

In this context, t-AC states serve as optimal quantum rotosensors (OQRs) [26, 27, 28]. Furthermore, we demonstrate here that t-AC subspaces automatically satisfy the Knill-Laflamme condition, a key requirement for quantum error-correction, suggesting their relevance for quantum computation [217–219].

In Section 4.3, we show an original result on the precise relation between the degree of anticoherence of a pure spin state and its entanglement. For instance, while a t-AC state maximise the entanglement negativity, it remained unclear how anticoherence compares to entanglement. We show that the Bures t-AC measure (see Subsection 4.1.2) can be directly connected to the negativity, establishing a direct relation between anticoherence and entanglement and giving an insightful geometric representation of the entanglement negativity of symmetric multiqubit pure states.

This insight motivates an extension of anticoherence measures to mixed states. Existing AC measures were originally formulated for pure states, but a naive extension leads to problems. For instance, the MMS $\rho_0 = \mathbb{I}/(2j+1)$, which is the most classical mixed state, is also anticoherent to any order $t \leq N$. Yet, it lacks the quantum features we associate with anticoherence. The key to resolving this lies in recognising that isotropy in spin states can arise either from coherent quantum superpositions or from classical mixtures. By leveraging the connection between the Bures AC measure and the negativity, we introduce a new measure of anticoherence that isolates the quantum contribution in mixed states. This new measure reduces to the Bures t-AC measure for pure states, correctly relating anticoherence of pure states solely to quantum coherence.

Experimentally, AC states have already been created and their properties for quantum metrology have already been asserted [31, 220]. However, to date, only a limited number of AC states have been realised, and only in multiphotonic systems. This underscores the need for protocols enabling their creation in other platforms such as atomic or solid-state systems. In Section 4.4, we address this need by introducing a simple protocol that allows the generation of AC states of arbitrary order. This protocol enables the generation of AC states with a high degree of anticoherence for both low-dimensional ($j \leq 24$) and high-dimensional ($j \gg 1$) systems. Conventional quantum control algorithms such as GRAPE or CRAB were not used due to their suboptimal performance in terms of time and accuracy, and their increased computational demands. Instead, we relied on the analytical form of the Hamiltonian evolution to design a pulse-based protocol. The pulse durations are optimised using the Nelder-Mead nonlinear algorithm. Our scheme requires only two types of operations, i.e. spin rotation and squeezing, both of which are already implemented in many experimental platforms. To our knowledge, no other protocol has achieved the generation of AC states with such a high order of anticoherence. Moreover, the pulse sequence provides an intuitive physical picture of how a coherent spin state is transformed into an anticoherent one.

4.1 Anticoherent states

4.1.1 Definitions

As introduced in Chapter 1, a pure spin-j state is said to be t-AC if it satisfies the condition

$$\frac{\partial}{\partial \mathbf{n}} \langle (\mathbf{J} \cdot \mathbf{n})^k \rangle = 0 \qquad \forall k = 1, 2, \ldots, t, \tag{4.1}$$

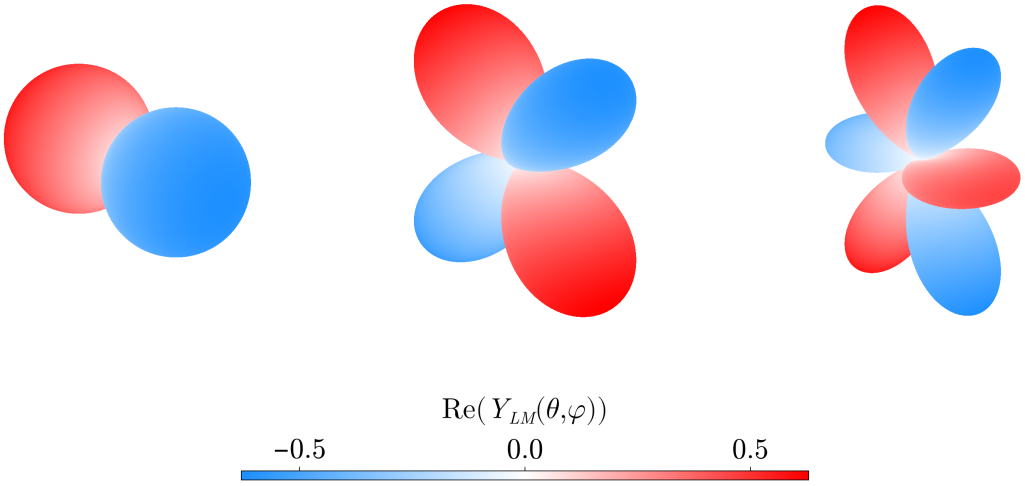

Figure 4.1: Radial representation of the real part of the spherical harmonics Y_{11}, Y_{21} and Y_{31}, from left to right [221].

where $\mathbf{J} = (J_x, J_y, J_z)$ is the spin operator and $\mathbf{n} = (n_x, n_y, n_z)$ is a unit vector in $\mathbb{R}^3$. This definition means that the first t moments of the spin projection are directionally isotropic. To gain further physical insight into t-AC states, we explore their phase-space representations. The Stratonovitch-Weyl phase-space functions admit the multipolar expansion (see Chapter 1)

$$F_\rho(\Omega) = \sqrt{\frac{4\pi}{2j+1}} \sum_{L=0}^{2j} \sum_{M=-L}^{L} \left(C^{jj}_{jj,L0}\right)^{-s} Y_{LM}(\Omega)\, \rho_{LM} \tag{4.2}$$

where $\Omega = (\theta, \varphi)$ denotes a point on the sphere and each spherical harmonic Y_{LM} is associated with the multipole ρ_{LM} of the spin state ρ. The spherical harmonics themselves take the form

$$Y_{LM}(\theta, \phi) = (-1)^M \sqrt{\frac{(2L+1)(L-M)!}{4\pi (L+M)!}} P_L^M(\cos\theta)\, e^{iM\phi}$$

with P_L^M denoting the associated Legendre polynomials. As shown in Figure 4.1, spherical harmonics of increasing order L exhibit finer angular structure. Consequently, a spin state whose phase-space representation is sharply localised will predominantly populate lower multipoles, while a state with delocalised phase-space function will show significant weights in higher L.

To quantify this, we define the cumulative multipole population up to order t as

$$r_t = \sum_{L=1}^{t} \sum_{M=-L}^{L} |\rho_{LM}|^2$$

which measures how much of the state lies in the lower multipoles. For pure states, $r_{2j} = 1$. Among such states, spin coherent states are known to maximise r_t for all $t < 2j$ [222], making them the pure states with the most localised phase-space function on the sphere.

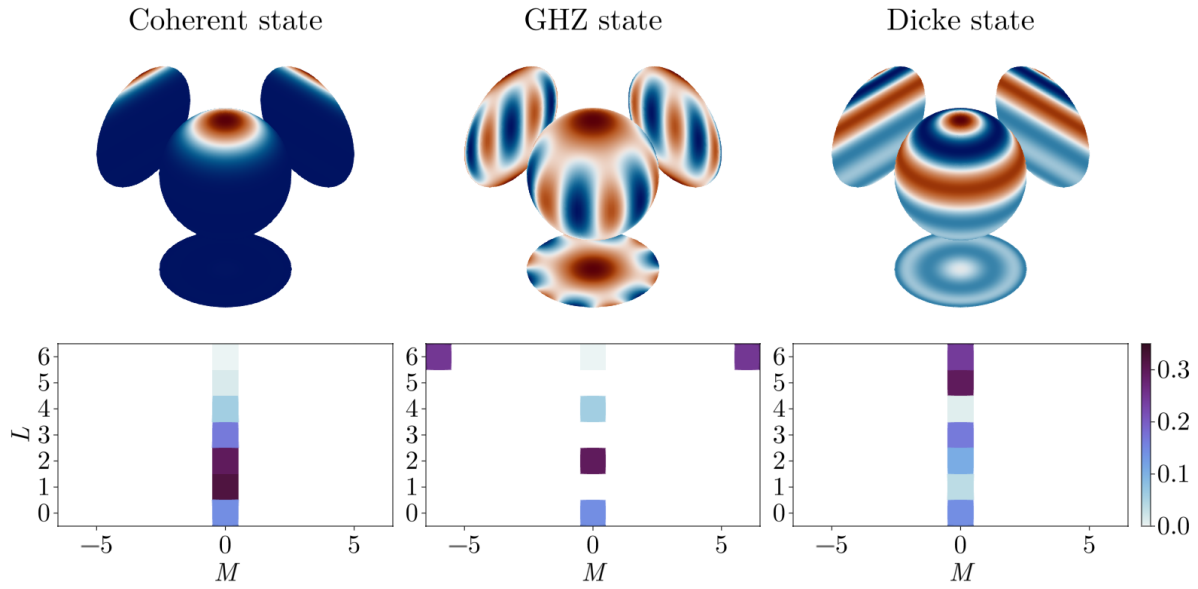

Figure 4.2: Top : Wigner function of the coherent state $|\theta = 0, \varphi = 0\rangle$, the GHZ state and the spin eigenstate $|j, m = 2\rangle$ for $j = 3$. Bottom : Modulus squared $|\rho_{LM}|^2$ of the corresponding state multipoles.

This trend is clearly illustrated in Figure 4.2 which compares, for $j = 3$, the Wigner function of the coherent state $|\theta = 0, \varphi = 0\rangle$, the GHZ state, which is a 1-AC state, and the spin eigenstate $|j, m = 2\rangle$. We observe that the coherent state is highly peaked, while the more non-classical states display high degree of delocalisation.

These observations naturally lead to an alternative and equivalent definition of anti-coherent states in terms of their multipolar expansion.

AC states from multipolar expansion. A pure spin state $|\psi\rangle$ is t-AC if and only if all multipoles up to order t vanish, i.e. [223]

$$\rho_{LM} = 0, \qquad \forall L = 1, \ldots, t \quad \text{and} \quad M = -L, \ldots, L. \tag{4.3}$$

In this sense, t-AC states are rotationally symmetric to order t, and their phase-space representations show high isotropy and delocalisation. A well-known example is the GHZ state, which is 1-AC and satisfies $\rho_{1M} = 0$ for $M = -1, 0$ and 1 as we can see from the multipoles depicted in Figure 4.2. Higher-order examples include [224]

$$\left|\psi_{t=2}^{\text{HOAP}}\right\rangle = \frac{1}{2}\left(|2, -2\rangle + i\sqrt{2}\,|2, 0\rangle + |2, 2\rangle\right) \tag{4.4}$$

$$\left|\psi_{t=3}^{\text{HOAP}}\right\rangle = \frac{1}{\sqrt{2}}\left(|3, -2\rangle + |3, 2\rangle\right) \tag{4.5}$$

$$\left|\psi_{t=4}^{\text{HOAP}}\right\rangle = \frac{1}{5}\left(\sqrt{7}\,|6, -5\rangle + \sqrt{11}\,|6, 0\rangle - \sqrt{7}\,|6, 5\rangle\right) \tag{4.6}$$

which are HOAP states of order 2,3 and 4, respectively. Their corresponding Wigner functions and the modulus squared of their multipoles are shown in Figure 4.3, further illustrating the relationship between low multipole suppression and spatial delocalisation.

If instead of a spin-j system we consider a system of $N = 2j$ qubits whose states are restricted to the symmetric subspace, we can relate the definition of t-anticoherence given

in (4.3) to the properties of the reduced density matrix of the state. Indeed, the t-qubit reduced state ρ_t can be expanded in the multipolar basis as (see Appendix 1.B)

$$\rho_t = \frac{\mathbb{I}}{t+1} + \sum_{L=1}^{t} \sum_{M=-L}^{L} \frac{t!}{(2j)!} \sqrt{\frac{(2j-L)!\,(2j+L+1)!}{(t-L)!\,(t+L+1)}} \rho_{LM} T_{LM}. \tag{4.7}$$

From this decomposition, a direct connection emerges between the vanishing of the multipoles of order $L \leq t$ and the reduced state. In particular, we obtain the following equivalent definition of t-anticoherence.

AC states from reduced states. A symmetric multiqubit state $|\psi\rangle$ is t-AC if and only if its t-qubit reduced state ρ_t is the t-qubit MMS in the symmetric subspace, that is

$$\rho_t = \frac{\mathbb{I}}{t+1}. \tag{4.8}$$

This means that while the global state $|\psi\rangle$ is pure and fully known, any of its subsystems composed of t or fewer qubits carry no information about it.

This feature lies at the heart of entanglement theory and directly implies that t-AC states are maximally entangled across all bipartitions $q|N-q$ with $q \leq t$. To further quantify this connection, we consider the negativity of a pure state, given by [117]

$$\mathcal{N}_t\left(|\psi\rangle\right) = \sum_{i>j=1}^{t+1} \sqrt{\lambda_i \lambda_j}$$

where the λ_i's are the eigenvalues of the reduced state ρ_t. As discussed in Chapter 1, the maximal possible negativity for such bipartition is

$$\mathcal{N}_t^{\max} = \frac{t}{2}$$

which occurs precisely when the reduced state has uniformly distributed eigenvalues, i.e. $\lambda_i = \frac{1}{t+1}$ for all $i = 1, 2, \ldots, t+1$. Therefore, a pure state reaches this maximal entanglement if and only if it is t-AC.

In Appendix 4.A, we list in Table 4.3 the HOAP states for $j \leq 5$ that are already known [224, 225].

4.1.2 Anticoherence measure of pure spin states

As discussed earlier, coherent states are the least anticoherent, as they completely fail to satisfy the conditions to be t-AC. But how much anticoherent are important quantum states like the GHZ state, the W state, or general Dicke states $\left|D_N^k\right\rangle$? To answer this, various measures of t-anticoherence have been proposed. These measures aim to quantify how close a given spin state is to being t-AC. Here, we introduce two main classes of anticoherence measures.

A measure of t-AC of a pure spin-j state $|\psi\rangle$ was defined as a positive function $\mathcal{A}_t$ satisfying the following minimal set of conditions [215]:

1. $\mathcal{A}_t\left(|\psi\rangle\right) = 0$ if and only if is $|\psi\rangle$ is a coherent state.

2. $\mathcal{A}_t\left(|\psi\rangle\right) = 1$ if and only if $|\psi\rangle$ is t-AC.

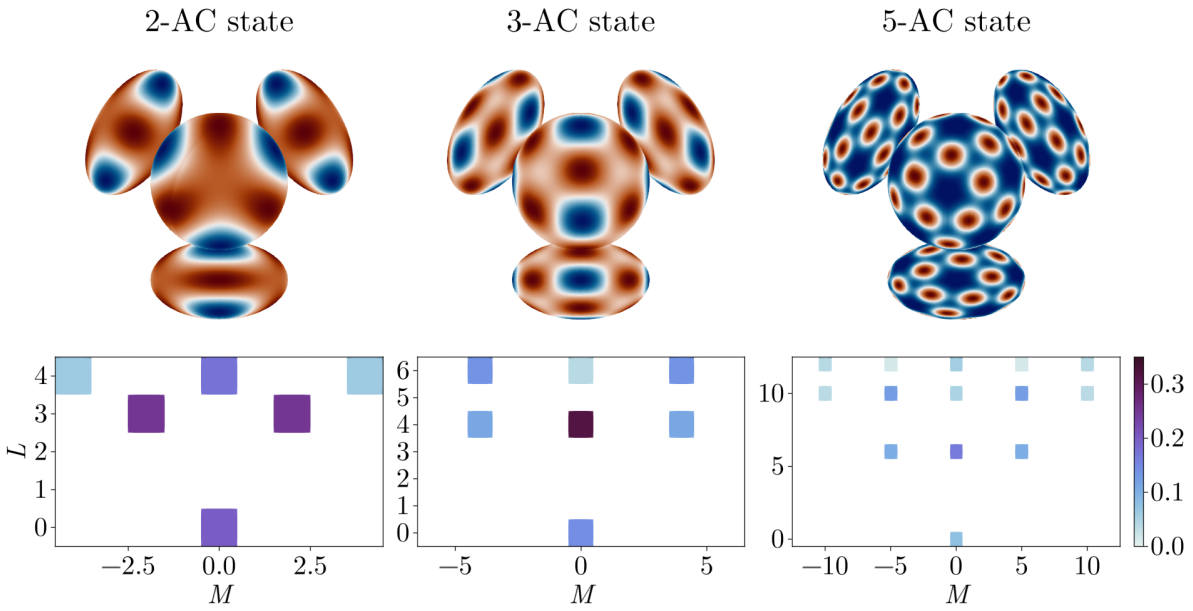

Figure 4.3: Wigner function and modulus squared of the multipoles of AC states of order $t = 2$, 3 and 5 for respectively $j = 2$, 3 and 6 given in (4.4), (4.5) and (4.6).

3. $\mathcal{A}_t(|\psi\rangle) \in [0,1]$ for any pure state $|\psi\rangle$.

4. $\mathcal{A}_t(|\psi\rangle)$ is invariant under global phase changes and arbitraty spin rotations.

The first three criteria ensure that coherent and t-AC states give respectively the minimum and maximum values of any measure. The last condition ensures that the value taken by measures of anticoherence does not depend on a particular orientation of the coordinate system.

Several inequivalent measures satisfying these criteria exist. Here, we focus on two widely used and physically meaningful ones: the purity-based and Bures distance-based measures. Both hinge on the fact that the t-qubit reduced state of a t-AC state is the MMS which has the lowest possible purity $R(\rho) = \frac{1}{t+1}$. In contrast, separable states have pure reduced states with $\mathrm{Tr}(\rho_t^2) = 1$. Since coherent states are the only pure separable spin states, these observations motivate the following measures.

Anticoherence measure based on purity. Let $\lambda_1, \lambda_2, \ldots, \lambda_{t+1}$ be the eigenvalues of the t-qubit reduced state of a pure spin state $|\psi\rangle$. The purity-based anticoherence measure of order t (purity t-AC measure) is defined as

$$\mathcal{A}_t^R(|\psi\rangle) = \frac{t+1}{t}\left[1 - R_t(|\psi\rangle)\right] \tag{4.9}$$

where

$$R_t(|\psi\rangle) \equiv \mathrm{Tr}\left(\rho_t^2\right) = \sum_{i=1}^{t+1} \lambda_i^2$$

is the purity of its t-qubit reduced density matrix and the rescaling $\frac{t+1}{t}$ is used so that $\mathcal{A}_t^R(|\psi\rangle) \in [0,1]$. It can be easily shown to verify all four conditions required for an anticoherence measure [215].

Anticoherence measures based on operator distances. Let $d(\rho,\sigma)$ be a distance between two density matrices ρ and σ. We require this distance to be invariant under unitary transformations and to attain its maximal value when $\rho = |\psi\rangle\langle\psi|$ is a pure state and $\sigma = \rho_0$ is the MMS. A distance-based measure of t-AC is given by

$$\mathcal{A}_t^d(|\psi\rangle) = 1 - \frac{1}{K_t} d(\rho_t, \rho_0) \tag{4.10}$$

where $\rho_0 = \frac{\mathbb{I}}{t+1}$ is the MMS and the normalisation factor K_t is the distance between a pure state and the MMS, i.e. $K_t = d(\mathrm{diag}(1,0,\ldots,0),\rho_0)$.

Some examples are the anticoherence measures based on the trace distance

$$d^{\mathrm{Tr}}(\rho,\sigma) = \frac{1}{2}\mathrm{Tr}\left[\sqrt{(\rho-\sigma)^2}\right]$$

and the Hilbert-Schmidt distance

$$d^{\mathrm{HS}}(\rho,\sigma) = \sqrt{\mathrm{Tr}\left[(\rho-\sigma)^2\right]}.$$

Note that the Hilbert-Schmidt-based measure is related to the purity-based one by $\mathcal{A}_t^{\mathrm{HS}} = 1 - \sqrt{1-\mathcal{A}_t^R}$.

In the following, we will rather focus on the Bures distance

$$d^{\mathrm{B}}(\rho,\sigma) = \sqrt{2-2\sqrt{F(\rho,\sigma)}}, \tag{4.11}$$

based on the Ulhman-Jozsa fidelity defined in Chapter 1 and for which $K_t = \sqrt{2\left(1-\frac{1}{\sqrt{t+1}}\right)}$. Equivalently, due to the purification theorem, the fidelity can be expressed as[1] [226, 227]

$$F(\rho,\sigma) \equiv \max_{\substack{|\psi\rangle\in\mathcal{P}(\rho)\\|\phi\rangle\in\mathcal{P}(\sigma)}} |\langle\psi|\phi\rangle|^2, \tag{4.12}$$

where $\mathcal{P}(\rho)$ is the set of all purifications of ρ. For pure states $\rho = |\psi\rangle\langle\psi|$, the fidelity between ρ_t and the MMS verifies

$$F(\rho_0,\rho_t) = \frac{1}{t+1}\left[\mathrm{Tr}\sqrt{\rho_t}\right]^2 = \frac{1}{t+1}\left[\sum_{i=1}^{t+1}\sqrt{\lambda_i}\right]^2, \tag{4.13}$$

and, consequently, for pure states, the anticoherence measure based on the Bures distance (Bures t-AC measure) can be written as

$$\mathcal{A}_t^{\mathrm{B}}(|\psi\rangle) = 1 - \sqrt{\frac{\sqrt{t+1}-\sum_{i=1}^{t+1}\sqrt{\lambda_i}}{\sqrt{t+1}-1}} \tag{4.14}$$

where $\lambda_1,\lambda_2,\ldots,\lambda_{t+1}$ are the eigenvalues of the t-qubit reduced state of ρ.

[1] Some authors use the name of fidelity for $\sqrt{F}$.

4.1.3 Anticoherent subspaces

While, for a given spin quantum number j, the HOAP state, i.e. the state with the maximal order of anticoherence, is often unique (up to arbitrary rotation), this is not the case for lower orders of anticoherence. For sufficiently small t, entire subspaces of the Hilbert space may consist exclusively of t-AC states. This motivates the definition of t-AC subspaces.

***t*-AC subspaces.** For a given j, a subspace $\mathcal{V}_{k,t}^{(j)} \subset \mathbb{C}^{2j+1}$ of dimension k is called a t-AC subspace if every state $|\psi\rangle \in \mathcal{V}_{k,t}^{(j)}$ is t-AC [213, 216].

An equivalent characterisation can be given in terms of multipolar tensor operators. A subspace $\mathcal{V}_{k,t}^{(j)}$ is t-AC if and only if a (not necessarily orthonormal) basis $\mathcal{B}_{k,t}^{(j)} = \{|\psi_i\rangle\}_{i=1}^{k}$ of $\mathcal{V}_{k,t}^{(j)}$ satisfies [213]

$$\langle\psi_i| T_{LM} |\psi_j\rangle = 0 \tag{4.15}$$

for all $i, j = 1, \ldots, k$ and any $L = 1, 2, \ldots, t$ and $M = -L, \ldots, L$. This shows that it is not sufficient for the elements of a basis $\mathcal{B}_{k,t}^{(j)}$ to be individually t-AC in order to span an anticoherent subspace. The stronger condition (4.15) must also be satisfied. For instance, a 1-AC subspace $\mathcal{V}_{k,1}^{(j)}$ must be spanned by a basis $\mathcal{B}_{k,1}^{(j)} = \{|\psi_i\rangle\}_{i=1}^{k}$ whose elements fulfill

$$\langle\psi_i| J_\alpha |\psi_j\rangle = 0, \quad \alpha = x, y, z$$

for all $i, j = 1, 2, \ldots, k$.

The smallest spin systems in which 1-AC and 2-AC subspaces are identified are $\mathcal{V}_{2,1}^{(2)}$ and $\mathcal{V}_{2,2}^{(7/2)}$, respectively. Explicit bases for these subspaces are, for $j = 2$,

$$|\psi_1\rangle = \frac{1}{2}\left(|2,-2\rangle + i\sqrt{2}\,|2,0\rangle + |2,2\rangle\right), \qquad |\psi_2\rangle = \frac{1}{2}\left(|2,-2\rangle - i\sqrt{2}\,|2,0\rangle + |2,2\rangle\right) \tag{4.16}$$

and, for $j = 7/2$,

$$|\psi_1\rangle = \sqrt{\frac{3}{10}}\left|\frac{7}{2},\frac{7}{2}\right\rangle + \sqrt{\frac{7}{10}}\left|\frac{7}{2},-\frac{3}{2}\right\rangle, \qquad |\psi_2\rangle = \sqrt{\frac{7}{10}}\left|\frac{7}{2},\frac{3}{2}\right\rangle - \sqrt{\frac{3}{10}}\left|\frac{7}{2},-\frac{7}{2}\right\rangle. \tag{4.17}$$

The Majorana representations of the states (4.17) are shown in Figure 4.4. Expected applications of AC subspaces are presented in Section 4.2.

Analogously to the fact that pure t-AC states are maximally entangled, it was shown in [213] that if a mixed state ρ verifies $\mathrm{im}(\rho) \in \mathcal{V}_{k,t}^{(j)}$, then ρ maximises the negativity with respect to the bipartition $t|N-t$ with $\mathcal{N}_t(\rho) = \frac{t}{2}$. For example, the family of mixed states

$$\rho(p) = p\,|\psi_1\rangle\langle\psi_1| + (1-p)\,|\psi_2\rangle\langle\psi_2|$$

with $|\psi_1\rangle$ and $|\psi_2\rangle$ given in (4.17), all satisfy $\mathcal{N}_1 = \frac{1}{2}$. This demonstrates that the connection between anticoherence and entanglement can persist even for mixed states.

4.2 Anticoherence for quantum metrology and error correction

In addition to their interesting theoretical properties, we further motivate our study of AC states in this section by a reminder about their usefulness in quantum metrology.

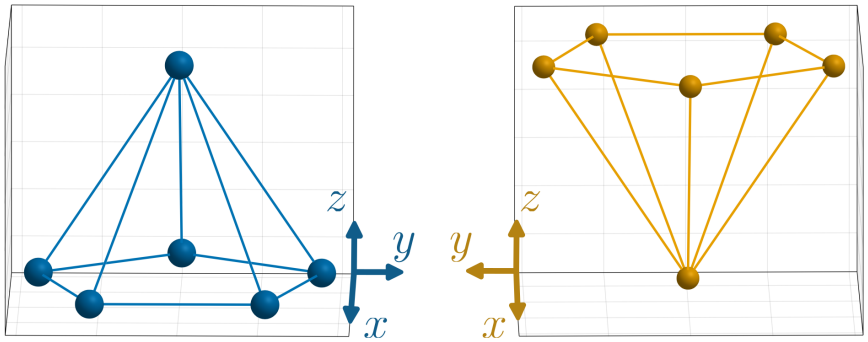

Figure 4.4: Majorana representation of the states $|\psi_1\rangle$ (left) and $|\psi_2\rangle$ (right) given in (4.17).

We note that t-AC states were also identified as optimal spin states for reference frames alignement [212] and that AC subspaces are good candidates for toponomic quantum computation [29]. Furthermore, we present here an original result on the possible use of AC subspaces for quantum error-correction.

4.2.1 Quantum metrology with AC states

In quantum metrology, the goal is to estimate an unknown parameter ω encoded in the quantum state ρ_ω of a system. Typically, one considers measurements performed simultaneously on N identical and independently prepared systems, each in the state ρ_ω. To extract information about ω, one introduces an estimator $\hat{\omega}(\mathbf{x})$, which is a function of the measurement outcomes $\mathbf{x} = (x_1, x_2, \ldots, x_N)$. A natural figure of merit for the estimator is the mean squared error, defined as [228]

$$\epsilon\left(\hat{\omega}(\mathbf{x}), \omega\right) = \frac{1}{N}\sum_{i=1}^{N}\left(\hat{\omega}(x_i) - \omega\right)^2.$$

For unbiased estimators, i.e. those satisfying $\sum_{i=1}^{\infty}\hat{\omega}(x_i) = \omega$, this quantity coincides with the variance $(\Delta\omega)^2$. In this case, for infinitesimal parameter change, the achievable precision is fundamentally limited by the Quantum Cramér-Rao (QCR) bound, which states that

$$(\Delta\omega)^2 \geq \frac{1}{N\mathcal{F}_Q(\omega)}$$

where $\mathcal{F}_Q(\omega)$ is the Quantum Fisher Information (QFI). The QFI is defined as

$$\mathcal{F}_Q(\omega) = \mathrm{Tr}\left(\rho_\omega L_\omega^2\right)$$

where L_ω is the symmetric logarithmic derivative determined by the differential equation

$$\partial_\omega \rho_\omega = \frac{1}{2}\left(\rho_\omega L_\omega + L_\omega \rho_\omega\right).$$

It is well-known that for N independent and non-entangled systems, the achievable precision scales as

$$(\Delta\omega)^2 \propto \frac{1}{N} \tag{4.18}$$

which is known as the shot noise scaling [229]. Fortunately, this scaling can be improved by using ensemble of entangled systems.

To build intuition for the QFI, it is helpful to connect it with the fidelity between quantum states. When estimating a parameter ω, the state ρ undergoes an evolution to ρ_ω, which depends explicitly on ω. The optimal choice of the input state ρ is one that maximises the distinguishability between ρ and ρ_ω. Therefore, it should minimise their fidelity (4.12)

$$F_\rho(\omega) = \left[\mathrm{Tr}\left(\sqrt{\sqrt{\rho}\rho_\omega\sqrt{\rho}}\right)\right]^2.$$

For infinitesimal parameter changes, this fidelity admits the approximation [230, 231, 232]

$$F_\rho(\omega) \simeq 1 - \frac{1}{4}\mathcal{F}_Q(\omega)\,\omega^2 \tag{4.19}$$

with [213]

$$\mathcal{F}_Q(\omega) = -2\left.\frac{\partial^2 F_\rho(\omega)}{\partial\omega^2}\right|_{\omega=0}. \tag{4.20}$$

Thus, the QFI corresponds to the leading non-vanishing term in the series expansion of the fidelity. In other words, the QFI quantifies how rapidly a quantum state changes under infinitesimal variations of the parameter ω.

The metrological problem we are interested in here is the measurement of the amplitude ω of some rotation applied on a system. Note that if this rotation is due to a magnetic field applied on a spin system, it can be reformulated as the measurement of the magnetic field intensity. In this manner, the optimal state $|\psi\rangle$ to measure the amplitude of a rotation with a known rotation axis $\mathbf{n}$ must minimise

$$F_\rho(\omega,\mathbf{n}) = \left[\mathrm{Tr}\left(\sqrt{\sqrt{\rho}R_{\mathbf{n}}(\omega)\,\rho R_{\mathbf{n}}^\dagger(\omega)\,\sqrt{\rho}}\right)\right]^2. \tag{4.21}$$

For an infinitesimal rotation, (4.21) takes the form

$$F_\rho(\omega,\mathbf{n}) \simeq 1 - (\Delta J_{\mathbf{n}})^2\,\omega^2 \tag{4.22}$$

and hence, one needs to maximise $(\Delta J_{\mathbf{n}})^2$ in order to find the optimal state to estimate the rotation amplitude around the axis $\mathbf{n}$. It is well-known that it is achieved by the spin cat state whose axis of symmetry is parallel to the rotation axis [233, 234]. For example, if the rotation axis is $\mathbf{n} = \mathbf{e}_z$, then the GHZ state

$$|\psi\rangle = \frac{1}{\sqrt{2}}\left(|j,j\rangle + |j,-j\rangle\right)$$

is optimal and achieves the Heisenberg scaling

$$(\Delta\omega)^2 \propto \frac{1}{N^2}$$

with $N = 2j$. While noise and decoherence must be taken into account, an improvement over non-entangled multiqubit systems has already been achieved experimentally using a GHZ state with beryllium and dysprosium atoms [235, 236].

In the following, we are interested in a similar setting in which we want to measure a rotation amplitude ω but whose axis $\mathbf{n} = (\cos\phi\sin\theta, \sin\phi\sin\theta, \cos\theta)$ is *not* known.

The quantum states that are optimal for this measurement problem are called optimal quantum rotosensors (OQR). To define OQRs we consider the overlap between the initial state and its rotated version, i.e. the fidelity between the two states where the rotation is $R_{\mathbf{n}}(\omega) = e^{i\omega J_{\mathbf{n}}}$ with $J_{\mathbf{n}} = J_x \cos\phi \sin\theta + J_y \sin\phi \sin\theta + J_z \cos\theta$. In the case that only the magnitude of the rotation ω is well-defined but not the rotation axis, the fidelity must be averaged over all possible directions $\mathbf{n}$. Hence, we must consider the average fidelity

$$F_\rho(\omega) = \frac{1}{4\pi}\int_{\mathcal{S}^2} F_\rho(\omega, \mathbf{n})\, d\mathbf{n}. \tag{4.23}$$

For infinitesimal angles ω, it is clear from (4.22) that the OQR must maximise

$$\int_{\mathcal{S}^2} (\Delta J_{\mathbf{n}})^2\, d\mathbf{n}.$$

This maximum is obtained for pure 2-AC states for which $\langle J_\alpha \rangle = 0$ and $J_\alpha^2 = \frac{j(j+1)}{3}$, with $\alpha = x, y, z$ [27], indicating that 2-AC states are optimal for small amplitudes rotation sensing. However, it is possible to go further. Indeed, a closed-form of (4.23) depending only on the purity t-AC measures of the pure state $\rho_\psi = |\psi\rangle\langle\psi|$ was found [26, 28]

$$F_{\rho_\psi}(\omega) = \varphi_0^{(j)}(\omega) + \sum_{t=1}^{\lfloor j \rfloor} \varphi_t^{(j)}(\omega)\, \mathcal{A}_t^R(|\psi\rangle)$$

where the $\varphi_t^{(j)}$ are real-valued trigonometric polynomials functions independent of $|\psi\rangle$. According to this closed-form, the average fidelity is a linear function that must attain its extremal values on the boundary of the domain of admissible values of purity t-AC measures $\mathcal{A}_t^R$. Unfortunately, characterising this domain is a well-known open problem for AC states. However, based on numerical results, it was shown that for small rotation amplitudes, the purity t-AC measures $\mathcal{A}_t^R$ must be maximised. As a result, for $j = 1$ and $3/2$, the OQRs are states verifying $\mathcal{A}_1^R = 1$. In Table 4.1, for $2 \leq j \leq 7/2$, we show the different optimal rotosensors, their purity t-AC measures and the largest rotation amplitude ω^* up to which the state is optimal. Sometimes, a trade-off between AC measures of different orders must be made. For example, the state with the maximal 3-AC measure for $j = 7/2$

$$|\psi\rangle = \frac{1}{\sqrt{2}}\left(\left|\frac{7}{2}, -\frac{5}{2}\right\rangle + \left|\frac{7}{2}, \frac{5}{2}\right\rangle\right)$$

verifies $\mathcal{A}_3^R = \frac{993}{1000}$ which is higher than the 3-AC measure of the optimal rotosensor in Table 4.1. However, its 2-AC measure is only $\mathcal{A}_2^R = \frac{995}{1000}$.

The fact that states with high AC measures are optimal for sensing small amplitudes rotation can be explained analytically as, in the vicinity of $\omega = 0$, the trigonometric functions $\varphi_t^{(j)}$ take the form [28]

$$\varphi_t^{(j)}(\omega) = \frac{b_{t,t}^{(j)}}{4^t}\omega^{2t} + \mathcal{O}\left(\omega^{2t+2}\right)$$

where $b_{t,t}^{(j)}$ are some coefficients strictly negative for $t \geq 1$. Hence it appears that to minimise the average fidelity, the anticoherence measures $\mathcal{A}_t^R$ must be maximised w.r.t. different orders t. For a given j, if an AC state of order $\lfloor j \rfloor$ exists then it is the OQR

	OQR in the standard spin basis	$\mathcal{A}_1^R$	$\mathcal{A}_2^R$	$\mathcal{A}_3^R$	ω^*
$j=2$	$\frac{1}{2}\left(\|2,-2\rangle+i\sqrt{2}\,\|2,0\rangle+\|2,2\rangle\right)$	1	1	$\frac{666}{1000}$	1.684
$j=5/2$	$\frac{1}{\sqrt{2}}\left(\|5/2,-3/2\rangle+\|5/2,3/2\rangle\right)$	1	$\frac{990}{1000}$	$\frac{880}{1000}$	1.497
$j=3$	$\frac{1}{\sqrt{2}}\left(\|3,-2\rangle+\|3,2\rangle\right)$	1	1	1	1.364
$j=7/2$	$\sqrt{\frac{2}{9}}\,\|7/2,-7/2\rangle-\sqrt{\frac{7}{18}}\,\|7/2,-1/2\rangle-\sqrt{\frac{7}{18}}\,\|7/2,5/2\rangle$	1	1	$\frac{986}{1000}$	0.717

Table 4.1: OQRs for different spin numbers j. The anticoherence measures up to order 3 are given for each state. These states are optimal only for rotation angles $\omega \in [0, \omega^*]$.

for small amplitude ω. This is the case for $j = 1$, $3/2$, 2 and 3. Similar results on the usefulness of using higher order t-AC states were shown in [214, 228].

Finally, even for mixed states, the anticoherence is necessary to obtain OQRs. It was shown that a mixed state ρ is an OQR if ρ is 2-AC, in the sense of (4.1), and $\mathrm{im}\,(\rho) \subset \mathcal{V}_{k,1}^{(j)}$ [213].

4.2.2 Quantum error correction with AC subspaces

A new result that we present in this chapter is that t-AC subspaces can be used for quantum algorithms error correction. One standard approach to error correction is to encode a logical qubit in a higher-dimensional system ($d > 2$). The logical states $|0\rangle$ and $|1\rangle$ are then represented by two orthogonal states $|\psi_1\rangle$ and $|\psi_2\rangle$ of the larger system. More generally, a quantum error-correcting code is a subspace $\mathcal{C} = \mathrm{span}\,\{|\psi_1\rangle, |\psi_2\rangle\}$, which is said to correct a set of errors $\mathcal{E}$ if there exists a recovery operation $R_{\mathcal{C}}$ such that for all $|\psi\rangle \in \mathcal{C}$ and all $E \in \mathcal{E}$, we have that [237]

$$R_{\mathcal{C}}\left(\frac{1}{\sqrt{p_{E|\psi}}}E\,|\psi\rangle\right) = |\psi\rangle\,,$$

where $p_{E|\psi} = \langle\psi|E^\dagger E|\psi\rangle$ is the probability that the error occurs during the algorithm. The dimension of the code space can be increased ($d_{\mathcal{C}} > 2$) to encode logical qudits. The celebrated Knill-Laflamme theorem provides the necessary and sufficient condition for correctability.

Theorem. ***Knill-Laflamme*** *A set of errors $\mathcal{E}$ is correctable on a code $\mathcal{C}$ if and only if [217]*

$$\langle\psi_i|\,E_\mu^\dagger E_\nu\,|\psi_j\rangle = \langle\psi_i|\,\psi_j\rangle\,c_{\mu\nu} \tag{4.24}$$

for all $E_\mu, E_\nu \in \mathcal{E}$, all $|\psi_i\rangle, |\psi_j\rangle \in \mathcal{C}$ and where the constants $c_{\mu\nu}$ depend only on E_μ and E_ν.

Based on this theorem, we obtain the following result.

Theorem. *Let $\mathcal{B} = \{|\psi_i\rangle\}_{i=1}^{d_{\mathcal{C}}}$ be a basis of an AC-subspace $\mathcal{V}_{d_{\mathcal{C}},t}^{(j)}$ of dimension d_c. Then the code $\mathcal{C} = \mathcal{B}$ corrects all errors $E_\mu \in \mathcal{E}$ such that*

$$E_\mu^\dagger E_\nu \equiv \prod_{i=1}^{q} J_{\alpha_i} \tag{4.25}$$

with $q = 1, 2, \ldots, t$ and $\alpha_i = 0, x, y, z$ and $J_0 \equiv \mathbb{I}$. In particular, 2-AC subspaces can correct all linear errors J_α ($\alpha = x, y, z$), while 4-AC subspaces can correct linear and quadratic errors $J_\alpha J_\beta$ which are among the most common in quantum computing.

Interestingly, the 2-AC subspace (4.17) was already proposed as a candidate quantum error-correcting code [218, 238]. We emphasise that our result holds even for a single-spin system, without the need for repetition codes, as required, for example, in spin-cat encodings [219].

Proof. The spin operators J_x, J_y and J_z can be expanded in the multipolar basis as

$$J_\alpha = \sum_{M=-1}^{1} c_M T_{1M} \tag{4.26}$$

where it is important to note that there are only multipolar tensors with $L = 1$. The product of two multipolar tensors takes the form

$$T_{L_1M_1} T_{L_2M_2} = \sum_{L=0}^{2j} (-1)^{2j+L} \sqrt{(2L_1+1)(2L_2+1)} \begin{Bmatrix} L_1 & L_2 & L \\ j & j & j \end{Bmatrix} C^{LM}_{L_1M_1,L_2M_2} T_{LM} \tag{4.27}$$

where $\begin{Bmatrix} L_1 & L_2 & L_3 \\ j_1 & j_2 & j_3 \end{Bmatrix}$ denotes a $6j$-symbol and $C^{L_3M_3}_{L_1M_1,L_2M_2}$ a Clebsch-Gordan coefficient [69]. Since Clebsch-Gordan coefficients are nonzero only when

$$|L_1 - L_2| \leq L \leq L_1 + L_2.$$

it follows that for $L_1 = L_2 = 1$, we have $0 \leq L \leq 2$. Thus, products of two spin operators yield multipoles with $L \leq 2$. More generally, a product of q spin operators produces multipoles of order at most $L = q$. Therefore, for all $q \leq t$ and for all $|\psi_i\rangle, |\psi_j\rangle \in \mathcal{V}^{(j)}_{d_\mathcal{C},t}$ we obtain

$$\langle\psi_i| E_\mu^\dagger E_\nu |\psi_j\rangle = E_{00}^{(\mu,\nu)} \langle\psi_i| T_{00} |\psi_j\rangle = \frac{E_{00}^{(\mu,\nu)}}{\sqrt{2j+1}} \langle\psi_i|\psi_j\rangle \tag{4.28}$$

where $T_{00} = \frac{\mathbb{I}}{\sqrt{2j+1}}$ and

$$E_{00}^{(\mu,\nu)} = \mathrm{Tr}\left(E_\mu^\dagger E_\nu T_{00}\right).$$

This is exactly of the Knill-Laflamme form with

$$c_{\mu\nu} = \frac{E_{00}^{(\mu,\nu)}}{\sqrt{2j+1}}$$

which depends only on E_μ and E_ν. Hence the theorem follows. □

4.3 Anticoherence measure of mixed spin states

As definitions (4.9) and (4.10) only depend on the reduced state ρ_t, t-AC measures can naturally be extended to mixed states. In this sense, the anticoherence is a measure of isotropy, as given by spin operator mean values (4.1), and can arise either from quantum superposition and/or classical mixture; the MMS being the highest order AC state verifying $\mathcal{A}^{\mathrm{B}}_{2j+1} = 1$. However, given the properties of pure t-AC states related to entanglement,

quantum metrology and error-correction, it would be interesting to distinguish these two sources of anticoherence. In this section, from a first result on the relation between the Bures AC measure and entanglement (Subsection 4.3.1), we extend the definition of AC measures to mixed states.

We will refer to the Bures t-AC measure as the *total* anticoherence measure, i.e.

$$\mathcal{A}_t^T \equiv \mathcal{A}_t^{\mathrm{B}} = 1 - \sqrt{\frac{1 - F(\rho_t, \rho_0)}{1 - \frac{1}{\sqrt{t+1}}}}$$

as it quantifies anticoherence coming from both classical mixtures and quantum superpositions. Based on our results on the relation between the Bures t-AC measure and the negativity, we will define *quantum* and *classical* anticoherence measures $\mathcal{A}_t^Q$ and $\mathcal{A}_t^C$ which only quantify isotropy/anticoherence of quantum or classical origin.

4.3.1 Relation between Bures AC measure and entanglement

Let us first prove that the Bures t-AC measure is in fact analytically related to the negativity of the partial transpose w.r.t. the bipartition $t|N-t$. Consider the reduced t-qubit state ρ_t of a symmetric N-qubit pure state $|\psi\rangle$. The eigenvalues of ρ_t naturally verifies

$$\left(\sum_{i=1}^{t+1} \sqrt{\lambda_i}\right)^2 = \underbrace{\sum_{i=1}^{t+1} \lambda_i}_{=1} + 2 \sum_{i>j=1}^{t+1} \sqrt{\lambda_i \lambda_j}.$$

Knowing that the negativity of a pure state is given by $\mathcal{N}_t(|\psi\rangle) = \sum_{i>j=1}^{t+1} \sqrt{\lambda_i \lambda_j}$ (see Chapter 1), we see that

$$\sum_{i=1}^{t+1} \sqrt{\lambda_i} = \sqrt{1 + 2\mathcal{N}_t(|\psi\rangle)}.$$

From (4.13), it follows that

$$F\left(\rho_{0,t}, \rho_t\right) = \frac{1 + 2\mathcal{N}_t(|\psi\rangle)}{t+1} \tag{4.29}$$

and the Bures t-AC measure can be written as

$$\mathcal{A}_t^{\mathrm{B}}\left(|\psi\rangle\right) = 1 - \sqrt{\frac{\sqrt{t+1} - \sqrt{1 + 2\mathcal{N}_t(|\psi\rangle)}}{\sqrt{t+1} - 1}}. \tag{4.30}$$

This shows that the Bures t-AC measure is in fact the same metric as the negativity w.r.t. bipartition $t|N-t$. This result directly relates anticoherence of pure spin states with entanglement. In the other way, it also gives a geometrical definition of the entanglement negativity of a symmetric multiqubit pure state $|\psi\rangle$. If we consider the Schmidt decomposition of $|\psi\rangle$ in a $t|N-t$ bipartition, then its reduced state has eigendecomposition $\rho_t = \sum_i \lambda_i |\phi_i\rangle \langle\phi_i|$ and

$$\left[\mathrm{Tr}\sqrt{\rho_t}\right]^2 = 1 + 2\mathcal{N}_t\left(|\psi\rangle\right) \tag{4.31}$$

and, based on the definition of the Bures distance (4.11), we get

$$\mathcal{N}_t(|\psi\rangle) = \frac{t+1}{2}\left[1 - \frac{1}{2}\left(d^{\mathrm{B}}(\rho_0, \rho_t)\right)^2\right]^2 - \frac{1}{2}.$$

Hence, the negativity increases when the Bures distance between ρ_t and the MMS decreases.

The equation (4.30) allows us to find an inequality for the negativity over different bipartitions of pure symmetric multiqubit states, similar to monogamy relations [239–241]. Consider the reduced mixed states ρ_t and ρ_{t+1} of a mixed symmetric N-qubit state ρ. It holds that $\mathcal{P}(\rho_{t+1}) \subseteq \mathcal{P}(\rho_t)$ and $\mathcal{P}(\rho_{0,t+1}) \subseteq \mathcal{P}(\rho_{0,t})$[2], where $\mathcal{P}(\rho)$ is the set of purifications $|\psi\rangle$ of ρ. Therefore, from definition (4.12), it is clear that $F(\rho_0, \rho_t) \geqslant F(\rho_0, \rho_{t+1})$, which implies that

$$d^{\mathrm{B}}(\rho_t, \rho_0) \leqslant d^{\mathrm{B}}(\rho_{t+1}, \rho_0).$$

and it follows that

$$\sqrt{1 - \frac{1}{\sqrt{t+1}}}\Big(1 - \mathcal{A}_t^{\mathrm{B}}(\rho)\Big) \leqslant \sqrt{1 - \frac{1}{\sqrt{t+2}}}\Big(1 - \mathcal{A}_{t+1}^{\mathrm{B}}(\rho)\Big).$$

In the case of pure states, the relation (4.30) between the negativity and the Bures t-AC measure gives additionally

$$\frac{t+2}{t+1}\left[1 + 2\mathcal{N}_t(|\psi\rangle)\right] \geq 1 + 2\mathcal{N}_{t+1}(|\psi\rangle), \tag{4.32}$$

The equality in (4.32) is obtained for t-AC states as their negativity w.r.t the bipartition $t|N-t$ is $\mathcal{N}_t = t/2$.

4.3.2 Mixed states anticoherence measure

4.3.2.1 generalised AC measure

One way to separate the quantum and classical contributions responsible for anticoherence is through the convex roof extensions of the respective measure of entanglement associated to the Bures t-AC measure. In other words, we can now define the quantum t-AC measure based on (4.30) as

$$\mathcal{A}_t^Q(\rho) \equiv 1 - \sqrt{\frac{\sqrt{t+1} - \sqrt{1 + 2\mathcal{N}_t^{CR}(\rho)}}{\sqrt{t+1} - 1}}$$

where we use the convex-roof extended negativity

$$\mathcal{N}_t^{CR}(\rho) = \min_{\{p_i, |\phi_i\rangle\}} \sum_i p_i \mathcal{N}_t(|\phi_i\rangle)$$

which is a faithful measure of entanglement, meaning that a mixed state ρ is entangled w.r.t. the bipartition $t|N-t$ if and only if $\mathcal{N}_t^{CR}(\rho) > 0$. Since $\mathcal{A}_t^Q$ is a monotonous function of $\mathcal{N}_t^{CR}$, it inherits all its properties with respect to convex combinations and SLOCC transformations [182]. Specifically, $\mathcal{A}_t^Q$ is a convex function (see Subsection 1.3.2), unlike the total t-AC measure $\mathcal{A}_t^T$. The main property, that we prove *a posteriori* is

$$\mathcal{A}_t^T(\rho) \geq \mathcal{A}_t^Q(\rho) \tag{4.33}$$

[2] We note $\rho_{0,t}$ the t-qubit MMS. We avoid this notation when the number of qubit is clear from the context.

for any state ρ. Hence, we can now define the difference

$$\mathcal{A}_t^C(\rho) \equiv \mathcal{A}_t^T(\rho) - \mathcal{A}_t^Q(\rho)$$

as the *classical* anticoherence measure. By construction, we have that $\mathcal{A}_t^T(\rho) = \mathcal{A}_t^Q(\rho)$ for pure states and that $\mathcal{A}_t^T(\rho) = \mathcal{A}_t^C(\rho)$ for separable states. We end this subsection with the proof of (4.33).

Theorem. *For any mixed quantum state ρ and any order of anticoherence t, it holds that*

$$\mathcal{A}_t^T(\rho) \geq \mathcal{A}_t^Q(\rho).$$

Proof. Using (4.30) and the definition of $\mathcal{A}_t^Q(\rho)$, the inequality reduces to

$$\left[\mathrm{Tr}\sqrt{\rho_t}\right]^2 \geq 1 + 2\mathcal{N}_t^{CR}(\rho).$$

By substituting the eigendecomposition $\rho = \sum_{i=1}^{N+1} \lambda_i |\psi_i\rangle \langle\psi_i|$ into the inequality, it suffices to show that

$$\left[\mathrm{Tr}\sqrt{\rho_t}\right]^2 \geq 1 + 2\sum_{i=1}^{N+1} \lambda_i \mathcal{N}_t\left(|\psi_i\rangle\right) \geq 1 + 2\mathcal{N}_t^{CR}(\rho).$$

For each pure state $|\psi_i\rangle$, we denote the t-qubit reduced state by $\sigma_i = \mathrm{Tr}_{N-t}(|\psi_i\rangle \langle\psi_i|)$. Using (4.31), we find

$$1 + 2\sum_{i=1}^{N+1} \lambda_i \mathcal{N}_t\left(|\psi_i\rangle\right) = 1 + 2\sum_{i=1}^{N+1} \lambda_i \left(\frac{\left[\mathrm{Tr}\sqrt{\sigma_i}\right]^2 - 1}{2}\right) = \sum_{i=1}^{N+1} \lambda_i \left[\mathrm{Tr}\sqrt{\sigma_i}\right]^2.$$

Since the reduced state of ρ is $\rho_t = \sum_i \lambda_i \sigma_i$, we get

$$\left[\mathrm{Tr}\sqrt{\sum_i \tilde{\sigma}_i}\right]^2 \geq \sum_{i=1}^{N+1} \left[\mathrm{Tr}\sqrt{\tilde{\sigma}_i}\right]^2,$$

with $\tilde{\sigma}_i = \lambda_i \sigma_i$. The last inequality can be written in terms of the Schatten p-antinorm of positive semi-definite matrices [242], $\|A\|_p \equiv \|\mathrm{Tr}A^p\|^{1/p}$, for $p = 1/2$, yielding

$$\left\|\sum_i \tilde{\sigma}_i\right\|_{1/2} \geq \sum_i \|\tilde{\sigma}_i\|_{1/2}.$$

The latter inequality is always fulfilled for any set of positive semi-definite matrices $\tilde{\sigma}_i$ by the definition of anti-norms [242]. □

4.4 Generation of anticoherent states

As we saw in the previous sections, t-AC states benefit from numerous theoretical properties and are expected to be useful in quantum metrology and quantum error correction. Hence, there is a need to find ways to generate experimentally these states for any order of anticoherence t. In this section, we present our protocol for generating a sequence of control operations that produce a pure AC state of a given order t in a spin-j system. Our analysis focuses exclusively on the unitary dynamics spanned by sequences of rotation and squeezing pulses. This section closely follows the presentation from [35] where we also study some dynamical decoupling sequences in order to mitigate the impact of decoherence on the protocol.

4.4.1 Controls and figure of merit

In order to find a protocol that will generate t-AC states, it is first necessary to define an objective function. This function will depend on the controls that are to be defined, and will serve as a figure of merit quantifying the quality of the final state produced. Our goal is to prepare a t-AC state, regardless of its specific form, rather than to aim for a predetermined target state. In the following, we consider the Bures t-AC measure $\mathcal{A}_t^B$ which will ensure that the pure states generated by our protocol have properties very close to those of a genuine t-AC state.

To explore the controlled generation of pure AC spin states, we consider a Hamiltonian capable of producing any SU$(2j+1)$ spin unitary transformation, and therefore of accessing the full state space[243, 244], which is of the form

$$H(t) = \Omega(t)\big[\cos\big(\phi(t)\big)J_x + \sin\big(\phi(t)\big)J_y\big] + \chi(t)J_z^2 \tag{4.34}$$

where $\Omega(t)$ is the rotation rate about an axis in the x-y plane oriented at an angle $\phi(t)$ to the x axis and $\chi(t)$ is the one-axis twisting rate which controls squeezing along the z direction. Squeezing is essential, as it is the only term in the Hamiltonian (4.34) responsible for the creation of non-classical states from spin-coherent states [245]. A Hamiltonian of this form has been successfully implemented in a variety of experimental settings, including the hyperfine manifolds of cesium atoms [246] and dysprosium atoms [236, 247] as well as in condensates of spin-1/2 particles [9, 248, 249], and in atomic ensembles in optical cavities where light-mediated interactions induce similar effective spin dynamics [250]. For strontium atoms, this Hamiltonian has been investigated numerically for the universal generation of quantum states and gates [251], and has also been realised experimentally [252]. In addition, the one-axis twisting term χJ_z^2 has already been realised on several experimental platforms [253–255].

We will show that the number of control parameters can be reduced while still allowing the generation of AC states. To do this, we fix $\phi(t) = \pi/2$. The Hamiltonian (4.34) then reduces to the well-studied one-axis twisting and rotation Hamiltonian $H(t) = \Omega(t)J_y + \chi(t)J_z^2$, which can be used to produce extreme spin squeezed states achieving the Heisenberg limit, see e.g. [256]. Our protocol exploits this Hamiltonian to maximise the objective function $\mathcal{A}_t^{\mathrm{B}}(|\psi\rangle\langle\psi|)$ starting from a pure coherent spin state $|\psi_0\rangle$. In QOC, the most efficient algorithms rely on the calculation of the gradient of the objective function with respect to the controls. However, in our case, gradient-based methods, such as LBFGS or gradient descent with the use of automatic differentiation, frequently only found local minima, resulting in a suboptimal set of parameters and anticoherence measure. Initially, to find controls that generate AC states, we used the well-known gradient-free CRAB algorithm [257] with the Hamiltonian (4.34), which gave satisfactory results for small orders of anticoherence. For example, we were able to find controls that generate spin states close to anticoherent states to order 5, with $1 - \mathcal{A}_5 < 10^{-3}$ for $j = 9$. However, we developed a pulse-based protocol that uses the same control parameters, specifically designed for the generation of AC states, which greatly outperformed CRAB in terms of speed, convergence and scalability. Despite the limitations of the gradient-free Nelder-Mead method, our approach has enabled us to find controls that can successfully produce higher-order AC states (up to $t = 9$ for $j = 24$) and that can handle large spins (up to $j = 5000$ for $t = 2$). Furthermore, because our protocol applies the pulses sequentially, it is not limited by the bandwidth of the control frequency, unlike in QOC.

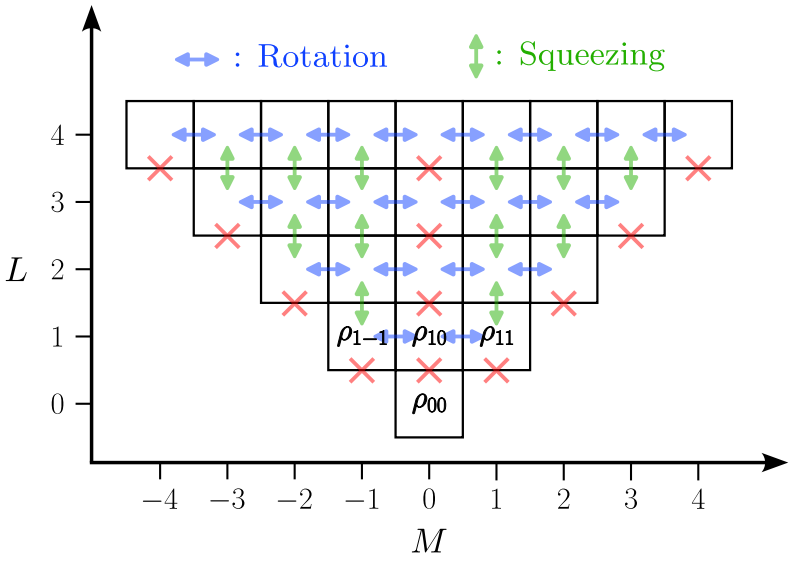

Figure 4.5: Diagram illustrating the coupling between state multipoles (for $j = 2$). Each square represents a multipole ρ_{LM} of the spin state from the multipolar expansion (these are shown explicitly for $L = 0, 1$). Blue and green arrows indicate the effects of rotation (J_y generator) and squeezing (J_z^2 generator), respectively. Red crosses denote either the absence of coupling between two multipoles or the absence of an adjacent multipole.

4.4.2 Pulse-based protocol

The key idea behind our pulse-based protocol lies in the distinct multipole coupling behaviors of the squeezing and rotation operations. Squeezing generated by J_z^2 couples a multipole ρ_{LM} only to its neighbors $\rho_{L\pm1,M}$, while the rotation generated by J_y affects only multipoles with the same L (see Figure 4.5 and Appendix 4.B for details). Through squeezing, population can therefore be transferred from a multipole at level L to one at level $L + 1$, which is desirable when seeking to generate anticoherent states, in which all multipole moments of order less than or equal to t are suppressed. While squeezing enables this upward transfer, it can also cause reverse coupling from $L + 1$ to L, which can reintroduce lower-order moments and prevent anticoherence from being achieved. However, this can be avoided by placing the $L+1$ multipoles in specific M states, namely $M = 0$ and $M = \pm L$, which are decoupled from the lower levels. By steering the population into these decoupled states, we can isolate the populated multipoles in the upper level while allowing those at L to transition upward to $L + 1$ without unwanted backflow. Figure 4.9 clearly demonstrates this behavior, see subsubsection 4.4.3.2.

Based on this idea, our protocol consists of a sequence of n_C cycles, where each cycle (except the first) applies a rotation about the y-axis followed by a squeezing operation along z. Thus, in the one-axis twisting and rotation Hamiltonian, we alternate between applying squeezing ($\chi(t) \neq 0$, $\Omega(t) = 0$) and rotation ($\Omega(t) \neq 0$, $\chi(t) = 0$) by activating only one term at a time. The corresponding operations are described by the operators

$$R_y(\theta) = e^{-iJ_y\theta}, \qquad S_z(\eta) = e^{-iJ_z^2\eta}$$

where θ and η are the amplitudes of the rotation and the squeezing. Note that this sequence of pulses is similar to the protocol presented in [256]. The final state of the

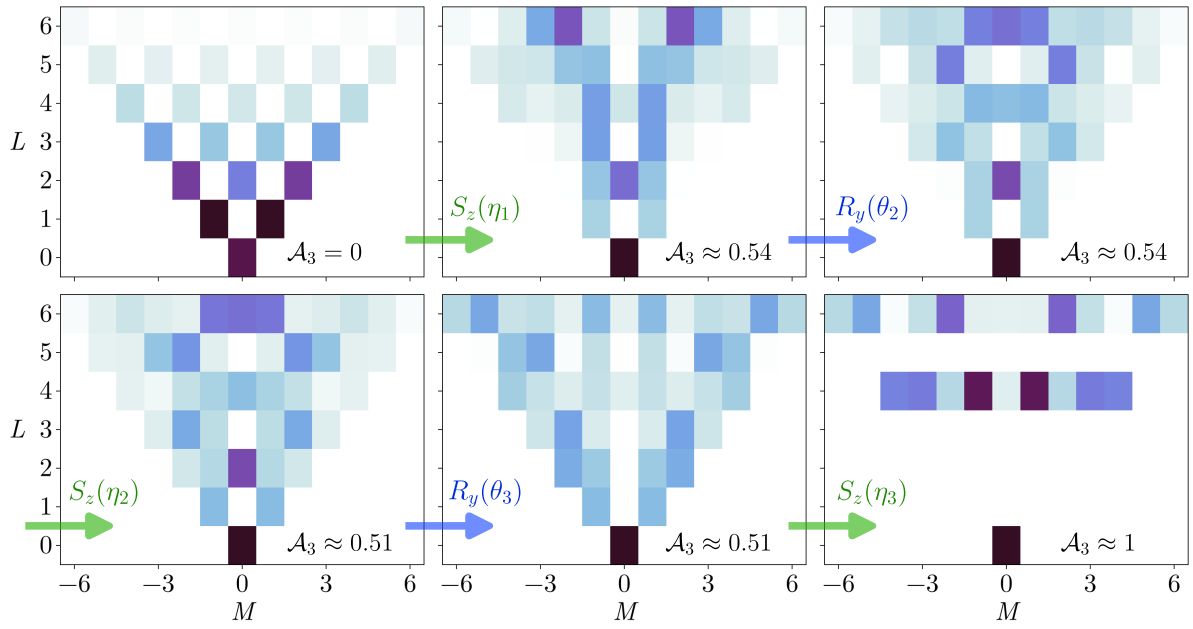

Figure 4.6: Protocol for generating anticoherent states of order 3 for spin $j = 3$ using $n_C = 3$ cycles. The optimization is performed over all parameters ($\eta_1, \eta_2, \eta_3, \theta_2$ and θ_3). Each colored rectangle represents the modulus squared of the corresponding multipole of the multipolar expansion. The final anticoherence measure reaches $1 - \mathcal{A}_3 < 10^{-7}$.

system after n_C cycles is then given by

$$|\psi_{n_C}\rangle = \left(\prod_{i=1}^{n_C} S_z(\eta_i)\, R_y(\theta_i) \right) |\psi_0\rangle$$

where θ_1 is always taken as zero since it is necessary to first perform a squeezing. The initial state $|\psi_0\rangle$ is the coherent state that points in the direction of the y-axis. For each sequence, we optimize the parameters $\{\theta_i,\, i = 2, 3, \ldots, n_C\}$ and $\{\eta_i,\, i = 1, 2, \ldots, n_C\}$ to generate an AC state of a given order, that is, a state that maximises the Bures t-AC measure for a given t. As we shall see, while this approach is fully realizable with the Hamiltonian (4.34), it is specifically tailored for AC state generation rather than producing arbitrary spin states.

4.4.3 Results

4.4.3.1 Numerical optimization

We first optimize the parameters η_i and θ_i numerically using the gradient-free Nelder-Mead algorithm. Figure 4.6 shows the pulse sequence obtained for $j = 3$, which prepares an AC state of order 3 with a deviation $1 - \mathcal{A}_3 < 10^{-7}$ in $n_C = 3$ cycles. The first squeezing operation, $S_z(\eta_1)$, transfers the population from the lower-order multipoles $\rho_{2\pm2}$ to the higher-order multipoles $\rho_{6\pm2}$. The subsequent rotation, $R_y(\theta_2)$, shifts the dominant population within $L = 6$ from $M = \pm2$ to $M = 0$. As discussed previously, the $M = 0$ components are decoupled from lower-order multipoles under squeezing, allowing the next squeezing step to preserve these higher-order contributions without transferring them back. Finally, the rotation $R_y(\theta_3)$ removes any residual population in ρ_{20} by transferring it to $\rho_{2\pm1}$ and $\rho_{2\pm2}$, which are completely eliminated by the final squeezing operation.

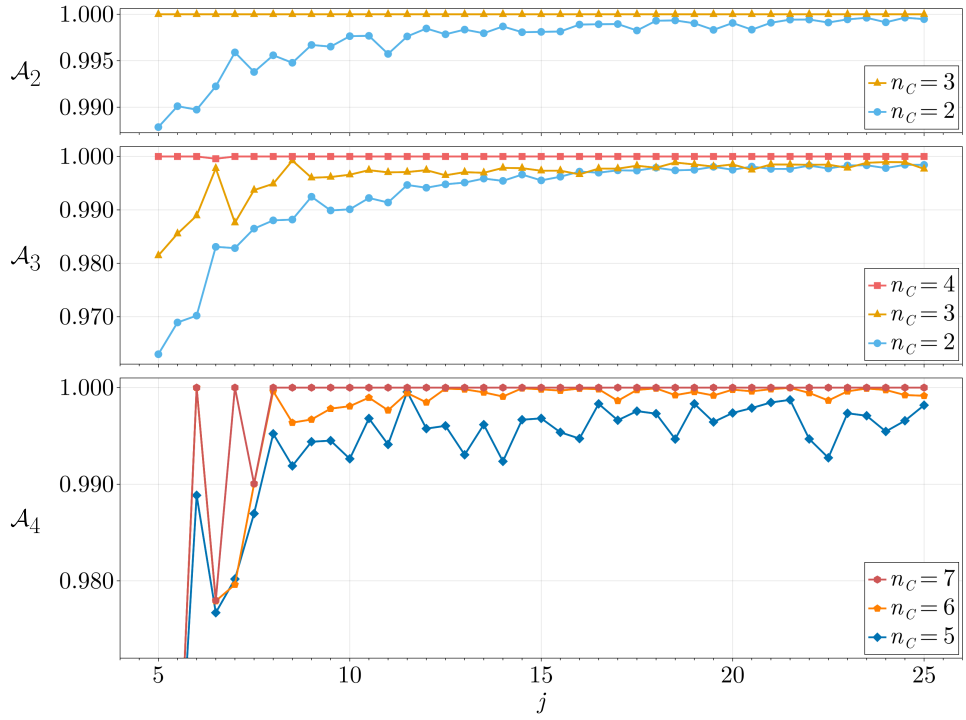

Figure 4.7: Highest anticoherence measure achieved using the pulse-based protocol for orders $t = 2, 3$ and 4 (from top to bottom), shown as a function of the spin quantum number j for different numbers of cycles n_C.

In Figure 4.7, we present the maximum AC measures of order $t = 2, 3$ and 4 obtained by optimizing this protocol, as a function of the spin quantum number j for different numbers of rotation-squeezing cycles n_C. The top panel reveals a clear qualitative difference between $n_C = 2$ and $n_C = 3$, the latter ensuring that all generated states satisfy $1 - \mathcal{A}_2 < 10^{-7}$. This suggests that $n_C = 3$ acts as a threshold in the pulse-based protocol to achieve AC to order $t = 2$. A similar threshold behavior is observed for $t = 1$ (data not shown), $t = 3$, and $t = 4$, occurring at $n_C = 1$, $n_C = 4$, and $n_C = 7$, respectively, as illustrated in the second and third panels. This seems to indicate that the pulse-based protocol is indeed specifically optimized to generate AC states. Finally, with $n_C = 14$, we are able to successfully generate a state with $\mathcal{A}_9 > 0.99$ for $j = 24$, corresponding to the highest AC order achievable with such precision before the number of cycles becomes too large for the Nelder-Mead optimization to remain effective.

In Table 4.2, we present the accumulated values of rotation and squeezing obtained for the generation of AC states of order $t = 2, 3, \ldots, 7$, up to numerical errors ($1 - \mathcal{A}_t < 10^{-15}$). These control parameters were obtained to minimise the total squeezing time, which is anticipated to be the limiting factor on the experimental duration of the protocol. The chosen spin number j is systematically the smallest one for which a given order of anticoherence t is theoretically possible. The values found for each parameter (for $j = 2, 3, 6$ and 12) are provided in a GitHub repository [258], alongside Julia code used to optimize our protocol. Based on the values in Table 4.2, this pulse-based protocol is experimentally accessible with current technology, both in terms of the necessary gates [256] and the attainable experimental parameters θ and η [259, 260]. For example, the coherence times of the coherent and spin cat states in a Sb donor nucleus ($j = 7/2$) implanted in silicon-based chip are respectively of $T \approx 100\,\text{ms}$ and $T \approx 14\,\text{ms}$. Based on

j	t	n_C	Total rotation $\sum_{i=1}^{n_C} \lvert\theta_i\rvert$	Total squeezing $\sum_{i=1}^{n_C} \lvert\eta_i\rvert$
2	2	2	0.560	1.323
3	3	3	3.824	1.325
6	4	6	9.818	0.959
6	5	6	6.496	1.043
12	6,7	12	17.812	1.953

Table 4.2: Minimum number of cycles n_C required to generate a pure AC state of order t (with $1 - \mathcal{A}_t < 10^{-15}$) in a spin-$j$ system. The values chosen for j are the smallest that still allow the generation of an AC state to order t. For those values, we observe that n_C always coincides with j. The last two columns of the table indicate the accumulated values of rotation and squeezing required to generate the state.

conservative value of the squeezing strength χ, a typical squeezing parameter $\eta = \chi t = \pi/2$ is achievable in 4.375 ms [259, 260], well within the coherence time of the system.

4.4.3.2 Analytical results for $t = 2$

Our numerical results show that the cat state, which is AC of order 1, can always be generated in a single cycle using $\eta_1 = \pi/2$ for any j, a finding previously reported and proved in [261–263].

Similarly, we have just seen in Figure 4.7 that AC states of order 2 can be generated from 3 cycles for all j. Based on this observation and on the intuition provided by Figure 4.5, we were able, for integer spin j, to derive analytical values for the required control parameters. By examining the effect of the control parameters on the multipoles T_{LM} for $L \leq 2$, we identified that 2-AC spin-j states could be generated using the following set of squeezing and rotation values

$$\eta_1 = \frac{\pi}{2}, \quad \theta_2 = -\frac{\pi}{4j}, \quad \theta_3 = \frac{\pi}{2}. \tag{4.35}$$

These were subsequently adopted as an ansatz for the next steps of our protocol. Using

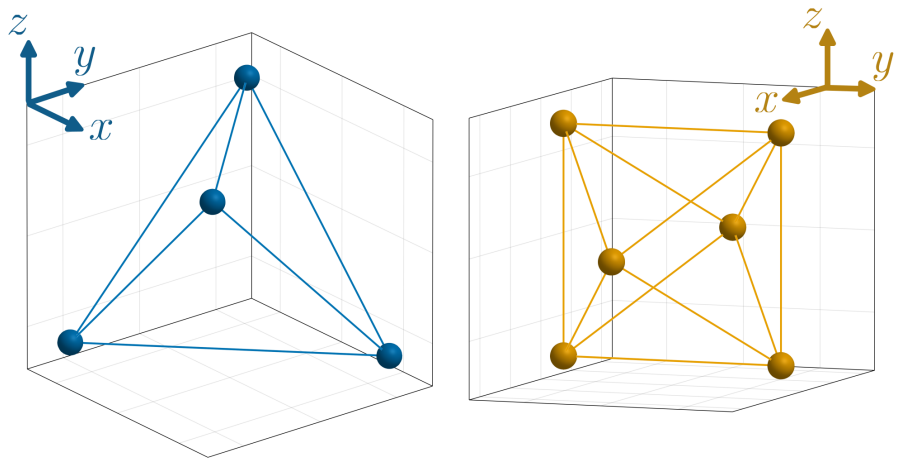

Figure 4.8: Majorana representation of the states (4.37) (left) and (4.39) (right) produced by 3 rotation-squeezing cycles.

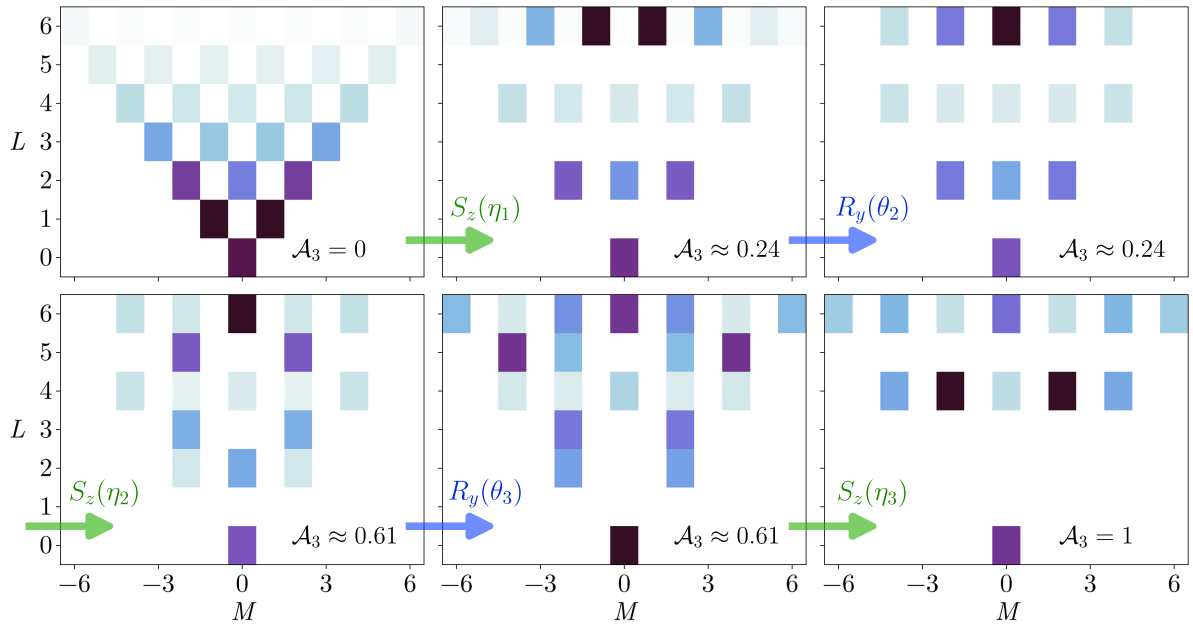

Figure 4.9: Protocol for generating spin-3 AC states of order 3 based on $n_C = 3$ cycles. The control parameters used are those given in (4.35) and (4.38).

a symbolic computation program and the results from Appendix 4.B, we further obtained the following squeezing parameters for $j = 2$

$$\eta_2 = -\frac{\operatorname{arccot}\sqrt{2}}{2}, \quad \eta_3 = \frac{\operatorname{arccot}\sqrt{2}}{4}. \tag{4.36}$$

With the control parameters (4.35) and (4.36), the generated state is the tetrahedron state (as shown in Figure 4.8)

$$\left|\psi_{t=2}^{\mathrm{HOAP}}\right\rangle = c_1|2,-2\rangle + c_2|2,0\rangle + c_1|2,2\rangle \tag{4.37}$$

where

$$c_1 = \frac{-1/\sqrt{2}+i}{\sqrt{6}}, \qquad c_2 = \frac{\sqrt{2}+i}{\sqrt{6}}.$$

For $j = 3$, we found the parameter values

$$\eta_2 = -\frac{\operatorname{arccot}\sqrt{2}}{2}, \quad \eta_3 = \frac{1}{8}\left[\pi - \arctan\left(2\sqrt{2}\right)\right] \tag{4.38}$$

leading to the octahedron state (also represented in Figure 4.8)

$$\left|\psi_{t=3}^{\mathrm{HOAP}}\right\rangle = c_1|3,-3\rangle + c_2|3,-1\rangle - c_2|3,1\rangle - c_1|3,3\rangle \tag{4.39}$$

where

$$c_1 = -\frac{1}{4}i\left(\frac{1}{3}\left(-241+22\sqrt{2}i\right)\right)^{\frac{1}{8}}, \qquad c_2 = -\frac{i\sqrt{5}}{4}\frac{\left(1+11\sqrt{2}i\right)^{1/4}}{3^{5/8}}.$$

The latter state is not only AC of order 2 but also of order 3. This is a special result, as it is the only AC state of order 3 that we could obtain with only $n_C = 3$ cycles. The other AC states of order 3 we found needed $n_C = 4$ cycles, as can be seen in Figure 4.7.

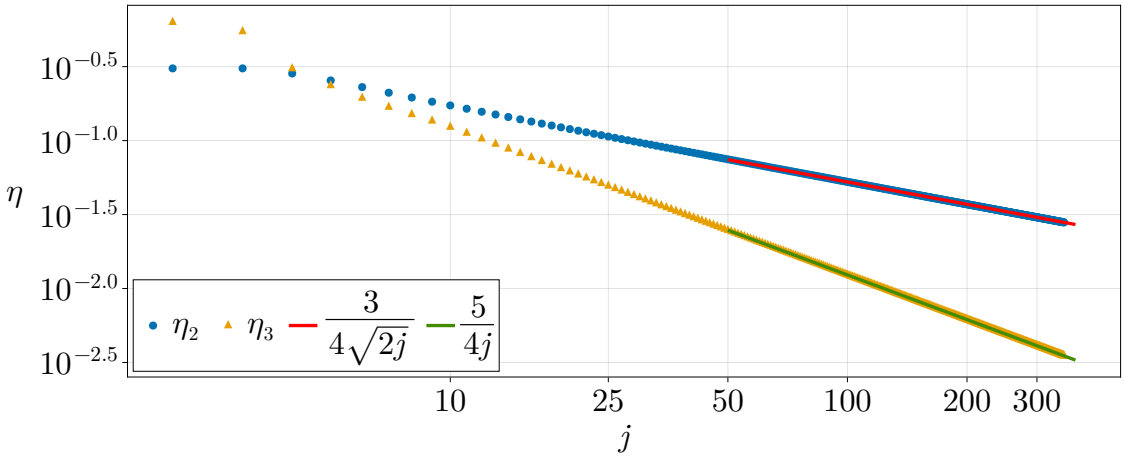

Figure 4.10: Squeezing parameters η_2 (blue dots) and η_3 (orange triangles) required for generating a 2-AC spin-j state with our pulse-based protocol. The other control parameters are set to $\eta_1 = \frac{\pi}{2}$, $\theta_1 = -\frac{\pi}{4j}$ and $\theta_2 = \frac{\pi}{2}$. The red and green lines represent the analytical approximations given in (4.40).

We show in Figure 4.9 the evolution of the state multipoles during the generation of the octahedron state (4.39). It can be compared to the protocol represented in Figure 4.6 which also gives an AC state of order 3 for $j = 3$. These analytical results are particularly remarkable because, although the applied controls do not allow the generation of arbitrary spin states, they can still produce exact AC states, as expected by our numerical results shown in Figure 4.7.

For $j > 3$, the parameters η_2 and η_3 are determined by numerical optimization to ensure that $1 - \mathcal{A}_2 < 10^{-6}$. For any j, the evolution of the multipoles to obtain an AC state of order 2 from the parameters (4.35) is similar to the evolution illustrated for $j = 3$ in Figure 4.9. The process begins by generating the cat state with $\eta_1 = \pi/2$. Next, the rotation $\theta_2 = -\pi/(4j)$ isolates the highly populated multipoles $\rho_{2j\pm1}$ from the lower levels by transferring them to ρ_{2j0}. This is followed by the squeezing η_2, which shifts the $\rho_{2\pm2}$ multipoles to higher L. The subsequent rotation $\theta_3 = \frac{\pi}{2}$ fully transfers ρ_{20} to $\rho_{2\pm2}$. Finally, the squeezing η_3 further moves these multipoles to higher L, completing the protocol.

This approach of first generating the 1-AC state and then the 2-AC state is not the most time-efficient in terms of squeezing and rotation durations. However, the initial cat state produced by the first squeezing $\eta_1 = \pi/2$ could be generated more rapidly using alternative dynamical methods [264–266] or based on post-selection [267], thus reducing the total time required for the spin squeezing. As this first large squeezing $\eta_1 = \pi/2$ represents a substantial portion of the total squeezing time, the exploration of alternative methods to generate the cat state could prove to be highly advantageous.

Additionally, these analytical values minimise the number of parameters that need optimization, enabling the generation of AC states of order 2 for larger spin numbers. Figure 4.10 shows the squeezing parameters η_2 and η_3, obtained via numerical optimization up to $j = 350$, as functions of j in log-log scale, providing strong evidence that they follow power laws well approximated by

$$\eta_2(j) = \frac{3}{4\sqrt{2j}}, \qquad \eta_3(j) = \frac{5}{4j}. \tag{4.40}$$

The validity of these expressions seems to extend well beyond the fitting region, since by using (4.40) for η_2 and η_3 for $j = 5000$, the generated state has a 2-AC measure close to 1 with a deviation $1 - \mathcal{A}_2 < 10^{-3}$.[3]

Conclusion

Over the last years, anticoherent states have garnered increasing attention due to their theoretical properties and practical applications. Since their initial definition based on isotropy properties (4.1), it was shown that their phase-space quasidistributions exhibit high degree of delocalisation and that t-AC states are maximally entangled symmetric states w.r.t. bipartition $t|N-t$. These are reliable indicators that AC states are highly non-classical. Following their quantum properties, AC states are optimal pure symmetric states for rotosensing, magnetometry and frame alignement tasks. Furthermore, we showed in this chapter that subspaces of pure AC states are good candidates for quantum error-correction algorithms since they verify the Knill-Laflamme condition.

We also clarified in this chapter the relation between anticoherence and entanglement. While in the case of pure states, the isotropy condition (4.1) can only be obtained by quantum superposition, it is no longer the case for mixed states for which isotropy can arise from classical mixture of states. However, mixed AC states can still show high degree of entanglement and quantum metrology usefulness. Hence, it was necessary to divide anticoherence measures into two distinct measures of classical and quantum anticoherence. We did so by using a first result on the relation between the Bures t-AC measure and the negativity of the partial transpose. It allowed us to define the quantum anticoherence measure as the convex-roof of the negativity and we showed that it is always smaller than the Bures t-AC measure, i.e. the total t-AC measure.

Finally, due to their potential use in quantum technologies, it is needed to find protocols to generate t-AC states for different experimental platforms. While some specific AC states were already produced in photonic systems, and their metrological usefulness ascertained, there was no clear path to generate general t-AC states in cold atoms experiments. Here, we presented a simple and efficient protocol for the deterministic generation and protection of AC states. Our pulse-based protocol, which involves cycles of rotations followed by squeezing, has demonstrated remarkable efficiency in producing AC states of different orders, achieving a high degree of anticoherence even for large spin quantum numbers. Through numerical optimization and analytical derivations, we have identified the optimum parameters for the rotation and squeezing operations, enabling the generation of AC states up to order 9 for spin-24 systems and order 2 for collective spin ensembles. Our protocols can be applied to any physical platform where rotation and squeezing operations are possible, such as magnetic atoms, spin ensembles, qudits or even Bose-Einstein condensates.

The results presented in this chapter suggest several new research directions. Firstly, as the purity t-AC measure for pure states is directly related to optimality of quantum metrology tasks and as mixed optimal quantum rotosensors are given by mixed AC states, a possible area for further research would be to establish a connection between the

[3]For large spin j, low-order AC measures of random states sampled according to the Haar measure can be significantly high (see related [268]). Therefore, we might suspect that the state we can generate for $j = 5000$ is simply a random state with a high 2-AC measure. However, this is not the case. For a sample of 5000 random states, we find an average value of $1 - \mathcal{A}_2 > 10^{-2}$ (with a standard deviation $\sigma < 3.3 \cdot 10^{-3}$), which is an order of magnitude larger than that of our generated state.

quantum measure of anticoherence and an indicator of optimality in quantum metrology, such as quantum Fisher information. This would give a direct link between optimality in quantum metrology and entanglement. Secondly, our result on the verification of the Knill-Laflamme condition by AC subspaces is a preliminary step on the possible use of AC states for quantum error correction. Further work is definitely needed to find concrete protocols able to correct errors from AC subspaces. As correction of high order errors seems possible by using only one spin system, it might be possible to implement QEC with AC subspaces without the need of repeating code. Finally, future research could explore the use of more sophisticated Hamiltonian dynamics, such as two-axis anisotropic countertwisting [269] or effective three-body collective-spin interactions [270], to further speed up the generation of AC states. Beyond deterministic coherent control schemes, AC states could also be generated probabilistically via post-selection [271] or through dissipative state preparation methods. An interesting direction to explore could be the use of quantum non-demolition measurement schemes based on multicolor probing, as demonstrated in [272], which may offer another approach to generate AC states in atomic ensembles with increased robustness against technical noise and inhomogeneous broadening. Investigating these alternatives may offer new avenues for producing practically useful AC states under less stringent coherence requirements, expanding their applicability to realistic experimental platforms.

4.A Table of anticoherent states

We give in Table 4.3 below examples of HOAP states (taken from Refs. [25, 66, 222]) expressed in both the standard angular momentum basis and the multipole operator basis.

4.B Evolution of the multipoles under squeezing

In this Appendix, we show that the rotation generator J_y couples a multipole of order M only to those of order $M \pm 1$, without changing the value of L, while the squeezing generator J_z^2 couples a multipole of order L only to those of order $L \pm 1$, without altering the value of M. Throughout this section, we set $\hbar = 1$.

4.B.1 Rotation

Under the unitary evolution generated by the Hamiltonian ΩJ_y, the density matrix in the multipolar basis evolves according to

$$i \sum_{LM} \dot{\rho}_{LM} T_{LM} = \Omega \sum_{LM} \rho_{LM} \left[J_y, T_{LM} \right]. \tag{4.41}$$

The operator J_y can be expressed in terms of the ladder operators as

$$J_y = \frac{J_+ - J_-}{2i}$$

and its commutator with any multipole operator is given by

$$[J_\pm, T_{LM}] = \sqrt{L(L+1)} C^{LM\pm1}_{LM,1\pm1} T_{LM\pm1}.$$

Therefore, the commutator in (4.41) can be rewritten in the form

$$[J_y, T_{LM}] = \frac{\sqrt{L(L+1)}}{2i} \left(C^{LM+1}_{LM,11} T_{LM+1} - C^{LM-1}_{LM,1-1} T_{LM-1} \right).$$

Using the relations

$$C^{LM-1}_{LM,1-1} = \frac{\sqrt{(L-M+1)(L+M)}}{\sqrt{2L(L+1)}} \qquad C^{LM+1}_{LM,11} = -\frac{\sqrt{(L+M+1)(L-M)}}{\sqrt{2L(L+1)}}$$

and the orthogonality relation

$$\mathrm{Tr}\left(T_{LM} T^\dagger_{L'M'} \right) = \delta_{LL'} \delta_{MM'} \tag{4.42}$$

we find that the evolution of any multipole component ρ_{LM} is governed by

$$\sum_{LM} \dot{\rho}_{LM} = \frac{\Omega}{2\sqrt{2}} \left[(L-M+1)(L+M) \rho_{LM-1} + (L+M+1)(L-M) \rho_{LM+1} \right]$$

which depends only on the neighboring multipoles $\rho_{LM\pm1}$.

[4] For the sake of brevity and due to the relation $\rho^*_{LM} = (-1)^M \rho_{L-M}$, only the state multipoles ρ_{L-M} with $M \geqslant 0$ are given in the table.

j	t	Pure spin-j HOAP state and its non-zero multipoles[4]
1	1	$\|\psi\rangle = \frac{1}{\sqrt{2}}\left(\|1,1\rangle + \|1,-1\rangle\right)$ $\rho_{00} = \frac{1}{\sqrt{3}},\ \rho_{2-2} = \frac{1}{2},\ \rho_{2-2} = \frac{1}{2}$
3/2	1	$\|\psi\rangle = \frac{1}{\sqrt{2}}\left(\left\|\frac{3}{2},\frac{3}{2}\right\rangle + \left\|\frac{3}{2},-\frac{3}{2}\right\rangle\right)$ $\rho_{00} = \frac{1}{\sqrt{4}},\ \rho_{20} = \frac{1}{2},\ \rho_{3-3} = \frac{1}{2}$
2	2	$\|\psi\rangle = \frac{1}{2}\left(\|2,2\rangle + i\sqrt{2}\,\|2,0\rangle + \|2,-2\rangle\right)$ $\rho_{00} = \frac{1}{\sqrt{5}},\ \rho_{3-2} = \frac{i}{2},\ \rho_{4-4} = \frac{1}{4},\ \rho_{40} = \frac{1}{2}\sqrt{\frac{7}{10}}$
5/2	1	$\|\psi\rangle = \frac{1}{\sqrt{2}}\left(\left\|\frac{5}{2},\frac{3}{2}\right\rangle + \left\|\frac{5}{2},-\frac{3}{2}\right\rangle\right)$ $\rho_{00} = \frac{1}{\sqrt{6}},\ \rho_{20} = -\frac{1}{2\sqrt{21}},\ \rho_{3-3} = \frac{1}{3}\ \rho_{40} = -\frac{3}{2\sqrt{7}},\ \rho_{5-3} = -\frac{\sqrt{5}}{6}$
3	3	$\|\psi\rangle = \frac{1}{\sqrt{2}}\left(\|3,2\rangle + \|3,-2\rangle\right)$ $\rho_{00} = \frac{1}{\sqrt{7}},\ \rho_{4-4} = \frac{1}{2}\sqrt{\frac{5}{11}},\ \rho_{40} = -\sqrt{\frac{7}{22}},\ \rho_{6-4} = -\sqrt{\frac{3}{22}},\ \rho_{60} = -\sqrt{\frac{3}{77}}$
7/2	2	$\|\psi\rangle = \frac{\sqrt{2}}{3}\left\|\frac{7}{2},\frac{7}{2}\right\rangle + \frac{\sqrt{\frac{7}{2}}}{3}\left(\left\|\frac{7}{2},\frac{1}{2}\right\rangle + \left\|\frac{7}{2},-\frac{5}{2}\right\rangle\right)$ $\rho_{00} = \frac{1}{\sqrt{8}},\ \rho_{3-3} = \frac{7}{3\sqrt{66}},\ \rho_{30} = \frac{7}{6\sqrt{66}},$ $\rho_{5-3} = \frac{7}{6\sqrt{78}},\ \rho_{50} = \frac{7}{6}\sqrt{\frac{7}{78}},\ \rho_{6-6} = \frac{1}{9}\sqrt{\frac{7}{2}},\ \rho_{6-3} = \frac{1}{18}\sqrt{\frac{77}{2}},$ $\rho_{60} = -\frac{1}{6}\sqrt{\frac{11}{6}},\ \rho_{7-6} = \frac{1}{9}\sqrt{\frac{7}{2}},\ \rho_{7-3} = -\frac{5}{18}\sqrt{\frac{35}{143}},\ \rho_{70} = -\frac{8}{3}\sqrt{\frac{2}{429}}$
4	3	$\|\psi\rangle = \frac{\sqrt{\frac{5}{6}}}{2}\left(\|4,4\rangle + \|4,-4\rangle\right) + \frac{\sqrt{\frac{7}{3}}}{2}\,\|4,0\rangle$ $\rho_{00} = \frac{1}{3},\ \rho_{4-4} = \frac{7}{6}\sqrt{\frac{5}{143}},\ \rho_{40} = \frac{7}{3}\sqrt{\frac{7}{286}},\ \rho_{6-4} = \frac{1}{3}\sqrt{\frac{35}{22}},$ $\rho_{60} = -\frac{1}{3}\sqrt{\frac{5}{11}},\ \rho_{8-8} = \frac{5}{24},\ \rho_{8-4} = \frac{1}{12}\sqrt{\frac{35}{13}},\ \rho_{80} = \frac{1}{4}\sqrt{\frac{55}{26}}$
9/2	3	$\|\psi\rangle = \frac{1}{\sqrt{6}}\left(\left\|\frac{9}{2},\frac{9}{2}\right\rangle + \left\|\frac{9}{2},-\frac{9}{2}\right\rangle\right) - \frac{1}{\sqrt{3}}\left(\left\|\frac{9}{2},\frac{3}{2}\right\rangle + \left\|\frac{9}{2},-\frac{3}{2}\right\rangle\right)$ $\rho_{00} = \frac{1}{\sqrt{10}},\ \rho_{3-3} = \frac{10\sqrt{429}-3\sqrt{2002}}{1287},\ \rho_{40} = \frac{4}{\sqrt{715}},$ $\rho_{5-3} = -\frac{1}{117}\left(6\sqrt{26}+\sqrt{273}\right),\ \rho_{6-6} = -\frac{1}{\sqrt{30}},$ $\rho_{60} = \frac{1}{2}\sqrt{\frac{5}{33}},\ \rho_{6-6} = -\frac{1}{\sqrt{30}},\ \rho_{60} = \frac{1}{2}\sqrt{\frac{5}{33}},\ \rho_{7-3} = -\frac{5\sqrt{3}-2\sqrt{14}}{\sqrt{2431}},$ $\rho_{8-6} = -\frac{1}{3}\sqrt{\frac{7}{10}},\ \rho_{80} = -\frac{1}{6}\sqrt{\frac{55}{13}},\ \rho_{9-9} = \frac{1}{6},\ \rho_{9-3} = -\frac{\sqrt{2}+2\sqrt{21}}{3\sqrt{221}}$
5	3	$\|\psi\rangle = \frac{1}{\sqrt{11}}\left(\|5,5\rangle + \|5,-5\rangle\right) + \sqrt{\frac{3}{5}}\,\|5,0\rangle$ $\rho_{00} = \frac{1}{\sqrt{11}},\ \rho_{40} = 3\sqrt{\frac{2}{143}},\ \rho_{5-5} = \frac{3}{5\sqrt{13}},$ $\rho_{60} = -3\sqrt{\frac{3}{935}},\ \rho_{7-5} = \frac{6}{\sqrt{221}},\ \rho_{80} = 2\sqrt{\frac{22}{1235}},$ $\rho_{9-5} = \frac{1}{5}\sqrt{\frac{21}{17}},\ \rho_{10-10} = \frac{1}{5},\ \rho_{100} = -\frac{29}{5}\sqrt{\frac{13}{3553}}$

Table 4.3: Examples of HOAP states for the smallest values of the spin quantum number j, and their state multipoles. Here, t is the order of anticoherence of the state.

4.B.2 Squeezing

Under the unitary evolution generated by the Hamiltonian χJ_z^2, the density matrix in the multipolar basis evolves according to

$$i\sum_{LM}\dot{\rho}_{LM}T_{LM}=\chi\sum_{LM}\rho_{LM}\left[J_z^2,T_{LM}\right]. \tag{4.43}$$

In the multipolar basis, the squeezing operator is given by

$$J_z^2=\frac{j(j+1)\sqrt{2j+1}}{3}T_{00}+\frac{1}{6\sqrt{5}}\sqrt{\frac{(2j+3)!}{(2j-2)!}}T_{20}.$$

Since T_{00} is proportional to the identity matrix, it does not contribute to the evolution of the density matrix, meaning only the term involving T_{20} need to be considered. We can now use the general commutator between two multipolar operators, given by [69]

$$\begin{aligned}[T_{L_1M_1},T_{L_2M_2}]=\sqrt{(2L_1+1)(2L_2+1)}\sum_L(-1)^{2j+L}\left(1-(-1)^{L_1+L_2+L}\right)\\ \times\begin{Bmatrix}L_1 & L_2 & L\\ j & j & j\end{Bmatrix}C^{LM_1+M_2}_{L_1M_1,L_2M_2}T_{LM_1+M_2},\end{aligned}$$

where we used the $6j$-symbol and Clebsch-Gordan coefficients. These coefficients are non-zero only when $|L_1-L_2|\leq L\leq L_1+L_2$. In our case, since $L_1=2$, the maximum multipolar order reachable from L_2 is $L=L_2\pm 2$. However, for $L=L_2\pm 2$ or $L=L_2$, the factor

$$1-(-1)^{L_1+L_2+L}$$

vanishes, leading to the final expression

$$\begin{aligned}\left[J_z^2,T_{LM}\right]=\frac{M}{\sqrt{2L+1}}\left(\sqrt{\frac{(L-M+1)(L+M+1)(2j-L)(2j+L+2)}{2L+3}}T_{L+1M}\right.\\ \left.+\sqrt{\frac{(L-M)(L+M)(2j-L+1)(2j+L+1)}{2L-1}}T_{L-1M}\right).\end{aligned}$$

Finally, using the orthogonality property (4.42), (4.43) simplifies to

$$\begin{aligned}\dot{\rho}_{LM}=\frac{\chi}{i}\frac{M}{\sqrt{2L+1}}\left(\sqrt{\frac{(L-M)(L+M)(2j-L+1)(2j+L+1)}{2L-1}}\rho_{L-1M}\right.\\ \left.\sqrt{\frac{(L-M+1)(L+M+1)(2j-L)(2j+L+2)}{2L+3}}\rho_{L+1M}\right),\end{aligned}$$

which clearly shows that a multipole of order L is coupled only to its adjacent multipoles of order $L\pm 1$.

Chapter 5

Extreme depolarisation of spin states

In experimental settings, quantum systems are inevitably coupled to their environment, often resulting in the detrimental loss of coherence and entanglement. A central figure of merit in assessing the quality of a quantum system is its coherence time—the timescale over which the system can reliably maintain quantum information or remain in a superposition before decoherence drives it into a statistical mixture. While decoherence is typically seen as a limitation, recent studies have highlighted its potential for constructive applications, including quantum state preparation via the Quantum Mpemba Effect (QME) [273, 274, 275] and in quantum thermometry [276, 277].

In the previous chapter, we examined the growing significance of spin systems with more than two levels as promising platforms for quantum technologies. These systems, which may be interpreted as multi-qubit ensembles restricted to the symmetric subspace, are now experimentally accessible with increasing precision. In this chapter, we turn our attention to fundamental aspects of decoherence in such spin systems. Most prior work on spin depolarisation has either followed a phenomenological approach based on a depolarisation channel [278, 279, 280, 281, 282], or has focused on dynamical decoherence of specific states, such as NOON states and coherent states [283, 284]. Our goal here is to go beyond these approaches and analyse spin depolarisation in a general framework, through two perspectives: purity loss and entanglement decay.

A key assumption of the dynamics we consider is that the total energy of the spin system and its environment is conserved, in accordance with thermodynamic principles [285, 286]. This assumption, which holds for all microscopic models yielding Markovian master equations, leads to nontrivial constraints on the decoherence rates. As we shall see, the time evolution has two important properties : it is unital and separability-preserving. Under such dynamics, an initial pure state $|\psi_0\rangle$ evolves into a mixed state ρ whose purity

$$R(\rho) \equiv \mathrm{Tr}\left(\rho^2\right)$$

decreases monotonically with time. Eventually, the state ρ converges to the unique stationary state, the MMS defined on $\mathcal{H} \simeq \mathbb{C}^{2j+1}$.

Throughout this process, quantum entanglement, quantified via negativity across various bipartitions of the N-qubit system, also decays. Interestingly, the state may transiently pass through PPT entangled states, but ultimately becomes separable after a finite time. Beyond this point, it remains separable indefinitely, eventually entering the ball of absolutely separable states (discussed in Chapter 2), from which no entanglement can be restored by unitary operations alone.

Building on our results on the depolarisation of spin systems, we explore its application in dynamical quantum metrology, where one wants to infer the value of the depolarisation

rate based on the dissipative dynamics of the system. This will allow us to find optimal states for isotropic noisy magnetic field and temperature sensing, both of which are critical in the calibration of precision instruments.

This chapter is organized as follows. In Section 5.1, we present the Lindblad master equation describing the depolarisation of an arbitrary spin and its expression in the multipolar tensor basis. We discuss a conservation law for the dynamics, its steady states and a general solution for the density matrix and its reductions. In Section 5.2, we study isotropic depolarisation, from the evolution of purities and entanglement, the condition of appearance of superdecoherence, and identify the HOAP states as the most sensitive states to isotropic depolarisation. Then, in Section 5.3, we analytically determine the initial states that experience the fastest purity loss under anisotropic depolarisation for any spin j and identify long-time optimal states for $j = 2$. Finally, we explore in Section 5.4 the estimation of dissipative rates in the context of depolarisation and relate it with dynamical quantum metrology, in particular quantum thermometry and noisy magnetometry. This chapter builds primarily on the results of [36]. However, the discussion presented here on the dynamical quantum metrology constitutes original additional contributions.

5.1 Depolarisation master equation

We consider the dynamics of a spin system governed by a master equation of the Lindblad form

$$\dot{\rho}(t) = \frac{i}{\hbar}[\rho(t), H] + \sum_{\alpha=x,y,z} \mathcal{D}_\alpha[\rho(t)] \tag{5.1}$$

with the Hamiltonian $H = \hbar\omega J_z$ and the dissipator

$$\mathcal{D}_\alpha[\rho] = \gamma_\alpha \left(2J_\alpha \rho J_\alpha - J_\alpha^2 \rho - \rho J_\alpha^2\right) \quad . \tag{5.2}$$

This describes a spin-j system undergoing Markovian depolarisation along the three spatial directions x, y and z with potentially different decoherence rates γ_x, γ_y and γ_z. In particular, our master equation describes the well-known pure dephasing of a spin when $\gamma_x = \gamma_y = 0$ and $\gamma_z \neq 0$. In the following, we will refer to *isotropic* depolarisation when $\gamma_x = \gamma_y = \gamma_z$ and to *anisotropic* depolarisation when $\gamma_x = \gamma_y \neq \gamma_z$.

Since the dissipator contains only Hermitian jump operators, the Lindblad generator is unital, implying that the purity of the state $\rho(t)$ can only decrease with time (see e.g. [287]). We present physical models that give rise to such master equations in Appendix 5.A. Notably, we show how a Hamiltonian, strongly driving a system which interacts with a thermal bath, can lead to anisotropic depolarisation. Various models leading to the same form of dynamical evolution have been proposed and studied in the literature. For instance, the derivation of a master equation describing isotropic depolarisation of multiphoton states was carried out in [283] based on SU(2) invariance. The effect of isotropic decoherence for a qubit on Uhlmann's mixed state geometric phase was studied in [288]. In Ref. [289], the anisotropic depolarisation of light stemming from its interaction with a material medium was analysed. A master equation describing anisotropic depolarisation of a spin-1/2 was derived from a microscopic Hamiltonian model in [290] and from disordered Hamiltonian ensembles in [291]. A non-Markovian version for a central spin-1/2 interacting with a spin bath has been derived in [292].

Note that microscopic models and thermodynamic principles constrain the allowed values of the decoherence rates γ_α. Under the assumptions that the spin environment is in thermal equilibrium and that the interaction Hamiltonian between the spin and the environment commutes with both Hamiltonians of the spin and the environment, a condition coined as strict conservation of energy, the unitary and dissipative evolutions necessarily commute [285, 286], i.e. $[\mathcal{U}, \mathcal{D}] = 0$ where $\mathcal{U}(\cdot) = (i/\hbar)\,[\cdot, H]$ and $\mathcal{D}(\cdot) = \sum_{\alpha=x,y,z} \mathcal{D}_\alpha(\cdot)$ for the master equation (5.1). For $\omega \neq 0$, the condition $[\mathcal{U}, \mathcal{D}] = 0$ holds only if $\gamma_x = \gamma_y$[1]. Physically, this reflects the fact that the unitary part induces a spin precession around the z-axis, and the dissipator is invariant under rotations about the z-axis only when $\gamma_x = \gamma_y$. For this reason, we will focus on the case $\gamma_x = \gamma_y \equiv \gamma_{\perp z}$. For isotropic depolarisation, $[\mathcal{U}, \mathcal{D}] = 0$ even for a more general Hamiltonian $H = \boldsymbol{\omega} \cdot \mathbf{J}$ with $\boldsymbol{\omega} = (\omega_x, \omega_y, \omega_z)$. When Hamiltonian evolution commutes with dissipative evolution, it has no impact on how the purity and entanglement of the state evolves with time. Since a linear Hamiltonian evolution conserves purity and entanglement of a state, we henceforth discard the Hamiltonian part of the evolution and focus entirely on the dissipative dynamics.

5.1.1 Master equation in the multipolar tensors basis

A general spin decoherence master equation can be expressed as

$$\dot{\rho} = \sum_{\alpha=x,y,z} \gamma_\alpha \left[\left[\rho, J_\alpha\right], J_\alpha\right] \tag{5.3}$$

In the MPB, each state multipole evolves according to

$$\dot{\rho}_{LM} = -\Gamma_{LM}\rho_{LM} - \Gamma_{LM+2}\rho_{LM+2} - \Gamma_{LM-2}\rho_{LM-2} \tag{5.4}$$

with the rates

$$\Gamma_{LM} = \gamma_z M^2 + \frac{\gamma_x + \gamma_y}{2}\left[L(L+1) - M^2\right] \tag{5.5}$$

$$\Gamma_{LM\pm2} = \frac{\gamma_x - \gamma_y}{4} d^{\pm}_{LM} \tag{5.6}$$

where

$$d^{\pm}_{LM} = \sqrt{(L \mp M)(L \pm M + 1)(L \mp M - 1)(L \pm M + 2)}. \tag{5.7}$$

Multipoles with different L are decoupled, as are components with even or odd M, resulting in a block-diagonal Liouvillian in the MPB, with $N+1$ blocks of size $2L+1$ for $L = 0, \ldots, N$. From (5.4), we see that the block for $L = 0$ is equal to 0, so that the stationary state has always a component on the MMS such that the component ρ_{00} remains equal to $1/\sqrt{N+1}$ at all times, which is simply due to normalisation of the state ρ. The blocks for $L > 0$ have diagonal elements $-\Gamma_{LM}$ for $M = -L, \ldots, L$ and symmetric off-diagonal elements $-\Gamma_{LM\pm2}$. When $\gamma_x = \gamma_y$, $\Gamma_{LM\pm2} = 0$ and the Liouvillian is diagonal in the MPB and each ρ_{LM} evolves independently.

Notably, it appears from (5.4) that the dynamics conserves the property of anticoherence of a state at any time. Indeed, if the state multipoles ρ_{LM} are initially equal to zero for some L and $\forall\ M = -L, \ldots, L$, they remain zero at all times. Therefore, an initial

[1] A direct calculation shows that $[\mathcal{U}(\rho), \mathcal{D}(\rho)] = \frac{i\omega}{2}(\gamma_x - \gamma_y)\sum_{LM}(\sum_\pm \pm d^{\pm}_{LM} T_{LM\pm2})\rho_{LM}$ with $d^{\pm}_{LM}$ defined in (5.7) and ρ_{LM} the state multipoles of ρ. Hence, the conclusion that $[\mathcal{U}(\rho), \mathcal{D}(\rho)] = 0$ for any ρ iff $\gamma_x = \gamma_y$.

q-AC state remains q-AC at any time[2]. We emphasise that this property would still hold if the γ_α rates were time dependent or took negative values to model non-Markovian dynamics. Therefore, the property of anticoherence of a state is very generally conserved under the model of decoherence corresponding to the master equation (5.1).

5.1.2 Exact solutions for ρ and its reductions

Under strict energy conservation ($\gamma_x = \gamma_y$), the state multipoles are fully decoupled and obey

$$\dot{\rho}_{LM} = -\Gamma_{LM}\rho_{LM} \tag{5.8}$$

whose general solution is given by

$$\rho_{LM}(t) = e^{-\Gamma_{LM}t}\rho_{LM}(0). \tag{5.9}$$

The solution (5.9) allows us to directly access the state multipoles of all the reduced states of ρ. Consequently, the state multipoles $\rho^{(q)}_{LM}$ of the q-qubit reduced density matrix $\rho_q = \mathrm{Tr}_{\neg q}[\rho]$ can be expressed in terms of the ρ_{LM} of ρ as

$$\rho^{(q)}_{LM}(t) = \frac{q!}{N!}\sqrt{\tfrac{(N-L)!(N+L+1)!}{(q-L)!(q+L+1)!}}\rho_{LM}(t) \tag{5.10}$$

for $L \leqslant q$ and $-L \leqslant M \leqslant L$. In the following, we will heavily rely on equations (5.9) and (5.10) for our analytical and numerical results. A first observation is that when $\gamma_{\perp z} = \gamma_x = \gamma_y \neq 0$, all multipoles decay exponentially, except ρ_{00}, and the system asymptotically approaches the MMS.

5.1.3 Decrease of purity

In order to identify the states that are the most prone to decoherence, we focus on the rate of change of the purity $\dot{R}(\rho)$ and its higher order time derivatives. These quantities can be expressed in a simple form when $\gamma_x = \gamma_y$ because then (5.8) implies that

$$d|\rho_{LM}|^2/dt = -2|\rho_{LM}|^2\Gamma_{LM}.$$

Repeated use of the latter equality together with the expression of the state purity in terms of its state multipoles yields for the n-th order time derivative

$$\frac{d^n R(\rho)}{dt^n} = (-2)^n \sum_{L,M} |\rho_{LM}|^2 (\Gamma_{LM})^n = (-2)^n \overline{(\Gamma_{LM})^n} R(\rho) \tag{5.11}$$

where we define the average value in state ρ of a function f of variables L and M by

$$\overline{f(L,M)} = \frac{\sum_{L,M}|\rho_{LM}|^2 f(L,M)}{\sum_{L,M}|\rho_{LM}|^2}. \tag{5.12}$$

In particular, the rate of change of purity, which is also equal to the opposite of the linear entropy production rate [293], is given by

$$\dot{R}(\rho) = -2\overline{\Gamma_{LM}}R(\rho) \leqslant 0. \tag{5.13}$$

[2]To avoid confusion with the time variable t, we now note the number of qubits in a reduced state and the anticoherence order by q.

Similarly, the second time derivative of $R(\rho)$ is given by

$$\ddot{R}(\rho) = 4\overline{(\Gamma_{LM})^2}R(\rho) \geqslant 0. \tag{5.14}$$

More generally, the solution (5.9) for the state multipole of $\rho(t)$ gives

$$R(t) = \frac{1}{N+1} + \sum_{L>0,M} |\rho_{LM}(0)|^2 e^{-2\Gamma_{LM}t}. \tag{5.15}$$

where we have set $R(t) \equiv R(\rho(t))$.

5.2 Isotropic depolarisation

When the decoherence rates are equal in all directions, $\gamma \equiv \gamma_x = \gamma_y = \gamma_z$, the spin system undergoes isotropic depolarisation. From (5.4) and (5.5), we find that the state multipoles ρ_{LM} decay exponentially over time as

$$\rho_{LM}(t) = \rho_{LM}(0)e^{-\gamma L(L+1)t}. \tag{5.16}$$

The evolution of the spin state is in this case similar with that of the well-known isotropic depolarisation channel [294]. Indeed, the MMS is the unique stationary state in both cases. However, we point out that the isotropic depolarisation based on the master equation is physically richer than the channel. In fact, under the isotropic depolarisation channel, every state multipoles decay at the same rate while the decay rates here depends on L.

5.2.1 Superdecoherence

From (5.13), the time derivative of the purity is

$$\dot{R}(\rho) = -2\overline{L(L+1)}\gamma R(\rho) \leqslant 0. \tag{5.17}$$

The purity of the $q = N-1$ qubit reduced state is (see Chapter 1)

$$\mathrm{Tr}\left[\rho_{N-1}^2\right] = \sum_{L=0}^{N-1}\sum_{M=-L}^{L} \tfrac{N(N+1)-L(L+1)}{N^2} |\rho_{LM}|^2 . \tag{5.18}$$

Using $\mathrm{Tr}(\rho^2) = \sum_{LM} |\rho_{LM}|^2$ and (5.18), we find that

$$\sum_{L=0}^{N}\sum_{M=-L}^{L} L(L+1)|\rho_{LM}|^2 = N(N+1)\mathrm{Tr}\left[\rho^2\right] - N^2\mathrm{Tr}\left[\rho_{N-1}^2\right]. \tag{5.19}$$

which is valid for any state ρ (pure or mixed). Consequently, (5.17) can be rewritten as

$$\dot{R}(\rho) = -2\gamma\left[N(N+1)R(\rho) - N^2 R(\rho_{N-1})\right] \tag{5.20}$$

where $R(\rho_{N-1})$ is the purity of the $N-1$-qubit reduced state of ρ. Due to the proportionality of the state multipoles expressed by the relation (5.10) and the diagonal form of the master equation in the MPB, the master equation keeps exactly the same form (5.8)

for the reduced states ρ_q than for the global state ρ. Using (5.20), we can thus write the closed set of equations for the purities

$$\begin{aligned} \dot{R}(\rho_1) &= -2\gamma\left[2R(\rho_1)-1\right] \\ \dot{R}(\rho_2) &= -2\gamma\left[6R(\rho_2)-4R(\rho_1)\right] \\ &\vdots \\ \dot{R}(\rho) &= -2\gamma\left[N(N+1)R(\rho)-N^2R(\rho_{N-1})\right]. \end{aligned} \tag{5.21}$$

Each equation in this system depends only on purities of subsystems of up to q-qubits, independent of N.

It is known that collective dephasing can lead to a phenomenon called superdecoherence [295–297], where the rate at which states lose their coherence scales as N^2 with N the number of qubits, contrary to individual decoherence for which the coherence loss rate scales as N. We show here that superdecoherence also arise in isotropic depolarisation.

5.2.1.1 Condition for superdecoherence

The following proposition gives a necessary condition for superdecoherence to occur.

Proposition. *Superdecoherence under isotropic depolarisation of a state ρ cannot occur if ρ is separable.*

Proof. Rewriting (5.20) as allows us to highlight both linear and quadratic contributions in N

$$\dot{R}(\rho) = -2\gamma R(\rho)N - 2\gamma\left[R(\rho)-R(\rho_{N-1})\right]N^2. \tag{5.22}$$

We now show that the coefficient in front of N^2 can only be negative for entangled states. To this end, we use the entanglement criterion based on the Rényi entropy S_q for $q=2$ [3], which states that if a state ρ is separable, then $R(\rho_q) \geqslant R(\rho)$ for any number of qubits $q < N$. This criterion reflects the fact that the reduced states of a separable state are always less mixed than the global state is [179]. Therefore, for separable states $R(\rho)-R(\rho_{N-1})$ is always negative. It can be positive only for entangled states. A consequence is that superdecoherence can never occur when the system starts from a separable state. Indeed, as we show in Appendix 5.C, isotropic depolarisation leads to a separability preserving (SEPP) dynamical map. This means that separable states can only evolve into separable states, which we have just shown cannot display superdecoherence. □

Interestingly, the situation is fundamentally different for the closely related phenomenon of superradiance, which can occur without any entanglement [298], starting for example from the separable state in which all atoms are excited.

5.2.1.2 Connection between superdecoherence and AC measures

A numerical optimization shows that $R(\rho)-R(\rho_{N-1})$ is smaller than or equal to $1/2$, where the value $1/2$ is reached when ρ is a pure 1-AC state. Hence, these states exhibit the largest depolarisation rate

$$\dot{R} = -\gamma N(N+2)$$

[3] The Rényi entropies are defined as $S_q(\rho) = \frac{1}{1-q}\ln\left[\mathrm{Tr}\left(\rho^q\right)\right]$ for $q>0$. For $q=2$, $S_2(\rho) = -\ln\left[\mathrm{Tr}\left(\rho^2\right)\right] = -\ln\left[R(\rho)\right]$ and we have $S_2(\rho) \geq S_2(\rho_t) \Leftrightarrow R(\rho) \leqslant R(\rho_t)$.

scaling quadratically with N. This connection between purity loss and anticoherence can be made explicit as for an initial pure state $|\psi_0\rangle$, the rate (5.22) at $t = 0$ can be rewritten as (see Appendix 5.D for more detail)

$$\dot{R}\Big|_{t=0} = -2\gamma\left(N + \frac{N^2}{2}\mathcal{A}_1^R\right) \tag{5.23}$$

where $\mathcal{A}_1^R$ is the purity 1-AC measure of $|\psi_0\rangle$ and expressible as

$$\mathcal{A}_1^R = 1 - \frac{1}{j^2}|\langle\psi_0|\mathbf{J}|\psi_0\rangle|^2.$$

The equation (5.23) relates superdecoherence to anticoherence (and thus to entanglement of $|\psi_0\rangle$) because the term scaling quadratically with the number of qubits is directly proportional to $\mathcal{A}_1^R$. This term vanishes for spin-coherent states ($\mathcal{A}_1^R = 0$) and is maximal for 1-AC states ($\mathcal{A}_1^R = 1$).

Higher-order time derivatives of the purity can be evaluated by repeated use of the set of equations (5.21). For example, at any time t, we have for the second-order time derivative of R

$$\begin{aligned}\ddot{R} &= -2\gamma\left[N(N+1)\dot{R}(\rho) - N^2\dot{R}(\rho_{N-1})\right] \\ &= 4\gamma^2N^2\left[(N+1)^2R(\rho) - 2N^2R(\rho_{N-1}) + (N-1)^2R(\rho_{N-2})\right].\end{aligned} \tag{5.24}$$

The quantity $\ddot{R}$ does not only depend on $R(\rho)$ and $R(\rho_{N-1})$ as $\dot{R}$ did, but also on $R(\rho_{N-2})$, the purity of the reduced density matrix of $N-2$ qubits. For an initial pure state $\rho = |\psi_0\rangle\langle\psi_0|$, (5.24) can be rewritten as

$$\ddot{R}\Big|_{t=0} = \frac{4}{3}\gamma^2N^2\left[6 + 3N^2\mathcal{A}_1^R - 2(N-1)^2\mathcal{A}_2^R\right] \tag{5.25}$$

where we have set $\mathcal{A}_q^R = \mathcal{A}_q^R(|\psi_0\rangle)$ for $q = 1, 2$. It can be seen from (5.25) that, among 1-AC states, 2-AC states yield the smallest value for $\ddot{R}|_{t=0}$ and that (5.25) with $\mathcal{A}_1^R = \mathcal{A}_2^R = 1$ gives immediately

$$\ddot{R}|_{t=0} = \frac{4}{3}\gamma^2N^2(N+2)^2.$$

It follows that 2-AC states not only lead to the highest rate of depolarisation $\dot{R}|_{t=0}$, but that this rate also decreases the slowest over time among all such states. In contrast, the maximal value of $\ddot{R}|_{t=0}$ is reached for GHZ states, for which $\mathcal{A}_1^R = 1$, $\mathcal{A}_2^R = 3/4$ and thus $\ddot{R}|_{t=0} = 2\gamma^2N^2(N^2+2N+3)$. This means that among the maximally entangled pure states with respect to the $1|N-1$ bipartition, the GHZ states are those for which the depolarisation rate decreases most rapidly with time.

From (5.16), it appears that the multipoles of higher L decay faster. Therefore, it clearly appears that the pure states which minimise (maximise) the cumulative distribution

$$r_q = \sum_{L=1}^{q}\sum_{M=-L}^{L}|\rho_{LM}|^2$$

are the states which maximise (minimise) the superdecoherence. From their definition in the multipolar basis, q-AC states minimise r_q and are thus the most superdecoherent states of all spin states. In the other extreme, it has been shown that spin coherent states

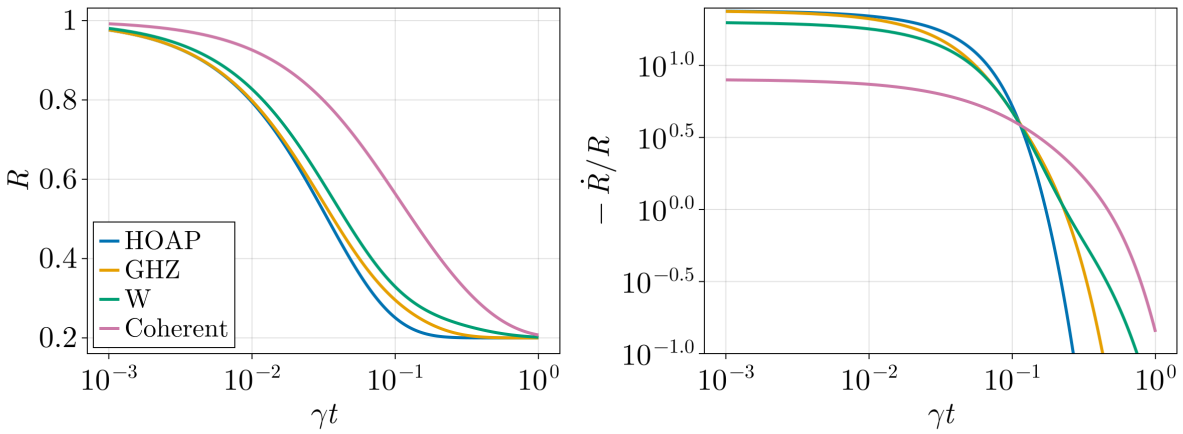

Figure 5.1: Isotropic depolarisation for different 4-qubit states: coherent state (pink), W state (green), GHZ state (orange) and HOAP state given by (5.26) (blue). Left: Purity as a function of time, monotonically decreasing towards the asymptotic value $1/N + 1$. Right: Purity loss rate as a function of time.

maximise r_q [222]. They are therefore the most robust to isotropic depolarisation. For $N = 4$, we show in Figure 5.1 the effect of isotropic depolarisation on the purity of a coherent state, the W and GHZ states and the 2-AC HOAP state

$$\left|\psi_{t=2}^{\mathrm{HOAP}}\right\rangle = \frac{1}{2}\left(\left|D_4^{(0)}\right\rangle + i\sqrt{2}\left|D_4^{(2)}\right\rangle + \left|D_4^{(4)}\right\rangle\right). \tag{5.26}$$

5.2.2 Entanglement dynamics

5.2.2.1 Entanglement survival time

Under isotropic depolarisation, a N-qubit system initially in a pure entangled symmetric state $|\psi\rangle$ gradually loses its purity and entanglement over time. Asymptotically, the system reaches its unique stationary state, i.e. the MMS which has the smallest purity and is separable [299]. After a finite time of the evolution leading the system from its initial state $|\psi\rangle$ to ρ_0, the state becomes separable and remains so because the dynamics is separability preserving (see Appendix 5.C). We call this particular time the entanglement survival time and denote it by t_{ES}. After a longer but still finite time, the system state enters the ball of SAS states centred on ρ_0 [33, 149] (see Chapter 2). From this point on, any entanglement between the qubits that could potentially be retrieved by global unitary transformations on the system is permanently lost.

Our aim is to study the scaling of the entanglement survival time with the number of qubits, in particular for the most rapidly decohering states. However, in general, it is not practically feasible to compute this time, as this reduces to determining whether a mixed state is entangled or separable, a notoriously difficult problem. We will therefore use entanglement or separability criteria to give upper and lower bounds for t_{ES}. As we shall see, these bounds follow the same scaling with N, which is consequently also the scaling of t_{ES} with N. In this work, we use the negativity to detect, and to some extent quantify, bipartite entanglement. A non-zero negativity indicates entanglement. We call the time when the negativity becomes zero the NPT (negative partial transpose) survival time t_{NPT}. It is a lower bound for the entanglement survival time, i.e. $t_{\mathrm{NPT}} \leqslant t_{\mathrm{ES}}$. Here,

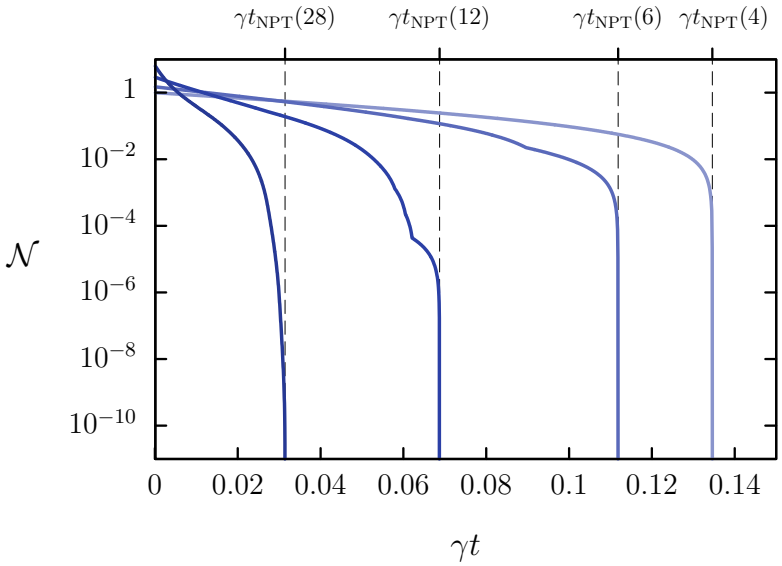

Figure 5.2: Negativity with respect to the $\lfloor N/2 \rfloor | \lceil N/2 \rceil$ bipartition of HOAP states [118, 119] for $N = 4, 6, 12, 28$ (from right to left) as a function of time for isotropic depolarisation. The dashed lines indicate when the negativity drops to zero.

we will not investigate whether the states produced by isotropic depolarisation are fully bound entangled [300], but will focus on the distillable entanglement that is detected by the PPT criterion for the different bipartitions of the system, in the same spirit as the works [279, 280].

Even before using the PPT criterion, we can obtain a lower bound on the entanglement survival time for pure q-AC initial states. We proceed as before by using the purity-based entanglement criterion which states that when $R(\rho) > R(\rho_q)$, the state ρ is entangled. Then, taking into account the fact that $R(\rho_q) = 1/(q+1)$ at any time because anticoherence is conserved now yields that $\rho(t)$ remains entangled for

$$t < \frac{\ln\left(\frac{N(q+1)}{N-q}\right)}{2\gamma N(N+1)} \leqslant t_{\mathrm{ES}}. \tag{5.27}$$

5.2.2.2 NPT survival time scaling

In this subsection, we analyse the scaling of the NPT survival time with the number of qubits. To begin, Figure 5.2 shows the negativity as a function of time for initial HOAP states with different number of qubits. The logarithmic scale used in the plot clearly shows that the negativity drops to zero after a finite time, the NPT survival time t_{NPT}, decreasing with the number of qubits[4]. We observe numerically that the balanced bipartition $\lfloor N/2 \rfloor | \lceil N/2 \rceil$ is, except for small numbers of qubits, the one for which t_{NPT} is the largest, while it is the smallest for the bipartition $1|N-1$. For this reason, in what follows, we focus only on these two bipartitions.

Figure 5.3 (top panel) shows t_{NPT} for the balanced bipartition as a function of N. We see that t_{NPT} falls off as an inverse power law in N for all states considered. The states

[4]To accurately estimate t_{NPT}, the moment when the negativity becomes zero, we had to work with octuple precision floats. We worked with the BigFloat type available in Julia for floating point numbers of arbitrary precision, which uses the GNU MPFR library.

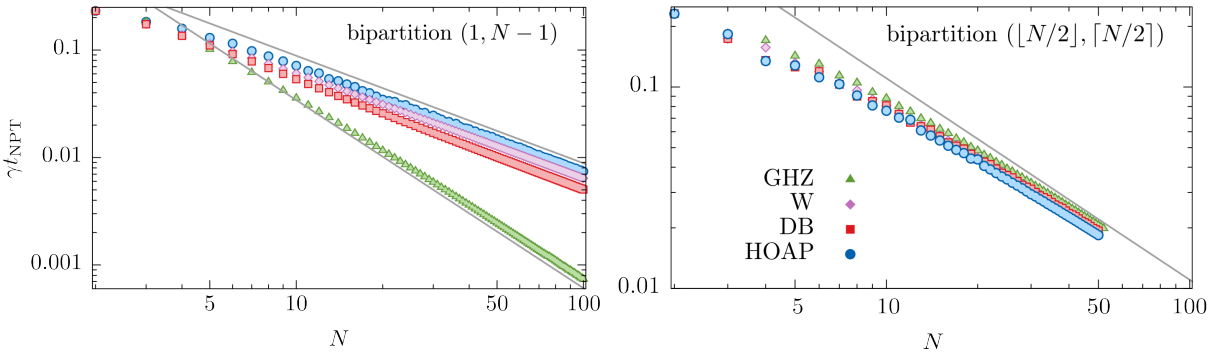

Figure 5.3: Negative partial transpose (NPT) survival time t_{NPT} as a function of N for (left) the bipartition $1|N-1$, with the grey solid lines showing the scalings $1/N$ and $1/N^{1.75}$, and (right) the bipartition $\lfloor N/2 \rfloor \,|\, \lceil N/2 \rceil$, with the grey solid line showing the scaling $1/N$.

that lose their entanglement the fastest and thus lead to the smallest value of t_{NPT} are the HOAP states, even though they have the largest initial negativity. Similar data for the bipartition $1|N-1$ are displayed in the bottom panel of Figure 5.3. In this case, the GHZ states are the most fragile states under isotropic depolarisation and we find that t_{NPT} falls off approximately as $N^{1.75}$. This observation can be contrasted with the fact that the entanglement in a GHZ state is known to be maximally fragile under the loss of a single qubit. Nevertheless, we see that the global entanglement is more robust than the local one and the HOAP states are found to be the first to become PPT with respect to any bipartition. Hence, AC states are not only the most rapidly decohering states, but also the ones that become PPT the fastest.

5.2.2.3 P function separability time

For an initial pure entangled state $\rho = |\psi\rangle\langle\psi|$, the P function is necessarily not everywhere positive because otherwise the state would be separable. Over time, based on (5.9), the P function takes the form

$$P_\rho(\Omega) = \sqrt{\frac{4\pi}{N+1}} \sum_{L,M} \left(C^{jj}_{jjL0}\right)^{-1} \rho_{LM}(0)\, e^{-\Gamma_{LM} t} Y_{LM}(\Omega) \tag{5.28}$$

where all the multipoles with $L > 0$ decay exponentially. Therefore, after a finite time $t_P \geqslant t_{\mathrm{ES}}$, the P function becomes everywhere positive, which is a sufficient condition for separability. Because the dynamics is separability preserving, the state remains separable for all $t \geqslant t_P$. In Figure 5.4, we show the time t_P as a function of the number of qubits. To estimate t_P numerically, we computed a discretized version of the P function for $\Omega = (\theta, \varphi) \in [0, \pi] \times [0, 2\pi]$ sampled on a grid with resolution $\delta\theta = \delta\varphi = 1/N^{3/4}$. Then we checked at what time, with precision $\delta t = 1/\left(4096\sqrt{N}\right)$, this discretized P function becomes everywhere positive. For all the different types of states considered, we find an inverse power law scaling of the form $t_P \sim 1/N$. It is for the HOAP states that t_P is the smallest and for W states that t_P is the largest for a given number of qubits.

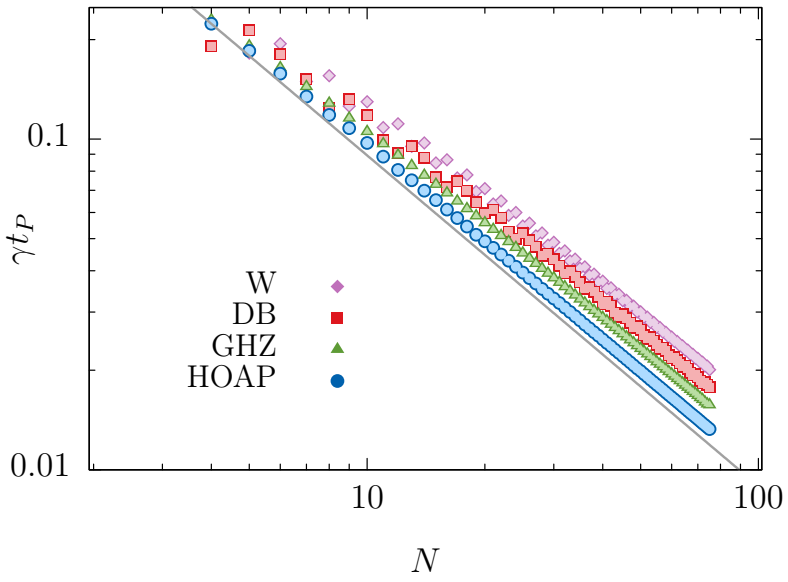

Figure 5.4: Shortest time after which the P function becomes everywhere positive, ensuring the separability of the state. The grey solid line shows the scaling $1/N$.

5.2.2.4 Time to reach the ball of SAS states

We have computed the time it takes for an initial pure state to enter, as a result of depolarisation, the set $\mathcal{S}_0$ defined by the ball of SAS states of radius (see Chapter 2)

$$r = \frac{1}{\sqrt{(2N+2)\left[(2N+1)\,C_{2N}^{N} - (N/2+1)\right]}} \tag{5.29}$$

centred on the MMS. Let us denote this time by $t_{r_{\max}}$. Figure 5.5 shows $t_{r_{\max}}$ as a function of N, the number of qubits. We can see that $t_{r_{\max}}$ increases linearly with N for GHZ and Dicke states. In stark contrast, for HOAP states, $t_{r_{\max}}$ is approximately independent of N, meaning that HOAP states become absolutely separable after a time that depends only on the decoherence rates and not on the size of the system. More precisely, our high-precision numerics shows that $t_{r_{\max}} \approx 0.384$ for HOAP states, $t_{r_{\max}} \approx 0.116(N+2)$ for GHZ and balanced Dicke states with even N, $t_{r_{\max}} \approx 0.341(N-2)$ for balanced Dicke states with odd N and $t_{r_{\max}} \approx 0.35N + 0.81$ for W states.

Our results are summarized in Table 5.1. It is interesting to compare them with those obtained for an ensemble of qubits subjected to *individual* decoherence. In that case, it has been shown that the time t_{NPT} calculated for the bipartition $\lfloor N/2 \rfloor | \lceil N/2 \rceil$ generally increases with N, notably for GHZ states [278–281, 301]. It was therefore concluded that the entanglement survival time t_{ES} also increases with N. Clearly, these conclusions are no longer valid for *collective* depolarisation since we have just shown that then both times decrease with N. Highly-entangled symmetric states thus appear to be more fragile to collective depolarisation than to individual depolarisation, which we attribute to superdecoherence that is absent for individual depolarisation.

5.2.2.5 Dynamical generation of PPT entangled states

We now focus in more detail on the case of a few qubits for which we can obtain further analytical results. To begin with, let us consider a 4-qubit system initially in the pure

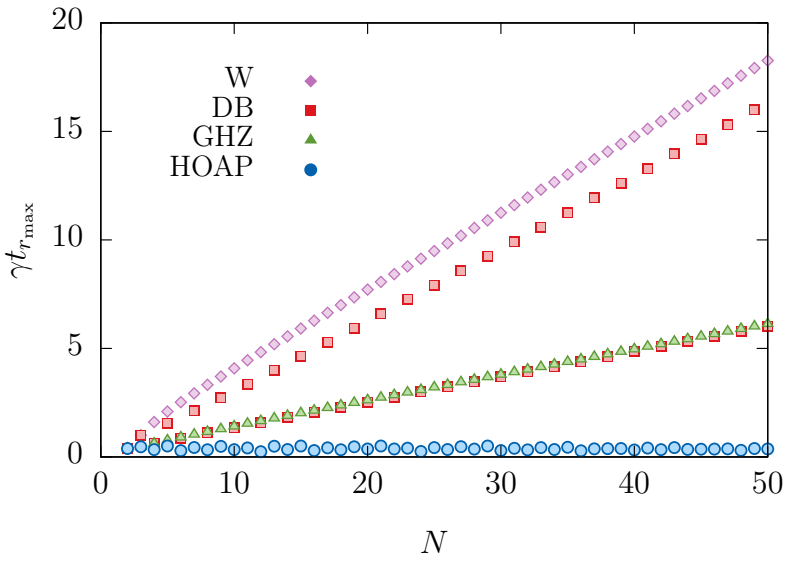

Figure 5.5: Time after which an initial pure N-qubit symmetric state enters the ball of radius (5.29) centred on the MMS as a result of depolarisation, shown here for various states as a function of N. Note the difference in behaviour for balanced Dicke states depending on the parity of N (red squares).

2-AC state (5.26). The time-evolved state $\rho(t)$, which follows from (5.16), is represented in the Dicke basis $\left\{|D_4^{(k)}\rangle : k = 0, \ldots, 4\right\}$ by the matrix

$$\begin{pmatrix} \frac{u+1}{5} & 0 & -\frac{iu^{3/5}}{2^{3/10}} & 0 & u \\ 0 & \frac{1-4u}{5} & 0 & 0 & 0 \\ \frac{iu^{3/5}}{2^{3/10}} & 0 & \frac{6u+1}{5} & 0 & \frac{iu^{3/5}}{2^{3/10}} \\ 0 & 0 & 0 & \frac{1-4u}{5} & 0 \\ u & 0 & -\frac{iu^{3/5}}{2^{3/10}} & 0 & \frac{u+1}{5} \end{pmatrix} \tag{5.30}$$

where $u = u(t) = e^{-20\gamma t}/4$. The partial transpose of (5.30) has only one eigenvalue that can potentially be negative, respectively denoted by $\lambda_-^{(1,3)}$ for the bipartition $1|3$ and $\lambda_-^{(2,2)}$ for the bipartition $2|2$. These eigenvalues are given by

$$\lambda_-^{(1,3)}(t) = \frac{e^{-20\gamma t}}{20}\left(e^{20\gamma t} - 5\,e^{8\gamma t} - 6\right)$$

	$\mathcal{N}$	t_{NPT}	t_{ES}	t_P	$t_{r_{\max}}$
GHZ	$1/2$	$\sim 1/N$	$\sim 1/N$	$\sim 1/N$	N
W	$1/2$	$\sim 1/N$	$\sim 1/N$	$\sim 1/N$	N
DB	$\sim \sqrt{N}$	$\sim 1/N$	$\sim 1/N$	$\sim 1/N$	N
HOAP	$\sim N$	$\sim 1/N$	$\sim 1/N$	$\sim 1/N$	const

Table 5.1: Scaling laws with the number of qubits of the initial negativity and the different characteristic times defined in the text for several families of states subject to isotropic depolarisation. The scaling laws for t_{ES} have been deduced from the inequalities $t_{\mathrm{NPT}} \leqslant t_{\mathrm{ES}} \leqslant t_P$ and the scaling laws for t_{NPT} and t_P.

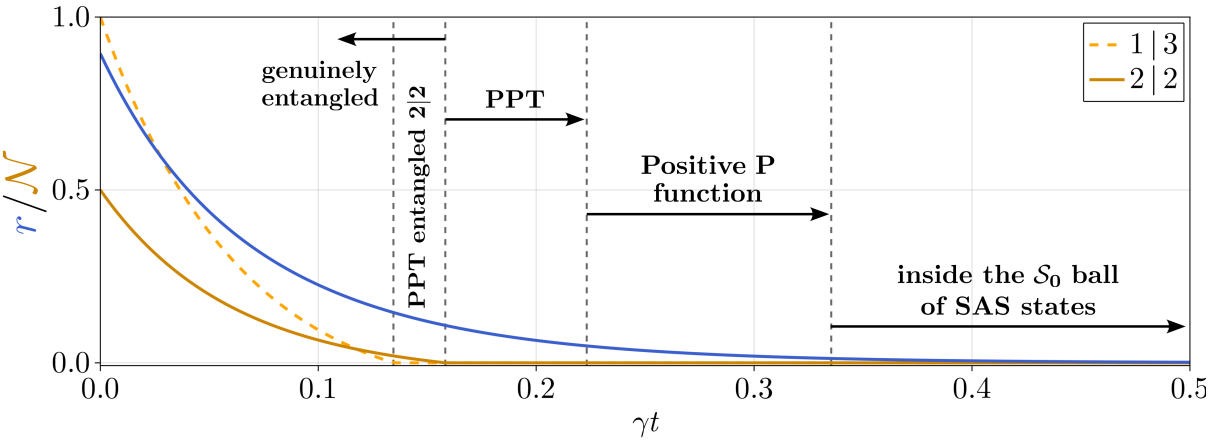

Figure 5.6: Distance r to the maximally mixed state (in blue) and negativity $\mathcal{N}$ for the two possible bipartitions 1|3 and 2|2 (in orange) as a function of time when starting from the 4-qubit 2-AC HOAP state (5.26).

and

$$\lambda_{-}^{(2,2)}(t) = -\frac{e^{-20\gamma t}}{30}\left(3 - 3e^{20\gamma t} + \sqrt{e^{16\gamma t}\left[4e^{4\gamma t}\left(e^{20\gamma t}+3\right)+75\right]+9}\right).$$

The eigenvalue $\lambda_{-}^{(2,2)}(t)$ cancels at a time $\gamma t_{\mathrm{NPT}}^{(2,2)} \approx 0.134582$, less than $\gamma t_{\mathrm{NPT}}^{(1,3)} \approx 0.158384$, the time at which $\lambda_{-}^{(3,1)}(t)$ cancels. Therefore, there is a time interval during which the negativity is zero for the bipartition 2|2 while it is non-zero for the bipartition 1|3. In this time interval, the state generated by isotropic depolarisation is PPT entangled with respect to the 2|2 bipartition, and thereby realises a 3×3 bipartite symmetric PPT entangled state [111]. Figure 5.6 illustrates this dynamical evolution of entanglement under collective depolarisation in this particular case. It should be noted that for the initial GHZ, W and Dicke states, no such PPT entanglement is produced during the dynamics. Similarly, we found that other types of PPT entangled states can be generated by isotropic depolarisation starting from pure AC states. For example, starting from the 5-qubit (resp. 6-qubit) HOAP state given in Table 4.3, isotropic depolarisation leads to PPT entangled states with respect to the 2|3 bipartition (resp. 3|3 bipartition).

5.3 Anisotropic depolarisation

In this section, we turn to anisotropic depolarisation, where the rates in the three spatial directions are not all equal, i.e. $\gamma_x = \gamma_y = \gamma_{\perp z} \neq \gamma_z$. We start in Subsection 5.3.2 by searching for the initial pure states with the largest purity decay rate and relate it with the variances of the state. In Subsection 5.3.2, we find the states minimising the purity at all times for $N = 2$ and 4.

5.3.1 Purity loss rate

In the more general case of anisotropic depolarisation ($\gamma_{\perp z} \neq \gamma_z$), the rate of change of the purity is given by

$$\dot{R} = -2\sum_{L,M}\left(M^2\gamma_z + [L(L+1) - M^2]\gamma_{\perp z}\right)|\rho_{LM}|^2. \tag{5.31}$$

For a pure state $|\psi\rangle$, $\dot{R}$ can be expressed only in terms of variances of the spin components in state $|\psi\rangle$. Indeed, for pure states, the following relations hold (see Appendix 5.D)

$$\Delta J_z^2 = \frac{1}{2}\sum_{L=0}^{N}\sum_{M=-L}^{L} M^2 \left|\rho_{LM}\right|^2 \tag{5.32}$$

$$\Delta J_x^2 + \Delta J_y^2 = \frac{1}{2}\sum_{L=0}^{N}\sum_{M=-L}^{L} \left[L(L+1) - M^2\right] \left|\rho_{LM}\right|^2 \tag{5.33}$$

that can be combined with (5.31) to obtain

$$\dot{R}_{|\psi\rangle} = -4\left[\gamma_z \Delta J_z^2 + \gamma_{\perp z}\left(\Delta J_x^2 + \Delta J_y^2\right)\right]. \tag{5.34}$$

The general result (5.34), which is valid for any pure spin state, suggests controlling depolarisation on short time scales by appropriately squeezing the initial state, i.e. making ΔJ_z^2 smaller or larger than $\Delta J_x^2 + \Delta J_y^2$, depending on the value of the depolarisation rates γ_z and $\gamma_{\perp z}$. Interestingly, a similar result applies to continuous variable quantum states [302]. In particular, for macroscopic quantum states, a slowing down of decoherence due to photon loss has been experimentally demonstrated via squeezing in phase space [303, 304].

5.3.2 Optimization of purity loss

In the following, we show how to find the pure states that maximise the purity loss rate (5.34). First, let us remark that the variances of the spin components verify

$$\Delta J_x^2 + \Delta J_y^2 + \Delta J_z^2 = \tfrac{N}{2}\left(\tfrac{N}{2}+1\right) - \left|\langle \mathbf{J}\rangle\right|^2 \tag{5.35}$$

because $\mathbf{J}^2 = \frac{N}{2}\left(\frac{N}{2}+1\right)\mathbf{1}$, and

$$0 \leqslant \Delta J_\alpha^2 = \langle J_\alpha^2\rangle - \langle J_\alpha\rangle^2 \leqslant \langle J_\alpha^2\rangle \leqslant \frac{N^2}{4}, \qquad \forall \alpha = x, y, z, \tag{5.36}$$

where the last inequality comes from the fact that the largest eigenvalue of J_α^2 is equal to $N/2$.

5.3.2.1 Case I: $\gamma_z > \gamma_{\perp z}$

In this case, the decoherence rate (5.34) is maximised by maximizing ΔJ_z^2. Let us show that the upper bound for the variance given in (5.36), equal to $N^2/4$, can be reached. It can only be reached when $\langle J_z\rangle = 0$. For a pure state $|\psi\rangle$ with expansion in the Dicke basis

$$|\psi\rangle = \sum_{k=0}^{N} d_k |D_N^{(k)}\rangle, \quad d_k \in \mathbb{C},$$

the condition $\langle J_z\rangle = 0$ reads

$$\sum_{k=0}^{N} |d_k|^2 (N-2k) = 0, \tag{5.37}$$

and the variance ΔJ_z^2 then reduces to

$$\left\langle J_z^2 \right\rangle = \frac{N^2}{4} + \sum_{k=0}^{N} |d_{N-k}|\, k\,(k-N)\,. \tag{5.38}$$

The latter expression is equal to $N^2/4$ when the sum on the right-hand side vanishes, which occurs when all Dicke coefficients d_k are equal to zero, except d_0 and d_N. But then, (5.37) gives $|d_0|^2 = |d_N|^2$ directly. The corresponding normalised state is the GHZ state, for which (5.34) yields the maximal purity loss rate for $\gamma_z > \gamma_{\perp z}$

$$\dot{R}_{|\mathrm{GHZ}\rangle} = -2\gamma_{\perp z} N - \gamma_z N^2. \tag{5.39}$$

5.3.2.2 Case II: $\gamma_z < \gamma_{\perp z}$

In this case, the decoherence rate (5.34) is maximised by maximizing $\Delta J_x^2 + \Delta J_y^2$. Rewriting (5.35) as

$$\Delta J_x^2 + \Delta J_y^2 = \tfrac{N}{2}\left(\tfrac{N}{2}+1\right) - \langle J_x\rangle^2 - \langle J_y\rangle^2 - \langle J_z\rangle^2\,,$$

we see that a state verifying $\langle J_x\rangle = \langle J_y\rangle = 0$ and, at the same time, $\langle J_z^2\rangle = 0$ is optimal. For even N, $\langle J_z^2\rangle$ given by (5.38) is equal to zero when $|d_k|^2 = 1$ for $k = N/2$ and $|d_k|^2 = 0$ otherwise. The corresponding state is the balanced Dicke state, which also verifies $\langle J_x\rangle = \langle J_y\rangle = 0$ and is thus optimal. Similarly, for odd N, we find that the optimal state has $|d_k|^2 = 1$ either for $k = (N+1)/2$ or $k = (N-1)/2$ and $|d_k|^2 = 0$ otherwise. In the end, the maximal purity loss rate for $\gamma_z < \gamma_{\perp z}$ is given by

$$\dot{R}_{|\mathrm{DB}\rangle} \;=\; \begin{cases} -\gamma_{\perp z} N(N+2) & \text{even } N \\ -\gamma_{\perp z}\left[N(N+2)-1\right] & \text{odd } N \end{cases} \tag{5.40}$$

and is independent of γ_z.

5.3.2.3 Minimisation of purity at any fixed time

Until now, we have identified the states which decohere the fastest *at short times* for any possible value of the rates $\gamma_{\perp z}$ and γ_z. It is much more difficult to answer the question of which initial pure states give the smallest purity after an arbitrary period of time t^*. Through a combination of analytical and numerical methods, we were able to answer this question for 2 and 4 qubits. First, we have observed that, for $N = 2$ and $N = 4$ (but not $N = 3$), the optimal initial states found numerically are always 1-AC. Taking this observation as a working hypothesis, we can perform the optimization analytically. To this end, let us denote by $R_{|\psi\rangle}(t^*)$ the purity of the spin state at time t^* when the system is initially in state $|\psi\rangle$. We then define the derivative of this purity with respect to a pure state $|\sigma\rangle$ as

$$\frac{dR_{|\psi\rangle}(t^*)}{d\,|\sigma\rangle} = \lim_{\epsilon\to 0} \frac{R_{|\psi_\epsilon\rangle}(t^*) - R_{|\psi\rangle}(t^*)}{\epsilon}, \tag{5.41}$$

where we define the normalized state $|\psi_\epsilon\rangle = \mathcal{N}\left(|\psi\rangle + \epsilon|\sigma\rangle\right)$ with $\mathcal{N}$ a normalisation constant. In order to find optimal states, we look for critical states that cancel the derivative (5.41) for a fixed value of t^*.

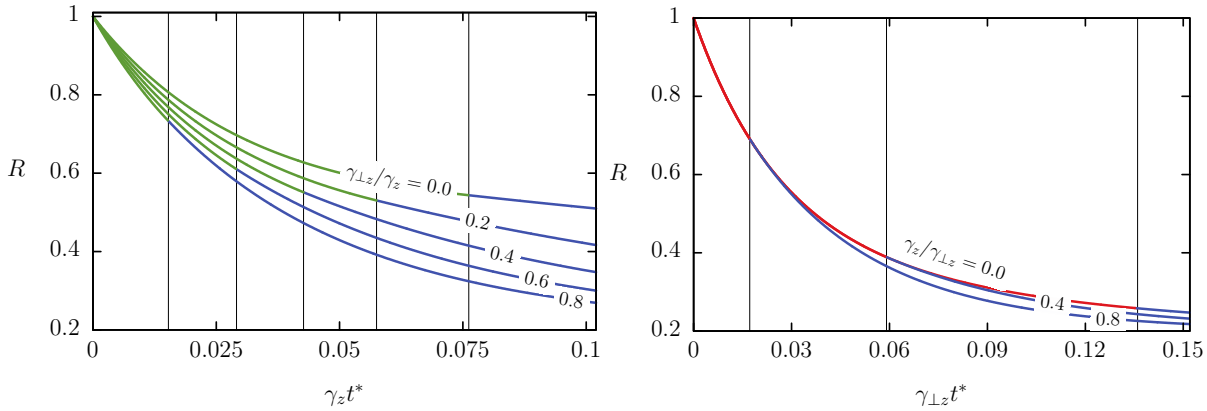

Figure 5.7: Minimum achievable purity at time t^* for different values of $\gamma_{\perp z}/\gamma_z < 1$ (left) and $\gamma_{\perp z}/\gamma_z > 1$ (right). The optimal initial states are the GHZ and balanced Dicke states (green and red curves, respectively) at short times and the $|\mu^*\rangle$ states given by (5.43) (blue curves) at longer times. Vertical lines locate the transition from GHZ to $|\mu^*\rangle$ which occurs when $\mathrm{Im}(\mu^*)$ vanishes.

5.3.2.4 $j = 1$ or $N = 2$ qubits

For $N = 2$, the only critical states are the GHZ and balanced Dicke states, whatever the value of t^*. They are both 1-AC [66]. The GHZ and balanced Dicke states were previously found to be optimal at short times for $\gamma_z > \gamma_{\perp z}$ and $\gamma_z < \gamma_{\perp z}$, respectively. Our numerics shows that this is also the case for longer times, and thus for any t^*.

5.3.2.5 $j = 2$ or $N = 4$ qubits

We assume that the optimal initial $N = 4$ qubits states are all 1-AC, which our numerics confirms, regardless of the final time t^* and the depolarisation rates. In [66], it was shown that any 1-AC 4-qubit state can be brought by rotation to the form

$$|\mu\rangle = \mathcal{N}\left(|D_4^{(0)}\rangle + \mu|D_4^{(2)}\rangle + |D_4^{(4)}\rangle\right) \tag{5.42}$$

with $\mu \in \mathbb{C}$ and $\mathcal{N}$ a normalisation constant. We can always find a critical state of the form (5.42). Indeed, by cancelling the derivative of the purity at time t^* for the initial state (5.42) and solve for the real and imaginary parts of μ, we find a critical value μ^* with $\mathrm{Re}\,(\mu^*) = 0$ and

$$\mathrm{Im}\,(\mu^*) = \sqrt{\frac{7\left(e^{8(4\gamma_{\perp z}-3\gamma_z)t^*} - e^{8\gamma_z t^*}\right)}{4e^{4(7\gamma_{\perp z}+2\gamma_z)t^*} - 7e^{24\gamma_{\perp z}t^*} + 3e^{8\gamma_z t^*}} + 2}. \tag{5.43}$$

Let us make some observations on this result. First, when $\gamma_{\perp z} = \gamma_z$, (5.43) reduces to $\mu^* = i\sqrt{2}$ and the purity AC measure then gives $\mathcal{A}_2 = 1$, so that we recover the result of the previous section that, for isotropic depolarisation, the optimal state for $N = 4$ is at any time the 2-AC state. Next, the critical value (5.43) exists only for times for which the argument in the square root is non negative, i.e. for $t^* > t^*_{\mu^*}$ with $t^*_{\mu^*}$ a time that depends only on the rates.

We show on the left panel of Figure 5.7 the evolution of the purity for the optimal state $|\mu^*\rangle$ for different values of $\gamma_{\perp z}/\gamma_z$ with $\gamma_z > \gamma_{\perp z}$. The vertical lines, drawn at $t^* = t^*_{\mu^*}$, indicate the time at which the initial optimal state changes from the GHZ state

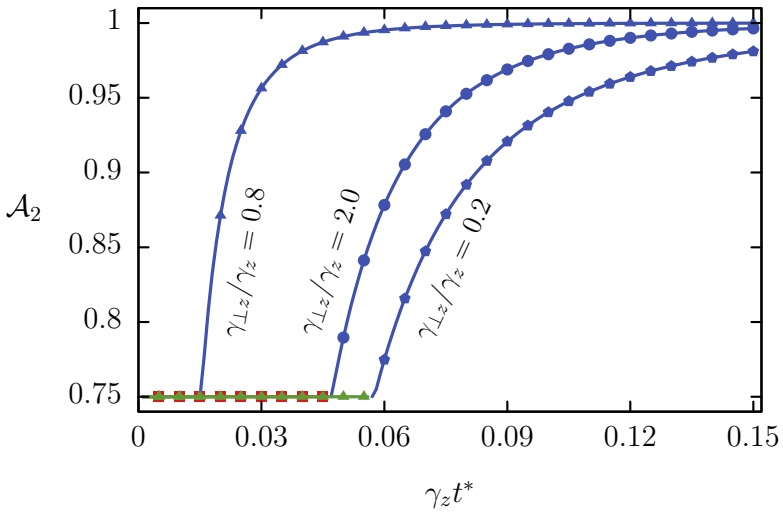

Figure 5.8: Measure of anticoherence to order 2 of optimal states minimising the purity as a function of the final time t^* for $N = 4$ and different values of the depolarisation rates. Symbols correspond to data obtained by numerical optimisation and solid curves show the analytical predictions based on (5.42) and (5.43).

to $|\mu^*\rangle$. Finally, we note that $\mu^* \to i\sqrt{2}$ when $t \to \infty$, meaning that the asymptotically optimal state always converges to the pure 2-AC state given in (5.26). The same type of behaviour can be seen on the right panel of Figure 5.7, where we let $\gamma_z/\gamma_{\perp z}$ vary with $\gamma_z < \gamma_{\perp z}$. Here, the optimal state changes from the balanced Dicke state to $|\mu^*\rangle$. As all non-zero state multipoles of the balanced Dicke state have $M = 0$, the purity decay is insensitive to the value of the rate γ_z.

Finally, in Figure 5.8, we compare the rotationally invariant measure of 2-AC of the numerically obtained optimal states and the $|\mu^*\rangle$ states as a function of t^*. As can be seen, both give the same results. At short times, $\mathcal{A}_2$ is constant and equal to 3/4. The corresponding state is either the GHZ state when $\gamma_z < \gamma_{\perp z}$, or the balanced Dicke state when $\gamma_z > \gamma_{\perp z}$. At longer times, $\mathcal{A}_2$ increases monotonically with t^* and tends to 1 as $t^* \to \infty$. All this shows that the optimization results of the purity for arbitrary times are already complex for a small number of qubits.

5.4 Dynamical quantum metrology

In the study of open quantum systems, a key objective is the accurate measurement of dissipative rates characterising the interaction of the system with its environment. This is particularly relevant in quantum thermometry, where one aims to infer the temperature T of a thermal bath coupled to a quantum probe. A standard strategy involves allowing the probe to thermalise with the bath, such that its steady state becomes a Gibbs state in the eigenbasis $\{|\epsilon_k\rangle\}$ of the system Hamiltonian [305]

$$\rho = \sum_k \frac{e^{-\epsilon_k/k_B T}}{\mathcal{Z}} |\epsilon_k\rangle \langle\epsilon_k|$$

where ϵ_k is the energy of the eigenstate $|\epsilon_k\rangle$, $\mathcal{Z} = \sum_k \exp(-\epsilon_k/k_B T)$ is the partition function and k_B is the Boltzmann constant. Temperature estimation is then performed through measurements on the thermalised state.

However, this equilibrium-based approach requires waiting for the system to fully thermalise, which may be experimentally challenging. An alternative is offered by dissipative quantum metrology, which focuses on extracting information about dissipative parameters, such as decay rates or temperature, from the transient (non-equilibrium) dynamics of a quantum probe. A notable example is dynamical quantum thermometry, where temperature is estimated before thermal equilibrium is reached [306]. In this context, we exploit analytical results on depolarising dynamics to identify states that optimally estimate depolarisation rates, with applications to magnetic noise characterisation and temperature sensing.

5.4.1 Relation between the fidelity and the purity

For parameter estimation, we introduce a dimensionless anisotropy parameter κ, such that

$$\gamma \equiv \gamma_z = \frac{\gamma_{\perp z}}{\kappa}$$

assuming κ is known and fixed. The depolarisation dynamics is therefore fully characterised by γ, which we aim to estimate.

As explained in Chapter 4, the optimal pure initial state $\rho_0 = |\psi_0\rangle\langle\psi_0|$ is the one that maximally distinguishes the evolved state from the initial one. This distinguishability can be quantified using the fidelity

$$F\left(\rho_0, \rho_\gamma\left(t\right)\right) = \mathrm{Tr}\left(\rho_0 \rho_\gamma\left(t\right)\right)$$

where $\rho_\gamma\left(t\right)$ is the time-evolved state under depolarising dynamics. In the MPB, the evolved density matrix reads (see (5.9))

$$\rho_\gamma\left(t\right) = \sum_{L=0}^{N} \sum_{M=-L}^{L} \rho_{LM}\left(0\right) e^{-\gamma t\left[M^2 + \kappa\left(L(L+1) - M^2\right)\right]} T_{LM},$$

which yields the fidelity

$$F\left(\rho_0, \rho_\gamma\left(t\right)\right) = \sum_{L=0}^{N} \sum_{M=-L}^{L} \left|\rho_{LM}\left(0\right)\right|^2 e^{-\gamma t\left[M^2 + \kappa\left(L(L+1) - M^2\right)\right]}. \tag{5.44}$$

Notably, this expression has the same structure as the purity under depolarisation (5.15) but with the depolarisation rates rescaled by a factor of $1/2$. Hence, the states that minimise fidelity are precisely those that minimise purity. For infinitesimal depolarisation, i.e. for small values of γt, the QFI associated with the parameter γ is given by (see (4.20))

$$\mathcal{F}_Q\left(\gamma\right) = -2 \sum_{L=0}^{N} \sum_{M=-L}^{L} \left|\rho_{LM}\left(0\right)\right|^2 \left[M^2 + \kappa\left(L\left(L+1\right) - M^2\right)\right]^2 t^2.$$

Therefore, the initial states that maximise the QFI are those maximising the factor

$$\left|\rho_{LM}\left(0\right)\right|^2 \left[M^2 + \kappa\left(L\left(L+1\right) - M^2\right)\right]^2.$$

Since the factor $M^2 + \kappa\left(L\left(L+1\right) - M^2\right)$ is always positive, this maximisation is directly related to (5.31), that is the rate of change of purity, and the results of Subsection 5.3.2.

5.4.2 Optimal states for quantum metrology

For isotropic depolarisation, we know that the pure states minimising the fidelity (5.44) are HOAP states. The rate of change of (5.44) is directly related to the purity 1-AC measure and, interestingly, this derivative scales as N^2 only if the initial state is entangled. This means that Heisenberg-limited precision in the measurement of the isotropic depolarisation rate is achievable only through entangled initial states.

In Appendix 5.A, we present several microscopic models that lead to depolarising dynamics in spin systems. In particular, we show that isotropic depolarisation emerges naturally from interaction with an isotropic noisy magnetic field. This has practical relevance in settings such as the calibration of MRI systems or the design of magnetically shielded environments, where weak magnetic fluctuations must be characterised. Importantly, as discussed in Chapter 4, HOAP states are also optimal for estimating coherent magnetic field intensities with unknown directions. This dual role highlights the versatility of HOAP states as they are optimal for sensing both coherent and incoherent magnetic field intensities, making them powerful resources in quantum sensing and metrology.

In the case of anisotropic depolarisation, we saw that the rate of change of the purity is maximal for GHZ and balanced Dicke state for $\gamma_z > \gamma_{\perp z}$ and $\gamma_{\perp z} > \gamma_z$ respectively. From (5.39) and (5.40), we see that the first derivative of the fidelity (5.44) for these two optimal states scales as N^2, again indicating that Heisenberg scaling is achievable. For longer times, however, the optimal state depends on system size. For instance, for $N = 4$ qubits, we identified the 2-AC state (5.26) as the one that maintains minimal purity throughout its evolution, and is thus optimal for late time estimation of the depolarisation rate.

In Appendix 5.A, we show that the dynamics of a spin system interacting with an electromagnetic thermal bath at arbitrary temperature T can also be effectively described by anisotropic depolarisation. The interaction with the bath leads to spontaneous and stimulated emission and absorption processes resulting in the following master equation for the spin density matrix ρ

$$\begin{aligned}\frac{d\rho}{dt} =&\gamma_0 (\bar{n}+1)\left[2J_-\rho J_+ - (J_+J_-\rho + \rho J_+J_-)\right] \\ &+ \gamma_0 \bar{n}\left[2J_+\rho J_- - (J_-J_+\rho + \rho J_-J_+)\right].\end{aligned} \tag{5.45}$$

where $\gamma_0 = 4\omega_0^3|\mathbf{d}|^2/3c^3$ is the spontaneous emission rate (with $\mathbf{d}$ is the electric dipole of the spin), $\bar{n} = (e^{\omega_0/k_BT} - 1)^{-1}$ is the mean number of thermal photons at the atomic transition frequency ω_0. By applying a strong driving field described by the Hamiltonian $H = \omega J_x$ with $\omega \gg \gamma_0(\bar{n}+1)$, we show that the master equation (5.45) can be expressed in the rotating frame with respect to the strong driving term ωJ_x as

$$\frac{d\rho}{dt} = \frac{\gamma_0(2\bar{n}+1)}{2}\left([J_x,[J_x,\rho]] + [J_y,[J_y,\rho]]\right) + \gamma_0(2\bar{n}+1)[J_z,[J_z,\rho]]. \tag{5.46}$$

which is of the form of anisotropic depolarisation. From this, we identify the depolarisation rates as

$$\gamma \equiv \gamma_z = \gamma_0(2\bar{n}+1) = 2\gamma_{\perp z}.$$

Since γ is directly related to the thermal occupation number $\bar{n}$, which in turn depends on the temperature T, the measurement of γ provides a method for inferring the temperature of the thermal bath, thus enabling dynamical quantum thermometry.

Conclusion

In this chapter, we presented a general study of the depolarisation dynamics of an arbitrary spin, equivalent to a multiqubit system in a symmetric state, using tools from quantum information theory. A simple analytical solution to the general master equation (5.1) was obtained in the multipole operator basis and exploited to find the states featuring the most rapid decoherence, both for isotropic and anisotropic depolarisation.

In the case of isotropic depolarisation, we proved that pure or mixed state entanglement between the constituent qubits is a necessary condition for superdecoherence to occur, in contrast to the closely related phenomenon of superradiance which can occur without any entanglement [298]. We found the relations (5.23) and (5.25) between the initial decoherence rate of pure states and their purity AC measures of order 1 and 2. This allowed us to identify the AC states as the spin states which exhibit the highest initial decoherence rates and lead to the states with the lowest purity at any time, starting from a pure state. The entanglement of the different families of states listed in Table 5.1 and its evolution over time was studied numerically. More precisely, the entanglement survival time, that we lower- and upper-bounded using the PPT entanglement criterion and a sufficient separability criterion based on the P function, was shown to scale as $1/N$ with N the number of qubits, consistently with the bound (5.27). Although other families of states show the same scaling, we found the entanglement of AC states to be more fragile to depolarisation than for GHZ, W or even Dicke states. The $t_{\mathrm{ES}} \sim 1/N$ scaling we found is also different from that of individual, rather than collective, decoherence. We attribute this difference to superdecoherence that is absent for individual depolarisation. A detailed analysis for a few qubits showed that isotropic depolarisation can lead to the dynamical creation of PPT entanglement across balanced bipartitions (see e.g. Figure 5.6). Then, we studied when a state enters the ball of SAS states of radius (5.29). The states belonging to this ball are too mixed for any unitary operation to create entanglement. It was found that pure states with maximum order of anticoherence enter this ball after a time roughly independent of the number of qubits, in sharp contrast to other states for which this time increases linearly with N. This again points to the extreme fragility of entanglement in AC states against depolarisation.

In the case of anisotropic depolarisation, we first related the initial purity loss rate to the variances of the spin components in a pure state (5.34). We then showed for any spin that the maximum purity loss rate at short times is achieved by the GHZ states for $\gamma_z > \gamma_{\perp z}$ and by the balanced Dicke state for $\gamma_z < \gamma_{\perp z}$. As for the dynamics at longer times, we have completely identified the pure states of $N = 2$ and $N = 4$ qubits that display the lowest purity after an arbitrary fixed time. The extremal states for $N = 4$ were found to exhibit a transition from the GHZ/balanced Dicke state to a parametric AC state given by (5.42).

Finally, we explored the use of depolarisation in dynamical quantum metrology. We showed that the fidelity between an initial pure state $\rho = |\psi\rangle\langle\psi|$ and its depolarised version $\rho(t)$ is directly related to the purity of $\rho(t)$. This allowed us to identify the states that lose their purity the fastest under isotropic and anisotropic depolarisation as the optimal state for dynamical quantum metrology tasks, such as quantum thermometry.

Regarding the perspectives of this work, the entanglement dynamics for anisotropic depolarisation deserves further investigation. In particular, the question remains whether entanglement between the constituent qubits is a necessary condition for superdecoherence to occur in this case. Another perspective this work suggests is to analyse the

potential of AC, GHZ and Dicke balanced spin states, which we have shown to be the most sensitive to isotropic or anisotropic depolarisation, for quantum parameter estimation and quantum sensing strategies based on decoherence, in line with the works [307, 308]. In particular, it would be interesting to find the optimal measurement time for the estimation of the depolarisation rate based on the results of Section 5.4 and compare our results with those present in other works [305].

5.A Models of depolarisation

In this Appendix, we present models that provide a physical basis for the master equation (5.3).

5.A.1 Noisy magnetic field

A first model, inspired from [309], is that of a spin system interacting with a fluctuating magnetic field $\mathbf{B}(t)$. The interaction Hamiltonian is

$$H_{\text{int}} = -\mu \mathbf{J} \cdot \mathbf{B}$$

where $\mathbf{J} = (J_x, J_y, J_z)$ and $\mathbf{m} = \mu \mathbf{J}$ is the spin magnetic moment. We choose a coarse-graining time Δt for the evolution and make the assumption that this time is much larger than the correlation time τ_c of the fluctuations of the magnetic field. Then, assuming white noise and isotropic magnetic field fluctuations, the two-time correlation functions of the components of $\mathbf{B}(t)$ are given by

$$\overline{B_\alpha(t_1) B_\beta(t_2)} = \frac{B^2}{3} \tau_c \delta(t_1 - t_2) \delta_{\alpha\beta}$$

where $\alpha, \beta = (x, y, z)$ and an overbar denotes the ensemble average over realizations of the stochastic process. Finally, if we make the Born approximation that no correlations appear between the system and the magnetic field, by taking the limit $\Delta t \to dt$, it can be shown that the evolution reduces to

$$\frac{d\rho}{dt} = \sum_{\alpha=x,y,z} \gamma \big[J_\alpha, [J_\alpha, \rho]\big]$$

where $\gamma = \tau_c \omega_0^2/2$ and $\omega_0 = \mu B/(\sqrt{3}\hbar)$ is the effective Larmor frequency. The limit $\Delta t \to dt$ is valid as long as $\Delta t \ll \tau_s$ where $\tau_s = 1/\gamma$ is the typical evolution time of the system, hence $\tau_c \ll \Delta t \ll \tau_s$.

5.A.2 Thermal bath

5.A.2.1 Infinite temperature

As a second model, we consider a collection of two-level atoms with electric dipole moment $\mathbf{d}$, interacting collectively with the electromagnetic field in thermal equilibrium. This system is governed by the standard superradiant master equation [310]

$$\begin{aligned} \frac{d\rho}{dt} &= \gamma_0 (\bar{n} + 1) \left[2 J_- \rho J_+ - (J_+ J_- \rho + \rho J_+ J_-)\right] \\ &\quad + \gamma_0 \bar{n} \left[2 J_+ \rho J_- - (J_- J_+ \rho + \rho J_- J_+)\right] \end{aligned} \tag{5.47}$$

where $\gamma_0 = 4\omega_0^3 |\mathbf{d}|^2/3\hbar c^3$ is the spontaneous emission rate and $\bar{n} = (e^{\hbar\omega_0/k_B T} - 1)^{-1}$ is the average number of thermal photons at the atomic transition frequency ω_0. The first term accounts for both spontaneous and thermally induced emission, while the second term describes absorption due to the thermal bath. In the high-temperature limit $k_B T \gg \hbar\omega_0$, we have $\overline{n} \gg 1$ and $\overline{n} + 1 \approx \overline{n}$, so that emission and absorption processes occur at approximately equal rates. Under this approximation, the master equation simplifies to

$$\frac{d\rho}{dt} = -\gamma_{\perp z} \left([J_x, [J_x, \rho]] + [J_y, [J_y, \rho]]\right)$$

where $\gamma_{\perp z} = 2\gamma_0 \overline{n}$ and thus provides a model for anisotropic depolarisation.

5.A.2.2 Finite temperature

Inspired by the results in [311], we now generalize the above result to describe a spin-j system coupled to a thermal electromagnetic bath at an arbitrary temperature T, under the influence of a strong coherent drive. The system is immersed in a thermal bath at temperature T, and we apply a strong driving Hamiltonian $H = \omega J_x$, where $\omega \gg \gamma_0(\bar{n}+1)$. The full dynamics of the density matrix is then governed by

$$\begin{aligned}\frac{d\rho}{dt} &= -i\left[H,\rho\right] + \gamma_0\left(\bar{n}+1\right)\left[2J_-\rho J_+ - \left(J_+J_-\rho + \rho J_+J_-\right)\right] \\ &\quad +\gamma_0\bar{n}\left[2J_+\rho J_- - \left(J_-J_+\rho + \rho J_-J_+\right)\right].\end{aligned} \tag{5.48}$$

Moving to the rotating frame with respect to the strong driving term ωJ_x, the ladder operators evolve as

$$\tilde{J}_\pm = e^{i\omega J_x t} J_\pm e^{-i\omega J_x t} = J_x \pm i\left(J_y\cos\left(\omega t\right) + J_z\sin\left(\omega t\right)\right)$$

We now compute the transformed dissipator. Focusing on the first term, we get

$$\begin{aligned}\tilde{J}_-\rho\tilde{J}_+ &= J_x\rho J_x + J_y\rho J_y\cos^2\left(\omega t\right) + J_z\rho J_z\sin^2\left(\omega t\right) \\ &\quad -iJ_x\rho J_y\cos\left(\omega t\right) - iJ_x\rho J_z\sin\left(\omega t\right) + iJ_y\rho J_z\cos\left(\omega t\right)\sin\left(\omega t\right) \\ &\quad +iJ_y\rho J_x\cos\left(\omega t\right) + +iJ_z\rho J_x\cos\left(\omega t\right) + iJ_z\rho J_y\cos\left(\omega t\right)\sin\left(\omega t\right).\end{aligned}$$

Because $\omega \gg \gamma_0(\bar{n}+1)$, we take the time-average over the fast oscillations, yielding the effective approximation

$$\tilde{J}_-\rho\tilde{J}_+ \simeq J_x\rho J_x + \frac{1}{2}\left(J_y\rho J_y + J_z\rho J_z\right)$$

Applying the same procedure to the remaining terms, we obtain the master equation

$$\frac{d\rho}{dt} = \gamma_0\left(2\bar{n}+1\right)\left[J_x,\left[J_x,\rho\right]\right] + \frac{\gamma_0\left(2\bar{n}+1\right)}{2}\left(\left[J_y,\left[J_y,\rho\right]\right] + \left[J_z,\left[J_z,\rho\right]\right]\right).$$

To recover the anisotropic depolarisation form, we perform a final rotation of the reference frame by an angle $\pi/2$ about the y-axis. The resulting master equation reads

$$\frac{d\rho}{dt} = \frac{\gamma_0\left(2\bar{n}+1\right)}{2}\left(\left[J_x,\left[J_x,\rho\right]\right] + \left[J_y,\left[J_y,\rho\right]\right]\right) + \gamma_0\left(2\bar{n}+1\right)\left[J_z,\left[J_z,\rho\right]\right]. \tag{5.49}$$

We thus obtain an anisotropic depolarisation model with rates

$$\gamma_z = \gamma_0\left(2\bar{n}+1\right) = 2\gamma_{\perp z}.$$

In Figure 5.9, we plot the average fidelity between the evolution predicted by the full master equation (5.48) and the effective depolarisation model (5.49) over 1000 random initial states. As expected, the agreement between the two improves with increasing ω, validating the approximation in the strong driving regime.

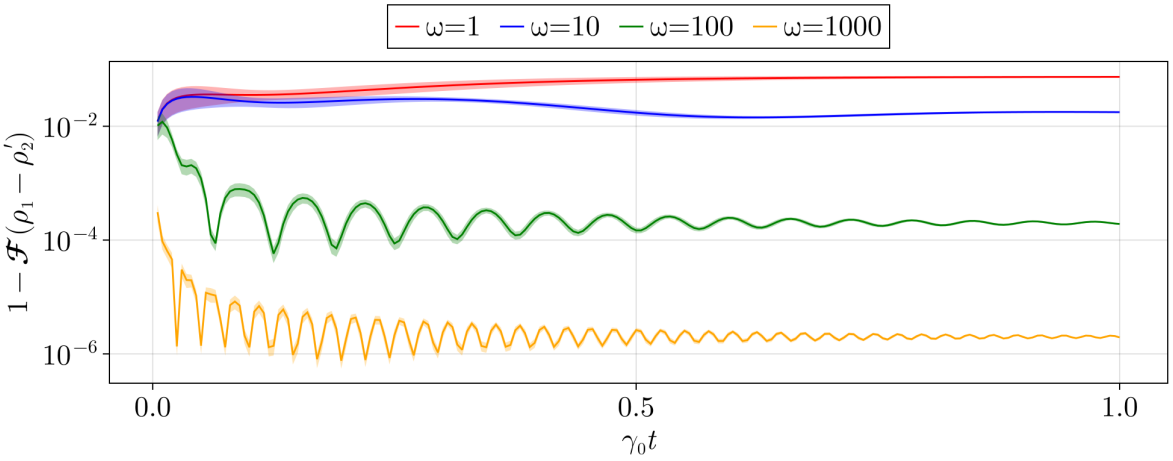

Figure 5.9: Average infidelity $1-\mathcal{F}(\rho_1,\rho_2')$ where $\rho_1(t)$ and $\rho_2(t) = e^{i\frac{\pi}{2}J_y}e^{iJ_x\gamma_0 t}\rho_2' e^{-iJ_x\gamma_0 t}e^{-i\frac{\pi}{2}J_y}$ evolve according to the master equations (5.48) and (5.49), respectively. The fidelity is computed over 1000 random initial pure states of $N=4$ qubits, evolved from $\gamma_0 t=0$ to $\gamma_0 t=1$ with $\bar{n}=2$, for different values of the driving strength ω. The colored areas represent the standard deviation based on the 1000 random state evolutions.

5.A.3 Continuous measurement

Finally, a third model is based on a weak continuous measurement of the spin components. When an observable A of a quantum system is continuously measured with an apparatus and that the measurement is not read out, the system evolves according to [312]

$$\frac{d\rho}{dt} = -\gamma\,[A,[A,\rho]] \tag{5.50}$$

with $\gamma>0$ a constant proportional to the strength of the measurement. We immediately recognize the form of the dissipator (5.2). Thus, in order to obtain the full master equation (5.3), the three collective spin observables J_x, J_y and J_z must be simultaneously subjected to a continuous measurement. Because these observables are not compatible, cross terms of the form $[J_\alpha,[J_\beta,\rho]]$ with $\alpha\neq\beta$ appear in addition to the simple sum of terms of the form (5.50). However, these extra terms can be neglected within the Born-Markov approximation [313].

5.B Master equation in the multipolar basis

In this appendix, we rewrite the master equation (5.1) in the multipolar basis which helps us to find analytical solutions to it as explained in the main text. To shorten the expressions, we use the short-hand notation $\sum_{L,M}$ for $\sum_{L=0}^{N}\sum_{M=-L}^{L}$.

As the Lindblad operators J_α ($\alpha=x,y,z$) are Hermitian, the dissipator

$$\mathcal{D}_\alpha(\rho) = \gamma_\alpha\left(2J_\alpha\rho J_\alpha - J_\alpha J_\alpha\rho - \rho J_\alpha J_\alpha\right)$$

can be rewritten as

$$\mathcal{D}_\alpha(\rho) = -\gamma_\alpha\,[J_\alpha,[J_\alpha,\rho]]\,.$$

Let us first consider $\mathcal{D}_z(\rho)$. Using [69]

$$[J_z, T_{LM}] = \sqrt{L\,(L+1)}C^{LM}_{LM;10}T_{LM},$$

we get

$$\mathcal{D}_z\,(\rho) = -\gamma_z \sum_{L,M} \rho_{LM}\,[L\,(L+1)]\,\left(C^{LM}_{LM;10}\right)^2 T_{LM}$$

From $C^{LM}_{LM;10} = M/\sqrt{L\,(L+1)}$, we conclude that the state multipoles ρ_{LM} evolve under depolarisation along z according to

$$\dot{\rho}_{LM}\,(t)\,|_{\mathcal{D}_z} \equiv \mathrm{Tr}\left[T^\dagger_{LM}\mathcal{D}_z\,(\rho)\right] = -\gamma_z\,M^2\rho_{LM}\,(t) \tag{5.51}$$

Next, we consider $\mathcal{D}_x\,(\rho)$. By writing $J_x = (J_+ + J_-)\,/2$ and using the commutator [69]

$$[J_\pm, T_{LM}] = \mp\sqrt{2L\,(L+1)}C^{LM\pm1}_{LM;1\pm1}T_{LM\pm1}$$

we get

$$\begin{aligned}
[J_x,\rho] &= \frac{1}{2}\sum_{L,M}\rho_{LM}\left([J_-,T_{LM}]+[J_+,T_{LM}]\right)\\
&= \frac{1}{2}\sum_{L,M}\sqrt{2L(L+1)}\rho_{LM}\times\\
&\qquad\left(C^{LM-1}_{LM;1-1}T_{LM-1} - C^{LM+1}_{LM;11}T_{LM+1}\right)
\end{aligned}$$

and therefore

$$\begin{aligned}
[J_x,[J_x,\rho]] = \frac{1}{2}\sum_{L,M}L(L+1)\rho_{LM}\Big[&C^{LM-1}_{LM;1-1}\left(C^{LM-2}_{LM-1;1-1}T_{LM-2} - C^{LM}_{LM-1;11}T_{LM}\right)\\
&- C^{LM+1}_{LM;11}\left(C^{LM}_{LM+1;1-1}T_{LM} - C^{LM+2}_{LM+1;11}T_{LM+2}\right)\Big].
\end{aligned}$$

Using the explicit formula for Clebsch-Gordan coefficients [69]

$$\begin{aligned}
C^{a+b-1\,\alpha+\beta}_{a\alpha;b\beta} &= 2\,(b\alpha - a\beta)\\
&\times\left(\frac{(2a+2b-1)\,(2a-1)!\,(2b-1)!\,(a+b+\alpha+\beta-1)!\,(a+b-\alpha-\beta-1)!}{(a+\alpha)!\,(a-\alpha)!\,(b+\beta)!\,(b-\beta)!\,(2a+2b)!}\right)^{1/2}
\end{aligned}$$

we eventually get

$$\dot{\rho}_{LM}(t)|_{\mathcal{D}_x} = -\frac{\gamma_x}{4}\left[2\left(L^2+L-M^2\right)\rho_{LM} + d^+_{LM}\,\rho_{LM+2} + d^-_{LM}\,\rho_{LM-2}\right] \tag{5.52}$$

where

$$d^\pm_{LM} = \sqrt{(L\mp M)(L\pm M+1)(L\mp M-1)(L\pm M+2)}.$$

A similar calculation for $J_y = (J_+ - J_-)/(2i)$ yields

$$\dot{\rho}_{LM}(t)|_{\mathcal{D}_y} = -\frac{\gamma_y}{4}\left[2\left(L^2+L-M^2\right)\rho_{LM} - d^+_{LM}\,\rho_{LM+2} - d^-_{LM}\,\rho_{LM-2}\right]. \tag{5.53}$$

Eventually, by adding all three contributions (5.51), (5.52) and (5.53), we get (5.4).

5.C Preservation of separability under isotropic depolarisation

In this Appendix, we show that the dynamics generated by the master equation (5.1) for $\gamma_x = \gamma_y = \gamma_z$ preserves the separability of states, i.e. that a separable state can only evolve into a separable state under isotropic depolarisation. As the Hamiltonian part only induces a rotation in the state space, it clearly preserves the separability of a state. For notational convenience, we set $\hbar = 1$ in the following. We start by rewriting the dissipative part of the master equation as

$$\sum_{\alpha=x,y,z} \mathcal{D}_\alpha(\rho) = \mathcal{D}_{+z}(\rho) + \mathcal{D}_{-z}(\rho) \tag{5.54}$$

where

$$\mathcal{D}_{\pm z}(\rho) = \gamma\Big(J_\pm \rho J_\mp - \frac{1}{2}\{J_\mp J_\pm, \rho\} + J_z \rho J_z - \frac{1}{2}\{J_z^2, \rho\}\Big).$$

We then follow the method of Gisin [314] to show that certain quantum diffusion equations for spin relaxation preserve spin-coherent states. This method is based on the unravelling of the master equation into stochastic quantum trajectories and will allow us to prove that both dissipators $\mathcal{D}_{\pm z}$ are separability preserving.

First, consider as in [314] the deterministic equation for the relaxation of a spin

$$\frac{d|\psi\rangle}{dt} = (\langle J_z\rangle - J_z)|\psi\rangle \tag{5.55}$$

If the initial state $|\psi\rangle$ is a coherent state, then at any later time the state will also be coherent (and therefore separable). This is because a state is coherent iff

$$|\langle \mathbf{J}\rangle|^2 \equiv \sum_{i=x,y,z} \langle J_i\rangle^2 = j^2,$$

and because $|\langle \mathbf{J}\rangle|^2$ is a quantity conserved under spin relaxation for a coherent initial state. Indeed, it holds that

$$\frac{d}{dt}|\langle \mathbf{J}\rangle|^2(t) = 2\sum_{i=x,y,z}\langle J_i\rangle\left(2\langle J_i\rangle\langle J_z\rangle - \langle\{J_i, J_z\}\rangle\right).$$

For a coherent state initially pointing in the direction of the unit vector $\mathbf{n}$, we have $\langle J_k\rangle = j n_k$ and $\langle\{J_k, J_\ell\}\rangle = j(2j+1)n_k n_\ell + j\delta_{k\ell}$, from which follows that

$$\frac{d}{dt}|\langle \mathbf{J}\rangle|^2(0) = 2j^2\sum_{i=x,y,z} n_k(n_k n_z - \delta_{kz}) = 0.$$

As the direction z in (5.55) is arbitrary, the result is equally valid for J_x and J_y. Moreover, a similar calculation shows that it is also valid for jump operators $J_\pm$. The next step is to write a stochastic differential equation (SDE) for the master equation (5.54). The Stratonovitch SDE associated with $\mathcal{D}_{\pm z}$ reads [315]

$$\begin{aligned} d|\psi\rangle \;=\; & \sqrt{\gamma}\left[(J_\pm - \langle J_\pm\rangle) + (J_z - \langle J_z\rangle)\right]|\psi\rangle\, d\xi \\ & + \gamma\left[\langle J_z\rangle(J_z - \langle J_z\rangle) - \frac{1}{2}J_z^2 + \frac{1}{2}\langle J_z^2\rangle\right]|\psi\rangle\, dt \\ & + \gamma\left[\langle J_\mp\rangle(J_\pm - \langle J_\pm\rangle) - \frac{1}{2}J_\mp J_\pm + \frac{1}{2}\langle J_\mp J_\pm\rangle\right]|\psi\rangle\, dt \end{aligned} \tag{5.56}$$

where the first line is the diffusion term and the second and third lines are the drift terms. Then, due to the relation $J_{\mp}J_{\pm} - J_z^2 = j\,(j+1) \mp J_z$, we can write

$$\begin{aligned}\langle J_-\rangle J_+ - \langle J_-\rangle \langle J_+\rangle &= \langle J_-\rangle (J_+ - \langle J_+\rangle)\langle J_-J_+\rangle + \langle J_z^2\rangle - J_-J_+ - J_z^2 \\ &= J_z - \langle J_z\rangle\end{aligned}$$

so that (5.56) can now be written as a sum of terms of the form (5.55) for the jump operators J_z and J_+. Both preserve spin-coherent states, which eventually shows that a coherent state remains coherent when subjected to isotropic depolarisation.

5.D Decoherence rates for pure states

In this Appendix, we use the short-hand notation $\sum_{L,M}$ for $\sum_{L=0}^{N}\sum_{M=-L}^{L}$. Our aim is to evaluate, for *pure states*, the decoherence rates of isotropic and anisotropic depolarisation appearing in (5.17) and (5.31). Up to a constant factor, these decoherence rates are given by

$$\sum_{L,M} L\,(L+1)\,|\rho_{LM}|^2$$

$$\sum_{L,M} M^2\,|\rho_{LM}|^2$$

$$\sum_{L,M} \left[L\,(L+1) - M^2\right]|\rho_{LM}|^2\,.$$

If the state is pure, we have

$$\mathrm{Tr}\left(\rho^2\right) = 1 \qquad \text{and} \qquad \mathrm{Tr}\left(\rho_{N-1}^2\right) = \mathrm{Tr}\left(\rho_1^2\right) \tag{5.57}$$

and (5.19) can be simplified into

$$\sum_{L,M} L\,(L+1)\,|\rho_{LM}|^2 = N\,(N+1) - N^2\mathrm{Tr}\left(\rho_1^2\right). \tag{5.58}$$

Now, it holds that for any state ρ (pure or mixed), $\mathrm{Tr}\,(\rho_1^2)$ can be expressed as a function of the sum of the variances $\Delta J_\alpha^2 = \langle J_\alpha^2\rangle - \langle J_\alpha\rangle$ of the spin components J_α ($\alpha = x, y, z$) in state ρ, a quantity also known as the total variance [316]

$$\mathbb{V} \equiv \sum_{\alpha=x,y,z} \Delta J_\alpha^2 = j\,(j+1) - |\langle \mathbf{J}\rangle|^2 \tag{5.59}$$

where $j = N/2$. The total variance quantifies the overall level of quantum fluctuations of the spin. It is minimal for spin coherent states and maximal for 1-AC states. In terms of total variance, we have [215]

$$\mathrm{Tr}\left(\rho_1^2\right) = 1 - \frac{\mathbb{V} - j}{2j^2} = \frac{N\,(N+1) - 2\mathbb{V}}{N^2}.$$

This relationship allows us to rewrite the first decoherence rate (5.58) as

$$\begin{aligned}\sum_{L,M} L\,(L+1)\,|\rho_{LM}|^2 &= 2\left(\Delta J_x^2 + \Delta J_y^2 + \Delta J_z^2\right) \\ &= N\left(\frac{N}{2}+1\right) - 2\,|\langle \mathbf{J}\rangle|^2\,.\end{aligned} \tag{5.60}$$

We then show that the second decoherence rate is given, for pure states, by

$$\sum_{L,M} M^2 \left|\rho_{LM}\right|^2 = 2\Delta J_z^2. \tag{5.61}$$

The left-hand side of this equation can be obtained by combining the commutator $[J_z, T_{LM}] = MT_{LM}$ with the expansion of the density operator in the MPB and the orthonormality relation $\mathrm{Tr}\left[T_{LM}^\dagger T_{L'M'}\right] = \delta_{LL'}\delta_{MM'}$ of the MPB as

$$\mathrm{Tr}\left(\left[J_z, \rho\right]\left[\rho, J_z\right]\right) = \sum_{L,M} M^2 \left|\rho_{LM}\right|^2. \tag{5.62}$$

For a pure state $\rho = |\psi\rangle\langle\psi|$, the left-hand side of (5.62) is equal to $2\Delta J_z^2$. Indeed, by expanding the commutators, we get

$$\mathrm{Tr}\left(\left[J_z, \rho\right]\left[\rho, J_z\right]\right) = 2\left[\mathrm{Tr}\left(J_z^2\rho^2\right) - \mathrm{Tr}\left(J_z\rho J_z\rho\right)\right].$$

The first term is given by

$$\mathrm{Tr}\left(J_z^2\rho^2\right) = \mathrm{Tr}\left(\langle\psi| J_z^2 |\psi\rangle\right) = \left\langle J_z^2\right\rangle$$

while the second term is given by

$$\begin{aligned}\mathrm{Tr}\left(J_z\rho J_z\rho\right) &= \mathrm{Tr}\left(J_z|\psi\rangle\langle\psi|J_z|\psi\rangle\langle\psi|\right)\\ &= \langle\psi|J_z|\psi\rangle\langle\psi|J_z|\psi\rangle = \langle J_z\rangle^2.\end{aligned}$$

Eventually, for pure states, it holds that $\mathrm{Tr}\left(\left[J_z, \rho\right]\left[\rho, J_z\right]\right) = 2\left(\left\langle J_z^2\right\rangle - \langle J_z\rangle^2\right) = 2\Delta J_z^2$.

Last, by substracting (5.61) from (5.60), we readily get the third decoherence rate

$$\sum_{L,M}\left[L\left(L+1\right) - M^2\right]\left|\rho_{LM}\right|^2 = 2\left(\Delta J_x^2 + \Delta J_y^2\right).$$

General conclusion and perspectives

This thesis has explored several fundamental aspects of spin and multiqubit quantum systems through the lens of entanglement, non-classicality, and anticoherence. The unifying theme of our work has been the interplay between these three manifestations of quantumness, examined from both theoretical and practical perspectives.

In the first part, from Chapter 2 to 3, we developed a rigorous framework for characterising the absolute non-classicality of spin-j states via Stratonovich-Weyl phase-space representations. We fully characterised the set of symmetric multiqubit states with absolutely positive linear phase-space representations via polytopes in the simplex of eigenvalues of the state ρ. Applied to the Sudarshan-Glauber P function, this extends our knowledge of symmetric absolutely separable states (SAS). Building on these results, we considered the phase-space representations of spin systems beyond the linear Stratonovitch-Weyl representations, to find larger sets of SAS states, for any number of qubits.

Leveraging again phase-space representations to characterise multiqubit entanglement, we established a quantitative link between the geometric measure of entanglement (GME) and Wehrl moments of the Husimi function. Using artificial neural networks, we showed that the GME of a state can be, in some cases, reliably estimated from partial information on the state, opening alternative ways to practical and scalable entanglement estimation protocols.

In Chapter 4, we focused on anticoherent (AC) states, a class of highly non-classical and maximally entangled symmetric multiqubit states. We illustrated the relation between the anticoherence of pure states and the delocalisation of their phase-space representations, highlighted their known utility in quantum metrology (rotosensing and magnetometry) and demonstrated their potential for quantum error correction, as AC subspaces automatically fulfill the Knill-Laflamme condition. Furthermore, we established a precise relationship between the Bures measure of anticoherence and entanglement negativity for pure states, showing that the two concepts are in fact intimately connected. Then, by disentangling the classical and quantum origins of anticoherence, we extended the measures of anticoherence to mixed states. Finally, we proposed an intuitive and experimentally implementable protocol for generating AC states across a variety of cold atoms platforms, via rotation and squeezing pulse-based controls.

Lastly, in Chapter 5, we studied the dynamics of spin systems under depolarisation, revealing the conditions for superdecoherence and its connection to entanglement. Our results show that AC states, while highly useful in metrology, are particularly fragile under isotropic depolarisation. This fragility, detrimental for rotosensing and magnetometry, could nevertheless be exploited in dissipative quantum metrology, for instance in noisy magnetometry. Similarly, GHZ states are sensitive to anisotropic depolarisation, a feature that can be harnessed in quantum thermometry to rapidly estimate environmental temperatures.

Overall, this thesis has contributed to uncover relations between phase-space nonclassicality, entanglement, and anticoherence in spin and symmetric multiqubit systems with both theoretical insights and experimental perspectives. The results open several research avenues, among which I find the following particularly promising.

Advanced protocols for generating AC states. A first direction concerns the design of more sophisticated protocols for the deterministic generation of AC states, possibly involving continuous control of rotations and squeezing. While the pulse-based protocol we proposed is already efficient and feasible in current experimental platforms, its intuitive structure could be the basis for finding improved protocols that could reduce generation time, thereby mitigating decoherence, and enhance robustness against control errors. Developing such protocols would strengthen the experimental viability of AC states as resources for quantum metrology and quantum computing (via quantum error-correction).

Nonlinear phase-space representations. Another direction lies in extending nonlinear phase-space representations of spin systems, potentially with the aid of new mathematical tools. Such generalisations would not only refine the characterisation of SAS states but could also shed new light on broader properties of spin systems. A central open question is whether the number of terms required in the multipolar expansion of phase-space representations (for $L > 2j + 1$) to fully characterise the SAS set is finite or infinite. Answering this would already advance our understanding of separability and phase-space structure in finite-dimensional quantum systems.

Quantum metrology from mixed anticoherence measures. A third avenue is to investigate the connection between our newly defined measure of anticoherence for mixed states and quantum metrology. Building on the relation established between the QFI and anticoherence measures of pure states, and noting that our anticoherence measure for mixed states are maximised precisely for optimal mixed quantum rotosensors [213], it would be highly valuable to establish a direct link between our AC measure and the QFI of rotosensing protocols for mixed states.

Bibliography

1. Einstein, A., Podolsky, B. & Rosen, N. Can Quantum-Mechanical Description of Physical Reality Be Considered Complete? *Phys. Rev.* **47,** 777–780. https://link.aps.org/doi/10.1103/PhysRev.47.777 (1935).
2. D'Ariano, G. M. & Perinotti, P. Quantum Information and Foundations. *Entropy* **22.** ISSN: 1099-4300. https://www.mdpi.com/1099-4300/22/1/22 (2020).
3. Bong, K.-W. *et al.* A strong no-go theorem on the Wigner's friend paradox. *Nature Physics* **16,** 1199–1205. ISSN: 1745-2481. https://doi.org/10.1038/s41567-020-0990-x (2020).
4. Horodecki, R., Horodecki, P., Horodecki, M. & Horodecki, K. Quantum entanglement. *Rev. Mod. Phys.* **81,** 865–942. https://link.aps.org/doi/10.1103/RevModPhys.81.865 (2009).
5. Gharibian, S. Strong NP-hardness of the quantum separability problem. *Quantum Info. Comput.* **10,** 343–360. ISSN: 1533-7146 (2010).
6. Horodecki, M., Horodecki, P. & Horodecki, R. Separability of mixed states: necessary and sufficient conditions. *Physics Letters A* **223,** 1–8. ISSN: 0375-9601. https://www.sciencedirect.com/science/article/pii/S0375960196007062 (1996).
7. Peres, A. Separability Criterion for Density Matrices. *Phys. Rev. Lett.* **77,** 1413–1415. https://link.aps.org/doi/10.1103/PhysRevLett.77.1413 (1996).
8. Bennett, C. H. *et al.* Teleporting an unknown quantum state via dual classical and Einstein-Podolsky-Rosen channels. *Phys. Rev. Lett.* **70,** 1895–1899. https://link.aps.org/doi/10.1103/PhysRevLett.70.1895 (1993).
9. Riedel, M. F. *et al.* Atom-chip-based generation of entanglement for quantum metrology. *Nature* **464,** 1170–1173. ISSN: 1476-4687. https://doi.org/10.1038/nature08988 (2010).
10. Chitambar, E. & Gour, G. Quantum resource theories. *Rev. Mod. Phys.* **91,** 025001. https://link.aps.org/doi/10.1103/RevModPhys.91.025001 (2 Apr. 2019).
11. Serrano-Ensástiga, E. & Martin, J. Maximum entanglement of mixed symmetric states under unitary transformations. *SciPost Phys.* **15,** 120. https://scipost.org/10.21468/SciPostPhys.15.3.120 (2023).
12. Abellanet-Vidal, J., Müller-Rigat, G., Rajchel-Mieldzioć, G. & Sanpera, A. *Improving absolute separability bounds for arbitrary dimensions* 2024. arXiv: 2410.22415 [quant-ph]. https://arxiv.org/abs/2410.22415.

13. Louvet, J., Serrano-Ensástiga, E., Bastin, T. & Martin, J. Nonequivalence between absolute separability and positive partial transposition in the symmetric subspace. *Phys. Rev. A* **111,** 042418. https://link.aps.org/doi/10.1103/PhysRevA.111.042418 (2025).

14. Wigner, E. On the Quantum Correction For Thermodynamic Equilibrium. *Phys. Rev.* **40,** 749–759. https://link.aps.org/doi/10.1103/PhysRev.40.749 (1932).

15. Bartlett, S. D., Sanders, B. C., Braunstein, S. L. & Nemoto, K. Efficient Classical Simulation of Continuous Variable Quantum Information Processes. *Phys. Rev. Lett.* **88,** 097904. https://link.aps.org/doi/10.1103/PhysRevLett.88.097904 (9 Feb. 2002).

16. Kenfack, A. & Życzkowski, K. Negativity of the Wigner function as an indicator of non-classicality. *Journal of Optics B: Quantum and Semiclassical Optics* **6,** 396. https://dx.doi.org/10.1088/1464-4266/6/10/003 (2004).

17. Siyouri, F., Baz, M. E. & Hassouni, Y. The negativity of Wigner function as a measure of quantum correlations. *Quantum Information Processing* **15,** 4237–4252. ISSN: 1573-1332. https://doi.org/10.1007/s11128-016-1380-2 (2016).

18. Cerf, N. J., Hertz, A. & Van Herstraeten, Z. Complex-valued Wigner entropy of a quantum state. *Quantum Studies: Mathematics and Foundations* **11,** 331–362. ISSN: 2196-5617. https://doi.org/10.1007/s40509-024-00325-8 (2024).

19. Husimi, K. Some Formal Properties of the Density Matrix. *Proceedings of the Physico-Mathematical Society of Japan. 3rd Series* **22,** 264–314 (1940).

20. Kano, Y. A New Phase-Space Distribution Function in the Statistical Theory of the Electromagnetic Field. *Journal of Mathematical Physics* **6,** 1913–1915. ISSN: 0022-2488. eprint: https://pubs.aip.org/aip/jmp/article-pdf/6/12/1913/19064852/1913_1_online.pdf. https://doi.org/10.1063/1.1704739 (1965).

21. Glauber, R. J. Coherent and Incoherent States of the Radiation Field. *Phys. Rev.* **131,** 2766–2788. https://link.aps.org/doi/10.1103/PhysRev.131.2766 (1963).

22. Sudarshan, E. C. G. Equivalence of Semiclassical and Quantum Mechanical Descriptions of Statistical Light Beams. *Phys. Rev. Lett.* **10,** 277–279. https://link.aps.org/doi/10.1103/PhysRevLett.10.277 (1963).

23. Wootters, W. K. A Wigner-function formulation of finite-state quantum mechanics. *Annals of Physics* **176,** 1–21. ISSN: 0003-4916. https://www.sciencedirect.com/science/article/pii/000349168790176X (1987).

24. Galvão, E. F. Discrete Wigner functions and quantum computational speedup. *Phys. Rev. A* **71,** 042302. https://link.aps.org/doi/10.1103/PhysRevA.71.042302 (4 Apr. 2005).

25. Zimba, J. " Anticoherent " Spin States via the Majorana Representation. *Electronic Journal of Theoretical Physics,* 143–156 (2006).

26. Chryssomalakos, C. & Hernández-Coronado, H. Optimal quantum rotosensors. *Phys. Rev. A* **95,** 052125. https://link.aps.org/doi/10.1103/PhysRevA.95.052125 (2017).

27. Goldberg, A. Z. & James, D. F. V. Quantum-limited Euler angle measurements using anticoherent states. *Phys. Rev. A* **98,** 032113. https://link.aps.org/doi/10.1103/PhysRevA.98.032113 (2018).

28. Martin, J., Weigert, S. & Giraud, O. Optimal Detection of Rotations about Unknown Axes by Coherent and Anticoherent States. *Quantum* **4,** 285. ISSN: 2521-327X. https://doi.org/10.22331/q-2020-06-22-285 (2020).

29. Chryssomalakos, C., Hanotel, L., Guzmán-González, E. & Serrano-Ensástiga, E. Toponomic quantum computation. *Modern Physics Letters A* **37,** 2250184. eprint: https://doi.org/10.1142/S021773232250184X. https://doi.org/10.1142/S021773232250184X (2022).

30. Rudziński, M., Burchardt, A. & Życzkowski, K. Orthonormal bases of extreme quantumness. *Quantum* **8,** 1234. ISSN: 2521-327X. https://doi.org/10.22331/q-2024-01-25-1234 (Jan. 2024).

31. Bouchard, F. *et al.* Quantum metrology at the limit with extremal Majorana constellations. *Optica* **4,** 1429–1432. https://opg.optica.org/optica/abstract.cfm?URI=optica-4-11-1429 (2017).

32. Denis, J., Davis, J., Mann, R. B. & Martin, J. Polytopes of Absolutely Wigner Bounded Spin States. *Quantum* **8,** 1550. ISSN: 2521-327X. https://doi.org/10.22331/q-2024-12-04-1550 (Dec. 2024).

33. Serrano-Ensástiga, E., Denis, J. & Martin, J. Absolute-separability witnesses for symmetric multiqubit states. *Phys. Rev. A* **109,** 022430. https://link.aps.org/doi/10.1103/PhysRevA.109.022430 (2024).

34. Denis, J., Damanet, F. & Martin, J. Estimation of the geometric measure of entanglement with Wehrl moments through artificial neural networks. *SciPost Phys.* **15,** 208. https://scipost.org/10.21468/SciPostPhys.15.5.208 (2023).

35. Denis, J., Read, C. & Martin, J. *Coherent Generation and Protection of Anticoherent Spin States* 2025. arXiv: 2505.06154 [quant-ph]. https://arxiv.org/abs/2505.06154.

36. Denis, J. & Martin, J. Extreme depolarization for any spin. *Phys. Rev. Res.* **4,** 013178. https://link.aps.org/doi/10.1103/PhysRevResearch.4.013178 (2022).

37. Bezanson, J., Edelman, A., Karpinski, S. & Shah, V. B. Julia: A fresh approach to numerical computing. *SIAM Review* **59,** 65–98. https://epubs.siam.org/doi/10.1137/141000671 (2017).

38. Danisch, S. & Krumbiegel, J. Makie.jl: Flexible high-performance data visualization for Julia. *Journal of Open Source Software* **6,** 3349. https://doi.org/10.21105/joss.03349 (2021).

39. Littlejohn, R. G. *Notes 12: Rotations in Quantum Mechanics, and Rotations of Spin 1/2 Systems* Physics 221 Lecture Notes, University of California, Berkeley. Course notes, 2021-22 edition. 2021. https://bohr.physics.berkeley.edu/classes/221/2122/221.html.

40. Rauch, H. *et al.* Verification of coherent spinor rotation of fermions. *Physics Letters A* **54,** 425–427. ISSN: 0375-9601. https://www.sciencedirect.com/science/article/pii/0375960175907987 (1975).

41. Werner, S. A., Colella, R., Overhauser, A. W. & Eagen, C. F. Observation of the Phase Shift of a Neutron Due to Precession in a Magnetic Field. *Phys. Rev. Lett.* **35,** 1053–1055. https://link.aps.org/doi/10.1103/PhysRevLett.35.1053 (1975).

42. Biedenharn, L. C. & Louck, J. D. *Angular Momentum in Quantum Physics: Theory and Application* (Cambridge University Press, 1984).

43. Staley, M. Understanding quaternions and the Dirac belt trick. *European Journal of Physics* **31,** 467. https://dx.doi.org/10.1088/0143-0807/31/3/004 (2010).

44. Del Castillo, G. F. T. & Rubalcava-Garcia, I. *The Jones vector as a spinor and its representation on the Poincaré sphere* 2013. arXiv: 1303.4496 [math-ph]. https://arxiv.org/abs/1303.4496.

45. Wigner, E. P. *Group Theory and Its Application to the Quantum Mechanics of Atomic Spectra* https://www.sciencedirect.com/bookseries/pure-and-applied-physics/vol/5/suppl/C (Elsevier, 1962).

46. Mukhopadhyay, A. K. Wigner's Symmetry Representation Theorem. *Resonance* **19,** 900–916. ISSN: 0973-712X. https://doi.org/10.1007/s12045-014-0107-x (2014).

47. Hall, B. C. *Lie Groups, Lie Algebras, and Representations: An Elementary Introduction* ISBN: 978-3-319-13467-3. https://link.springer.com/book/10.1007/978-3-319-13467-3 (Springer International Publishing, 2015).

48. Cohen-Tannoudji, C., Diu, B. & Laloë, F. *Quantum Mechanics, Volume 2: Angular Momentum, Spin, and Approximation Methods* 2nd. ISBN: 9783527345540 (Wiley-VCH, Weinheim, Germany, 2019).

49. Erhard, M., Fickler, R., Krenn, M. & Zeilinger, A. Twisted photons: new quantum perspectives in high dimensions. *Light: Science & Applications* **7,** 17146. ISSN: 2047-7538. https://doi.org/10.1038/lsa.2017.146 (2018).

50. Satoor, T. *et al.* Partitioning dysprosium's electronic spin to reveal entanglement in nonclassical states. *Phys. Rev. Res.* **3,** 043001. https://link.aps.org/doi/10.1103/PhysRevResearch.3.043001 (2021).

51. Low, P. J., White, B. M., Cox, A. A., Day, M. L. & Senko, C. Practical trapped-ion protocols for universal qudit-based quantum computing. *Phys. Rev. Res.* **2,** 033128. https://link.aps.org/doi/10.1103/PhysRevResearch.2.033128 (2020).

52. Neeley, M. *et al.* Emulation of a Quantum Spin with a Superconducting Phase Qudit. *Science* **325,** 722–725. eprint: https://www.science.org/doi/pdf/10.1126/science.1173440. https://www.science.org/doi/abs/10.1126/science.1173440 (2009).

53. Sawant, R. *et al.* Ultracold polar molecules as qudits. *New Journal of Physics* **22,** 013027. https://dx.doi.org/10.1088/1367-2630/ab60f4 (2020).

54. Happer, W. Optical Pumping. *Rev. Mod. Phys.* **44,** 169–249. https://link.aps.org/doi/10.1103/RevModPhys.44.169 (1972).

55. Sha, W. E. I., Lan, Z., Chen, M. L. N., Chen, Y. P. & Sun, S. Spin and Orbital Angular Momenta of Electromagnetic Waves: From Classical to Quantum Forms. *IEEE Journal on Multiscale and Multiphysics Computational Techniques* **9,** 113–117 (2024).

56. Krenn, M., Malik, M., Erhard, M. & Zeilinger, A. Orbital angular momentum of photons and the entanglement of Laguerre-Gaussian modes. *Philosophical Transactions of the Royal Society A* **375.** https://doi.org/10.1098/rsta.2015.0442 (2017).

57. Erhard, M., Krenn, M. & Zeilinger, A. Advances in high-dimensional quantum entanglement. *Nature Reviews Physics* **2,** 365–381. ISSN: 2522-5820. https://doi.org/10.1038/s42254-020-0193-5 (2020).

58. Willner, A. E. *et al.* Perspectives on advances in high-capacity, free-space communications using multiplexing of orbital-angular-momentum beams. *APL Photonics* **6,** 030901. ISSN: 2378-0967. eprint: https://pubs.aip.org/aip/app/article-pdf/doi/10.1063/5.0031230/20019188/030901_1_5.0031230.pdf. https://doi.org/10.1063/5.0031230 (2021).

59. Marrucci, L., Manzo, C. & Paparo, D. Optical Spin-to-Orbital Angular Momentum Conversion in Inhomogeneous Anisotropic Media. *Phys. Rev. Lett.* **96,** 163905. https://link.aps.org/doi/10.1103/PhysRevLett.96.163905 (2006).

60. Yurke, B., McCall, S. L. & Klauder, J. R. SU(2) and SU(1,1) interferometers. *Phys. Rev. A* **33,** 4033–4054. https://link.aps.org/doi/10.1103/PhysRevA.33.4033 (1986).

61. Dalton, B. J. & Ghanbari, S. Two mode theory of Bose-Einstein condensates: interferometry and the Josephson model. *Journal of Modern Optics* **59,** 287–353 (2012).

62. Schwinger, J. *On Angular Momentum* tech. rep. (Harvard Univ., Cambridge, MA (United States); Nuclear Development Associates, Inc. (US), 1952). https://www.osti.gov/biblio/4389568.

63. Chryssomalakos, C., Guzmán-González, E. & Serrano-Ensástiga, E. Geometry of spin coherent states. *Journal of Physics A: Mathematical and Theoretical* **51,** 165202. https://dx.doi.org/10.1088/1751-8121/aab349 (2018).

64. Jones, R. R. *Spin Coherent States and Statistical Physics* in (2019). https://api.semanticscholar.org/CorpusID:216142772.

65. Greenberger, D. M., Horne, M. A., Shimony, A. & Zeilinger, A. Bell's theorem without inequalities. *American Journal of Physics* **58,** 1131–1143. ISSN: 0002-9505. eprint: https://pubs.aip.org/aapt/ajp/article-pdf/58/12/1131/11479397/1131_1_online.pdf. https://doi.org/10.1119/1.16243 (Dec. 1990).

66. Baguette, D., Damanet, F., Giraud, O. & Martin, J. Anticoherence of spin states with point-group symmetries. *Phys. Rev. A* **92,** 052333. https://link.aps.org/doi/10.1103/PhysRevA.92.052333 (2015).

67. Baguette, D., Bastin, T. & Martin, J. Multiqubit symmetric states with maximally mixed one-qubit reductions. *Phys. Rev. A* **90,** 032314. https://link.aps.org/doi/10.1103/PhysRevA.90.032314 (2014).

68. Thompson, W. J. in *Angular Momentum* 305–344 (John Wiley & Sons, Ltd, 1994). ISBN: 9783527617821. eprint: https://onlinelibrary.wiley.com/doi/pdf/10.1002/9783527617821.ch8. https://onlinelibrary.wiley.com/doi/abs/10.1002/9783527617821.ch8.

69. Varshalovich, D. A., Moskalev, A. N. & Khersonskii, V. K. *Quantum Theory of Angular Momentum* (World Scientific, Singapore, 1988).

70. Agarwal, G. S. Relation between atomic coherent-state representation, state multipoles, and generalized phase-space distributions. *Phys. Rev. A* **24,** 2889–2896. https://link.aps.org/doi/10.1103/PhysRevA.24.2889 (1981).

71. Majorana, E. Atomi orientati in campo magnetico variabile. *Il Nuovo Cimento* **9,** 43. https://doi.org/10.1007/BF02960953 (1932).

72. Devi, A. R. U., Sudha & Rajagopal, A. K. Majorana representation of symmetric multiqubit states. *Quantum Inf. Process.* **11,** 685–710. https://doi.org/10.1007/s11128-011-0280-8 (2012).

73. Baguette, D. *Intrication maximale d'états multiqubits symétriques et interprétation en termes d'états de spin* French. PhD thesis (ULiège - Université de Liège, 2017).

74. Hillery, M., O'Connell, R., Scully, M. & Wigner, E. Distribution functions in physics: Fundamentals. *Physics Reports* **106,** 121–167. ISSN: 0370-1573. https://www.sciencedirect.com/science/article/pii/0370157384901601 (1984).

75. O'Connell, R. & Wigner, E. Quantum-mechanical distribution functions: Conditions for uniqueness. *Physics Letters A* **83,** 145–148. ISSN: 0375-9601. https://www.sciencedirect.com/science/article/pii/0375960181908707 (1981).

76. Dowling, J. P., Agarwal, G. S. & Schleich, W. P. Wigner distribution of a general angular-momentum state: Applications to a collection of two-level atoms. *Phys. Rev. A* **49,** 4101–4109. https://link.aps.org/doi/10.1103/PhysRevA.49.4101 (1994).

77. Curtright, T. L., Fairlie, D. B. & Zachos, C. K. *A Concise Treatise on Quantum Mechanics in Phase Space* eprint: https://www.worldscientific.com/doi/pdf/10.1142/8870. https://www.worldscientific.com/doi/abs/10.1142/8870 (WORLD SCIENTIFIC, 2014).

78. Davies, B. I. *et al.* Visualizing spin degrees of freedom in atoms and molecules. *Phys. Rev. A* **100,** 042102. https://link.aps.org/doi/10.1103/PhysRevA.100.042102 (2019).

79. Brif, C. & Mann, A. Phase-space formulation of quantum mechanics and quantum-state reconstruction for physical systems with Lie-group symmetries. *Phys. Rev. A* **59,** 971–987. https://link.aps.org/doi/10.1103/PhysRevA.59.971 (1999).

80. Tian, Y. *et al.* Measurement of complete and continuous Wigner functions for discrete atomic systems. *Phys. Rev. A* **97,** 013840. https://link.aps.org/doi/10.1103/PhysRevA.97.013840 (2018).

81. Chen, B. *et al.* Quantum state tomography of a single electron spin in diamond with Wigner function reconstruction. *Applied Physics Letters* **114,** 041102. ISSN: 0003-6951. eprint: https://pubs.aip.org/aip/apl/article-pdf/doi/10.1063/1.5082878/13034696/041102_1_online.pdf. https://doi.org/10.1063/1.5082878 (2019).

82. Rundle, R. P., Mills, P. W., Tilma, T., Samson, J. H. & Everitt, M. J. Simple procedure for phase-space measurement and entanglement validation. *Phys. Rev. A* **96,** 022117. https://link.aps.org/doi/10.1103/PhysRevA.96.022117 (2017).

83. Zurek, W. H. Decoherence and the Transition from Quantum to Classical. *Physics Today* **44,** 36–44. ISSN: 0031-9228. eprint: https://pubs.aip.org/physicstoday/article-pdf/44/10/36/8303336/36_1_online.pdf. https://doi.org/10.1063/1.881293 (1991).

84. Huber, J., Kirton, P. & Rabl, P. Phase-space methods for simulating the dissipative many-body dynamics of collective spin systems. *SciPost Phys.* **10,** 045. https://scipost.org/10.21468/SciPostPhys.10.2.045 (2021).

85. Mink, C. D., Petrosyan, D. & Fleischhauer, M. Hybrid discrete-continuous truncated Wigner approximation for driven, dissipative spin systems. *Phys. Rev. Res.* **4,** 043136. https://link.aps.org/doi/10.1103/PhysRevResearch.4.043136 (2022).

86. Mink, C. D. & Fleischhauer, M. Collective radiative interactions in the discrete truncated Wigner approximation. *SciPost Phys.* **15,** 233. https://scipost.org/10.21468/SciPostPhys.15.6.233 (2023).

87. Howard, M., Wallman, J., Veitch, V. & Emerson, J. Contextuality supplies the 'magic' for quantum computation. *Nature* **510,** 351–355. ISSN: 1476-4687. https://doi.org/10.1038/nature13460 (2014).

88. Delfosse, N., Allard Guerin, P., Bian, J. & Raussendorf, R. Wigner Function Negativity and Contextuality in Quantum Computation on Rebits. *Phys. Rev. X* **5,** 021003. https://link.aps.org/doi/10.1103/PhysRevX.5.021003 (2015).

89. Groenewold, H. On the principles of elementary quantum mechanics. *Physica* **12,** 405–460. ISSN: 0031-8914. https://www.sciencedirect.com/science/article/pii/S0031891446800594 (1946).

90. Moyal, J. E. Quantum mechanics as a statistical theory. *Mathematical Proceedings of the Cambridge Philosophical Society* **45,** 99–124 (1949).

91. Koczor, B., Zeier, R. & Glaser, S. J. Continuous phase-space representations for finite-dimensional quantum states and their tomography. *Phys. Rev. A* **101,** 022318. https://link.aps.org/doi/10.1103/PhysRevA.101.022318 (2020).

92. Khvedelidze, A. Generalizing Stratonovich–Weyl Axioms for Composite Systems. *Physics of Particles and Nuclei* **54,** 1025–1028. ISSN: 1531-8559. https://doi.org/10.1134/S1063779623060175 (2023).

93. Hudson, R. When is the wigner quasi-probability density non-negative? *Reports on Mathematical Physics* **6,** 249–252. ISSN: 0034-4877. https://www.sciencedirect.com/science/article/pii/003448777490007X (1974).

94. Luis, A. & Perina, J. Discrete Wigner function for finite-dimensional systems. *Journal of Physics A: Mathematical and General* **31,** 1423. https://dx.doi.org/10.1088/0305-4470/31/5/012 (1998).

95. Villegas, C. A. M., Chavez, A. C., Chumakov, S., Fofanov, Y. & Klimov, A. B. *On Discrete Quasiprobability Distributions* 2003. arXiv: quant-ph/0307051 [quant-ph]. https://arxiv.org/abs/quant-ph/0307051.

96. Žunkovič, B. Continuous phase-space methods on discrete phase spaces. *Europhysics Letters* **112,** 10003. https://dx.doi.org/10.1209/0295-5075/112/10003 (2015).

97. Schrödinger, E. Discussion of Probability Relations between Separated Systems. *Mathematical Proceedings of the Cambridge Philosophical Society* **31,** 555–563 (1935).

98. Bell, J. S. On the Einstein Podolsky Rosen paradox. *Physics Physique Fizika* **1,** 195–200. https://link.aps.org/doi/10.1103/PhysicsPhysiqueFizika.1.195 (3 Nov. 1964).

99. Freedman, S. J. & Clauser, J. F. Experimental Test of Local Hidden-Variable Theories. *Phys. Rev. Lett.* **28,** 938–941. https://link.aps.org/doi/10.1103/PhysRevLett.28.938 (1972).

100. Aspect, A., Dalibard, J. & Roger, G. Experimental Test of Bell's Inequalities Using Time-Varying Analyzers. *Phys. Rev. Lett.* **49,** 1804–1807. https://link.aps.org/doi/10.1103/PhysRevLett.49.1804 (1982).

101. Acín, A. *et al.* The quantum technologies roadmap: a European community view. *New Journal of Physics* **20,** 080201. https://dx.doi.org/10.1088/1367-2630/aad1ea (2018).

102. Bennett, C. H. & Brassard, G. Quantum cryptography: Public key distribution and coin tossing. *Theoretical Computer Science* **560.** Theoretical Aspects of Quantum Cryptography - celebrating 30 years of BB84, 7–11. ISSN: 0304-3975. https://www.sciencedirect.com/science/article/pii/S0304397514004241 (2014).

103. Huang, J., Zhuang, M. & Lee, C. Entanglement-enhanced quantum metrology: From standard quantum limit to Heisenberg limit. *Applied Physics Reviews* **11,** 031302. ISSN: 1931-9401. eprint: https://pubs.aip.org/aip/apr/article-pdf/doi/10.1063/5.0204102/20027645/031302_1_5.0204102.pdf. https://doi.org/10.1063/5.0204102 (2024).

104. Jozsa, R. & Linden, N. On the role of entanglement in quantum-computational speed-up. *Proceedings of the Royal Society A: Mathematical, Physical and Engineering Sciences* **459,** 2011–2032 (2003).

105. Werner, R. F. Quantum states with Einstein-Podolsky-Rosen correlations admitting a hidden-variable model. *Phys. Rev. A* **40,** 4277–4281. https://link.aps.org/doi/10.1103/PhysRevA.40.4277 (1989).

106. Kuś, M. & Życzkowski, K. Geometry of entangled states. *Phys. Rev. A* **63,** 032307. https://link.aps.org/doi/10.1103/PhysRevA.63.032307 (3 Feb. 2001).

107. Johnston, N. Separability from spectrum for qubit-qudit states. *Phys. Rev. A* **88,** 062330. https://link.aps.org/doi/10.1103/PhysRevA.88.062330 (6 Dec. 2013).

108. Gurvits, L. & Barnum, H. Largest separable balls around the maximally mixed bipartite quantum state. *Phys. Rev. A* **66,** 062311. https://link.aps.org/doi/10.1103/PhysRevA.66.062311 (6 Dec. 2002).

109. Friis, N., Vitagliano, G., Malik, M. & Huber, M. Entanglement certification from theory to experiment. *Nature Reviews Physics* **1,** 72–87. ISSN: 2522-5820. https://doi.org/10.1038/s42254-018-0003-5 (2019).

110. Hansenne, K. *Quantum Entanglement: A Study of Recent Separability Criteria* Master's thesis (Université de Liège, Liège, Belgium, 2020). https://hdl.handle.net/2268.2/9319.

111. Tóth, G. & Gühne, O. Entanglement and Permutational Symmetry. *Phys. Rev. Lett.* **102,** 170503. https://link.aps.org/doi/10.1103/PhysRevLett.102.170503 (2009).

112. Tóth, G. & Gühne, O. Separability criteria and entanglement witnesses for symmetric quantum states. *Applied Physics B* **98,** 617–622. ISSN: 1432-0649. https://doi.org/10.1007/s00340-009-3839-7 (2010).

113. Eckert, K., Schliemann, J., Bruß, D. & Lewenstein, M. Quantum Correlations in Systems of Indistinguishable Particles. *Annals of Physics* **299,** 88–127. ISSN: 0003-4916. https://www.sciencedirect.com/science/article/pii/S0003491602962688 (2002).

114. Giraud, O., Braun, P. & Braun, D. Classicality of spin states. *Phys. Rev. A* **78,** 042112. https://link.aps.org/doi/10.1103/PhysRevA.78.042112 (2008).

115. Plenio, M. B. & Virmani, S. *An introduction to entanglement measures* 2006. arXiv: quant-ph/0504163 [quant-ph]. https://arxiv.org/abs/quant-ph/0504163.

116. Vidal, G. & Werner, R. F. Computable measure of entanglement. *Phys. Rev. A* **65,** 032314. https://link.aps.org/doi/10.1103/PhysRevA.65.032314 (2002).

117. Johnston, N. & Patterson, E. The inverse eigenvalue problem for entanglement witnesses. *Linear Algebra and its Applications* **550,** 1–27. ISSN: 0024-3795. https://www.sciencedirect.com/science/article/pii/S002437951830154X (2018).

118. http://www.oq.ulg.ac.be/libspinACstates.html. Accessed: 2024-11-24.

119. http://polarization.markus-grassl.de/. Accessed: 2024-11-24.

120. Wei, T.-C. & Goldbart, P. M. Geometric measure of entanglement and applications to bipartite and multipartite quantum states. *Phys. Rev. A* **68,** 042307. https://link.aps.org/doi/10.1103/PhysRevA.68.042307 (2003).

121. Hübener, R., Kleinmann, M., Wei, T.-C., González-Guillén, C. & Gühne, O. Geometric measure of entanglement for symmetric states. *Phys. Rev. A* **80,** 032324. https://link.aps.org/doi/10.1103/PhysRevA.80.032324 (2009).

122. Martin, J., Giraud, O., Braun, P. A., Braun, D. & Bastin, T. Multiqubit symmetric states with high geometric entanglement. *Phys. Rev. A* **81,** 062347. https://link.aps.org/doi/10.1103/PhysRevA.81.062347 (2010).

123. Lee, S., Chi, D. P., Oh, S. D. & Kim, J. Convex-roof extended negativity as an entanglement measure for bipartite quantum systems. *Phys. Rev. A* **68,** 062304. https://link.aps.org/doi/10.1103/PhysRevA.68.062304 (2003).

124. Streltsov, A., Kampermann, H. & Bruß, D. Linking a distance measure of entanglement to its convex roof. *New Journal of Physics* **12,** 123004. https://dx.doi.org/10.1088/1367-2630/12/12/123004 (2010).

125. Fernholz, T. *et al.* Spin Squeezing of Atomic Ensembles via Nuclear-Electronic Spin Entanglement. *Phys. Rev. Lett.* **101,** 073601. https://link.aps.org/doi/10.1103/PhysRevLett.101.073601 (7 Aug. 2008).

126. Wong, H. Y. in *Quantum Computing Architecture and Hardware for Engineers: Step by Step* 129–142 (Springer Nature Switzerland, Cham, 2025). ISBN: 978-3-031-78219-0. https://doi.org/10.1007/978-3-031-78219-0_10.

127. Gilmore, R. Q and P representatives for spherical tensors. *Journal of Physics A: Mathematical and General* **9,** L65. https://dx.doi.org/10.1088/0305-4470/9/7/001 (1976).

128. Usha Devi, A. R., Prabhu, R. & Rajagopal, A. K. Collective multipolelike signatures of entanglement in symmetric N-qubit systems. *Phys. Rev. A* **76,** 012322. https://link.aps.org/doi/10.1103/PhysRevA.76.012322 (2007).

129. Davis, J., Kumari, M., Mann, R. B. & Ghose, S. Wigner negativity in spin-j systems. *Phys. Rev. Res.* **3,** 033134. https://link.aps.org/doi/10.1103/PhysRevResearch.3.033134 (2021).

130. Klimov, A. B., Romero, J. L. & De Guise, H. Generalized SU (2) covariant Wigner functions and some of their applications. *Journal of Physics A: Mathematical and Theoretical* **50,** 323001. https://doi.org/10.1088/1751-8121/50/32/323001 (2017).

131. Akim, È. L. & Levin, A. *A generating function for the Clebsch–Gordan coefficients* in *Doklady Akademii Nauk* **138** (1961), 503–505.

132. Gradshteyn, I. S. & Ryzhik, I. M. *Table of integrals, series, and products* (Academic press, 2014).

133. Champagne, G., Johnston, N., MacDonald, M. & Pipes, L. Spectral properties of symmetric quantum states and symmetric entanglement witnesses. *Linear Algebra Its Appl.* **649,** 273–300. ISSN: 0024-3795. http://dx.doi.org/10.1016/j.laa.2022.05.004 (2022).

134. Gross, D. Hudson's theorem for finHudsonite-dimensional quantum systems. *Journal of Mathematical Physics* **47,** 122107. ISSN: 0022-2488. eprint: https://pubs.aip.org/aip/jmp/article-pdf/doi/10.1063/1.2393152/16702548/122107_1_online.pdf. https://doi.org/10.1063/1.2393152 (2006).

135. Gross, D., Flammia, S. T. & Eisert, J. Most Quantum States Are Too Entangled To Be Useful As Computational Resources. *Phys. Rev. Lett.* **102,** 190501. https://link.aps.org/doi/10.1103/PhysRevLett.102.190501 (2009).

136. Gottesman, D. *The Heisenberg Representation of Quantum Computers* 1998. arXiv: quant-ph/9807006 [quant-ph]. https://arxiv.org/abs/quant-ph/9807006.

137. Aaronson, S. & Gottesman, D. Improved simulation of stabilizer circuits. *Phys. Rev. A* **70,** 052328. https://link.aps.org/doi/10.1103/PhysRevA.70.052328 (2004).

138. Veitch, V., Ferrie, C., Gross, D. & Emerson, J. Negative quasi-probability as a resource for quantum computation. *New Journal of Physics* **14,** 113011. https://dx.doi.org/10.1088/1367-2630/14/11/113011 (2012).

139. Mari, A. & Eisert, J. Positive Wigner Functions Render Classical Simulation of Quantum Computation Efficient. *Phys. Rev. Lett.* **109,** 230503. https://link.aps.org/doi/10.1103/PhysRevLett.109.230503 (2012).

140. Pashayan, H., Wallman, J. J. & Bartlett, S. D. Estimating Outcome Probabilities of Quantum Circuits Using Quasiprobabilities. *Phys. Rev. Lett.* **115,** 070501. https://link.aps.org/doi/10.1103/PhysRevLett.115.070501 (2015).

141. Delfosse, N., Okay, C., Bermejo-Vega, J., Browne, D. E. & Raussendorf, R. Equivalence between contextuality and negativity of the Wigner function for qudits. en. *New J. Phys.* **19,** 123024. ISSN: 1367-2630 (2017).

142. Schmid, D., Du, H., Selby, J. H. & Pusey, M. F. Uniqueness of Noncontextual Models for Stabilizer Subtheories. *Phys. Rev. Lett.* **129,** 120403. https://link.aps.org/doi/10.1103/PhysRevLett.129.120403 (2022).

143. Veitch, V., Hamed Mousavian, S. A., Gottesman, D. & Emerson, J. The resource theory of stabilizer quantum computation. *New J. Phys.* **16,** 013009. ISSN: 1367-2630 (2014).

144. Wang, X., Wilde, M. M. & Su, Y. Quantifying the magic of quantum channels. *New J. Phys.* **21,** 103002. ISSN: 1367-2630 (2019).

145. Abgaryan, V., Khvedelidze, A. & Torosyan, A. The Global Indicator of Classicality of an Arbitrary N-Level Quantum System. *J. Math. Sci.* **251,** 301–314. https://doi.org/10.1007/s10958-020-05092-6 (2020).

146. Abgaryan, V. & Khvedelidze, A. On Families of Wigner Functions for N-Level Quantum Systems. *Symmetry* **13,** 1013. https://doi.org/10.3390/sym13061013 (2021).

147. Marshall, A. W., Olkin, I. & Arnold, B. C. *Inequalities: Theory of Majorization and its applications* 2nd ed. (Springer New York, 2010).

148. Abgaryan, V., Khvedelidze, A. & Torosyan, A. Kenfack – Życzkowski indicator of nonclassicality for two non-equivalent representations of Wigner function of qutrit. *Phys. Lett. A* **412,** 127591. https://doi.org/10.1016/j.physleta.2021.127591 (2021).

149. Bohnet-Waldraff, F., Giraud, O. & Braun, D. Absolutely classical spin states. *Phys. Rev. A* **95,** 012318. https://link.aps.org/doi/10.1103/PhysRevA.95.012318 (2017).

150. Gherardini, S. & De Chiara, G. Quasiprobabilities in Quantum Thermodynamics and Many-Body Systems. *PRX Quantum* **5,** 030201. https://link.aps.org/doi/10.1103/PRXQuantum.5.030201 (2024).

151. Cahill, K. E. & Glauber, R. J. Density Operators and Quasiprobability Distributions. *Phys. Rev.* **177,** 1882–1902. https://link.aps.org/doi/10.1103/PhysRev.177.1882 (1969).

152. Lee, C. T. Measure of the nonclassicality of nonclassical states. *Phys. Rev. A* **44,** R2775–R2778. https://link.aps.org/doi/10.1103/PhysRevA.44.R2775 (1991).

153. Ganguly, N., Chatterjee, J. & Majumdar, A. S. Witness of mixed separable states useful for entanglement creation. *Phys. Rev. A* **89,** 052304. https://link.aps.org/doi/10.1103/PhysRevA.89.052304 (2014).

154. Arunachalam, S., Johnston, N. & Russo, V. Is absolute separability determined by the partial transpose? *Quantum Inf. Comput.* **15,** 694. https://doi.org/10.26421/QIC15.7-8-10 (2015).

155. Abbasli, N. *et al.* On Measures of Classicality/Quantumness in Quasiprobability Representations of Finite-Dimensional Quantum Systems. *Phys. Part. Nuclei* **51,** 443–447. https://doi.org/10.1134/s1063779620040024 (2020).

156. Ekert, A. K. *et al.* Direct Estimations of Linear and Nonlinear Functionals of a Quantum State. *Phys. Rev. Lett.* **88,** 217901. https://link.aps.org/doi/10.1103/PhysRevLett.88.217901 (2002).

157. Dunkl, C. & Życzkowski, K. Volume of the set of unistochastic matrices of order 3 and the mean Jarlskog invariant. *Journal of Mathematical Physics* **50,** 123521. ISSN: 0022-2488. https://doi.org/10.1063/1.3272543 (2009).

158. Diţă, P. Separation of unistochastic matrices from the double stochastic ones: Recovery of a 3×3 unitary matrix from experimental data. *Journal of Mathematical Physics* **47,** 083510. ISSN: 0022-2488. https://doi.org/10.1063/1.2229424 (2006).

159. Smith, A. C. *Unistochastic Matrices and Related Problems* in *Mathematics and Computing* (eds Mohapatra, R. N., Chowdhury, D. R. & Giri, D.) (Springer India, New Delhi, 2015), 239–250. ISBN: 978-81-322-2452-5.

160. Bengtsson, I., Ericsson, Å., Kuś, M., Tadej, W. & Życzkowski, K. Birkhoff's polytope and unistochastic matrices, N= 3 and N= 4. *Communications in mathematical physics* **259,** 307–324. https://doi.org/10.1007/s00220-005-1392-8 (2005).

161. Dahl, J. P., Mack, H., Wolf, A. & Schleich, W. P. Entanglement versus negative domains of Wigner functions. *Phys. Rev. A* **74,** 042323. https://link.aps.org/doi/10.1103/PhysRevA.74.042323 (2006).

162. Walschaers, M., Fabre, C., Parigi, V. & Treps, N. Entanglement and Wigner Function Negativity of Multimode Non-Gaussian States. *Phys. Rev. Lett.* **119,** 183601. https://link.aps.org/doi/10.1103/PhysRevLett.119.183601 (2017).

163. Arkhipov, I. I., Barasiński, A. & Svozilík, J. Negativity volume of the generalized Wigner function as an entanglement witness for hybrid bipartite states. *Scientific Reports* **8,** 16955. ISSN: 2045-2322. https://doi.org/10.1038/s41598-018-35330-6 (2018).

164. Zaw, L. H. Certifiable Lower Bounds of Wigner Negativity Volume and Non-Gaussian Entanglement with Conditional Displacement Gates. *Phys. Rev. Lett.* **133,** 050201. https://link.aps.org/doi/10.1103/PhysRevLett.133.050201 (2024).

165. Chabaud, U., Ghobadi, R., Beigi, S. & Rahimi-Keshari, S. Phase-space negativity as a computational resource for quantum kernel methods. *Quantum* **8,** 1519. ISSN: 2521-327X. https://doi.org/10.22331/q-2024-11-07-1519 (2024).

166. Huber, M., Erker, P., Schimpf, H., Gabriel, A. & Hiesmayr, B. Experimentally feasible set of criteria detecting genuine multipartite entanglement in n-qubit Dicke states and in higher-dimensional systems. *Phys. Rev. A* **83,** 040301. https://link.aps.org/doi/10.1103/PhysRevA.83.040301 (2011).

167. Tóth, G. Detection of multipartite entanglement in the vicinity of symmetric Dicke states. *J. Opt. Soc. Am. B* **24,** 275–282. https://opg.optica.org/josab/abstract.cfm?URI=josab-24-2-275 (2007).

168. Novo, L., Moroder, T. & Gühne, O. Genuine multiparticle entanglement of permutationally invariant states. *Phys. Rev. A* **88,** 012305. https://link.aps.org/doi/10.1103/PhysRevA.88.012305 (2013).

169. Weinbrenner, L. T. & Gühne, O. *Quantifying entanglement from the geometric perspective* 2025. arXiv: 2505.01394 [quant-ph]. https://arxiv.org/abs/2505.01394.

170. Hayashi, M., Markham, D., Murao, M., Owari, M. & Virmani, S. Bounds on Multipartite Entangled Orthogonal State Discrimination Using Local Operations and Classical Communication. *Phys. Rev. Lett.* **96,** 040501. https://link.aps.org/doi/10.1103/PhysRevLett.96.040501 (2006).

171. Bremner, M. J., Mora, C. & Winter, A. Are Random Pure States Useful for Quantum Computation? *Phys. Rev. Lett.* **102,** 190502. https://link.aps.org/doi/10.1103/PhysRevLett.102.190502 (2009).

172. Orús, R. Universal Geometric Entanglement Close to Quantum Phase Transitions. *Phys. Rev. Lett.* **100,** 130502. https://link.aps.org/doi/10.1103/PhysRevLett.100.130502 (2008).

173. Orús, R., Dusuel, S. & Vidal, J. Equivalence of Critical Scaling Laws for Many-Body Entanglement in the Lipkin-Meshkov-Glick Model. *Phys. Rev. Lett.* **101,** 025701. https://link.aps.org/doi/10.1103/PhysRevLett.101.025701 (2008).

174. Gnutzmann, S. & Życzkowski, K. Renyi-Wehrl entropies as measures of localization in phase space. *Journal of Physics A: Mathematical and General* **34,** 10123. https://dx.doi.org/10.1088/0305-4470/34/47/317 (2001).

175. Pilatowsky-Cameo, S. *et al.* Identification of quantum scars via phase-space localization measures. *Quantum* **6,** 644. ISSN: 2521-327X. https://doi.org/10.22331/q-2022-02-08-644 (2022).

176. Calixto, M. & Romera, E. Identifying topological-band insulator transitions in silicene and other 2D gapped Dirac materials by means of Renyi-Wehrl entropy. *Europhysics Letters* **109,** 40003. https://dx.doi.org/10.1209/0295-5075/109/40003 (2015).

177. Calixto, M., Cordero, N. A., Romera, E. & Castanos, O. Signatures of topological phase transitions in higher Landau levels of HgTe/CdTe quantum wells from an information theory perspective. *Physica A: Statistical Mechanics and its Applications* **605,** 128057. ISSN: 0378-4371. https://www.sciencedirect.com/science/article/pii/S0378437122006598 (2022).

178. Sugita, A. & Aiba, H. Second moment of the Husimi distribution as a measure of complexity of quantum states. *Phys. Rev. E* **65,** 036205. https://link.aps.org/doi/10.1103/PhysRevE.65.036205 (2002).

179. Bengtsson, I. & Życzkowski, K. *Geometry of Quantum States: An Introduction to Quantum Entanglement* 2nd ed. (Cambridge University Press, 2017).

180. Lieb, E. H. & Solovej, J. P. Proof of an entropy conjecture for Bloch coherent spin states and its generalizations. *Acta Mathematica* **212,** 379–398. https://doi.org/10.1007/s11511-014-0113-6 (2014).

181. Hardy, G., Littlewood, J. & Pólya, G. *Inequalities* ISBN: 9781107647398. https://books.google.be/books?id=EfvZAQAAQBAJ (Cambridge University Press, 1988).

182. Bastin, T. *et al.* Operational Families of Entanglement Classes for Symmetric N-Qubit States. *Phys. Rev. Lett.* **103,** 070503. https://link.aps.org/doi/10.1103/PhysRevLett.103.070503 (2009).

183. Wächter, A. & Biegler, L. T. On the Implementation of a Primal-Dual Interior Point Filter Line Search Algorithm for Large-Scale Nonlinear Programming. *Mathematical Programming* **106,** 25–57 (2006).

184. Streltsov, A., Kampermann, H. & Bruß, D. Simple algorithm for computing the geometric measure of entanglement. *Phys. Rev. A* **84,** 022323. https://link.aps.org/doi/10.1103/PhysRevA.84.022323 (2011).

185. Zhu, X., Zhang, C., An, Z. & Zeng, B. *Unified Framework for Calculating Convex Roof Resource Measures* 2024. arXiv: 2406.19683 [quant-ph]. https://arxiv.org/abs/2406.19683.

186. Zhang, Z., Dai, Y., Dong, Y.-L. & Zhang, C. Numerical and analytical results for geometric measure of coherence and geometric measure of entanglement. *Scientific Reports* **10,** 12122. https://doi.org/10.1038/s41598-020-68979-z (2020).

187. Watrous, J. *Semidefinite programs for completely bounded norms* 2009. arXiv: 0901.4709 [quant-ph]. https://arxiv.org/abs/0901.4709.

188. Watrous, J. *Simpler semidefinite programs for completely bounded norms* 2012. arXiv: 1207.5726 [quant-ph]. https://arxiv.org/abs/1207.5726.

189. Dunjko, V. & Briegel, H. J. Machine learning & artificial intelligence in the quantum domain: a review of recent progress. *Reports on Progress in Physics* **81,** 074001. https://dx.doi.org/10.1088/1361-6633/aab406 (2018).

190. Carleo, G. *et al.* Machine learning and the physical sciences. *Rev. Mod. Phys.* **91,** 045002. https://link.aps.org/doi/10.1103/RevModPhys.91.045002 (2019).

191. Torlai, G. *et al.* Neural-network quantum state tomography. *Nature Physics* **14,** 447–450. ISSN: 1745-2481. https://doi.org/10.1038/s41567-018-0048-5 (2018).

192. Ahmed, S., Sánchez Muñoz, C., Nori, F. & Kockum, A. F. Quantum State Tomography with Conditional Generative Adversarial Networks. *Phys. Rev. Lett.* **127,** 140502. https://link.aps.org/doi/10.1103/PhysRevLett.127.140502 (2021).

193. Quek, Y., Fort, S. & Ng, H. K. Adaptive quantum state tomography with neural networks. *npj Quantum Information* **7,** 105. ISSN: 2056-6387. https://doi.org/10.1038/s41534-021-00436-9 (2021).

194. Cimini, V., Barbieri, M., Treps, N., Walschaers, M. & Parigi, V. Neural Networks for Detecting Multimode Wigner Negativity. *Phys. Rev. Lett.* **125,** 160504. https://link.aps.org/doi/10.1103/PhysRevLett.125.160504 (2020).

195. Zhang, X.-M., Wei, Z., Asad, R., Yang, X.-C. & Wang, X. When does reinforcement learning stand out in quantum control? A comparative study on state preparation. *npj Quantum Information* **5,** 85. ISSN: 2056-6387. https://doi.org/10.1038/s41534-019-0201-8 (2019).

196. Mavadia, S., Frey, V., Sastrawan, J., Dona, S. & Biercuk, M. J. Prediction and real-time compensation of qubit decoherence via machine learning. *Nature Communications* **8,** 14106. ISSN: 2041-1723. https://doi.org/10.1038/ncomms14106 (2017).

197. Fösel, T., Tighineanu, P., Weiss, T. & Marquardt, F. Reinforcement Learning with Neural Networks for Quantum Feedback. *Phys. Rev. X* **8,** 031084. https://link.aps.org/doi/10.1103/PhysRevX.8.031084 (2018).

198. Che, M., Qi, L., Wei, Y. & Zhang, G. Geometric measures of entanglement in multipartite pure states via complex-valued neural networks. *Neurocomputing* **313,** 25–38. ISSN: 0925-2312. https://www.sciencedirect.com/science/article/pii/S0925231218306799 (2018).

199. Koutný, D. *et al.* Deep learning of quantum entanglement from incomplete measurements. *Science Advances* **9,** eadd7131. eprint: https://www.science.org/doi/pdf/10.1126/sciadv.add7131. https://www.science.org/doi/abs/10.1126/sciadv.add7131 (2023).

200. Harney, C., Pirandola, S., Ferraro, A. & Paternostro, M. Entanglement classification via neural network quantum states. *New Journal of Physics* **22,** 045001. https://dx.doi.org/10.1088/1367-2630/ab783d (2020).

201. Harney, C., Paternostro, M. & Pirandola, S. Mixed state entanglement classification using artificial neural networks. *New Journal of Physics* **23,** 063033. https://dx.doi.org/10.1088/1367-2630/ac0388 (2021).

202. Berkovits, R. Extracting many-particle entanglement entropy from observables using supervised machine learning. *Phys. Rev. B* **98,** 241411. https://link.aps.org/doi/10.1103/PhysRevB.98.241411 (2018).

203. Kingma, D. P. & Ba, J. *Adam: A Method for Stochastic Optimization* 2017. arXiv: 1412.6980 [cs.LG]. https://arxiv.org/abs/1412.6980.

204. Aulbach, M., Markham, D. & Murao, M. The maximally entangled symmetric state in terms of the geometric measure. *New Journal of Physics* **12,** 073025. https://dx.doi.org/10.1088/1367-2630/12/7/073025 (2010).

205. *R. H. Hardin and N. J. A. Sloane, Spherical Designs* http://neilsloane.com/sphdesigns/. Accessed: 2024-11-24.

206. Delsarte, P., Goethals, J. M. & Seidel, J. J. Spherical codes and designs. *Geom. Dedicata* **6,** 363. https://link.springer.com/article/10.1007/BF03187604 (1977).

207. Brif, C. & Mann, A. Inverted spectroscopy and interferometry for quantum-state reconstruction of systems with SU(2) symmetry. *Journal of Optics B: Quantum and Semiclassical Optics* **2,** 245. https://dx.doi.org/10.1088/1464-4266/2/3/305 (2000).

208. Bondarenko, A., Radchenko, D. & Viazovska, M. Optimal asymptotic bounds for spherical designs. English. *Ann. Math. (2)* **178,** 443–452. ISSN: 0003-486X (2013).

209. Wehrl, A. General properties of entropy. *Rev. Mod. Phys.* **50,** 221–260. https://link.aps.org/doi/10.1103/RevModPhys.50.221 (1978).

210. Wehrl, A. On the relation between classical and quantum-mechanical entropy. *Reports on Mathematical Physics* **16,** 353–358. ISSN: 0034-4877. https://www.sciencedirect.com/science/article/pii/0034487779900703 (1979).

211. Carleo, G. & Troyer, M. Solving the quantum many-body problem with artificial neural networks. *Science* **355,** 602–606. eprint: https://www.science.org/doi/pdf/10.1126/science.aag2302. https://www.science.org/doi/abs/10.1126/science.aag2302 (2017).

212. Kolenderski, P. & Demkowicz-Dobrzanski, R. Optimal state for keeping reference frames aligned and the platonic solids. *Phys. Rev. A* **78,** 052333. ISSN: 2469-9934 (2008).

213. Serrano-Ensástiga, E., Chryssomalakos, C. & Martin, J. Quantum metrology of rotations with mixed spin states. *Phys. Rev. A* **111,** 022435. https://link.aps.org/doi/10.1103/PhysRevA.111.022435 (2025).

214. Hervas, J. R. *et al.* Beyond the Quantum Cramér-Rao Bound. *Phys. Rev. Lett.* **134,** 010804. https://link.aps.org/doi/10.1103/PhysRevLett.134.010804 (2025).

215. Baguette, D. & Martin, J. Anticoherence measures for pure spin states. *Phys. Rev. A* **96,** 032304. https://link.aps.org/doi/10.1103/PhysRevA.96.032304 (2017).

216. Pereira, R. & Paul-Paddock, C. Anticoherent subspaces. *Journal of Mathematical Physics* **58,** 062107. ISSN: 0022-2488. eprint: https://pubs.aip.org/aip/jmp/article-pdf/doi/10.1063/1.4986413/14062628/062107_1_online.pdf. https://doi.org/10.1063/1.4986413 (2017).

217. Knill, E. & Laflamme, R. Theory of quantum error-correcting codes. *Phys. Rev. A* **55,** 900–911. https://link.aps.org/doi/10.1103/PhysRevA.55.900 (1997).

218. Gross, J. A. Designing Codes around Interactions: The Case of a Spin. *Phys. Rev. Lett.* **127,** 010504. https://link.aps.org/doi/10.1103/PhysRevLett.127.010504 (2021).

219. Omanakuttan, S., Buchemmavari, V., Gross, J. A., Deutsch, I. H. & Marvian, M. Fault-Tolerant Quantum Computation Using Large Spin-Cat Codes. *PRX Quantum* **5,** 020355. https://link.aps.org/doi/10.1103/PRXQuantum.5.020355 (2024).

220. Ferretti, H. *et al.* Generating a 4-photon tetrahedron state: toward simultaneous super-sensitivity to non-commuting rotations. *Optica Quantum* **2,** 91–102. https://opg.optica.org/opticaq/abstract.cfm?URI=opticaq-2-2-91 (2024).

221. *L. Alonso, Beautiful Makie* https://beautiful.makie.org/dev/. Accessed: 2025-02-14.

222. Björk, G. *et al.* Extremal quantum states and their Majorana constellations. *Phys. Rev. A* **92,** 031801. https://link.aps.org/doi/10.1103/PhysRevA.92.031801 (2015).

223. Giraud, O., Braun, D., Baguette, D., Bastin, T. & Martin, J. Tensor Representation of Spin States. *Phys. Rev. Lett.* **114,** 080401. https://link.aps.org/doi/10.1103/PhysRevLett.114.080401 (2015).

224. Martin, J. *Library of spin anticoherent states* Online webpage. Accessed: 2025-06-02. 2025. http://www.oq.ulg.ac.be/libspinACstates.html.

225. Grassl, M. *Markus Grassl's Homepage - Research on Polarization & Quantum Codes* http://polarization.markus-grassl.de/. Accessed: 2025-07-17. 2025.

226. Uhlmann, A. The "transition probability" in the state space of a *-algebra. *Rep. Math. Phys.* **9,** 273–279. ISSN: 0034-4877. https://www.sciencedirect.com/science/article/pii/0034487776900604 (1976).

227. Jozsa, R. Fidelity for Mixed Quantum States. *J. Mod. Opt.* **41,** 2315–2323. https://doi.org/10.1080/09500349414552171 (1994).

228. Hervas, J. R. *et al.* Higher-order corrections to the quantum Cramér-Rao bound. *Phys. Rev. A* **112,** 022426. https://link.aps.org/doi/10.1103/ltz3-163t (2 Aug. 2025).

229. Tóth, G. & Apellaniz, I. Quantum metrology from a quantum information science perspective. *Journal of Physics A: Mathematical and Theoretical* **47,** 424006. https://dx.doi.org/10.1088/1751-8113/47/42/424006 (2014).

230. Braunstein, S. L. & Caves, C. M. Statistical distance and the geometry of quantum states. *Phys. Rev. Lett.* **72,** 3439–3443. https://link.aps.org/doi/10.1103/PhysRevLett.72.3439 (22 1994).

231. Zhou, S. & Jiang, L. *An exact correspondence between the quantum Fisher information and the Bures metric* 2019. arXiv: 1910.08473 [quant-ph]. https://arxiv.org/abs/1910.08473.

232. Sidhu, J. S. & Kok, P. Geometric perspective on quantum parameter estimation. *AVS Quantum Science* **2,** 014701. ISSN: 2639-0213. eprint: https://pubs.aip.org/avs/aqs/article-pdf/doi/10.1116/1.5119961/16700179/014701_1_online.pdf. https://doi.org/10.1116/1.5119961 (2020).

233. Ma, J., Wang, X., Sun, C. & Nori, F. Quantum spin squeezing. *Physics Reports* **509,** 89–165. ISSN: 0370-1573. https://www.sciencedirect.com/science/article/pii/S0370157311002201 (2011).

234. Yang, Y. A. *et al.* Minute-scale Schrödinger-cat state of spin-5/2 atoms. *Nature Photonics* **19,** 89–94. ISSN: 1749-4893. https://doi.org/10.1038/s41566-024-01555-3 (2025).

235. Leibfried, D. *et al.* Toward Heisenberg-Limited Spectroscopy with Multiparticle Entangled States. *Science* **304,** 1476–1478. eprint: https://www.science.org/doi/pdf/10.1126/science.1097576. https://www.science.org/doi/abs/10.1126/science.1097576 (2004).

236. Chalopin, T. *et al.* Quantum-enhanced sensing using non-classical spin states of a highly magnetic atom. *Nature* **9.** https://doi.org/10.1038/s41467-018-07433-1 (2018).

237. Wright, J. *Lecture 4: Knill–Laflamme Conditions* Scribe notes, CS 294: Quantum Coding Theory, UC Berkeley. Scribe: Shilun Li. Lecture given on February 2, 2024. Feb. 2024. https://people.eecs.berkeley.edu/~jswright/quantumcodingtheory24/scribe%20notes/lecture04.pdf.

238. Lim, S., Liu, J. & Ardavan, A. Fault-tolerant qubit encoding using a spin-7/2 qudit. *Phys. Rev. A* **108,** 062403. https://link.aps.org/doi/10.1103/PhysRevA.108.062403 (2023).

239. Tian, T., Luo, Y. & Li, Y. Generalised monogamy relation of convex-roof extended negativity in multi-level systems. *Scientific Reports* **6,** 36700. ISSN: 2045-2322. https://doi.org/10.1038/srep36700 (2016).

240. Yang, X. & Luo, M.-X. Unified monogamy relation of entanglement measures. *Quantum Information Processing* **20,** 108. ISSN: 1573-1332. https://doi.org/10.1007/s11128-021-03041-z (2021).

241. Tao, Y.-H., Zheng, K., Jin, Z.-X. & Fei, S.-M. Tighter Monogamy Relations for Concurrence and Negativity in Multiqubit Systems. *Mathematics* **11.** ISSN: 2227-7390. https://www.mdpi.com/2227-7390/11/5/1159 (2023).

242. Bourin, J.-C. & Hiai, F. Norm and anti-norm inequalities for positive semi-definite matrices. *International Journal of Mathematics* **22,** 1121–1138. eprint: https://doi.org/10.1142/S0129167X1100715X. https://doi.org/10.1142/S0129167X1100715X (2011).

243. Giorda, P., Zanardi, P. & Lloyd, S. Universal quantum control in irreducible state-space sectors: Application to bosonic and spin-boson systems. *Phys. Rev. A* **68,** 062320. https://link.aps.org/doi/10.1103/PhysRevA.68.062320 (2003).

244. Merkel, S. T., Jessen, P. S. & Deutsch, I. H. Quantum control of the hyperfine-coupled electron and nuclear spins in alkali-metal atoms. *Phys. Rev. A* **78,** 023404. https://link.aps.org/doi/10.1103/PhysRevA.78.023404 (2008).

245. Kitagawa, M. & Ueda, M. Squeezed spin states. *Phys. Rev. A* **47,** 5138–5143. https://link.aps.org/doi/10.1103/PhysRevA.47.5138 (1993).

246. Chaudhury, S. *et al.* Quantum Control of the Hyperfine Spin of a Cs Atom Ensemble. *Phys. Rev. Lett.* **99,** 163002. https://link.aps.org/doi/10.1103/PhysRevLett.99.163002 (2007).

247. Evrard, A. *et al.* Enhanced Magnetic Sensitivity with Non-Gaussian Quantum Fluctuations. *Phys. Rev. Lett.* **122,** 173601. https://link.aps.org/doi/10.1103/PhysRevLett.122.173601 (2019).

248. Leroux, I. D., Schleier-Smith, M. H. & Vuletić, V. Implementation of Cavity Squeezing of a Collective Atomic Spin. *Phys. Rev. Lett.* **104,** 073602. https://link.aps.org/doi/10.1103/PhysRevLett.104.073602 (2010).

249. Gross, C., Zibold, T., Nicklas, E., Estève, J. & Oberthaler, M. K. Nonlinear atom interferometer surpasses classical precision limit. *Nature* **464,** 1165–1169. ISSN: 1476-4687. https://doi.org/10.1038/nature08919 (2010).

250. Li, Z. *et al.* Collective Spin-Light and Light-Mediated Spin-Spin Interactions in an Optical Cavity. *PRX Quantum* **3.** ISSN: 2691-3399. http://dx.doi.org/10.1103/PRXQuantum.3.020308 (2022).

251. Omanakuttan, S., Mitra, A., Martin, M. J. & Deutsch, I. H. Quantum optimal control of ten-level nuclear spin qudits in ^{87}Sr. *Phys. Rev. A* **104,** L060401. https://link.aps.org/doi/10.1103/PhysRevA.104.L060401 (2021).

252. Segura Carrillo, E. *et al. Quantum Computing with Strontium-87: New Capabilities for Neutral Atom Systems* in *APS Division of Atomic, Molecular and Optical Physics Meeting Abstracts* **2024** (2024), D00.089.

253. Sørensen, A. S. & Mølmer, K. Entangling atoms in bad cavities. *Phys. Rev. A* **66,** 022314. https://link.aps.org/doi/10.1103/PhysRevA.66.022314 (2002).

254. Hosten, O., Krishnakumar, R., Engelsen, N. J. & Kasevich, M. A. Quantum phase magnification. *Science* **352,** 1552–1555. https://www.science.org/doi/abs/10.1126/science.aaf3397 (2016).

255. Bohnet, J. G. *et al.* Quantum spin dynamics and entanglement generation with hundreds of trapped ions. *Science* **352,** 1297–1301. https://www.science.org/doi/abs/10.1126/science.aad9958 (2016).

256. Carrasco, S. C. *et al.* Extreme Spin Squeezing via Optimized One-Axis Twisting and Rotations. *Phys. Rev. Appl.* **17,** 064050. https://link.aps.org/doi/10.1103/PhysRevApplied.17.064050 (2022).

257. Müller, M. M., Said, R. S., Jelezko, F., Calarco, T. & Montangero, S. One decade of quantum optimal control in the chopped random basis. *Reports on Progress in Physics* **85,** 076001. https://dx.doi.org/10.1088/1361-6633/ac723c (2022).

258. https://github.com/Jerome-Denis/ACStatesGeneration.

259. Asaad, S. *et al.* Coherent electrical control of a single high-spin nucleus in silicon. *Nature* **579,** 205–209. ISSN: 1476-4687. https://doi.org/10.1038/s41586-020-2057-7 (2020).

260. Gupta, P., Vaartjes, A., Yu, X., Morello, A. & Sanders, B. C. Robust macroscopic Schrödinger's cat on a nucleus. *Phys. Rev. Res.* **6,** 013101. https://link.aps.org/doi/10.1103/PhysRevResearch.6.013101 (2024).

261. Agarwal, G. S., Puri, R. R. & Singh, R. P. Atomic Schrödinger cat states. *Phys. Rev. A* **56,** 2249–2254. https://link.aps.org/doi/10.1103/PhysRevA.56.2249 (1997).

262. Mølmer, K. & Sørensen, A. Multiparticle Entanglement of Hot Trapped Ions. *Phys. Rev. Lett.* **82,** 1835–1838. https://link.aps.org/doi/10.1103/PhysRevLett.82.1835 (1999).

263. Cieśliński, P., Kłobus, W., Kurzyński, P., Paterek, T. & Laskowski, W. The fastest generation of multipartite entanglement with natural interactions. *New Journal of Physics* **25,** 093040. https://dx.doi.org/10.1088/1367-2630/acf953 (2023).

264. Huang, J., Huo, H., Zhuang, M. & Lee, C. Efficient generation of spin cat states with twist-and-turn dynamics via machine optimization. *Phys. Rev. A* **105,** 062456. https://link.aps.org/doi/10.1103/PhysRevA.105.062456 (2022).

265. Dengis, S., Wimberger, S. & Schlagheck, P. Accelerated creation of NOON states with ultracold atoms via counterdiabatic driving. *Phys. Rev. A* **111,** L031301. https://link.aps.org/doi/10.1103/PhysRevA.111.L031301 (2025).

266. Ansel, Q., Sugny, D. & Bellomo, B. Exploring the limits of the generation of non-classical states of spins coupled to a cavity by optimal control. *Physical Review A* **105.** ISSN: 2469-9934. http://dx.doi.org/10.1103/PhysRevA.105.042618 (2022).

267. Alexander, B., Bollinger, J. J. & Uys, H. Generating Greenberger-Horne-Zeilinger states with squeezing and postselection. *Physical Review A* **101.** ISSN: 2469-9934. http://dx.doi.org/10.1103/PhysRevA.101.062303 (2020).

268. Goldberg, A. Z. *et al.* Robust quantum metrology with random Majorana constellations. *Quantum Science and Technology* **10,** 015053. ISSN: 2058-9565. http://dx.doi.org/10.1088/2058-9565/ad9ac7 (2024).

269. Dziurawiec, M. *et al.* Accelerating many-body entanglement generation by dipolar interactions in the Bose-Hubbard model. *Phys. Rev. A* **107,** 013311. https://link.aps.org/doi/10.1103/PhysRevA.107.013311 (2023).

270. Zhang, X., Hu, Z. & Liu, Y.-C. Fast Generation of GHZ-like States Using Collective-Spin XYZ Model. *Phys. Rev. Lett.* **132,** 113402. https://link.aps.org/doi/10.1103/PhysRevLett.132.113402 (2024).

271. Alexander, B. J., Bollinger, J. J. & Tame, M. S. Robustness of the projected squeezed state protocol. *Phys. Rev. A* **109,** 052614. https://link.aps.org/doi/10.1103/PhysRevA.109.052614 (2024).

272. Saffman, M., Oblak, D., Appel, J. & Polzik, E. S. Spin squeezing of atomic ensembles by multicolor quantum nondemolition measurements. *Physical Review A* **79.** ISSN: 1094-1622. http://dx.doi.org/10.1103/PhysRevA.79.023831 (2009).

273. Carollo, F., Lasanta, A. & Lesanovsky, I. Exponentially Accelerated Approach to Stationarity in Markovian Open Quantum Systems through the Mpemba Effect. *Phys. Rev. Lett.* **127,** 060401. https://link.aps.org/doi/10.1103/PhysRevLett.127.060401 (2021).

274. Moroder, M., Culhane, O., Zawadzki, K. & Goold, J. Thermodynamics of the Quantum Mpemba Effect. *Phys. Rev. Lett.* **133,** 140404. https://link.aps.org/doi/10.1103/PhysRevLett.133.140404 (2024).

275. Zhang, J. *et al.* Observation of quantum strong Mpemba effect. *Nature Communications* **16,** 301. ISSN: 2041-1723. https://doi.org/10.1038/s41467-024-54303-0 (2025).

276. Cavina, V. *et al.* Bridging thermodynamics and metrology in nonequilibrium quantum thermometry. *Phys. Rev. A* **98,** 050101. https://link.aps.org/doi/10.1103/PhysRevA.98.050101 (2018).

277. Frazão, G., Pezzutto, M., Omar, Y., Zambrini Cruzeiro, E. & Gherardini, S. Coherence-Enhanced Single-Qubit Thermometry out of Equilibrium. *Entropy* **26.** ISSN: 1099-4300. https://www.mdpi.com/1099-4300/26/7/568 (2024).

278. Simon, C. & Kempe, J. Robustness of multiparty entanglement. *Phys. Rev. A* **65,** 052327. https://link.aps.org/doi/10.1103/PhysRevA.65.052327 (2002).

279. Dür, W. & Briegel, H.-J. Stability of Macroscopic Entanglement under Decoherence. *Phys. Rev. Lett.* **92,** 180403. https://link.aps.org/doi/10.1103/PhysRevLett.92.180403 (2004).

280. Hein, M., Dür, W. & Briegel, H.-J. Entanglement properties of multipartite entangled states under the influence of decoherence. *Phys. Rev. A* **71,** 032350. https://link.aps.org/doi/10.1103/PhysRevA.71.032350 (2005).

281. Aolita, L., Chaves, R., Cavalcanti, D., Acín, A. & Davidovich, L. Scaling Laws for the Decay of Multiqubit Entanglement. *Phys. Rev. Lett.* **100,** 080501. https://link.aps.org/doi/10.1103/PhysRevLett.100.080501 (2008).

282. Wang, X., Miranowicz, A., Liu, Y.-x., Sun, C. P. & Nori, F. Sudden vanishing of spin squeezing under decoherence. *Phys. Rev. A* **81,** 022106. https://link.aps.org/doi/10.1103/PhysRevA.81.022106 (2010).

283. Rivas, Á. & Luis, A. SU(2)-invariant depolarization of quantum states of light. *Phys. Rev. A* **88,** 052120. https://link.aps.org/doi/10.1103/PhysRevA.88.052120 (2013).

284. Benedict, M. G. & Czirják, A. Wigner functions, squeezing properties, and slow decoherence of a mesoscopic superposition of two-level atoms. *Phys. Rev. A* **60,** 4034–4044. https://link.aps.org/doi/10.1103/PhysRevA.60.4034 (1999).

285. Kosloff, R. Quantum Thermodynamics: A Dynamical Viewpoint. *Entropy* **15,** 2100–2128. ISSN: 1099-4300. https://www.mdpi.com/1099-4300/15/6/2100 (2013).

286. Dann, R. & Kosloff, R. Open system dynamics from thermodynamic compatibility. *Phys. Rev. Res.* **3,** 023006. https://link.aps.org/doi/10.1103/PhysRevResearch.3.023006 (2021).

287. Lidar, D., Shabani, A. & Alicki, R. Conditions for strictly purity-decreasing quantum Markovian dynamics. *Chemical Physics* **322.** Real-time dynamics in complex quantum systems, 82–86. ISSN: 0301-0104. https://www.sciencedirect.com/science/article/pii/S0301010405002752 (2006).

288. Tidström, J. & Sjöqvist, E. Uhlmann's geometric phase in presence of isotropic decoherence. *Phys. Rev. A* **67,** 032110. https://link.aps.org/doi/10.1103/PhysRevA.67.032110 (2003).

289. Klimov, A. B., Romero, J. L. & Sánchez-Soto, L. L. Simple quantum model for light depolarization. *J. Opt. Soc. Am. B* **23,** 126–133. https://opg.optica.org/josab/abstract.cfm?URI=josab-23-1-126 (2006).

290. Arsenijevic, M., Jeknic-Dugic, J. & Dugic, M. Generalized Kraus Operators for the One-Qubit Depolarizing Quantum Channel. *Brazilian Journal of Physics* **47,** 339–349. ISSN: 1678-4448. https://doi.org/10.1007/s13538-017-0502-3 (2017).

291. Chen, H.-B. Effects of symmetry breaking of the structurally-disordered Hamiltonian ensembles on the anisotropic decoherence of qubits. *Scientific Reports* **12,** 2869. ISSN: 2045-2322. https://doi.org/10.1038/s41598-022-06891-4 (2022).

292. Bhattacharya, S., Misra, A., Mukhopadhyay, C. & Pati, A. K. Exact master equation for a spin interacting with a spin bath: Non-Markovianity and negative entropy production rate. *Phys. Rev. A* **95,** 012122. https://link.aps.org/doi/10.1103/PhysRevA.95.012122 (2017).

293. Hornberger, K. in *Entanglement and Decoherence: Foundations and Modern Trends* (eds Buchleitner, A., Viviescas, C. & Tiersch, M.) 221–276 (Springer Berlin Heidelberg, Berlin, Heidelberg, 2009). ISBN: 978-3-540-88169-8. https://doi.org/10.1007/978-3-540-88169-8_5.

294. Nielsen, M. A. & Chuang, I. L. *Quantum Computation and Quantum Information: 10th Anniversary Edition* (Cambridge University Press, 2010).

295. Kattemölle, J. & van Wezel, J. Conditions for superdecoherence. *Quantum* **4,** 265. ISSN: 2521-327X. https://doi.org/10.22331/q-2020-05-14-265 (2020).

296. Berman, G. P., Kamenev, D. I. & Tsifrinovich, V. I. Collective decoherence of the superpositional entangled states in the quantum Shor algorithm. *Phys. Rev. A* **71,** 032346. https://link.aps.org/doi/10.1103/PhysRevA.71.032346 (2005).

297. Monz, T. *et al.* 14-Qubit Entanglement: Creation and Coherence. *Phys. Rev. Lett.* **106,** 130506. https://link.aps.org/doi/10.1103/PhysRevLett.106.130506 (2011).

298. Wolfe, E. & Yelin, S. F. Certifying Separability in Symmetric Mixed States of N Qubits, and Superradiance. *Phys. Rev. Lett.* **112,** 140402. https://link.aps.org/doi/10.1103/PhysRevLett.112.140402 (2014).

299. Korbicz, J. K., Cirac, J. I. & Lewenstein, M. Spin Squeezing Inequalities and Entanglement of N Qubit States. *Phys. Rev. Lett.* **95,** 120502. https://link.aps.org/doi/10.1103/PhysRevLett.95.120502 (2005).

300. Horodecki, M., Horodecki, P. & Horodecki, R. Mixed-State Entanglement and Distillation: Is there a "Bound" Entanglement in Nature? *Phys. Rev. Lett.* **80,** 5239–5242. https://link.aps.org/doi/10.1103/PhysRevLett.80.5239 (1998).

301. Aolita, L., de Melo, F. & Davidovich, L. Open-system dynamics of entanglement:a key issues review. *Reports on Progress in Physics* **78,** 042001. https://dx.doi.org/10.1088/0034-4885/78/4/042001 (2015).

302. Serafini, A., Siena, S. D., Illuminati, F. & Paris, M. G. A. Minimum decoherence cat-like states in Gaussian noisy channels. *Journal of Optics B: Quantum and Semiclassical Optics* **6,** S591. https://dx.doi.org/10.1088/1464-4266/6/6/019 (2004).

303. Le Jeannic, H., Cavaillès, A., Huang, K., Filip, R. & Laurat, J. Slowing Quantum Decoherence by Squeezing in Phase Space. *Phys. Rev. Lett.* **120,** 073603. https://link.aps.org/doi/10.1103/PhysRevLett.120.073603 (2018).

304. Brewster, R. A., Pittman, T. B. & Franson, J. D. Reduced decoherence using squeezing, amplification, and antisqueezing. *Phys. Rev. A* **98,** 033818. https://link.aps.org/doi/10.1103/PhysRevA.98.033818 (2018).

305. Mehboudi, M., Sanpera, A. & Correa, L. A. Thermometry in the quantum regime: recent theoretical progress. *Journal of Physics A: Mathematical and Theoretical* **52,** 303001. https://dx.doi.org/10.1088/1751-8121/ab2828 (2019).

306. Jevtic, S., Newman, D., Rudolph, T. & Stace, T. M. Single-qubit thermometry. *Phys. Rev. A* **91,** 012331. https://link.aps.org/doi/10.1103/PhysRevA.91.012331 (2015).

307. Gebbia, F. *et al.* Two-qubit quantum probes for the temperature of an Ohmic environment. *Phys. Rev. A* **101,** 032112. https://link.aps.org/doi/10.1103/PhysRevA.101.032112 (2020).

308. Kukita, S., Matsuzaki, Y. & Kondo, Y. *Heisenberg-limited quantum metrology using collective dephasing* 2021. arXiv: 2103.11612 [quant-ph]. https://arxiv.org/abs/2103.11612.

309. Müller, C. in *Entanglement and Decoherence: Foundations and Modern Trends* (eds Buchleitner, A., Viviescas, C. & Tiersch, M.) 277–314 (Springer Berlin Heidelberg, Berlin, Heidelberg, 2009). ISBN: 978-3-540-88169-8. https://doi.org/10.1007/978-3-540-88169-8_6.

310. Agarwal, G. S. in *Quantum Optics* (ed Höhler, G.) 1–128 (Springer Berlin Heidelberg, Berlin, Heidelberg, 1974). ISBN: 978-3-540-37918-8. https://doi.org/10.1007/BFb0042382.

311. Aharony Shapira, S. *et al.* Inverse Mpemba Effect Demonstrated on a Single Trapped Ion Qubit. *Phys. Rev. Lett.* **133,** 010403. https://link.aps.org/doi/10.1103/PhysRevLett.133.010403 (2024).

312. Jacobs, K. & Steck, D. A. A straightforward introduction to continuous quantum measurement. *Contemporary Physics* **47,** 279–303. eprint: https://doi.org/10.1080/00107510601101934. https://doi.org/10.1080/00107510601101934 (2006).

313. Jiang, C. & Watanabe, G. Quantum dynamics under simultaneous and continuous measurement of noncommutative observables. *Phys. Rev. A* **102,** 062216. https://link.aps.org/doi/10.1103/PhysRevA.102.062216 (2020).

314. Gisin, N. & Cibils, M. B. Quantum diffusions, quantum dissipation and spin relaxation. *Journal of Physics A: Mathematical and General* **25,** 5165. https://dx.doi.org/10.1088/0305-4470/25/19/024 (1992).

315. Diósi, L., Gisin, N. & Strunz, W. T. Non-Markovian quantum state diffusion. *Phys. Rev. A* **58,** 1699–1712. https://link.aps.org/doi/10.1103/PhysRevA.58.1699 (1998).

316. Klyachko, A. A. & Shumovsky, A. S. Entanglement, local measurements and symmetry. *Journal of Optics B: Quantum and Semiclassical Optics* **5,** S322. https://dx.doi.org/10.1088/1464-4266/5/3/364 (2003).